Land Subsidence and Rebound in the Houston Ship Channel and Downtown Houston (2000-2018)

A Thesis Presented to

the Faculty of the Department of Earth and Atmospheric Sciences

University of Houston

In Partial Fulfillment

of the Requirements for the Degree

Master of Science

By

Zachary Lawrence Parra

May 2019

Land Subsidence and Rebound in the Houston Ship Channel and Downtown Houston (2000-2018)

Zachary L. Parra

APPROVED:

Dr. Guoquan Wang, Chairman

Dr. Alexander Robinson

Dr. Juan Carlos Fernandez Diaz

Dr. Dan E. Wells, Dean, College of Natural Sciences and Mathematics

ACKNOWLEDGEMENTS

I would first like to acknowledge my indebtedness to my supervisor, Dr. Guoquan Wang, whose vested interest made this research project possible. His guidance and expertise have been invaluable throughout all stages of this work. I would also like to extend my gratitude to my research committee members, Dr. Alexander Robinson and Dr. Juan Carlos Fernandez Diaz, for their patience and insight.

Thanks to the United States Geological Survey (USGS) and National Geodetic Survey (NGS) for providing the raw groundwater and geodetic data utilized for this study. The public availability of their data archives allows the scientific community to conduct meaningful research. It is my sincerest hope that the research completed in this work will provided insight and aid in the efforts of local organizations to better understand linked subsidence and groundwater issues occurring in Houston.

Lastly, to my parents and fellow students that have helped me along, I cannot thank you enough.

Land Subsidence and Rebound in the Houston Ship Channel and Downtown Houston (2000-2018)

A Thesis Presented to

the Faculty of the Department of Earth and Atmospheric Sciences

University of Houston

In Partial Fulfillment

of the Requirements for the Degree

Master of Science

By

Zachary Lawrence Parra

May 2019

ABSTRACT

Widespread land subsidence resulting from the overexploitation of groundwater from the Gulf Coast Aquifer system has occurred and been observed in Greater Houston, TX for nearly a century. Extraction of groundwater can generate permanent land subsidence by causing the inelastic compaction of susceptible aquifer systems, typically unconsolidated alluvial systems comprised of interbedded aquifer and aquitard material. Although land subsidence persists to some degree throughout a majority of Greater Houston, slight land rebound has been observed within Downtown Houston and the area along the Houston Ship Channel. The purpose of this study is to summarize ground deformation, sediment compaction, and groundwater level changes that have occurred within the area of observed land rebound from 2000-2018. Moreover, the relationship between ground deformation and groundwater levels is utilized to estimate local preconsolidation heads. Global Positioning System (GPS) and borehole extensometer observations indicate that land rebound began in the region starting from 2001-2004 and that current rates of uplift range from ~0.6-4.0 mm/year. Borehole extensometer observations and seasonal modeling of GPS displacement and groundwater level time-series reveal that sediment compaction was widely confined within the Chicot aquifer in the area of observed land rebound. Preconsolidation head levels are considered to coincide with the termination of inelastic compaction and the onset of land rebound. Estimated preconsolidation heads for Downtown Houston and the Houston Ship Channel fall between 25-65 meters (Chicot) and 30-70 meters (Evangeline) below the land surface. The results from this study are important for understanding the mechanism of groundwater-withdrawal-induced land subsidence and for managing groundwater resources in the north and western parts of Greater Houston, where moderate to rapid land subsidence (~1-3 cm/year) is ongoing.

TABLE OF CONTENTS

LIST OF FIGURES

1 INTRODUCTION AND MOTIVATION

Land subsidence occurs in many regions around the world, particularly in populated urban and industrial sectors. Critical consequences of land subsidence include but are not limited to infrastructure damage, increased flooding risk, induced faulting, and reduction in total aquifer storage. Thus, land subsidence represents a geological hazard at a global scale. Since the early twentieth century, Greater Houston, Texas has provided one of the most extreme cases of land subsidence in the United States. Greater Houston, as intended in this study, is comprised of Harris, Galveston, Montgomery, Fort Bend, and Brazoria Counties (**Figure 1-1**). Accumulated land subsidence more than three meters during the last century has been well documented within a large area of southeast Houston encompassing the cities of Pasadena, Baytown, Texas City, and Galveston (Kasmarek et al., 2009). Land subsidence within the region is predominately caused by the depressurization and compaction of aquifer sediment due to excessive groundwater production (Kasmarek et al., 2012). In Greater Houston, groundwater has represented the primary water source for municipal, agricultural, and industrial usage throughout a majority of the twentieth century. Additionally, regional faults, salt dome movements, and hydrocarbon extraction (Coplin and Galloway, 1999) further compound the complexity of land subsidence within the region.

Recognizing the significance of land subsidence within Greater Houston, the United States Geological Survey (USGS) and Texas Legislature have established several groundwater regulatory districts since 1975 with the purpose of preventing further land subsidence: Harris-Galveston Subsidence District (HGSD), Fort Bend Subsidence

District (FBSD), Lone Star Groundwater Conservation District (LSGCD), and Brazoria County Groundwater District (BCGCD). These entities have worked in close conjunction with the USGS, National Geodetic Survey (NGS), University of Houston, and the City of Houston to develop infrastructure for monitoring land subsidence and other related ground deformation (Wang et al., 2015). From 1973 to 1980, the USGS established a network of borehole extensometers to quantify accumulated sediment compaction in the region. During the early 1990s, the HGSD and NGS established a network of approximately 20 Global Positioning System (GPS) stations to further monitor ongoing land subsidence (Zilkoski et al., 2003). Moreover, numerous Light Detection and Ranging (LiDAR) and Interferometric Synthetic Aperture Radar (InSAR) studies concerning land subsidence in Greater Houston have been undertaken (Qu et al., 2015; Khan et al., 2014; USGS, 2002; Bawden et al., 2012).

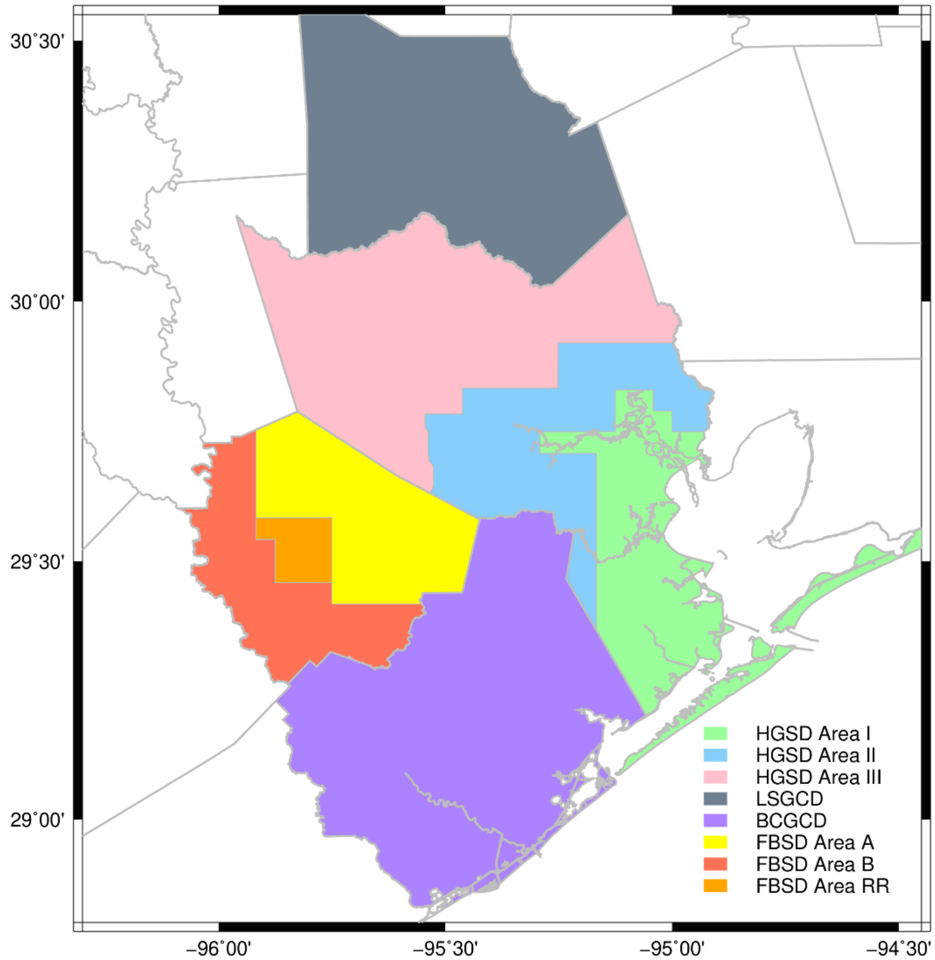

Figure 1-1: Map displaying subsidence and groundwater conservation districts located in Greater Houston. Boundary geospatial data from HGSD (2013).

When groundwater is removed from a confined or semi-confined aquifer, the potentiometric surface is lowered resulting in an increase of effective stress and resulting sediment compaction which subsequently leads to land subsidence (Lofgren and Klausing, 1964). In order to fully characterize the relationship between ground deformation and groundwater levels, local preconsolidation heads must be considered. Preconsolidation head refers to the hydraulic head level at which the effective stress acting on an aquifer system coincides with the preconsolidation stress (Sneed and Galloway, 2000). If hydraulic heads are above or below this level, aquifer compaction is elastic or inelastic, respectively (Wilson and Gorelick, 1996). Thus, subsidence will continue to occur in areas of lowered hydraulic head until groundwater levels recover to the preconsolidation head. Preconsolidation head estimates are of potential value for government agencies and policymakers in groundwater regulations to avoid permanent, irreversible land subsidence.

Currently, widespread land subsidence persists throughout much of Greater Houston, however, local ground rebound has been observed predominately near the Houston Ship Channel and Downtown Houston (**Figure 1-2**). The scope of this study is to investigate the relationship of ground deformation, specifically land rebound trends, sediment compaction, and groundwater levels in HGSD Area I and II, which encompasses Downtown Houston and the Houston Ship Channel, from 2000 to 2018. Preconsolidation head levels will be derived through this relationship. In addition, this study will also discuss the effectiveness of local groundwater regulations.

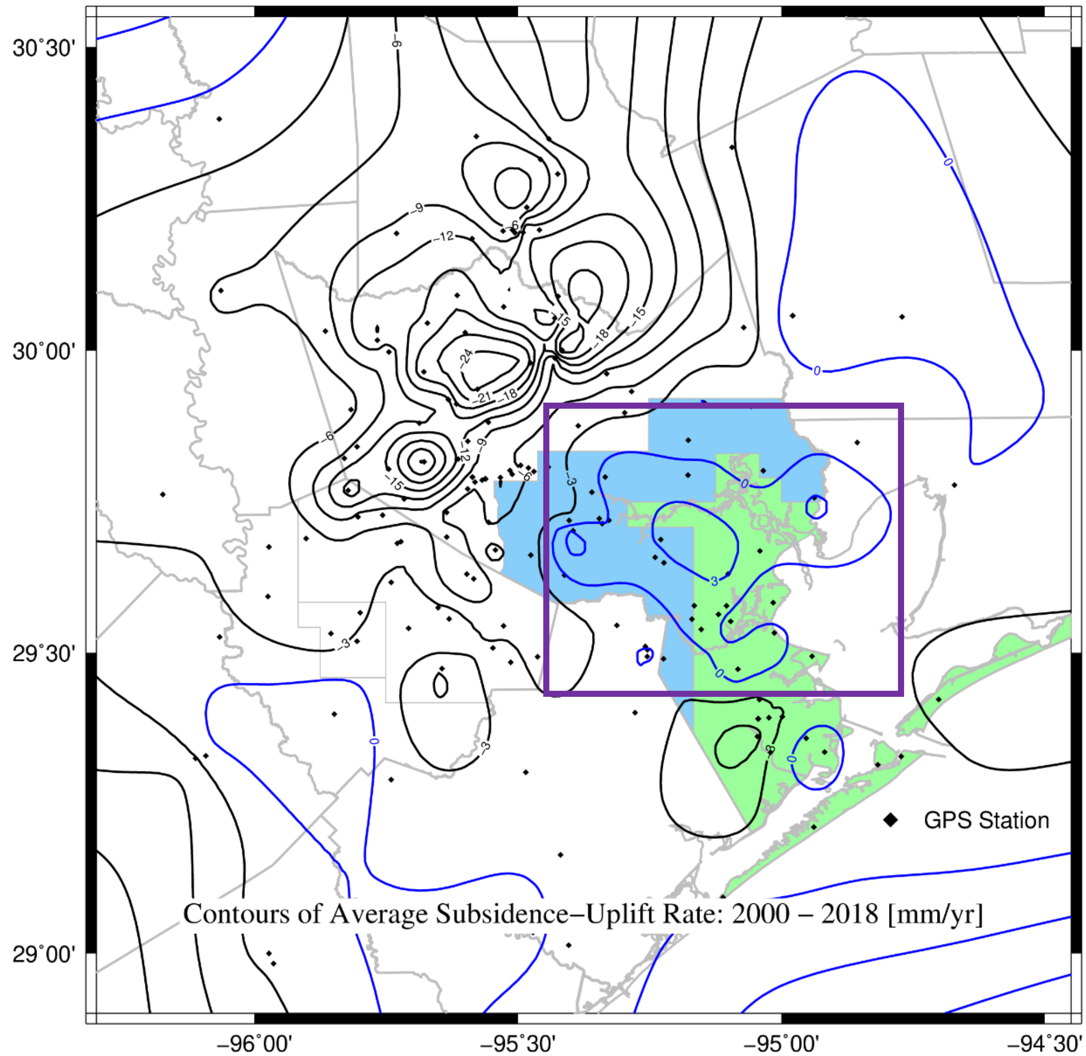

Figure 1-2: Contour map showing the recent land subsidence rate (2000-2018) within Greater Houston. *Black* contours indicate areas of negative vertical displacement (subsidence). *Blue* contours indicate areas of 0 or positive vertical displacement (uplift). Local land rebound is predominately observed adjacent to the Houston Ship Channel and Downtown Houston, as indicated by the *purple* rectangle.

2 REGIONAL GEOLOGY AND HYDROGEOLOGY

2.1 STRUCTURAL EVOLUTION OF THE GULF OF MEXICO

Houston is situated in southeast Texas alongside the northwestern edge of the Gulf of Mexico. The structural evolution of the Gulf of Mexico began in the Late Triassic with the separation of the supercontinent Pangaea (Salvador, 1991). In the Late Triassic-Early Jurassic, extension and thinning of continental crust created a series of basement grabens and topographic lowlands (Galloway, 2008). Continued stretching through Early-Middle Jurassic eventually generated a broad crustal sag and connected this opening basin to the Pacific Ocean across central Mexico. This subsequently flooded the opening basin generating the Gulf of Mexico as an ephemeral, enclosed marginal sea. As the Gulf of Mexico was a restricted basin at this time, hypersaline water conditions persisted leading to the deposition of Louann Salt and associated evaporite deposits. Deposition of Louann Salt ceased in the Late Jurassic (~161 Ma) with the onset of seafloor spreading and generation of oceanic crust (Bird et al., 2005). Continued seafloor spreading rotated the Yucatan Block southward and the Florida-Bahamas block southeastward thus opening the Gulf of Mexico fully. Seafloor spreading terminated by the Early Cretaceous (~140 Ma) and sediment derived from surrounding continents were deposited in the basin (Galloway, 2008). The Cenozoic structural evolution of the Gulf of Mexico is dominated by clastic sedimentation, loading subsidence, and growth faulting with the cooling of basin crust (**Figure 2-1**). Depositional episodes in the Cenozoic were widely controlled by erosion related to the Laramide Orogeny or crustal heating and volcanism in the southwestern United States and Mexico (Frazier, 1969).

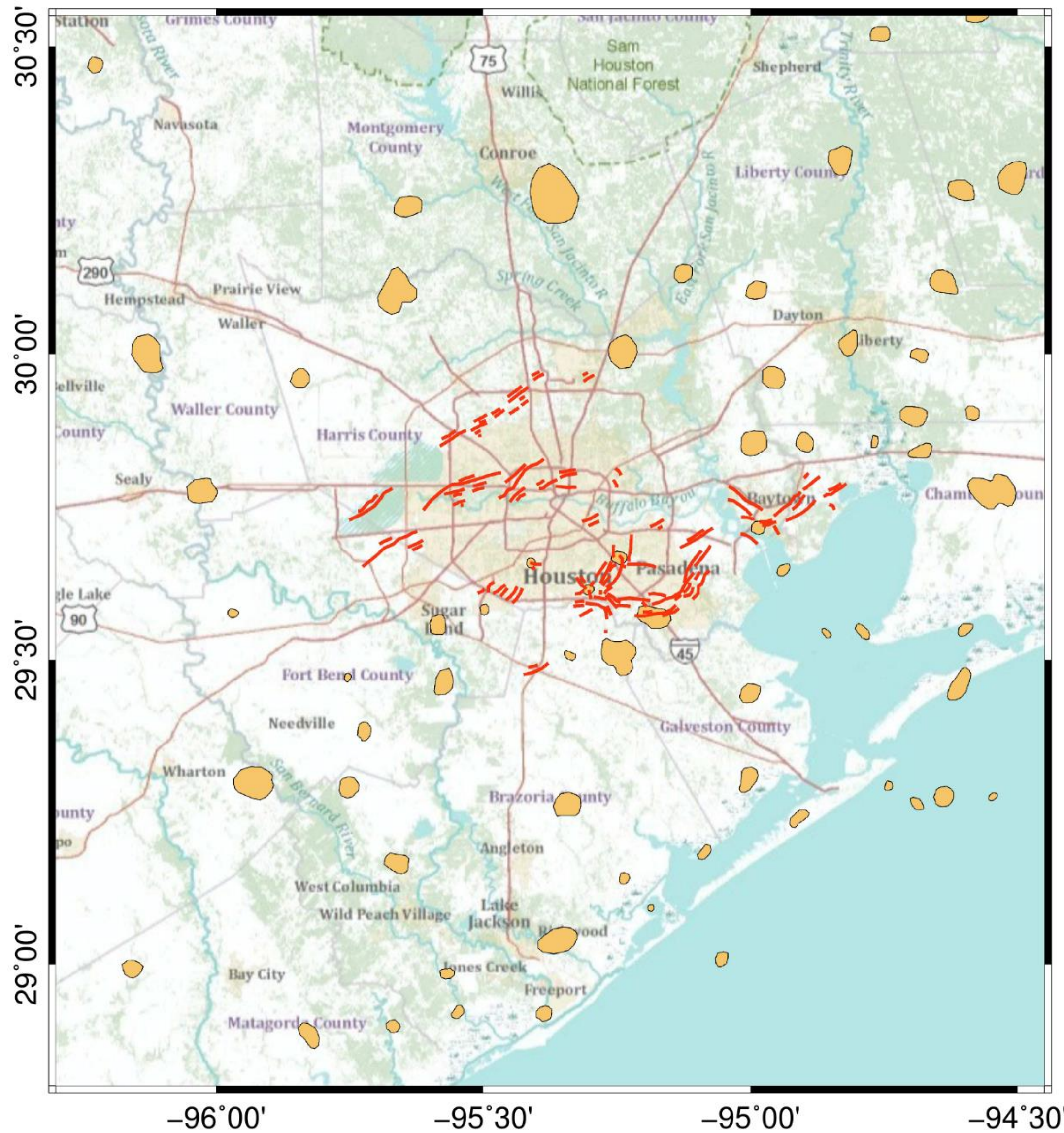

Figure 2-1: Map displaying locations of principal salt domes (*orange* polygons) and faults (*red* lines) located within Greater Houston. Principal fault geospatial information from the USGS (Shah and Lanning-Rush, 2005). Location of salt domes from the American Association of Petroleum (2011).

2.2 REGIONAL HYDROGEOLOGY

The Gulf Coast Aquifer is the main aquifer system paralleling the Gulf of Mexico coastline in Texas (Ashford and Hopkins, 1995). In Texas, upwards of 1.3 billion cubic meters of groundwater is withdrawn annually from this aquifer system for municipal, agricultural and industrial usage (Chowdhury and Turco, 2006). Baker (1979) classified the aquifer system into five principal components based on hydraulic and facies properties: the Chicot aquifer, the Evangeline aquifer, Burkeville confining unit, the Jasper aquifer, and the Catahoula aquifer (**Figure 2-2**). Historically, groundwater production has primarily been confined within the Chicot and Evangeline aquifers with production from the Jasper being far less significant (Baker, 1979).

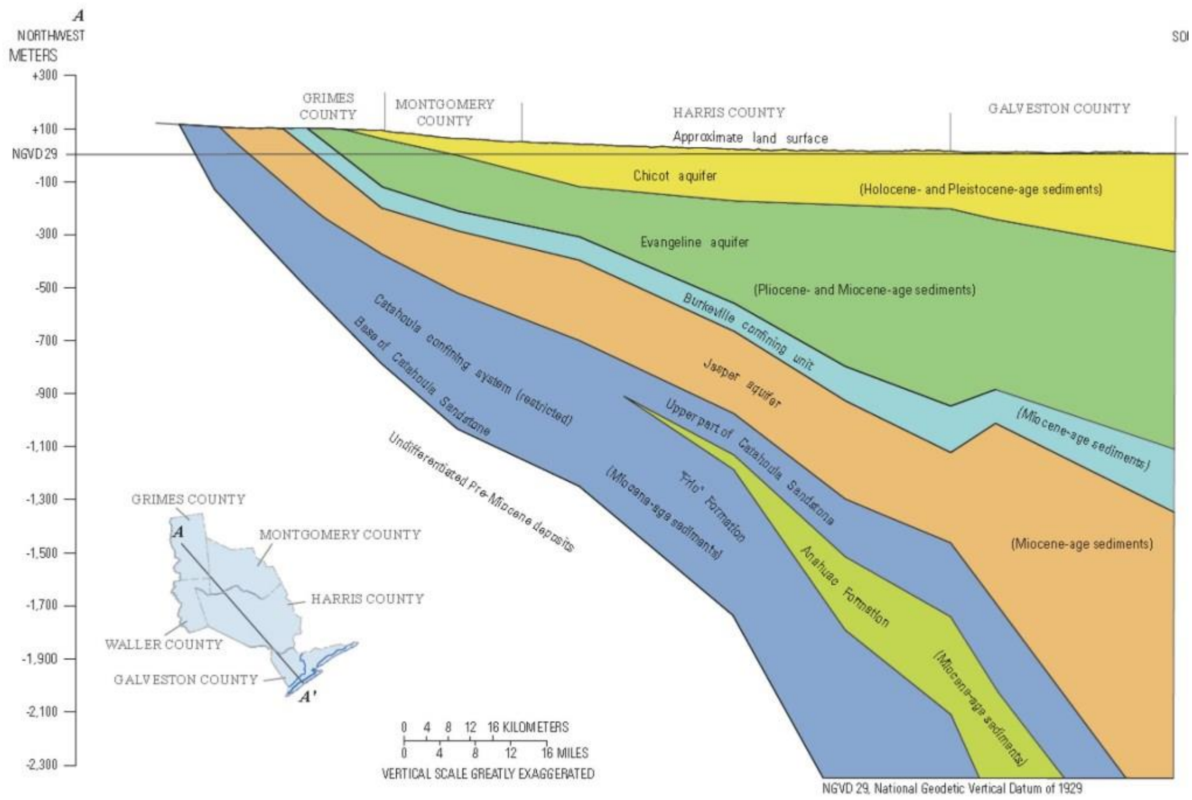

Figure 2-2: Schematic hydrogeologic cross-section of the Gulf Coast Aquifer system. From Bawden et al. (2012)

The Chicot aquifer is the shallowest aquifer of the Gulf Coast Aquifer system. Due to the complexity of its interlayered composition and the regional extent of its exposure, the Chicot aquifer behaves as an unconfined aquifer near the surface and as a semi-confined aquifer at depth (Kasmarek and Robinson, 2004). Along the coastal regions of the Gulf of Mexico, the Chicot aquifer is ~370 meters thick and thins inland (Chowdhury and Mace, 2003). The Chicot aquifer is composed of Pleistocene- to Holocene-aged interbedded, discontinuous layers of sand, gravel, silt and clay deposited in fluvial-deltaic to shallow marine paleo-environments (Baker, 1979). The specific stratigraphic formations compromising the Chicot include the Beaumont, Lissie, Montgomery, Bentley, and Willis Formations, and Holocene alluvium (**Figure 2-3**). The updip limit of the Chicot aquifer within the study area is located within Montgomery County (**Figure 2-4**).

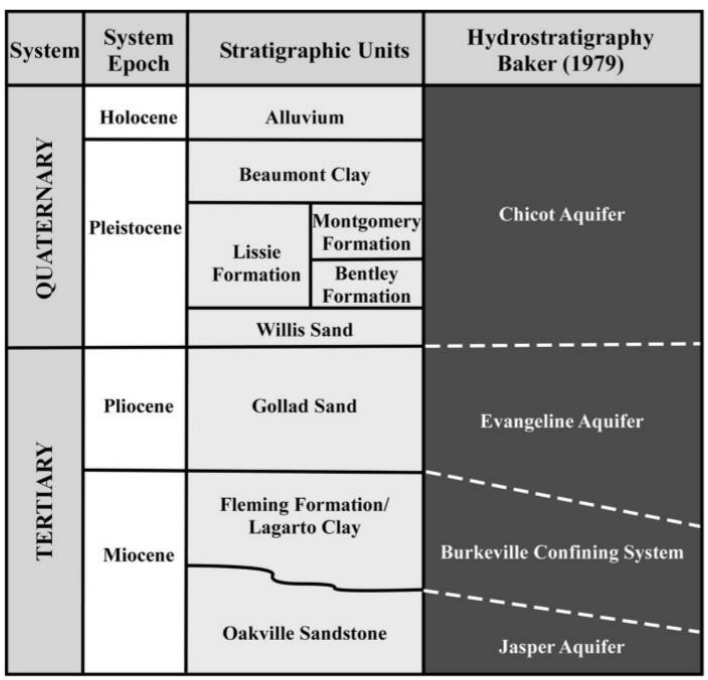

Figure 2-3: Hydrostratigraphic units of the Gulf Coast Aquifer system and stratigraphic units of Houston and surrounding areas. From Baker (1979).

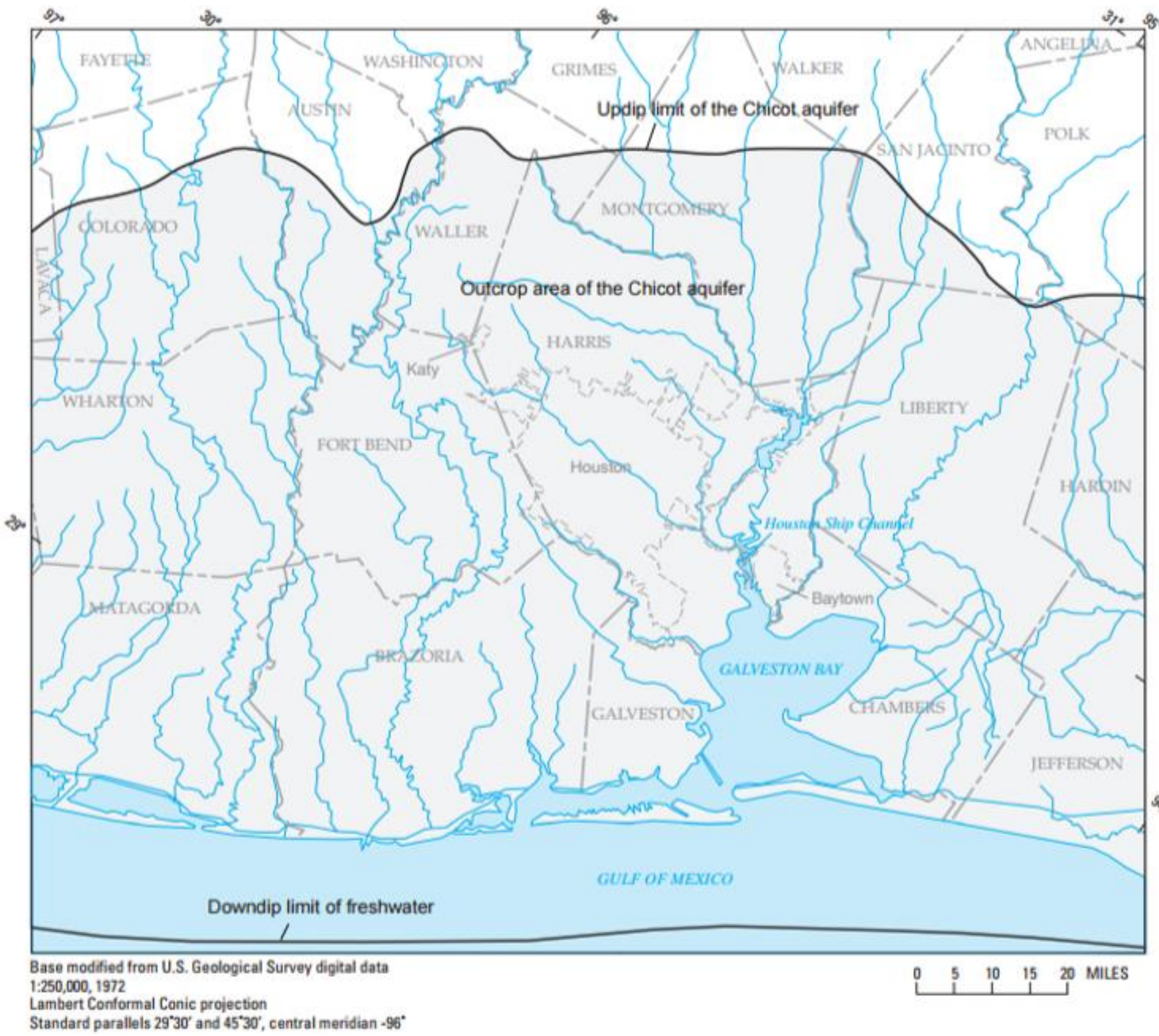

Figure 2-4: Regional outcrop limits of the Chicot aquifer. From Kasmarek and Strom (2002).

The Evangeline aquifer is overlain by the Chicot aquifer and underlain by the Burkeville confining unit. The Evangeline at is ~580 meters at its thickest near the Gulf of Mexico and thins landward. Stratigraphically, the Evangeline aquifer consists of Miocene- to Pleistocene-aged Fleming and Goliad Formations (Baker, 1979). These formations contain sand with interbedded clay, marl, and caliche (**Figure 2-3**) (Hosman, 1991). The Chicot and Evangeline aquifers are hydraulically connected as there is no complete confining unit. Thus, groundwater is able to flow freely between the two aquifers (Ashworth, 1995). The updip limit of the Evageline aquifer within the study area is located within Montgomery County (**Figure 2-5**).

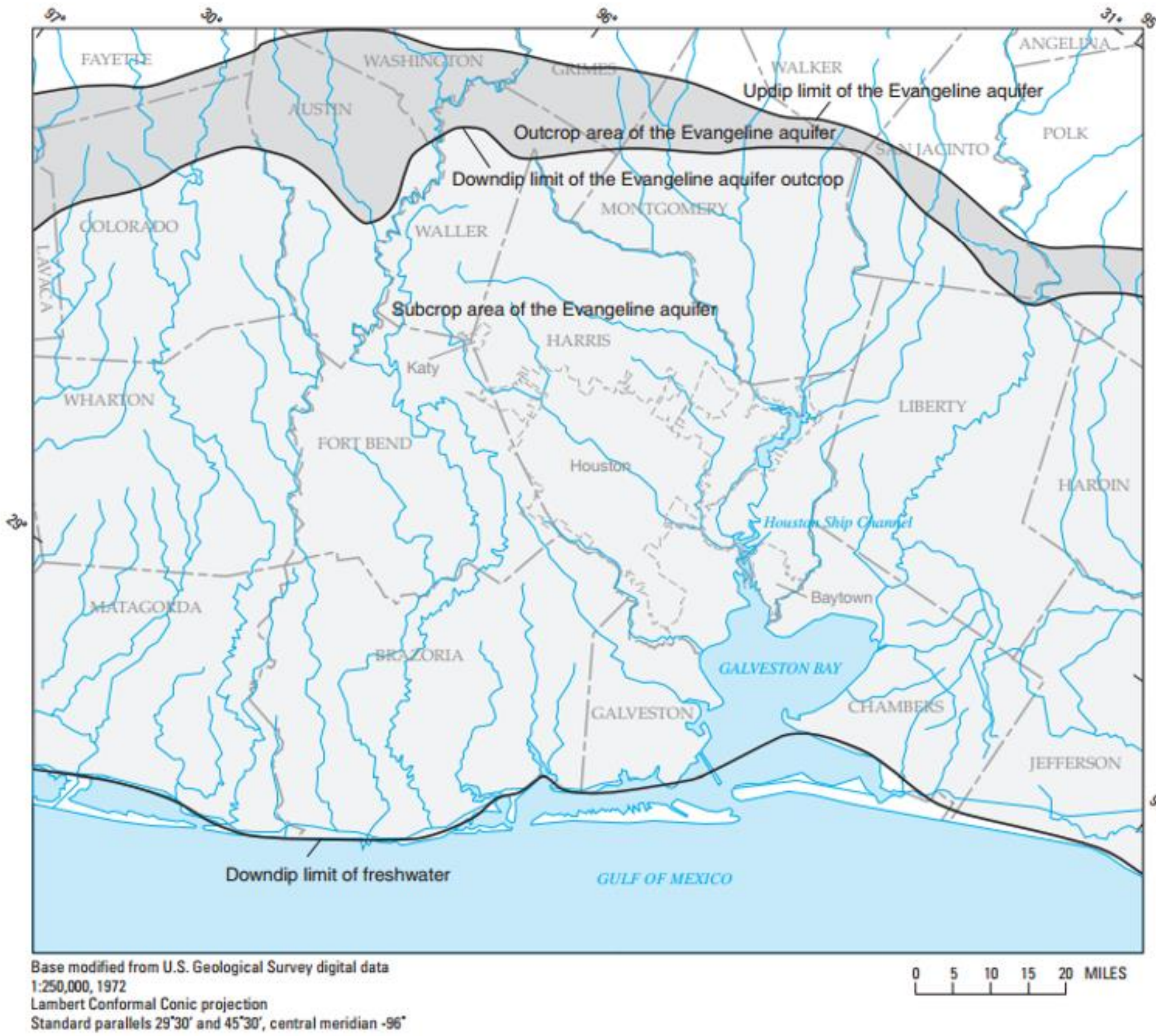

Figure 2-5: Regional outcrop limits of the Evangeline aquifer. From Kasmarek and Strom (2002).

3 LAND DEFORMATION MONITORING AND DATA

3.1 GEODETIC DATA

3.1.1 *GPS Introduction*

The Global Positioning System (GPS) is a satellite-based radio-navigation system that provides robust three-dimensional positioning and navigation globally. The concept of GPS was originally conceived and developed by the United States Department of Defense following the launch of the Soviet Union satellite Sputnik 1 in 1957. Following the launch of Sputnik 1, scientists at Johns Hopkins Applied Physics Laboratory monitored transmitted signals from the satellite and realized that they could delineate its orbit and position utilizing the Doppler Effect (Guier and Weiffenback, 1997). ollowing a number of satellite and radio-navigation advancements since the launch of Sputnik 1, the first experimental GPS satellite was launched was launched in 1978. The system, originally, was designed solely for military capabilities of United States. However, following the Korean Air Lines (KAL) Flight 007 Incident in 1983, then US President Ronald Reagan declared dual-usage of the GPS for both military and civil applications upon completion. Despite allowing civilian usage of GPS, Selective Availability (SA), intentional degradation of public GPS signals for the sake of national security, was utilized until being discontinued in 2000 by President Bill Clinton.

GPS is based on the concept of satellite ranging, or the distance from satellites to the point of observation on Earth. If the distance from at least four satellites is known, a unique position can be determined through the process of trilateration. Satellite ranges, in principal, can be determined by the following kinematic equation:

$$d = vt$$

where d is distance, v is velocity, and t is time. The velocity, in this case, is known as radio waves are electromagnetic waves that travel at the speed of light ($v = 3.00 \cdot 10^8$ m/s). To compute a distance, a GPS receiver must be able to determine precisely when the satellite signal was transmitted as well when it was received. The error in calculating the range, Δd, for an error in measuring time, Δt, is given by:

$$\Delta d = v\Delta t$$

where *v* is the speed of light. Therefore, an error in measuring time by one millisecond yields a ranging error of 300,000 meters (~186 miles). All GPS satellites are equipped with atomic clocks, therefore, the time of transmission is always known to a high-degree of accuracy. However, GPS receivers do not have atomic clocks and thus there is a discrepancy in measuring the arrival time of the radio signal. To remediate this discrepancy, a 'mathematical' clock is utilized:

-Upon signal transmission from the satellite, a GPS receiver on Earth generates a synchronized signal at exactly the same time.

-Once the transmitted signal is received by the GPS receiver, the time lag, *dt*, can be computed by comparing the transmitted signal and synchronized, copied signal.

-This time lag represents the amount of time it takes for the radio signal to travel from the satellite to the receiver on Earth.

3.1.2 *GPS in Subsidence Monitoring*

For more than two decades, GPS technology has been applied to study land subsidence in many regions, such as Groningen, Netherlands (Krijnen and de Heus, 1995), Rafsanjan Plain, Iran (Mousavi et al., 2000), Mexico City, Mexico (Osmanoglu et al., 2011), Central Valley, California (Argus et al., 2014), and New Orleans, Louisiana (Dixon et al., 2006). Since 1993, the HGSD and NGS have worked in close conjunction to establish a dense network of GPS stations for monitoring and quantifying land subsidence throughout Greater Houston. Stations constructed by these organizations can be principally divided into two groups: Continuously Operating Reference Stations (CORS) and Port-A-Measure (PAM). PAM stations utilize a campaign-style data collection paradigm whereas CORS are operated continuously (Zilkosi et al., 2003). Starting in 2012, a third network of continuously operating GPS stations, HoustonNet, was established to further contribute in land subsidence monitoring. The project, headed by Dr. Guoquan Wang at the University of Houston, was funded through the National Science Foundation (NSF). The network currently consists of 67 permanent GPS monitoring sites. Data from HoustonNet stations is archived and publically available through UNAVCO.

GPS stations throughout Greater Houston provide three-component positional and displacement measurements at regular sampling intervals. **Figure 3-1** illustrates an example of a three-dimensional displacement time-series for GPS station UH01. This study investigates vertical ground deformation trends over an 18-year period (2000-2018). Respective rates of land subsidence or uplift are computed by applying a linear regression model to the vertical displacement time-series. All available GPS stations in the region which recorded positional measurements within this time span and have a recording history of more than 2.5 years are utilized (**Figure 3-2**). In total, this includes 166 stations (**Figure 3-3**). Moreover, 48 specific GPS stations located in HGSD Area I and II are more closely investigated. Individual vertical displacement time-series graphs for each respective GPS station are provided in **Appendix I**.

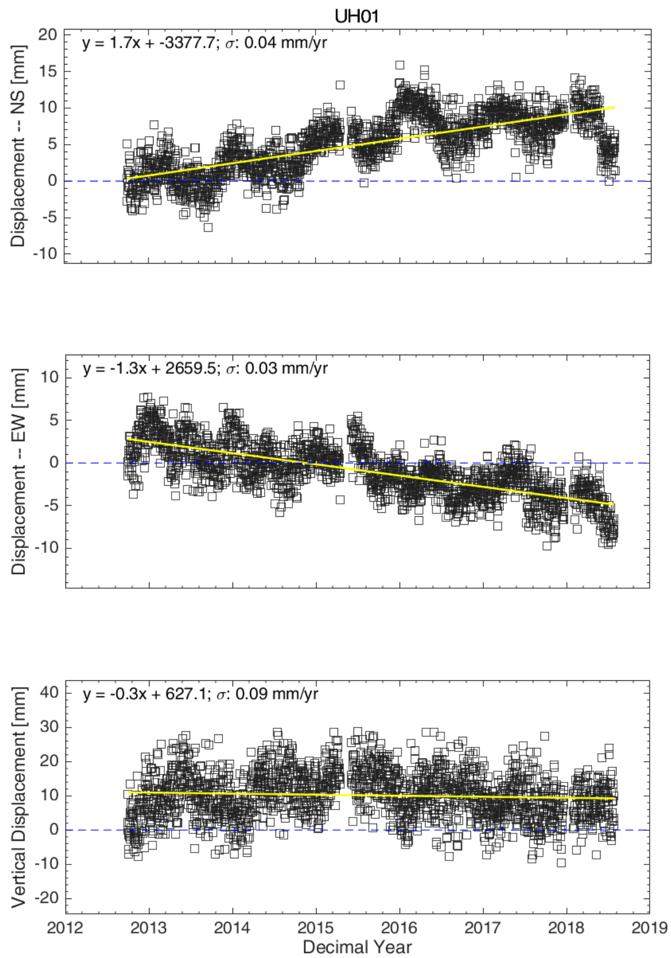

Figure 3-1: Three-component displacement time-series (2012-2018) derived from continuous GPS observations at UH01 with respect to the Stable Houston Reference Frame of 2016 (Houston16). UH01 is located atop Science and Research 1 (SR1) at the University of Houston.

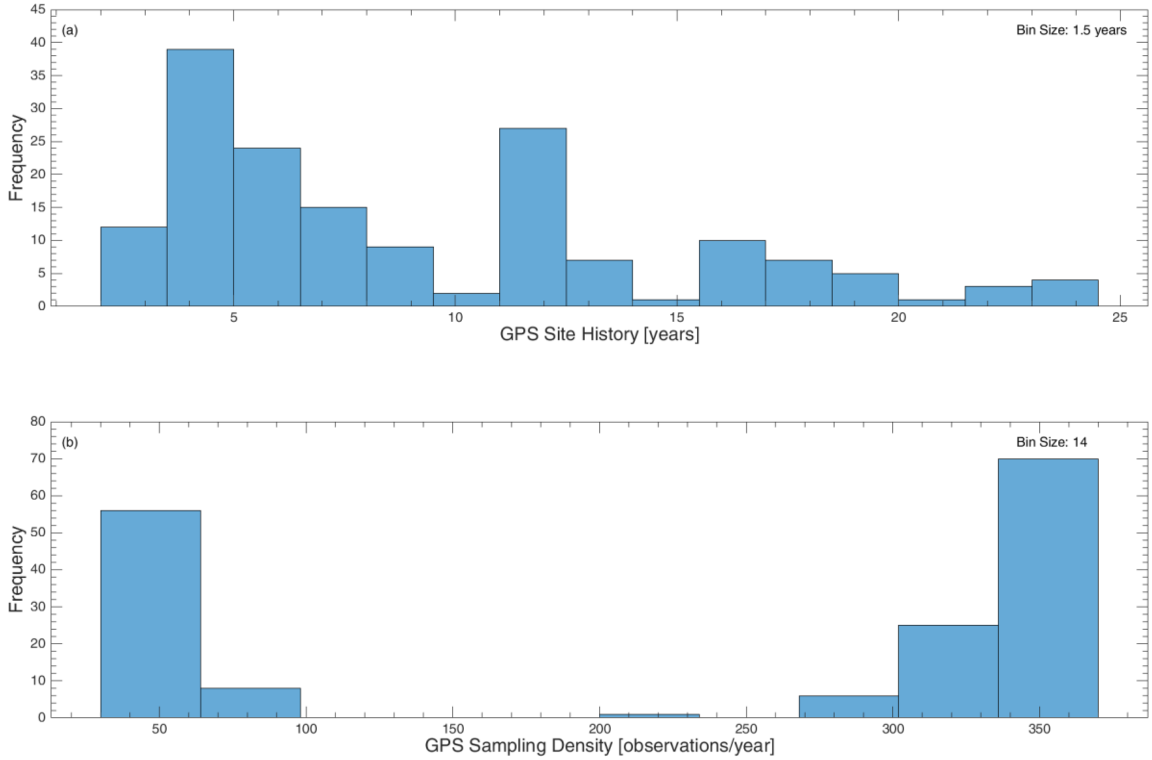

Figure 3-2: Histograms of (a) GPS observational history length and (b) average annual sampling density.

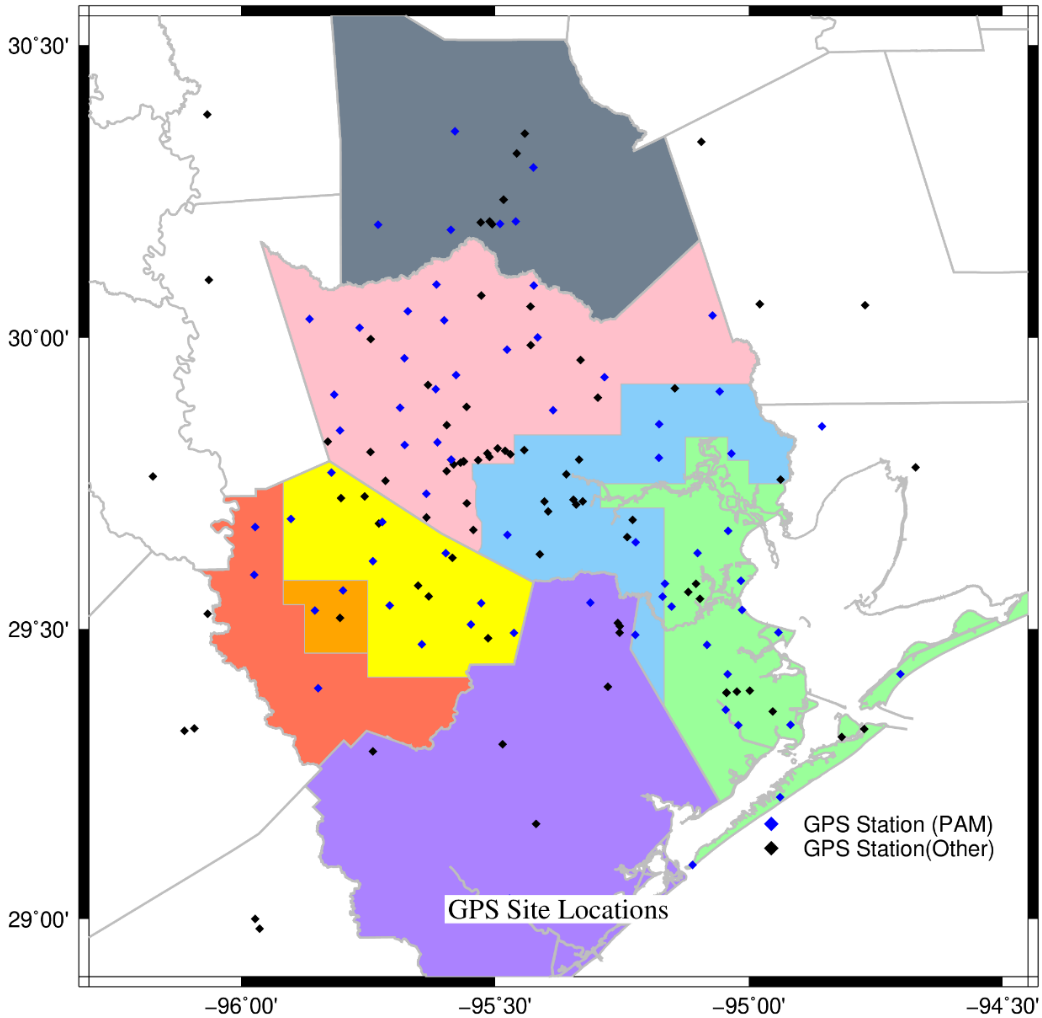

Figure 3-3: Map showing geographical location of all GPS stations utilized in the study.

3.1.3 *GPS Data Processing*

Surveying-grade GPS units record satellite signals and do not directly provide high-precision positions worthy of scientific investigation. Therefore, additional information, such as precise satellite orbits, clock information, error modeling, and numerous complex calculations are required to obtain high-precision positions. GPS data post-processing algorithms generally implement one of two approaches: relative positioning and absolute positioning. Relative GPS positioning methods utilizes simultaneous observations from two or more GPS units with known locations to eliminate or mitigate common errors. Contrarily, absolute positioning techniques solve for the position of a single GPS station without the usage of simultaneous observations (Wang et al., 2017). The distinct advantage of absolute positioning techniques is that it does not require any reference stations as the processing parameters are obtained and computed from a global distribution of GPS stations. This means that a single GPS receiver may be post-processed even without other stations in close proximity. Moreover, absolute positioning techniques reduce the total number of required calculations and provided better consistency in positioning compared to relative positioning techniques (Píriz et al., 2009; Zumberge et al., 1997).

Currently, there are many GPS post-processing software packages and online utilities available including GAMIT, GIPSY-OASIS, OPUS, and AUSPOS for scientific research. For this study, GNSS (Global Navigation Satellite System)-Inferred Positioning System and Orbit Analysis Simulation Software (GIPSY-OASIS) was utilized to process GPS data. GIPSY-OASIS utilizes a Precise Point Positioning (PPP), a common absolute positioning technique, to process GPS data. PPP utilizes data from a global reference network of GPS reference ground stations for generating precise satellite orbits and clock products to fix phase ambiguities for a position of interest. A complete documentation of the theoretical development of PPP is found in Zumberge et al. (1997). Processing through GIPSY-OASIS has been empirically proven to provide more coherent and slightly higher-accuracy positional information compared to other processing paradigms (Wang et al., 2017). The precision, or repeatability, of GPS measurements post-processed through GIPSY-OASIS falls within 3-4 millimeters horizontally and 6-8 millimeters vertically within the region of interest (Wang et al., 2015).

3.1.4 *Reference Frame Transformation and Stable Houston Reference Frame of 2016*

In order to achieve optimal positional accuracy, GPS data must be related to an appropriate coordinate system or stable reference frame. Reference frames may either be global, continental, regional, or local in scale. Predominately, initial GPS positions are provided as a set of coordinates with respect to a global reference frame. Global geodetic reference frames, such as the International GNSS Service reference frame of 2008 (IGS08), are realized by minimizing the overall movements of a large number of selected reference stations distributed worldwide (Rebischung et al., 2012). As a consequence, the positional coordinates for a majority of the GPS stations change over time with respect to a global reference frame. Site movements with respect to a global reference frame are predominately controlled by long-term drift and rotations of tectonic plates. Thus, localized and temporal ground deformation could be obscured or biased by large-scale plate motions. Therefore, a stable regional or local reference frame is required in order to precisely delineate localized ground displacements. A stable geodetic reference frame indicates that regional, common, movements have been removed or minimized.

In regards to this study, the Stable Houston Reference Frame of 2016 (Houston16) developed by Kearns et al. (2018) is utilized to investigate ground deformations in Greater Houston (**Figure 3-4**). Initial GPS coordinates, Earth-Centered Earth-Fixed- (ECEF) *XYZ*, are referred to IGS08 after utilizing GIPSY-OASIS for post-processing and are subsequently transformed to Houston16 coordinates. In geodesy, the Helmert transformation is utilized to produce a distortion-free transformation of ECEF-*XYZ* coordinates between two reference frames. The Helmert transformation for a position from an arbitrary reference frame *A* to *B* can be expressed as:

$$\begin{bmatrix} X_B \\ Y_B \\ Z_B \end{bmatrix} = \begin{bmatrix} T_X \\ T_Y \\ T_Z \end{bmatrix} + 1(1+s) \times \begin{bmatrix} 1 & -R_Z & R_y \\ R_Z & 1 & -R_x \\ -R_y & R_x & 1 \end{bmatrix} \times \begin{bmatrix} X_A \\ Y_A \\ Z_A \end{bmatrix},$$

where X_A, Y_A, and Z_A are the *XYZ* coordinates with respect to the original reference frame *A*; X_B, Y_B, and Z_B are the transformed *XYZ* coordinates with respect to the new reference frame *B*; T_x, T_y, and T_z are three translational shifts between the two reference frames along the *x*, *y*, *z* coordinate axes; R_x, R_y, and R_z are three rotations about the *x*, *y*, *z* coordinate axes; and *s* is a scale factor. The seven parameters (T_x, T_y, T_z, R_x, R_y, R_z, *s*) may be computed utilizing a minimum of three common points with known three-dimensional coordinates with respect to both reference frames. Often, more common points are utilized to solve the inverse problem by a least-squares adjustment method. Coordinate transformation of a GPS-derived positional time-series from IGS08 to Houston16 can be calculated through the following set of equations:

$$X(t)_{Houston16} = X(t)_{IGS08} + T_x' \cdot (t - t_0) + R_z' \cdot (t - t_0) \cdot Y(t)_{IGS08} - R_y' \cdot (t - t_0) \cdot Z(t)_{IGS08}$$

$$Y(t)_{Houston16} = Y(t)_{IGS08} + T_y' \cdot (t - t_0) - R_z' \cdot (t - t_0) \cdot X(t)_{IGS08} + R_x' \cdot (t - t_0) \cdot Z(t)_{IGS08}$$

$$Z(t)_{Houston16} = Z(t)_{IGS08} + T_Z' \cdot (t - t_0) + R_y' \cdot (t - t_0) \cdot X(t)_{IGS08} - R_x' \cdot (t - t_0) \cdot Y(t)_{IGS08}$$

where t_0 denotes a specific time epoch used to align the two reference frames; $X(t)_{Houston16}$, $Y(t)_{Houston16}$, and $Z(t)_{Houston16}$ are the computed coordinates with respect to Houston16; $X(t)_{IGS08}$, $Y(t)_{IGS08}$, and $Z(t)_{IGS08}$ are positional coordinates with respect to IGS08; T'_x, T'_y, T'_z, R'_x, R'_y, and R'_z are the one-time derivatives of the translational and rotational parameters, respectively (Wang et al., 2018). **Table 3-1** displays the values required for the transformation equations provided above. **Figure 3-5** demonstrates the difference in the position of GPS station TXLI with respect to three difference reference frames.

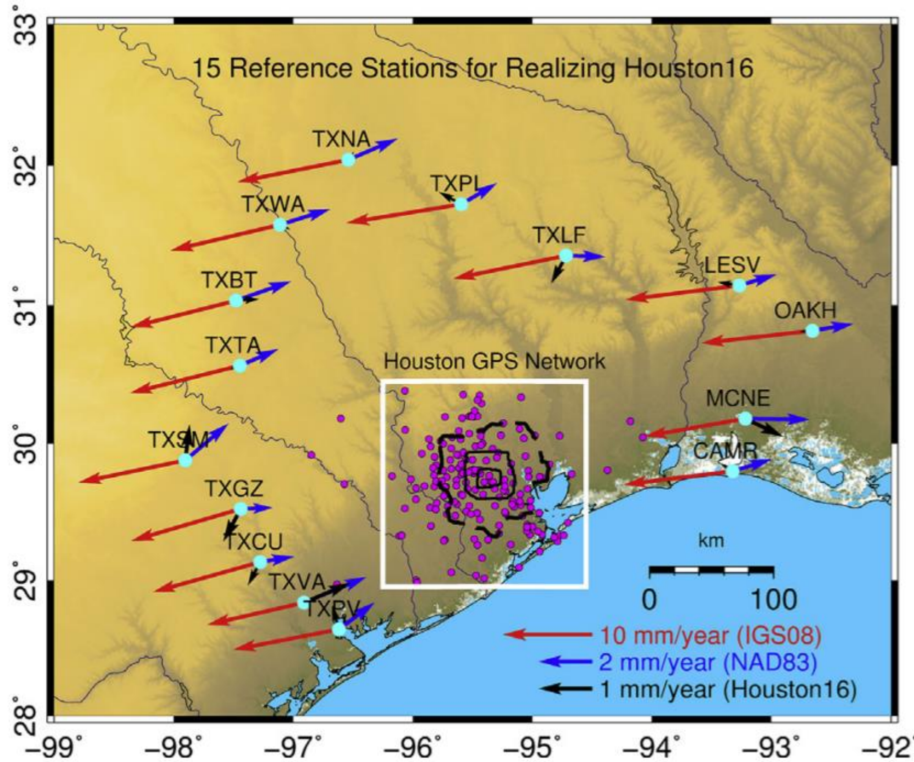

Figure 3-4: Map showing the geographic locations of the 15 reference GPS stations utilized to realize the Stable Houston Reference Frame of 2016 (Houston16). The vectors plotted represent the horizontal velocity vectors with respect to IGS08 (red), NAD83 (blue), and Houston16 (black). From Kearns et al. (2018).

Table 3-1: Seven parameters for transforming Earth-Centered Earth-Fixed (ECEF)-XYZ coordinates to Houston16. From (Kearns et al., 2018).

Parameters	*Unit*	*IGS08 to Houston16*
T_x'	m/year	1.1427832E-02
T_y'	m/year	-2.4771197E-03
T_z'	m/year	5.8795944E-04
R_x'	radian/year	2.0734184E-10
R_y'	radian/year	-2.0205941E-09
R_z'	radian/year	1.0549129E-09
t_0	year	2012.0

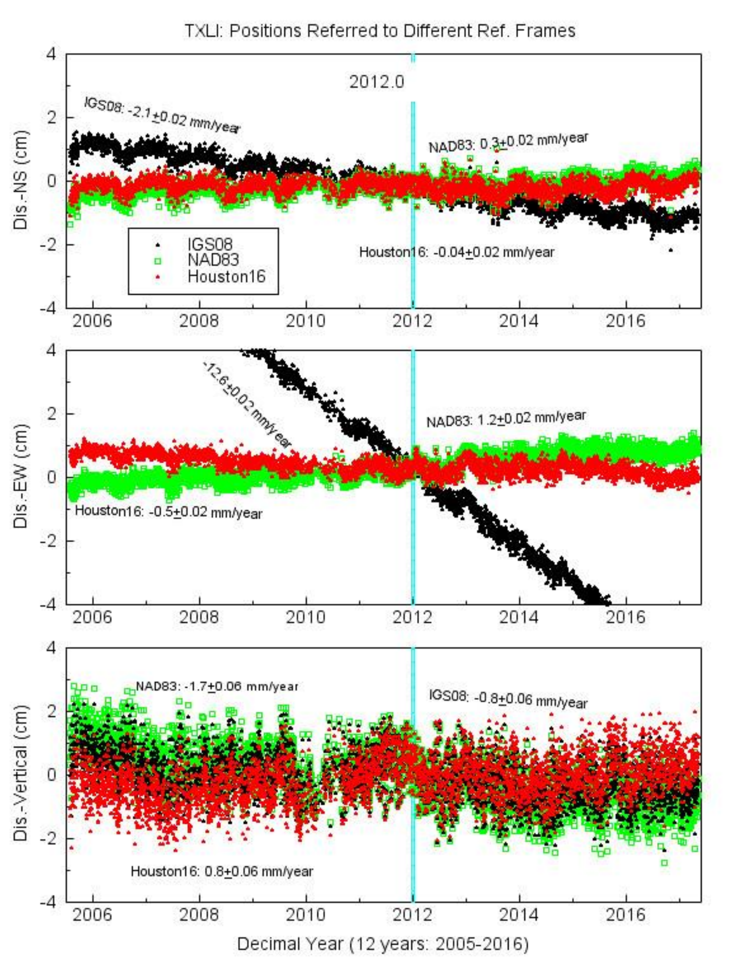

Figure 3-5: Example of GPS-derived three-component displacement time-series of station TXLI with respect to IGS08, NAD83, and Houston16.

3.2 HYDROLOGIC DATA

3.2.1 *Groundwater Wells and Locations*

Groundwater hydraulic heads in Houston are closely monitored in conjunction with GPS and extensometer observation in order to understand the relationship between groundwater production and land subsidence. Groundwater observational wells within Greater Houston are drilled, maintained and monitored by the USGS. Observational wells are completed at various depths within the Gulf Coast Aquifer to provide comprehensive coverage of the system. A majority of the observational wells have observations dating back to 1950-1970. Sampling rates widely vary from daily, monthly, bimonthly, or yearly. All groundwater measurements presented in this study are given as a negative number representing the depth below the point of measurement on the land surface. Larger negative numbers indicate deeper hydraulic heads. Groundwater wells screened in both the Chicot and Evangeline aquifers are ignored in this study. Groundwater data for Greater Houston is publicly available through the USGS Groundwater Watch. **Figure 3-6** provides the location of all groundwater observational wells completed in the Chicot and Evangeline aquifers utilized in this study.

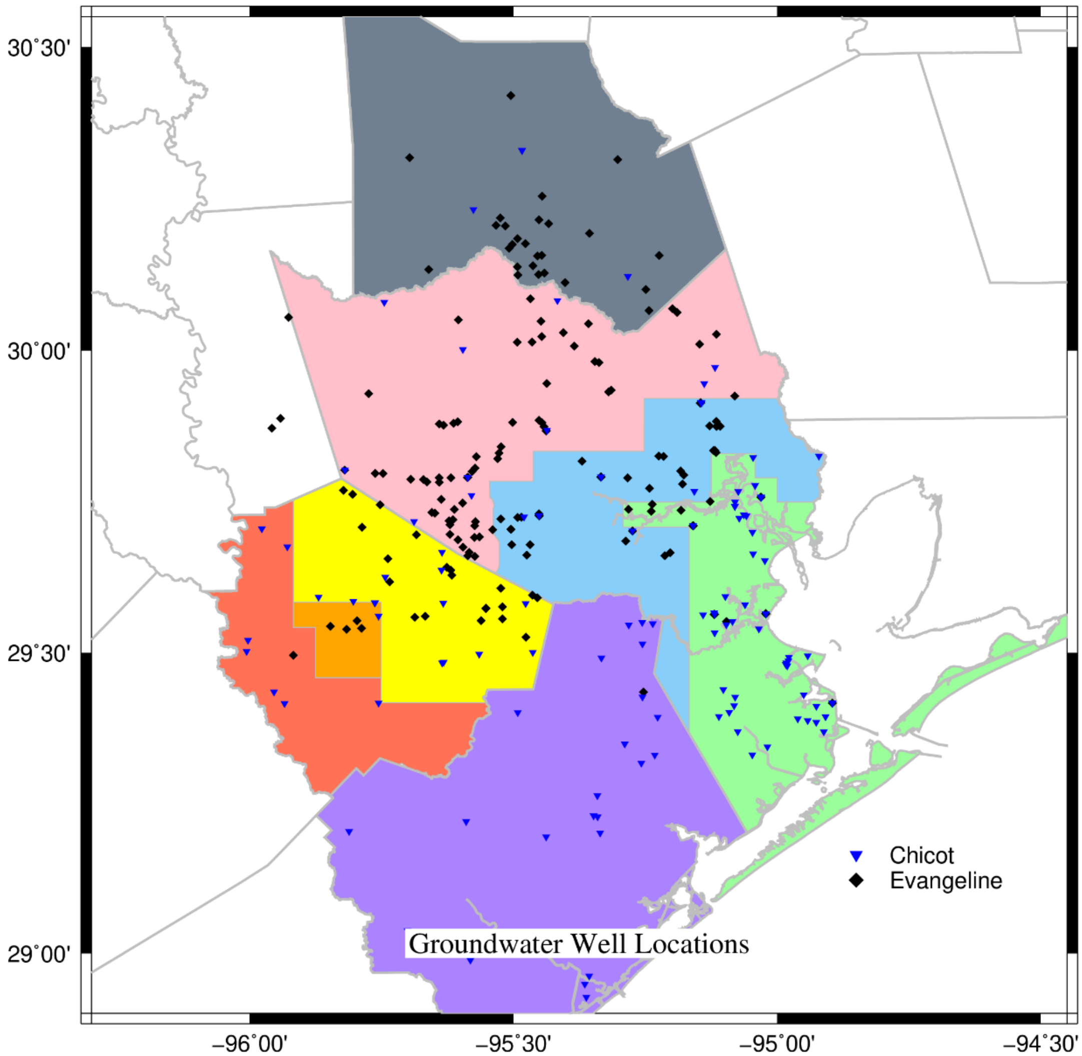

Figure 3-6: Locations of all Chicot (*blue* triangles) and Evangeline (*black* diamonds) groundwater wells utilized in this study.

3.2.2 *Borehole Extensometer Data*

Borehole extensometer sites within Greater Houston have been established, maintained, and monitored by the USGS in conjunction with the HGSD since 1973. Borehole extensometers measure sediment compaction by measuring the land surface with respect to a fixed datum. **Figure 3-7** illustrates a schematic diagram of a borehole extensometer utilized in Greater Houston. In total, there are 13 extensometer sites completed at 11 sites. **Figure 3-8** displays the location and site names for borehole extensometers located within the region of interest. Two specific sites, Clear Lake and Baytown, have two completed borehole extensometers at different depths. This dual-extensometer setup provides information about the distribution of compaction as a function of depth (Yu et al., 2014). In addition, all extensometer sites are collocated with groundwater observational wells completed in both the Chicot and Evangeline aquifers. This collocation of borehole extensometers of groundwater wells are invaluable in deriving the relationship between aquifer compaction and groundwater level.

Previous studies indicate a close relationship between borehole extensometer readings and GPS observations (Wang et al., 2014). **Figure 3-9** displays collocated observations from Addicks borehole extensometer and GPS stations PA05 and ADKS. The Addicks extensometer measures sediment compaction within the Chicot and Evangeline aquifers. Further, ADKS is a special GPS station fixed to the outer casing of the borehole extensometer. Thus, ADKS measures sediment compaction occurring beneath the depth interval of the Addicks borehole extensometer. The close correlation between Addicks borehole extensometer and PA05 observations indicate that both provide similar information about the compaction in the Chicot and Evangeline aquifers. In addition, the flatness of the ADKS displacement time-series indicates no appreciable sediment compaction beneath the Chicot and Evangeline aquifers.

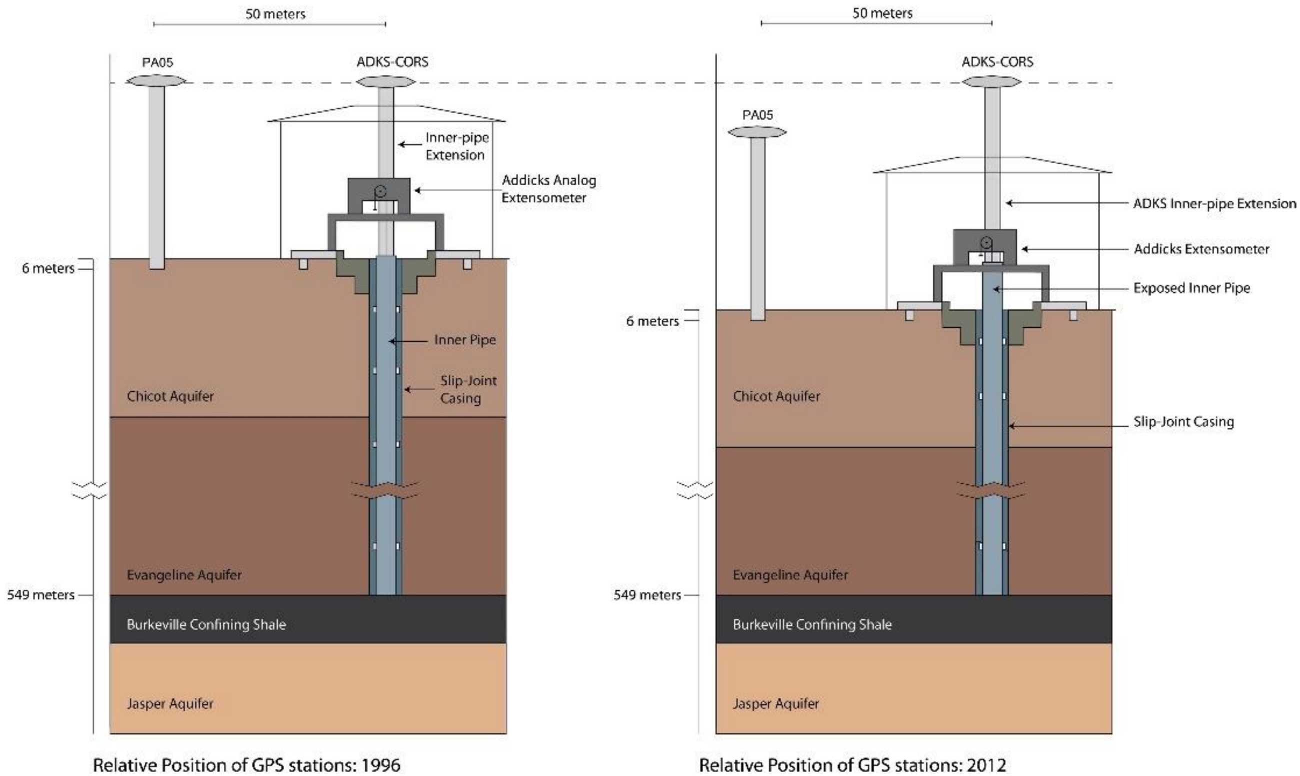

Figure 3-7: Schematic diagram of a borehole extensometer utilized to quantify sediment compaction in Greater Houston. From Wang et al. (2014)

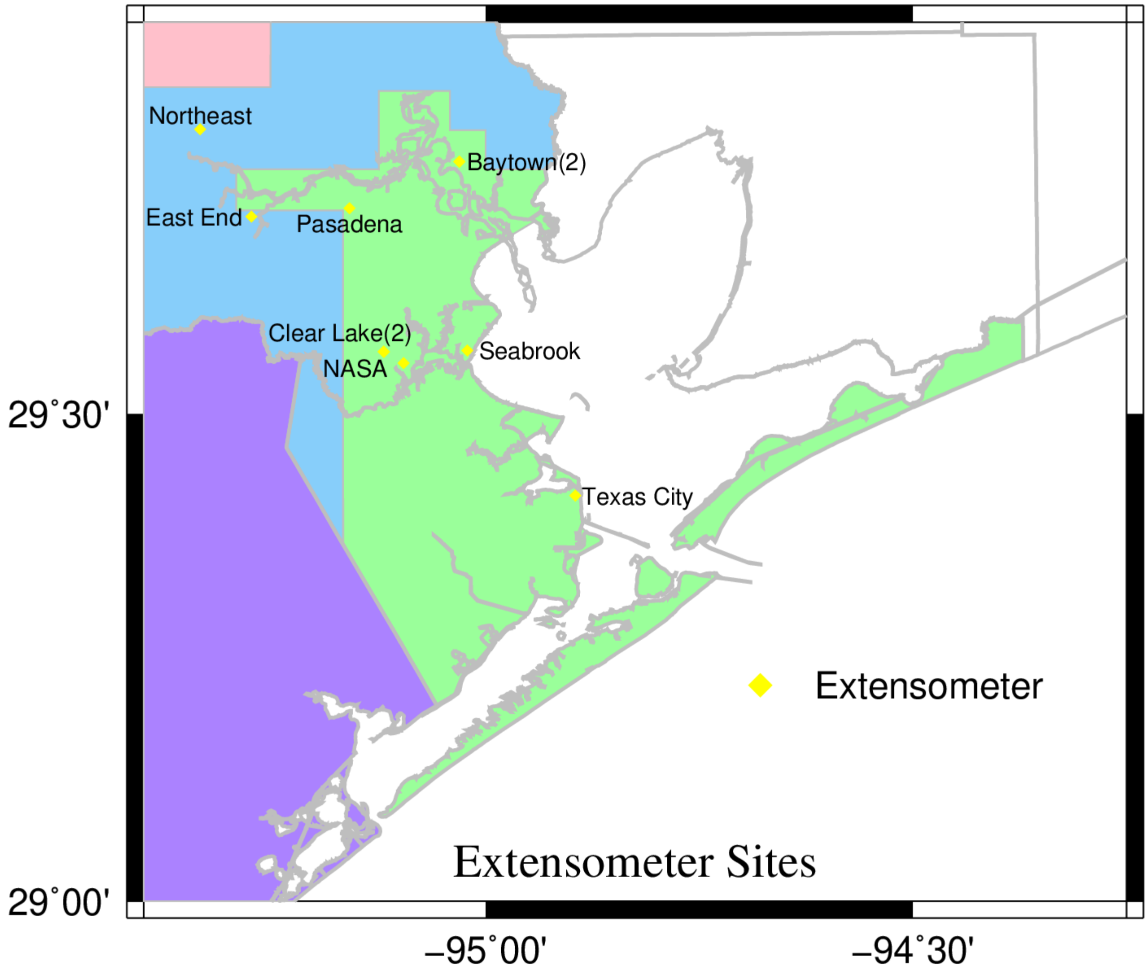

Figure 3-8: Map displaying the geographic locations and site names of the 10 bore extensometer sites located within the region of interest. Clear Lake and Baytown sites have two borehole extensometers.

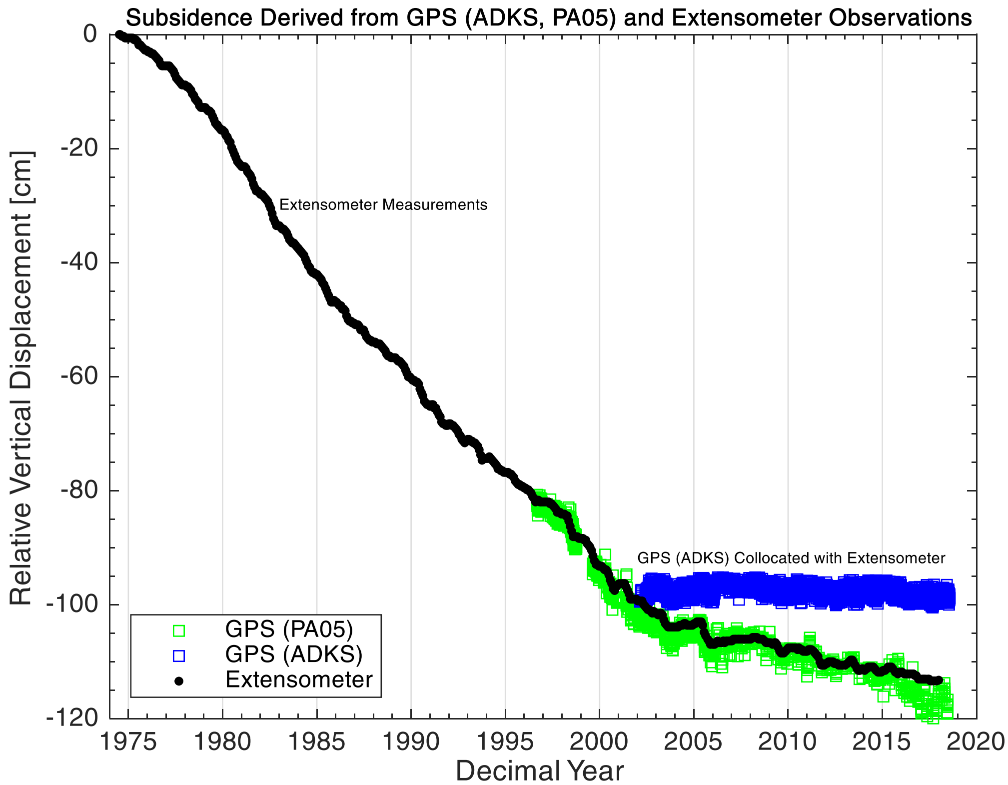

Figure 3-9: Correlation between borehole extensometer and GPS observation in Addicks Reservoir, Texas.

4 AQUIFER DEFORMATION

4.1 GROUNDWATER WITHDRAWAL AND LAND SUBSIDENCE

Land subsidence associated with groundwater production has been well documented and studied in many regions of the world (Konikow and Kendy, 2005; Schumann and Poland, 1969). Fundamental to the study of groundwater-induced land subsidence is the concept of effective stress. The concept of effective stress is outlined by the one-dimensional soil stress model introduced by Terzaghi (1925). The model assumes a uniaxial stress state in which the vertical stress resulting from the overburden is counteracted by pore-fluid pressure. Therefore, the effective stress acting on a given point can be expressed as:

$$\sigma_e = \sigma_T - p$$

where σ_e is the effective stress, σ_T is the total stress (overburden), and p is the pore-fluid pressure. Thus, the equation implies that a reduction in pore-fluid pressure will yield a corresponding increase in effective stress. In studies regarding land subsidence, compaction is considered to be the consequence of an increase in the effective stress acting on a volume of sediment related to changes in groundwater level (Galloway and Burbey, 2011).

In terms of the Principle of Effective Stress, a reduction in the potentiometric surface of a confined or semi-confided aquifer reflects a reduction in pore pressure. Consequently, there is an increase in the effective stress acting on the aquifer system and compaction of the aquifer (**Figure 4-1**). The location from which a production well is withdrawing groundwater acts as a point source for the reduction in the potentiometric surface and is generally where the largest magnitude of compaction is expected to occur (Bull, 1975). The size of the resulting cone of depression is dependent on the rate of pumping, rate of groundwater released from storage, rate of recharge, and rate of discharge (Ryder, 1996). In order for the potentiometric surface to remain stable during groundwater production, the amount of water discharged through natural processes and production must not exceed the amount of groundwater recharged in a given period of time (Smith, 1982).

Compaction of an aquifer skeleton subjected to increased effective stress may be elastic (recoverable) or inelastic (largely non-recoverable) in nature. In general, compaction is elastic until a certain stress threshold is reached. This particular stress threshold is the preconsolidation stress.

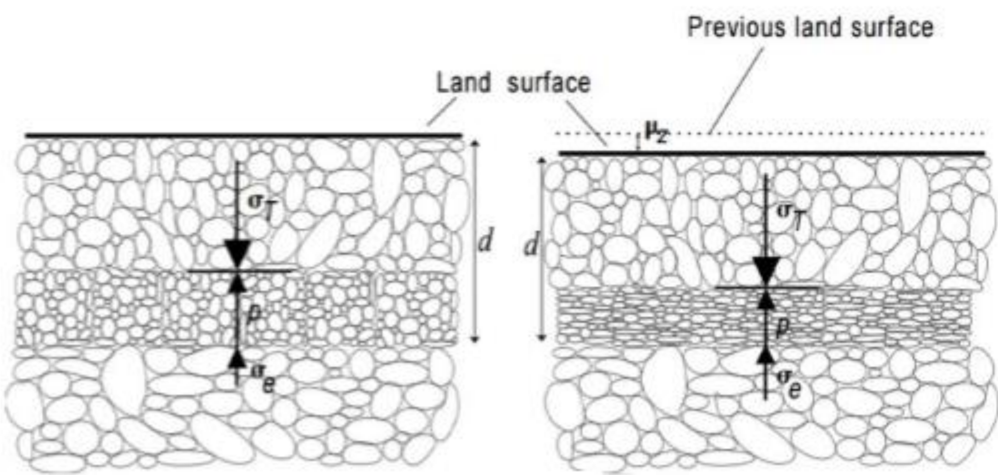

Figure 4-1: Conceptual diagram of land subsidence in terms of the Principle of Effective Stress. Modified from Sneed and Galloway (2000).

4.2 PRECONSOLIDATION STRESS AND AQUITARD DRAINAGE MODEL

Preconsolidation stress is defined as the maximum effective stress that a sediment volume has sustained in the past. Once this threshold is exceeded, generally, the sediment volume will experience permanent, inelastic deformation resulting from the realignment of its internal structure (Sneed and Galloway, 2000). Each time this threshold is exceeded, the new maximum stress experienced becomes the new preconsolidation stress. Additionally, any applied stress to the sediment volume below the current preconsolidation stress will typically result in elastic deformation (Sneed and Galloway, 2000). Preconsolidation head refers to the hydraulic head level that coincides with the preconsolidation stress (Leake, 1990).

The aquitard drainage model is utilized to describe drainage of an aquifer system consisting of materials of variable permeability. The model is principally based on Terzaghi's Principle of Effective Stress and the theory of hydrodynamic consolidation (Holzer, 1995). The theory of hydrodynamic consolidation describes the lag in the equilibration of pore pressure between adjacent, draining aquitard and aquifer material. In other words, as pore pressure in an aquifer decreases as a consequence of groundwater production, there is a delay in the reduction of pore pressure in aquitard material due to their intrinsic lower permeability (Schiffman, 1958). Aquitard material will continuously drain until the hydraulic pressure between aquitard and aquifer material reaches an equilibrium state (Riley, 1998). When the effective stress experienced by aquitard material exceeds the initial preconsolidation stress, the aquitard material will compact and deform inelastically. The primary component of permanent land subsidence is considered to be the inelastic compaction of slowly draining aquitard material (Tolman and Poland, 1940). In addition, it is common for aquitard material to continue compacting even after hydraulic heads in adjacent aquifer material begin to recover (Sneed and Galloway, 2000). Inelastic aquitard compaction will cease only when hydraulic heads between aquitard and aquifer material reaches equilibrium. The hydraulic head level that coincides with this equilibrium state represents the preconsolidation head. Therefore, inelastic compaction or permanent land subsidence, would not be expected to reinitiate unless hydraulic heads are lowered past the preconsolidation head (Holzer and Galloway, 2005).

Predevelopment, or native, preconsolidation head refers to the natural hydraulic head level in an aquifer system prior to anthropogenic groundwater production. Predevelopment preconsolidation stress is often larger in magnitude than the natural state of effective stress experienced by an aquifer prior to the onset of groundwater production (Galloway et al., 1999). Such a situation is known as over-consolidation (Sneed and Galloway, 2000). A number of reasons have been provided for how this may occur naturally and include erosion, pre-historic groundwater level decline, and diagenesis (Holzer, 1981). Moreover, current preconsolidation stress may not coincide with predevelopment preconsolidation stress, especially in systems which have experienced periods of lowered hydraulic heads and are affected by hydrodynamic lag (Galloway et al., 1999). **Figure 4-2** illustrates a conceptual model for groundwater-induced land deformation and illustrates the concept of hydrodynamic consolidation. As groundwater is produced starting at time t_0, sediment compaction slowly increases until groundwater levels fall below the preconsolidation head. After this threshold, compaction is rapid until groundwater production is ceased at time t_{stop}. As groundwater levels rise after time t_{stop}, compaction continues to slow until groundwater levels reach the preconsolidation head. Once hydraulic heads have recovered to or surpass the new preconsolidation head, slight land rebound is observed.

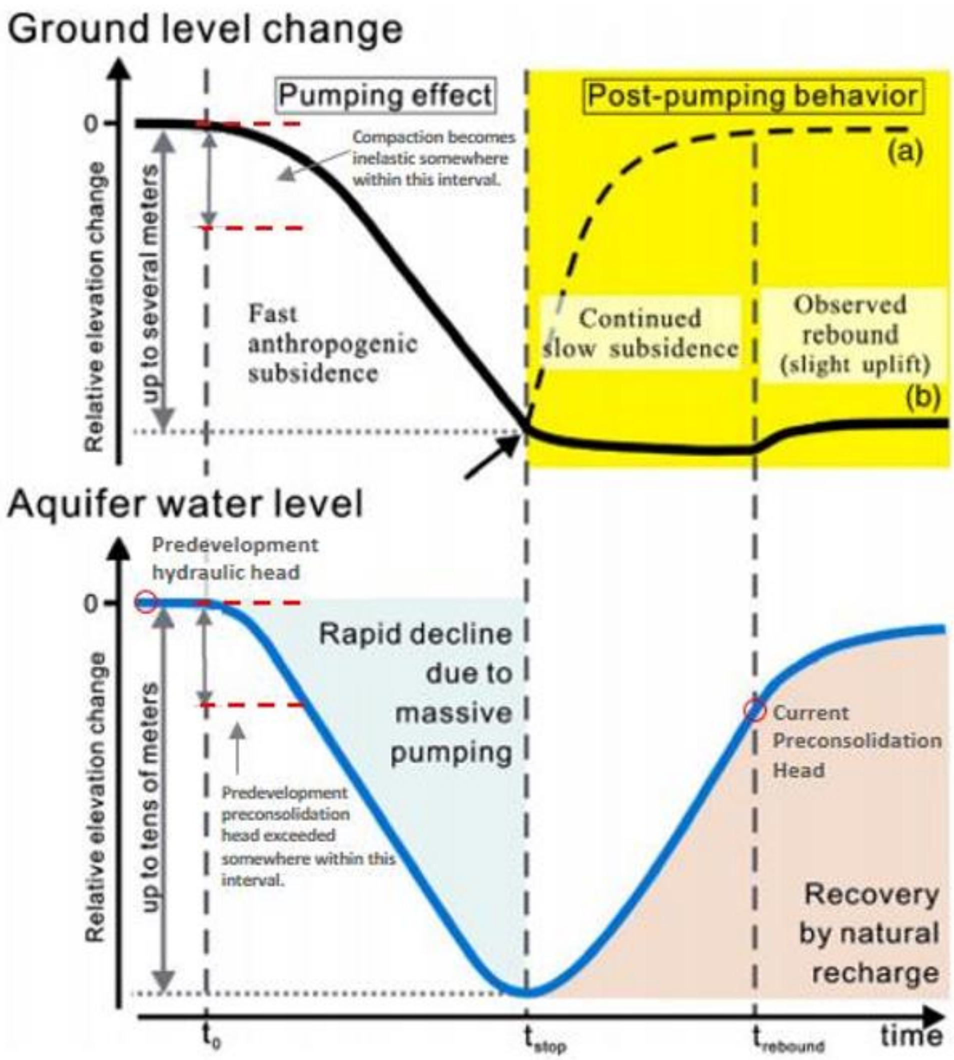

Figure 4-2: Conceptual model of groundwater-induced ground deformation in a system experiencing hydrodynamic consolidation. Modified from Chen et al. (2007).

5 RECENT GROUND DEFORMATION AND COMPACTION TRENDS

5.1 DERIVATION OF GROUND DEFORMATION TRENDS

Ground deformation trends in Greater Houston are derived utilizing GPS data from monitoring stations in the CORS, PAM, and HoustonNet networks. Initially, GPS positions are referred to ECEF-XYZ coordinates. Displacement can be subsequently computed and analyzed as individual vertical and horizontal components or as a resultant vector. Studies regarding land subsidence often assume a one-dimensional ground deformation model as horizontal displacements tend to be much smaller in magnitude compared to vertical displacements in areas experiencing land subsidence (Holzer, 1984). In Greater Houston, it has been documented that horizontal ground displacements are small, lack spatial consistency, and are not well correlated with vertical displacements (Kearns et al., 2015). Therefore, for the purposes of this study, only the vertical component of the GPS data will be considered.

Recent, 2000-2018, respective rates of land subsidence or uplift are computed by applying a linear regression model to the vertical displacement time-series of 166 GPS stations. In this case, negative slope values represent land subsidence, whereas positive slope values represent land rebound. Individual vertical displacement time-series graphs for each respective GPS station are provided in **Appendix I**. The standard error (σ) is also displayed with the computed linear regression model. Standard error, in this context, means that there is a 95% possibility that the true value of the site velocity (v) lies between $v - 2\sigma$ and $+2\sigma$. A contour map depicting the regional ground deformation trends was created utilizing Generic Mapping Tools (GMT) (Wessel et al., 2013). The

GMT 5.4 command *blockmea*n was utilized to grid the discrete velocity measurements within the region. Subsequently, contours were created utilizing the command *grdcontour* (**Figure 5-1**). A more local ground deformation map is derived for HGSD Area I and II by taking a spatial subset of the regional data and utilizing the GMT 5.4 command *surface* (**Figure 5-2**).

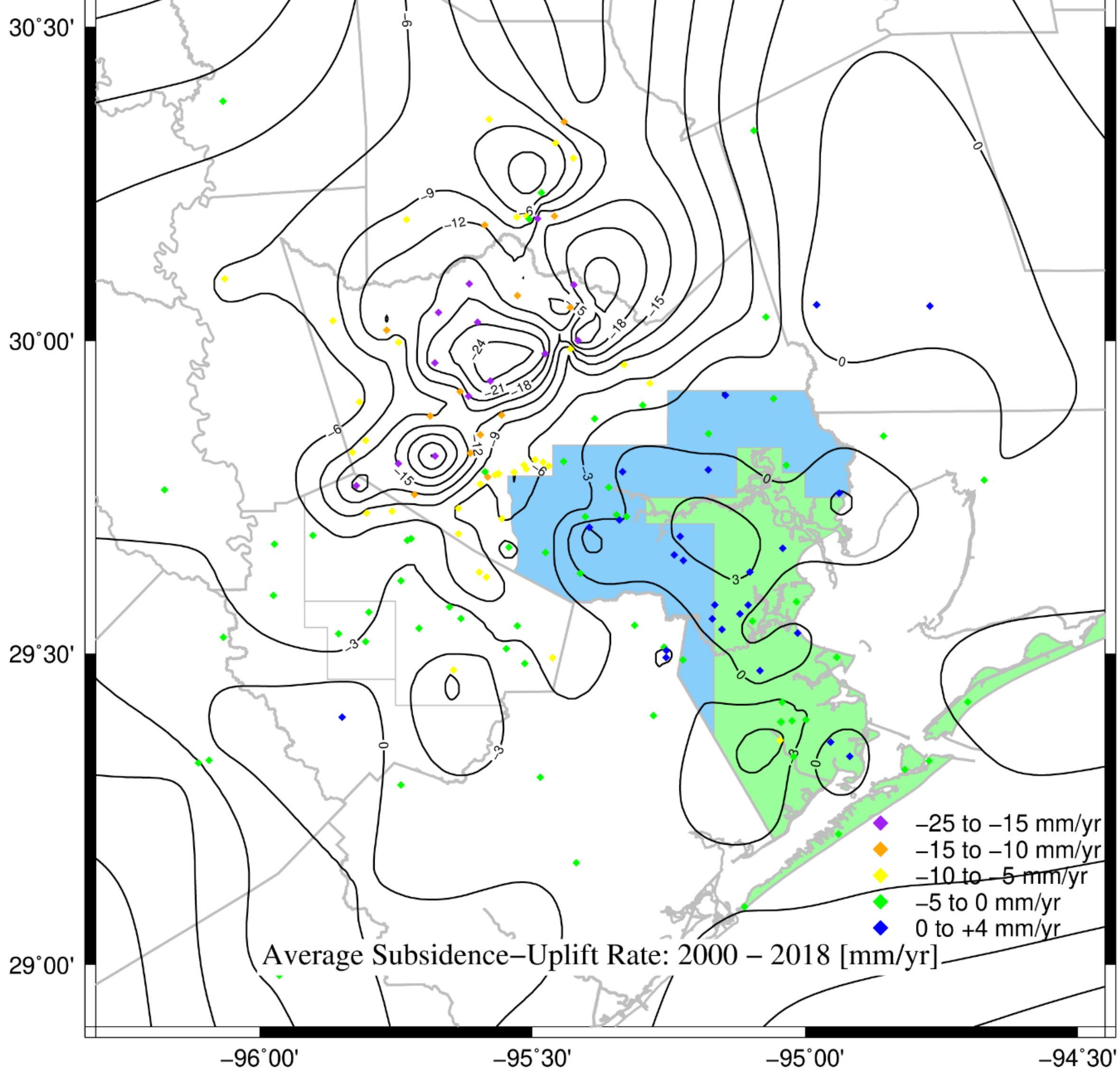

Figure 5-1: Contour map showing the recent land subsidence rate (2000-2018) within Greater Houston. Individual GPS site locations (diamonds) are color-coded corresponding to their respective vertical site velocity. Predominately, halted subsidence and rebound (*blue* diamonds) is seen in HGSD Area I and II.

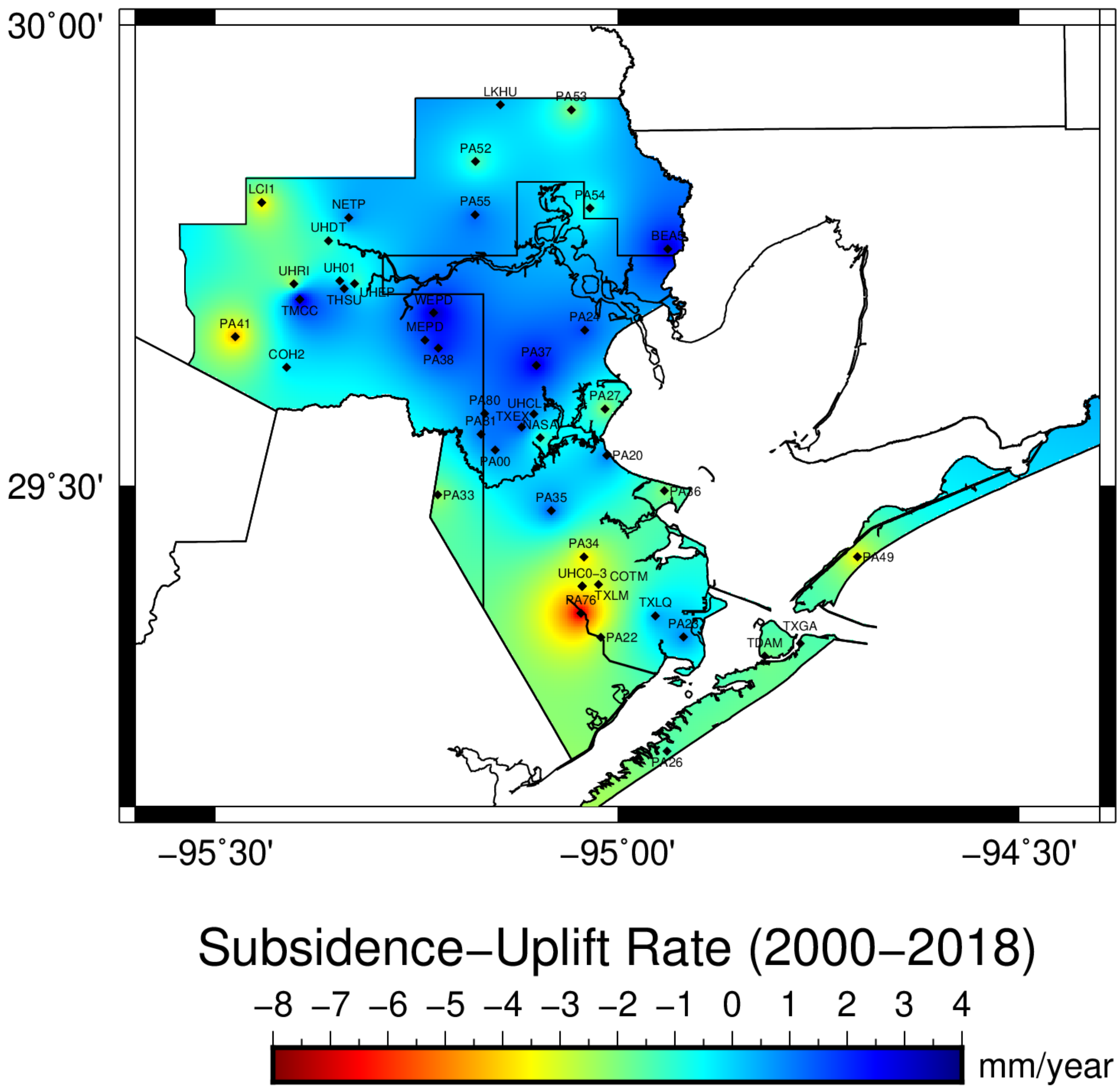

Figure 5-2: Map displaying ground deformation rates from 2000-2018 derived from all applicable stations (>2.5 year sampling history) in Harris-Galveston Subsidence District (HGSD) Area I and II. Rebound (*cool* colors) is predominantly observed at GPS stations along the Houston Ship Channel including NETP, WEPD, PA54, and PA24.

5.2 REGIONAL GROUND DEFORMATION TRENDS IN GREATER HOUSTON

From 2000 to 2018, land subsidence persists to some degree at the location of 138 of 166 GPS stations examined within Greater Houston. Observed subsidence is predominantly occurring in northwest Harris and Montgomery County (**Figure 5-1**). Rapid land subsidence (>10 mm/year) is observed in northwest Harris County (HGSD Area III) in the communities of Jersey Village, Addicks, Spring, and The Woodlands. Localized subsidence of this magnitude is also seen in Katy (FBSD Area A). Moderate land subsidence (<10 mm/year) is observed in Montgomery County (LSGCD), central Harris County, Fort Bend County (FBSD), and Brazoria County (BCGCD). Regionally, subsidence rates decrease from the northwest towards the southeast transitioning to land rebound in areas within Downtown Houston and the Houston Ship Channel.

Twenty of the twenty-eight GPS stations indicating land rebound or ceased land subsidence from 2000-2018 are locating within HGSD Area I and II. **Figure 5-3** provides the vertical displacement time-series for all rebounding GPS stations located within the region. The remaining sites indicating land rebound are isolated and do not appear to be spatial correlated. As the majority of rebounding sites are located in close proximity, a more regional rebound trend is apparent. The largest magnitude of land rebound (~3.7 mm/year) is observed at station TMCC located south of Downtown Houston. Other GPS stations recording appreciable land rebound (BEA5 ~3.3 mm/year; MEPD ~1.7 mm/year; PA24 ~1.8 mm/year; PA37 ~3.1 mm/year; PA55 ~1.4 mm/year; PA80 ~1.1 mm/year; WEPD ~3.5 mm/year) are located adjacent to or south of the Houston Ship Channel. At sites with sufficiently long histories (PA00, PA20, PA24), the onset of land rebound can be distinguished. Rebound at these site locations appears to have begun between 2001 and 2004. Some degree of land subsidence persists within HGSD Area I and II predominately northwest of Downtown Houston (PA41 ~-4.8 mm/year; LCI1 ~-3.8 mm/year) and near La Marque (PA76 ~-7.6 mm/year; PA34 ~-3.8 mm/year; TXLM ~-3.1 mm/year).

The observed land rebound occurring within HGSD Area I and II are interpreted to be the product of hydraulic head trends in the region. Land uplift after halting groundwater pumping has been observed in several other land subsidence regions including the Las Vegas Valley, Nevada (Hoffmann et al., 2001), Santa Clara Valley, California (Schmidt and Burgmann, 2003), and Taipei Basin, Taiwan (Chen et al., 2007). A number of salt domes scattered throughout Greater Houston are documented to be experiencing active diapirism which can subsequently lead to slight land uplift. Uplift related to the diapirism in the region is relatively small in magnitude, estimated to occur at ~0.45 mm/year and only affects land in the near vicinity of a given salt dome (Jackson and Seni, 1983; Jackson and Talbot 1986; Pittman, 1994). Therefore, salt diapirism is not interpreted to significantly contribute to the land rebound occurring and will not be considered in the scope of this study.

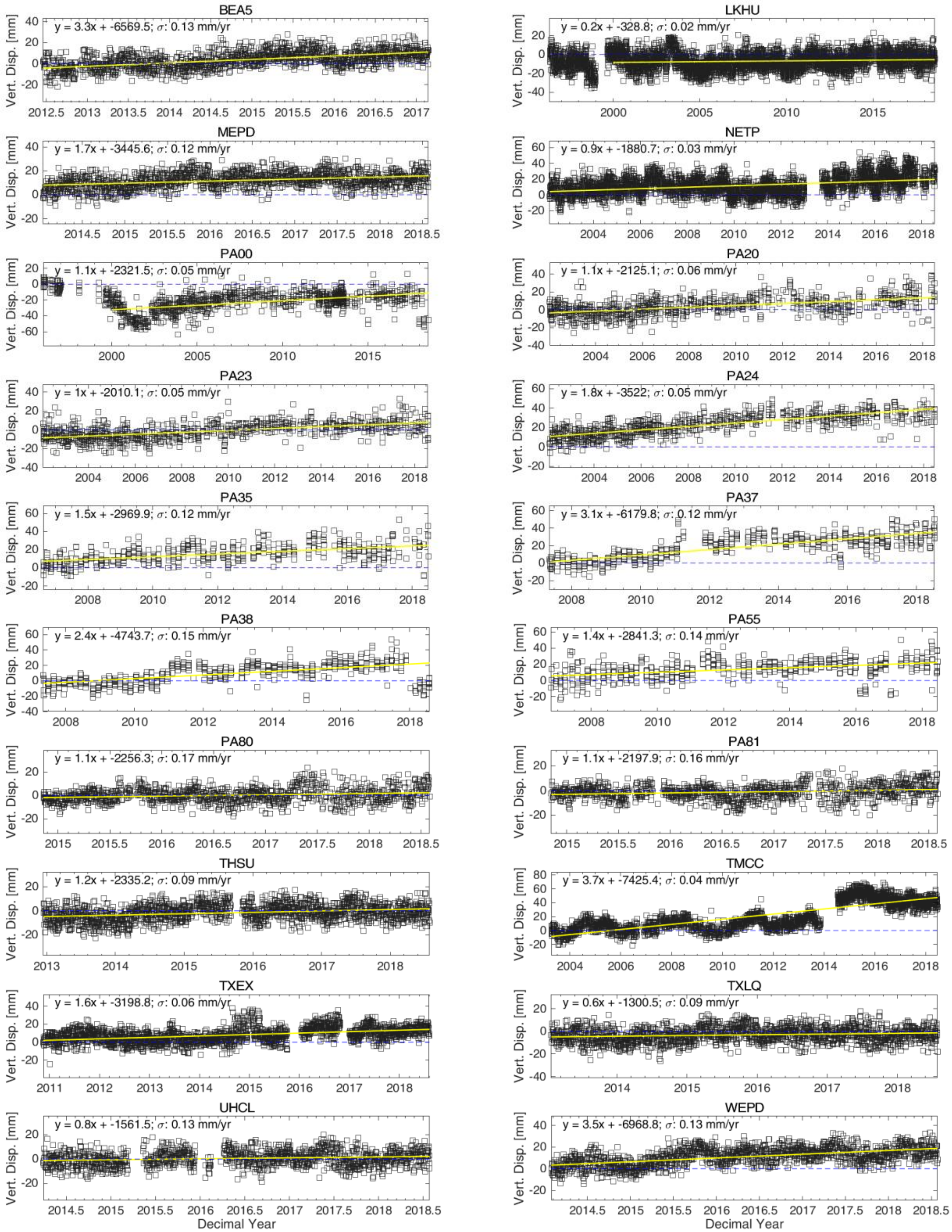

Figure 5-3: Vertical displacement time-series of rebounding GPS stations located within HGSD Area I and II. A linear regression model is fit to all sites from 2000, or at the start of recording later, to 2018

5.3 BOREHOLE EXTENSOMETER COMPACTION DATA

A majority of borehole extensometers completed in the region are situated within HGSD Area I and II. In the region of interest, there are a total of 10 borehole extensometers completed at 8 unique sites. Two sites in particular, Baytown and Clear Lake, have two borehole extensometers completed at different depth intervals. Groundwater measurements for both the Chicot and Evangeline aquifers are available for all extensometer sites from collocated observational wells. **Figure 5-4** displays the long-period time-series (1962-2018) of aquifer sediment compaction and groundwater head at the 8 aforementioned extensometer sites. Individual extensometer and corresponding groundwater head time-series are displayed in **Figure 5-5 (a-i)**. The rate of sediment compaction observed at each borehole extensometer site varies because of different groundwater withdrawal rates in adjacent areas of each site as well as the varying clay-to-sand ratios of the subsurface sediments (Kasmarek et al., 2012). Nevertheless, at most sites, compaction has slowed, or even reversed, as groundwater heads have steadily risen during the past 35 to 40 years.

The borehole extensometers located at the Northeast, East End, NASA and Seabrook have shown compaction which has slowed dramatically as hydraulic heads in the Chicot aquifers have increased throughout the entirety of their site histories (**Figure 5-5c**, **Figure 5-5d**, **Figure 5-5f**, and **5-5h**). Rapid aquifer compaction (> 2.5 cm/year) persisted at these extensometer sites until the late 1980s and early 1990s. Thereafter, aquifer compaction rates sharply decrease sharply, which correlates with increasing groundwater levels in the Chicot and Evangeline aquifers (**Figure 5-6**).

Currently, a small component of continued inelastic compaction can be obsereved at the sites.

Figure 5-5e illustrates the compaction time-series for the two extensometers located at Clear Lake. The two extensometers at Clear Lake are completed within the Evangeline at 530 and 936 meters below the land surface. Both extensometers have consistently recorded approximately the same amount of compaction from 1976 to 2018. This observation indicates that there was no significant aquifer compaction between the 530 to 936 meter interval. In other words, compaction at the Clear Lake site occurs within sediments shallower than 530 m below the land surface, which includes the whole Chicot aquifer and the upper Evangeline aquifer. **Figure 5-5a** illustrates the compaction time-series for the two extensometers located at Baytown, which are completed at 131 and 450 m. The two compaction time-series indicate that rapid subsidence occurred from 1973 to 1983. The compaction accumulated within the Chicot aquifer (-6 to -131 meters, ~1.5 cm/year), measured by the shallow extensometer, accounts for nearly 50% of the total compaction (-6 to -450, ~3.0 cm/year) during this time frame. Compaction thereafter, from 1984 to 2009, was rather insignificant for both borehole extensometers (~0.2 cm/year). Observations provided by these extensometers suggest that a majority of the compaction was confined within the Chicot aquifer and the uppermost Evangeline aquifer.

The Pasadena and Texas City extensometers are the only sites that have seen a period of appreciable reversal of compaction. Between 1990 and 2010, ~5 cm of sediment expansion occurred at the Pasadena extensometer (**Figure 5-5b**). Evangeline groundwater levels at the Pasadena site have increased steadily from 1981 to 2018 (~0.45 m/year) since experiencing a rapid decline from 1976 to the end of 1980 (~2.0 m/year). In the case of the Chicot aquifer at the site, Chicot aquifer heads declined by ~10 m from 1975 and 1991 before recovering an accumulated 15 m from 1991 to 2018. Rapid aquifer compaction (~4 cm/year) was observed by the extensometer from 1976 to 1979 before slowing significantly. This slowing of the compaction rate closely aligns with increasing Chicot and Evangeline groundwater heads during that time. Compaction persisted at the site until 1990 when it sharply reversed showing an expansion of ~0.25 cm/year. In regards to the Texas City extensometer, ~3 centimeters of expansion was observed from 1980 to 2000 (**Figure 5-5i**). Hydraulic heads in both the Chicot and Evangeline aquifer have risen since 1977 at ~0.35 m/year. Compaction observed by the extensometer was observed from 1974 to 1981 (~0.85 cm/year) before changing to expansion.

Paradoxically, since 2010, Baytown and Pasadena extensometers have been recording apparent rapid compaction (**Figure 5-5a** and **Figure 5-5b**). The observed compaction trends post 2010 do not correlate with collocated groundwater levels nor GPS observations. It is suggested by Yu et al. (2014) that the observed anomalous behaviors are indicative of a mechanical problem with the extensometers. Borehole extensometers are known to mechanical fatigue and as such have limited life-spans. Thus, I interpret these two sites to no longer provide meaningful compaction information.

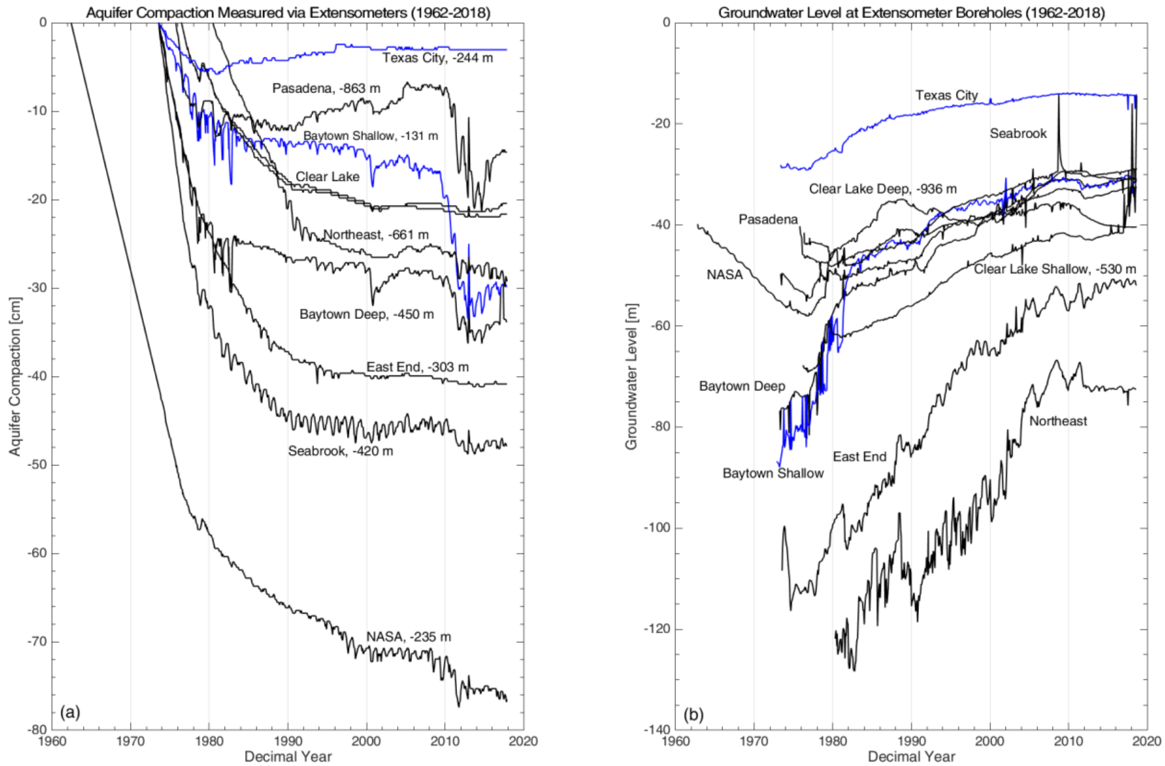

Figure 5-4: Plots depicting history of aquifer compaction (left) and corresponding groundwater head (right) at 8 extensometer sites within the vicinity of the Houston Ship Channel. The completion depth of each extensometer is marked with the corresponding time-series. *Blue* and *black* lines represent boreholes that are completed within the Chicot and Evangeline aquifers, respectively.

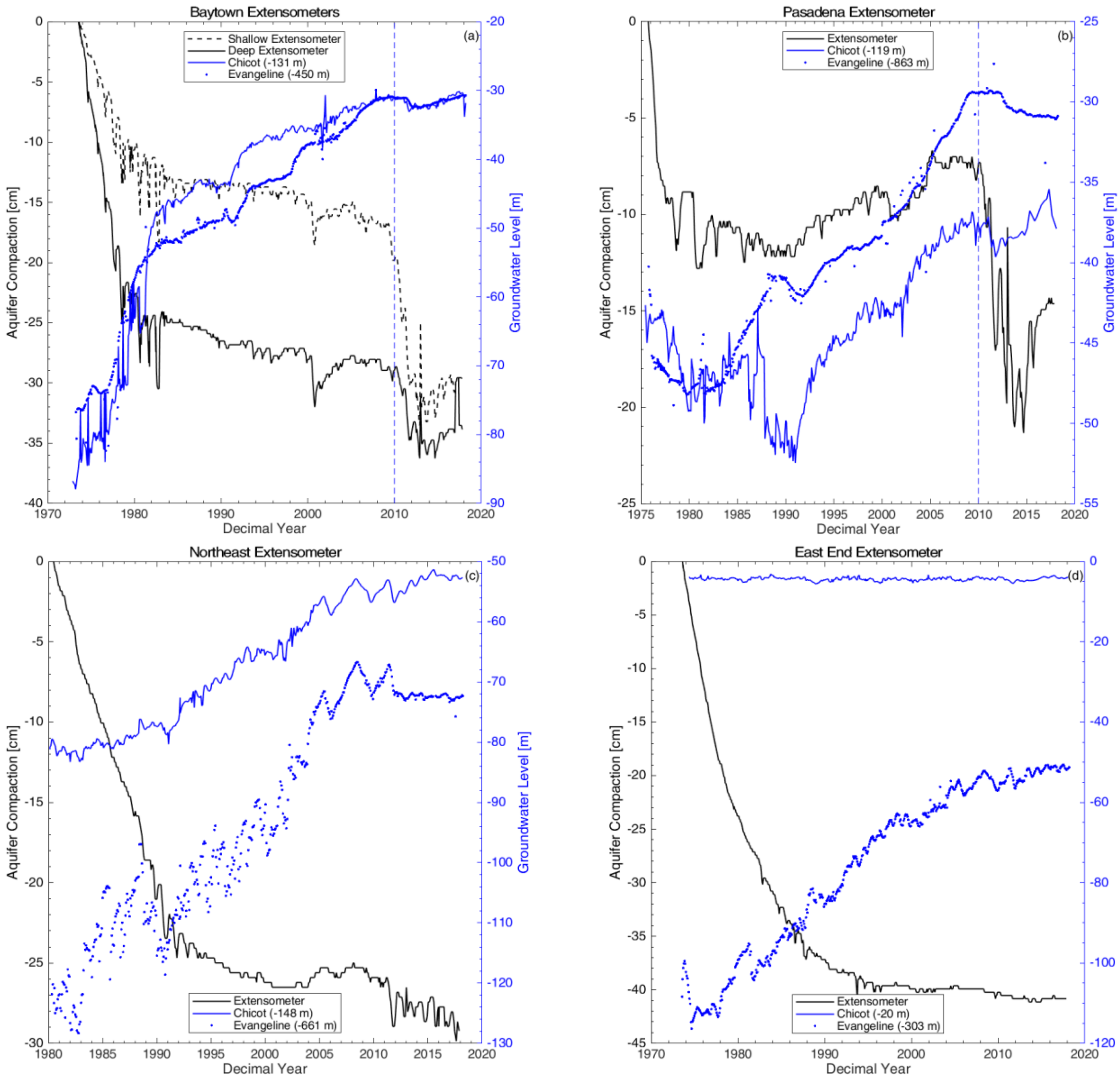

Figure 5-5 (a-d): Borehole extensometer compaction observations plotted against groundwater measurements in both the Chicot and Evangeline aquifers from co-located observation wells. Depths of groundwater observational wells are indicated within the plot legend. Depth of borehole extensometers may be referenced from **Figure 5-4**. Both Baytown and Pasadena extensometers appear to record anomalous, rapid sediment compaction after 2010, indicated by the vertical dashed line.

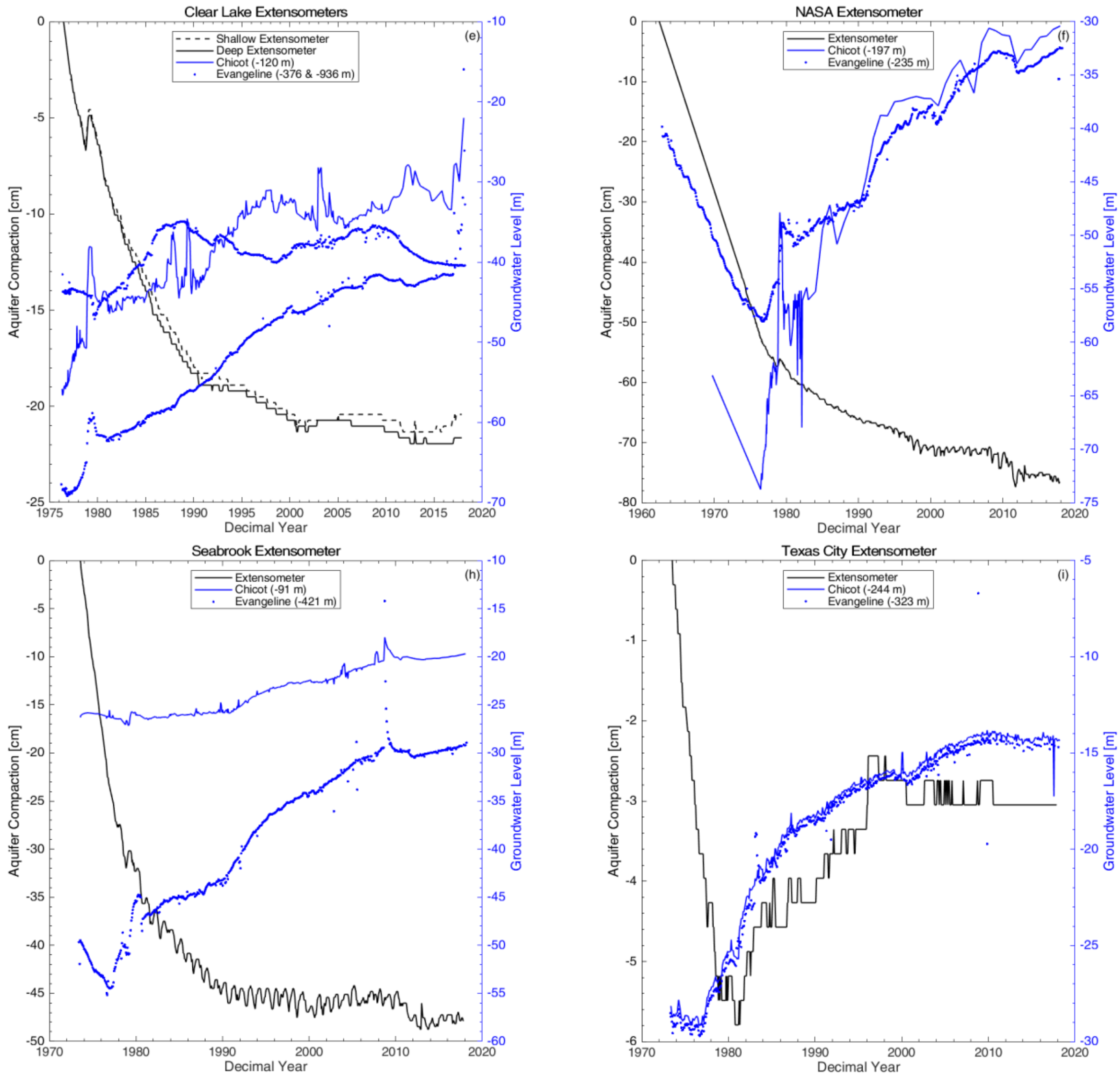

Figure 5-5 (e-i): Borehole extensometer compaction observations plotted against groundwater measurements in both the Chicot and Evangeline aquifers from co-located observation wells. Depths of groundwater observational wells are indicated within the plot legend. Depth of borehole extensometers may be referenced from **Figure 5-4**.

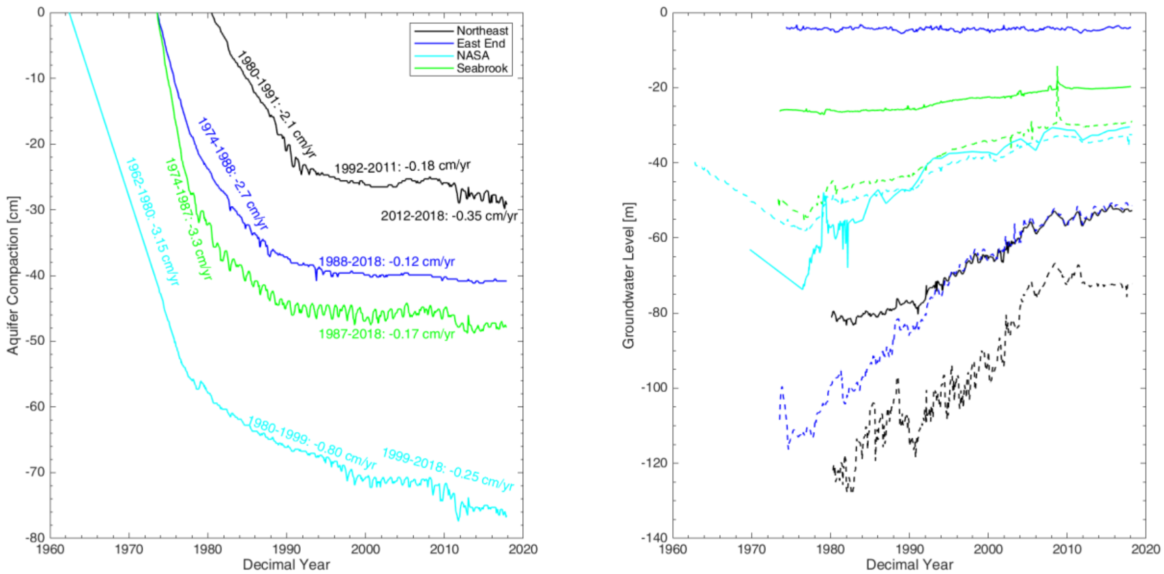

Figure 5-6: Plot showing aquifer compaction time-series observed by extensometers (left) located at Northeast (*black*), East End (*blue*), Seabrook (*green*), and NASA (*cyan*) versus respective groundwater levels. Solid and dashed lines indicate groundwater levels in the Chicot and Evangeline aquifer, respectively.

6 GROUNDWATER HEADS IN THE CHICOT AND EVANGELINE AQUIFERS

6.1 DERIVATION OF POTENTIOMETRIC SURFACES

Data from local groundwater wells were analyzed for the derivation of potentiometric surfaces of the Chicot and Evangeline aquifers for both 2000 and 2018. In total, 131 and 183 wells were analyzed in the Chicot and Evangeline aquifers, respectively. Groundwater heads as of 2000 and 2018 at each well are derived by first resampling and imputing data gaps utilizing the K-Nearest Neighbor (KNN) imputation method to achieve evenly-sampled data. The KNN imputation method interpolates missing data based on the distance-weighted average of *k* neighboring points (Little and Rubin, 2019). Once the raw groundwater data is imputed and even-sampled, Seasonal and Trend using Locally Estimated Scatterplot Smoothing (STL) decomposition (Cleveland et al., 1990) is then applied to extract the trend, seasonal, and residual components from the data. In this case, an additive decomposition model of the form:

$$y(t) = T(t) + S(t) + R(t)$$

is utilized where $y(t)$ is the input signal, $T(t)$ is the trend component, $S(t)$ is the seasonal component, and $R(t)$ is the residual component. **Figure 6-1** provides an example of applying STL decomposition on a groundwater level time-series and subsequent output components. Thereafter, trend values at the beginning of 2000 and the end of 2018 were extracted to represent the desired groundwater levels.

Contour maps depicting the potentiometric surface in each aquifer at 2000 and 2018 were then derived utilizing GMT commands *blockmean* and *grdcontour* discussed previously (**Figure 6-2** and **Figure 6-3**). Additional contours representing the change in the potentiometric surface from 2000 to 2018 were also derived for both the Chicot and Evangeline aquifers (**Figure 6-4** and **Figure 6-5**). The created contours are then overlain on GPS-derived ground deformation results to analyze the spatial relationship between current groundwater heads, change in groundwater heads, and ground deformation trends.

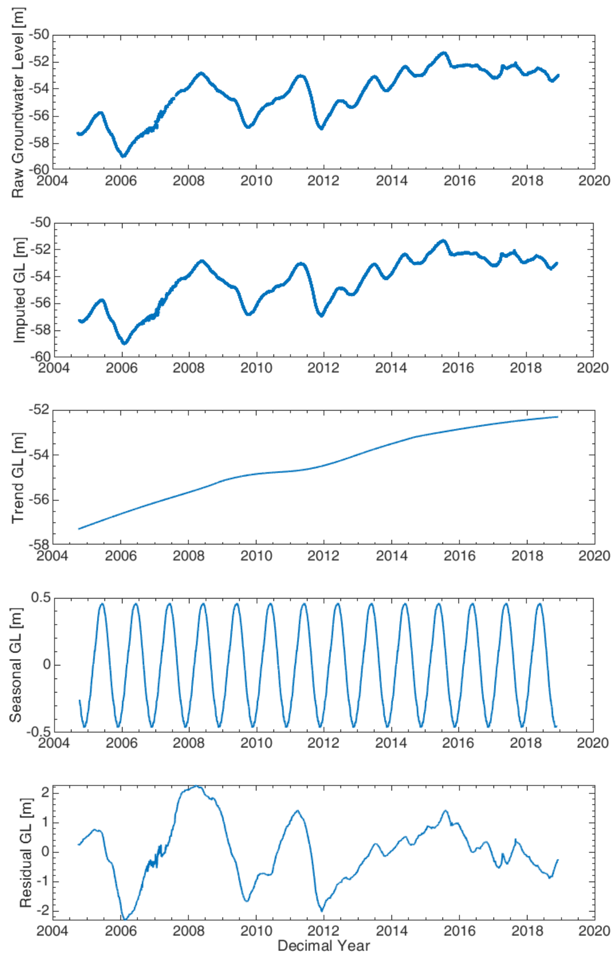

Figure 6-1: Graphs showing imputation and STL decomposition results for daily-monitored observational well 294728095200103 (LJ-65-14-738) completed in the Chicot aquifer.

6.2 OBSEREVED HYDRAULIC HEADS, CHANGES, AND GROUND DEFROMATION

Figure 6-2 displays the determined potentiometric surface for the Chicot aquifer as of 2018 overlaid on GPS-derived ground deformation trends. Regionally, hydraulic heads of the Chicot aquifer in 2018 were largely less than 30 m below the land surface (abbreviated hereafter as -30 m). Deeper hydraulic heads of -40 to -60 m were seen in southwest and central Harris County (HGSD Area III). The deepest hydraulic heads are observed in southern Harris County at -60 m. In areas of recorded rapid subsidence (>15 mm/year), Chicot aquifer levels vary from -30 to -50 m. To the southeast, in the area of observed land rebound, hydraulic heads fall predominantly between -10 to -40 m. Regionally, land rebound does not necessarily occur where hydraulic heads of the Chicot aquifer fall within in this range such as a majority of Fort Bend and Montgomery County.

Figure 6-3 displays the determined potentiometric surface for the Evangeline aquifer as of 2018 overlaid on GPS-derived ground deformation trends. Hydraulic heads in the Evangeline aquifer are generally 20 m deeper than the Chicot aquifer regionally. Large spatial drops in the hydraulic head of the Evangeline correlate with areas experiencing rapid land subsidence (>15 mm/year). Hydraulic heads in the rapidly subsiding Jersey Village and The Woodlands areas vary from -90 to -135 m. In the area of observed land rebound (HGSD Area I and II), hydraulic heads of the Evangeline aquifer vary from -30 to -60 m.

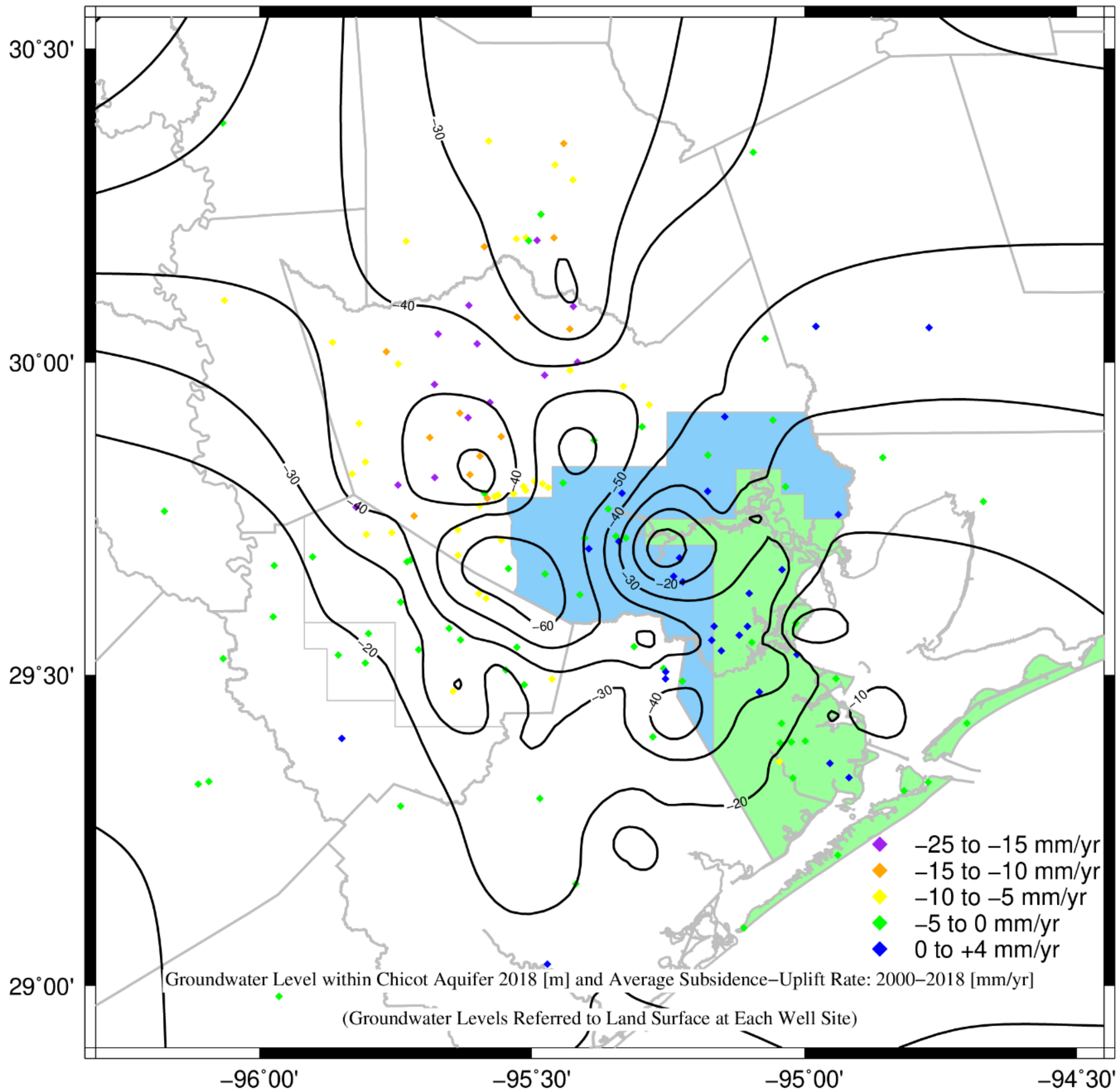

Figure 6-2: Contours (*black* lines) showing groundwater levels in the Chicot aquifer at the end of 2018 overlain on GPS-derived ground deformation trends. Individual GPS site locations (diamonds) are color-coded corresponding to their respective vertical site velocity.

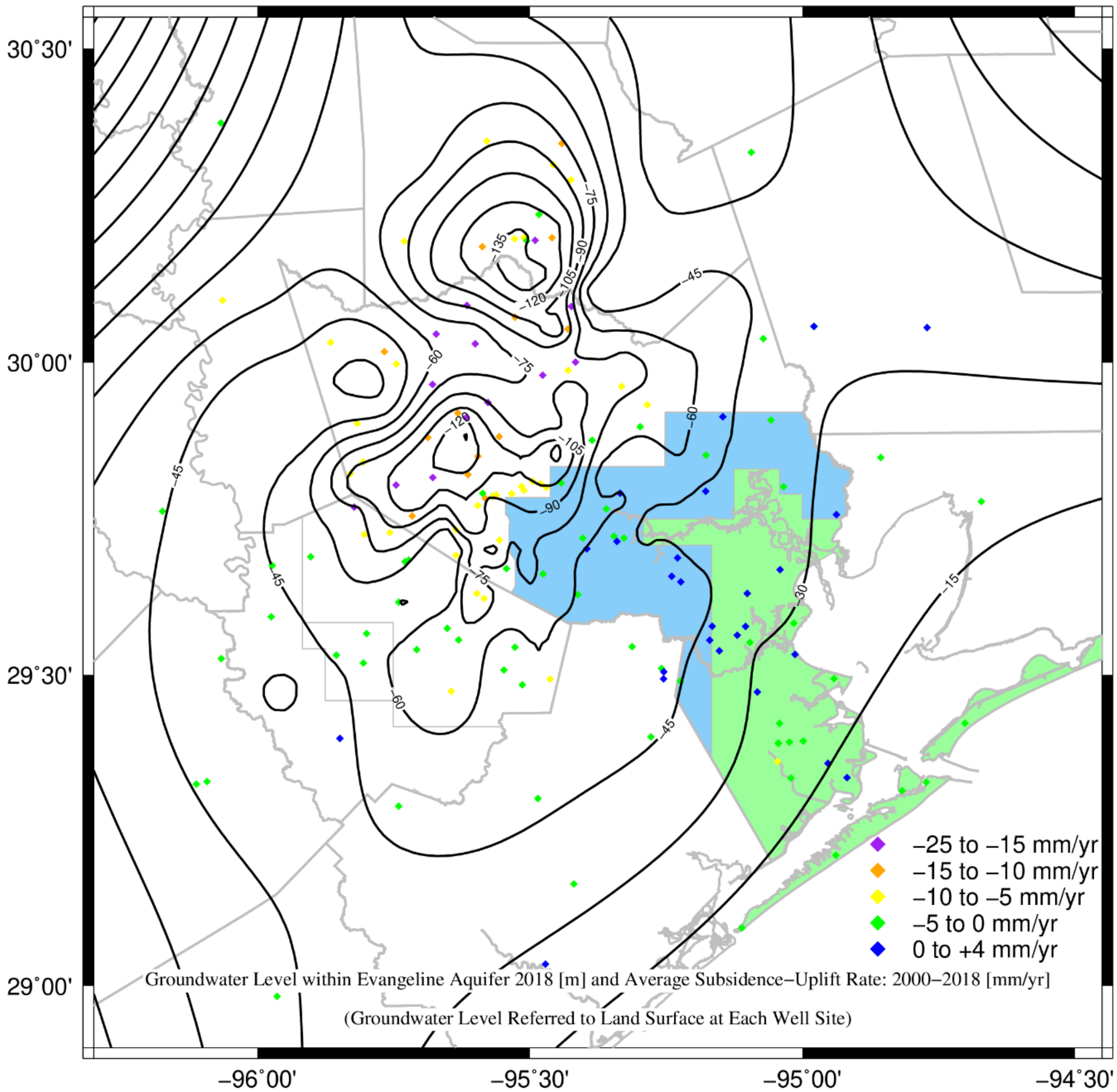

Figure 6-3: Contours (*black* lines) showing groundwater levels in the Evangeline aquifer at the end of 2018 overlain on GPS-derived ground deformation trends. Individual GPS site locations (diamonds) are color-coded corresponding to their respective vertical site velocity.

Figure 6-4 depicts contours of the change in hydraulic head of the Chicot aquifer from 2000 to 2018. Localized decreases in the hydraulic head of the Chicot aquifer of no more than 5 m were observed near The Woodlands and Katy. The largest magnitude increases in groundwater level upwards of 5-25 m was observed in southern Harris County (HGSD Area II and III). However, modest land subsidence (-5 to -10 mm/year) can still be observed despite the large increase in groundwater level. In areas of most rapid land subsidence such as Jersey Village, Chicot aquifer heads rose a modest 5-10 m or saw no significant change. In the region of observed land rebound, groundwater levels predominantly remained constant or increased by only 5 m.

Figure 6-5 depicts contours of the change in hydraulic head of the Evangeline aquifer from 2000 to 2018. Overall, the Evangeline aquifer experienced more drastic changes in hydraulic head compared to the Chicot aquifer. Large localized drops in hydraulic head were observed in Katy (-10 to -15 m) and The Woodlands (-10 to -40 m), which coincide with relatively rapid subsidence. Regionally, however, the Evangeline aquifer hydraulic heads predominantly increased from 2000 to 2018. The largest increase of 20-40 m in hydraulic head was observed in central Harris County near Jersey Village, where the highest rates of subsidence occurred. Hydraulic heads in the area of land rebound rose generally between 10-20 m. While the areas of greatest spatial hydraulic head decrease appear to occur in proximity to areas of greatest land subsidence, there is not a direct correlation between hydraulic head change and ground deformation.

From the observations presented in this chapter, there is no apparent universal, direct correlation between changes in hydraulic head and ground deformation within

Greater Houston. Thus, preconsolidation heads must be considered and further investigated.

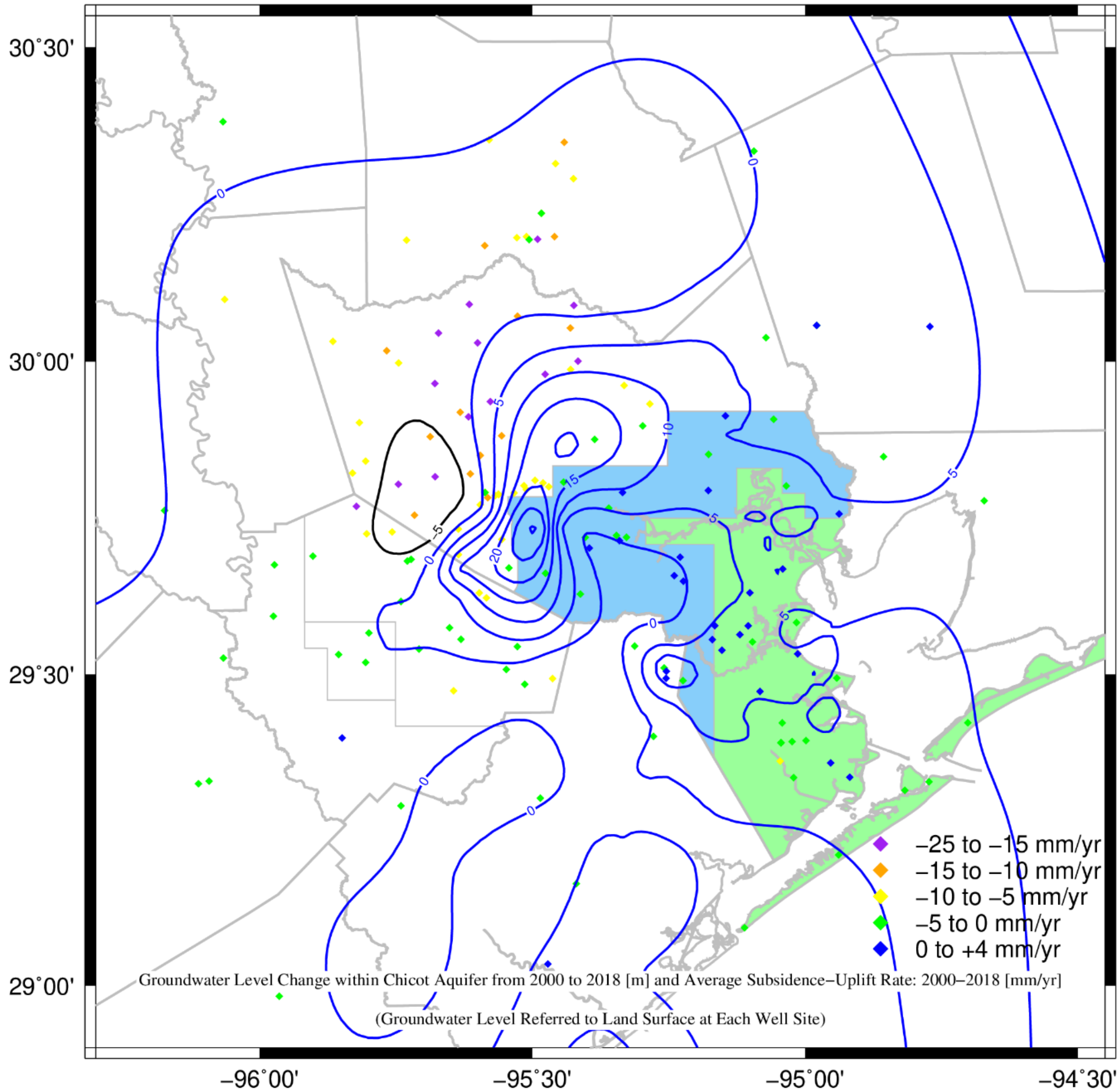

Figure 6-4: Contours showing the change in groundwater levels in the Chicot aquifer from 2000 to 2018 overlain on GPS-derived ground deformation trends. *Black* and *blue* contours indicate decreases and increases in groundwater level head, respectively. Individual GPS site locations (diamonds) are color-coded corresponding to their respective vertical site velocity.

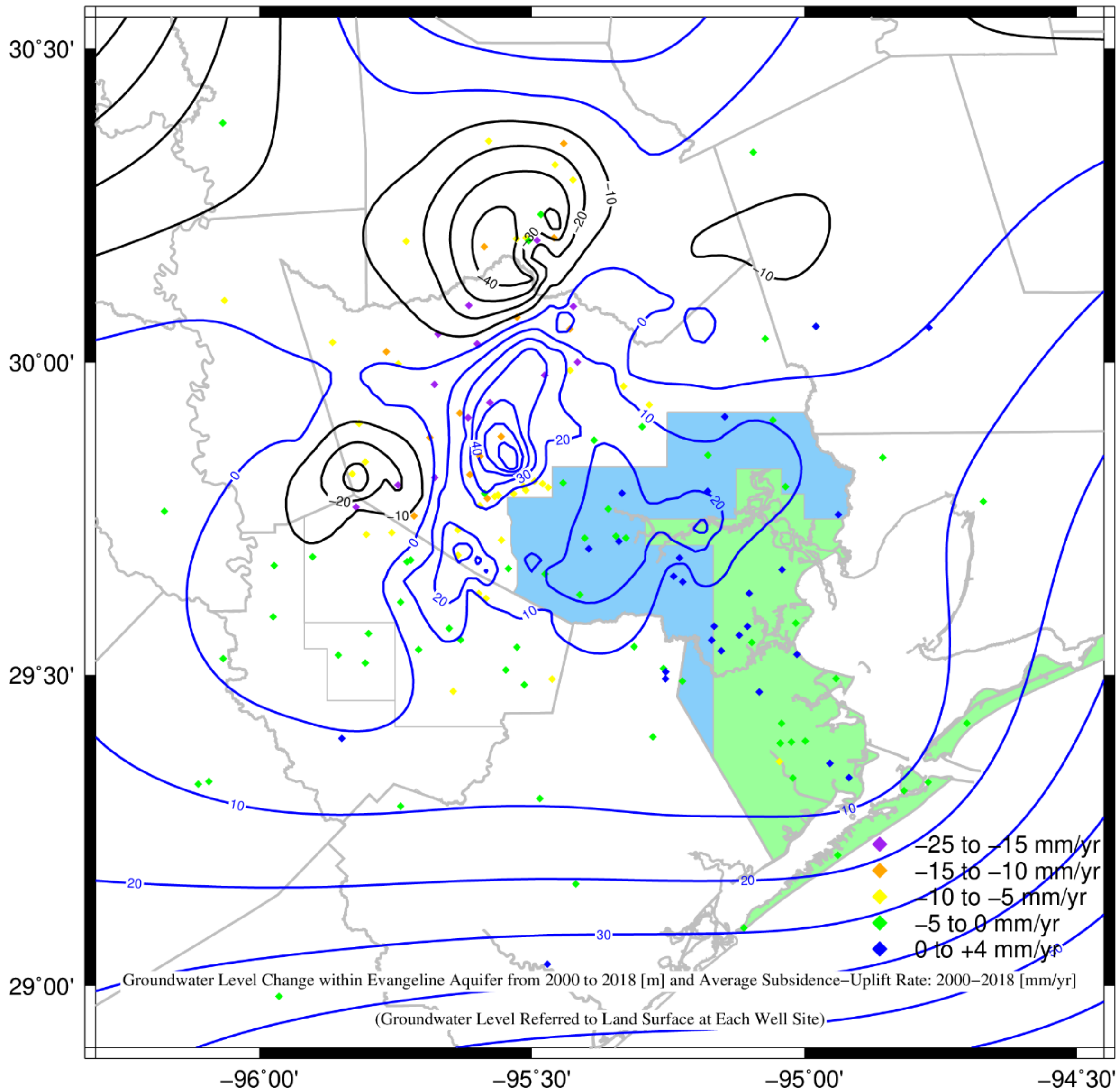

Figure 6-5: Contours showing the change in groundwater levels in the Evangeline aquifer from 2000 to 2018 overlain on GPS-derived ground deformation trends. *Black* and *blue* contours indicate decreases and increases in groundwater level head, respectively. Individual GPS site locations (diamonds) are color-coded corresponding to their respective vertical site velocity.

7 SEASONAL GROUNDWATER AND GPS DEFORMATION ANALYSIS

7.1 MOTIVATION AND DERIVATION OF SEASONAL MODELS

Previous investigations on the vertical distribution of sediment compaction in Greater Houston by Jorgensen (1975) and Yu et al. (2014) suggest that sediment compaction in southeastern Harris and Galveston County largely occurs within the extent of the Chicot aquifer, whereas compaction further northwest occurs predominantly within the Evangeline aquifer. To validate this, the seasonal elastic deformation in GPS time-series is compared with seasonal variations in groundwater levels for the Chicot and Evangeline aquifers. It is observed that GPS time-series in Greater Houston show elastic seasonal deformation superimposed on long-term residual land rebound or uplift. The redistribution of groundwater is known to produce a poro-elastic effect which can be observed as a surface deformation signal (Rice and Cleary, 1976).

Groundwater seasonal signals for the Chicot and Evangeline aquifer are derived by applying STL, previously discussed in **Chapter 6**, on two daily-sampled groundwater observation wells located within HGSD Area II (**Figure 7-1**). GPS seasonal signals are derived by first fitting a linear regression model to the vertical displacement time-series and computing the model residual. In this case, the residual time-series ($r(t)$) resembles the seasonal elastic deformation component and is subsequently modeled by fitting an annual and half-annual Fourier series of the form:

$$r(t) = c_1 \sin(2\pi t) + c_2 \cos(2\pi t) + c_3 \sin(4\pi t) + c_4 \cos(4\pi t).$$

The constants (c_1,c_2,c_3,c_4) are computed utilizing the MATLAB function *fit* employing a non-linear least-squares method (Levenberg, 1944; Marquardt, 1963). In total, seasonal signals from 12 GPS located within a ten-kilometer radius of the two groundwater observation wells are computed (**Figure 7-1**). Lastly, the seasonal signals are compared to determine whether fluctuations in the Chicot or Evangeline aquifer dominate the elastic seasonal deformation observed in the GPS observations. The dominating groundwater seasonal signal will have a smaller measured phase lag with the GPS seasonal signal (**Figure 7-2**).

7.2 SEASONAL MODEL RESULTS

Figure 7-3 (a-l) displays the computed linear regression models and residuals for all applicable GPS stations as well as a comparison of the derived seasonal models. Stations to the northwest (UHRI, PA41, LCI1, HSMN, CSTE, TSFT) exhibit seasonal elastic compaction that more closely correlates with the Evangeline-derived seasonal model. Stations to the southeast (TMCC, UH01, UHDT, THSU, UHEP, NETP) exhibit seasonal elastic compaction that more closely correlates with the Chicot-derived seasonal model. These observations seen through seasonal modeling provide evidence that supports the hypothesis and findings by Jorgensen (1975) and Yu et al. (2014). Furthermore, observations at the Clear Lake and Baytown extensometers sites, previously discussed, further substantiate these observations.

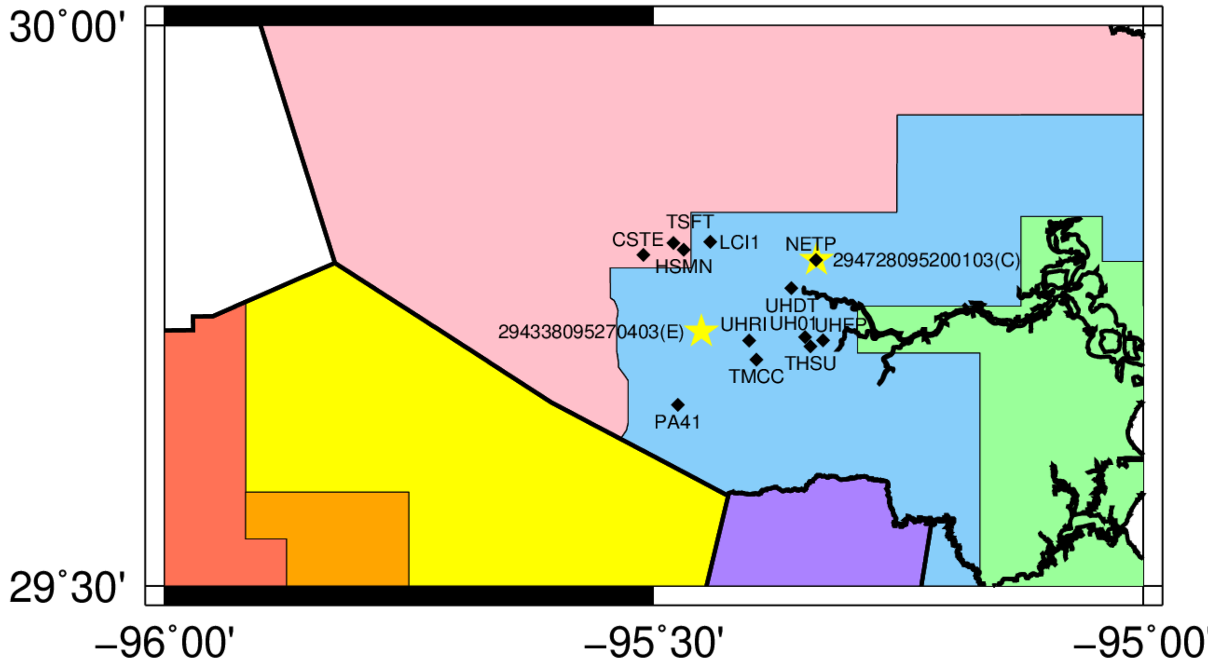

Figure 7-1: Map displaying the locations of GPS stations (*black* diamonds) and groundwater observation wells (*yellow* stars) utilized in seasonal modeling. Groundwater well ID 294728095200103 (149 m deep) and 294338095270403 (592 m deep) have a daily sampling rate and are completed in the Chicot and Evangeline aquifer, respectively. All GPS stations lie within a 10-km radius of the two groundwater observational wells.

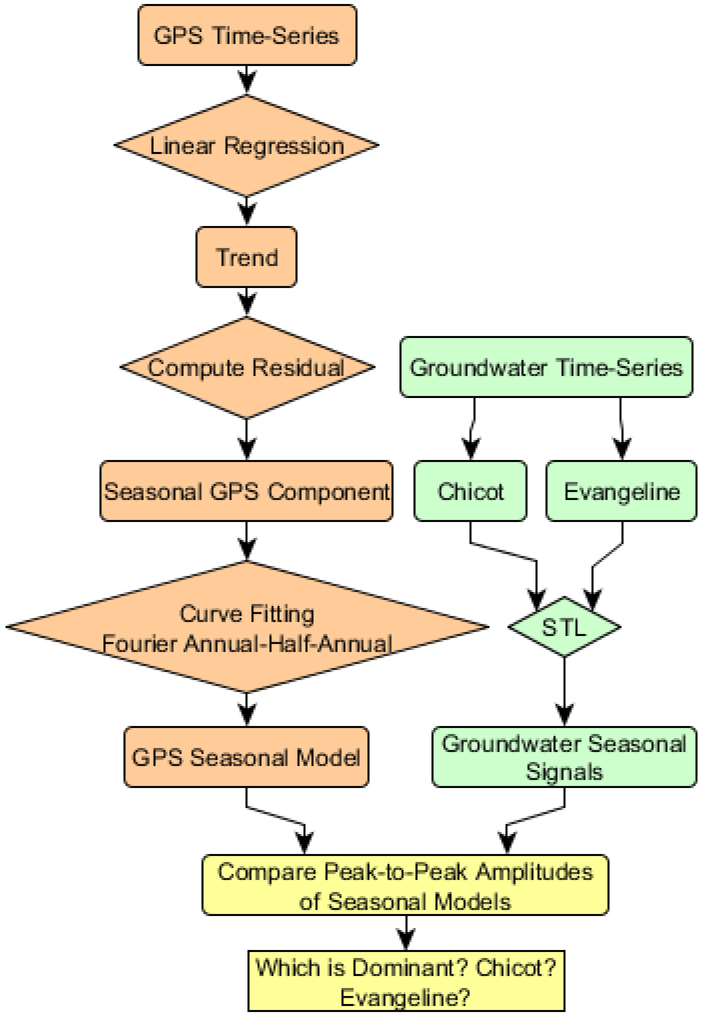

Figure 7-2: Schematic workflow diagram of seasonality analysis.

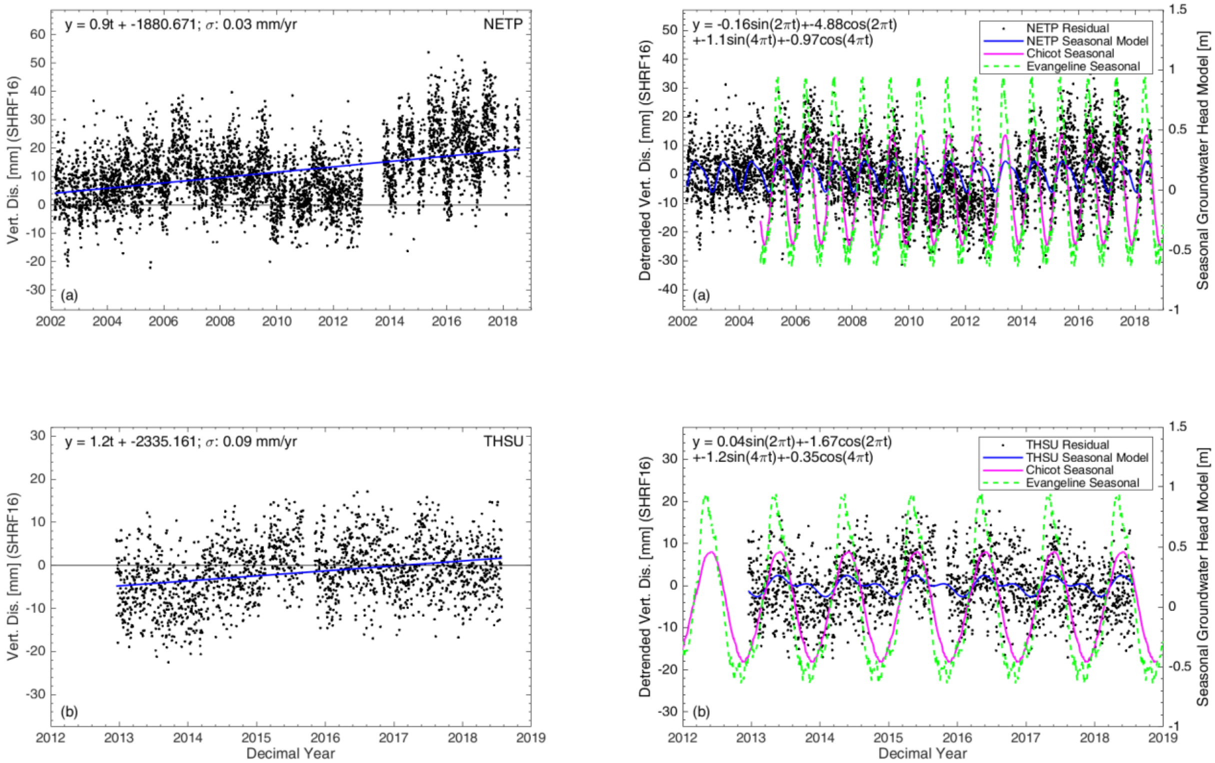

Figure 7-3 (a-b): Plots displaying GPS vertical displacement time-series (left column) and comparison of GPS and groundwater seasonal signals (right column) for stations NETP and THSU. Locations of GPS stations are shown in **Figure 7-1**.

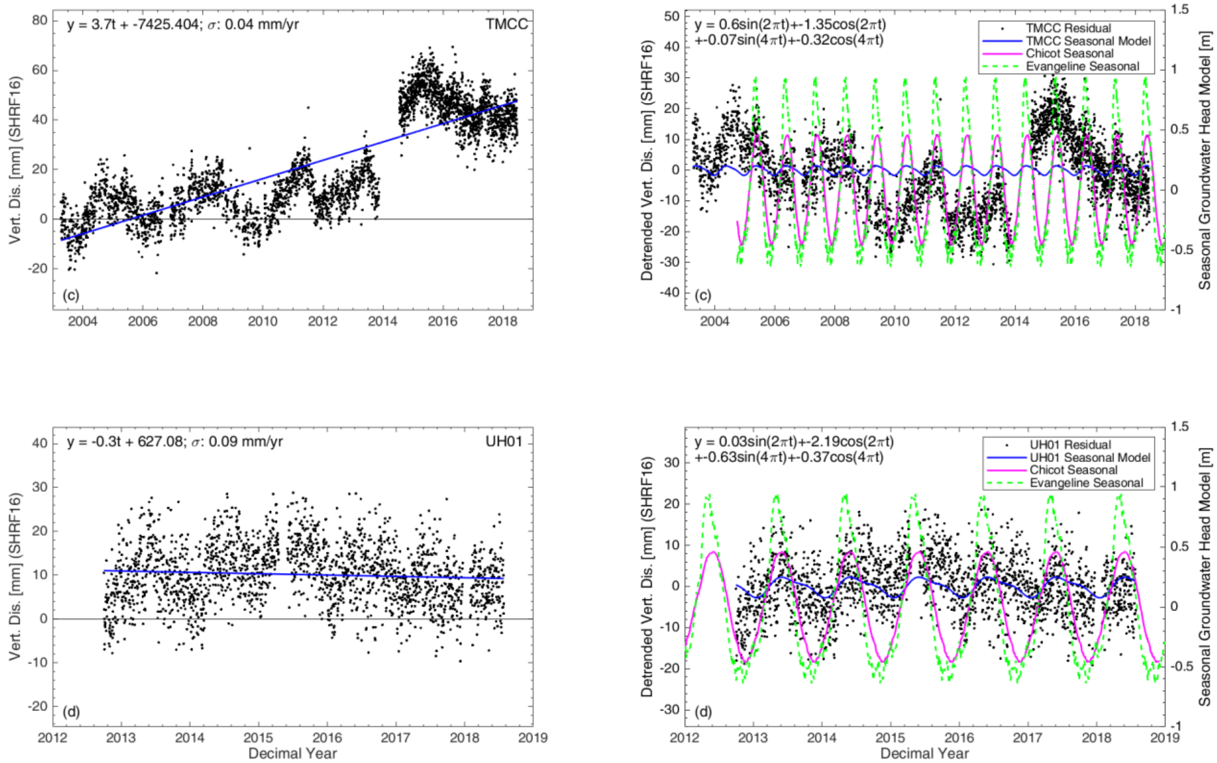

Figure 7-3 (c-d): Plots displaying GPS vertical displacement time-series (left column) and comparison of GPS and groundwater seasonal signals (right column) for stations TMCC and UH01. Locations of GPS stations are shown in **Figure 7-1**.

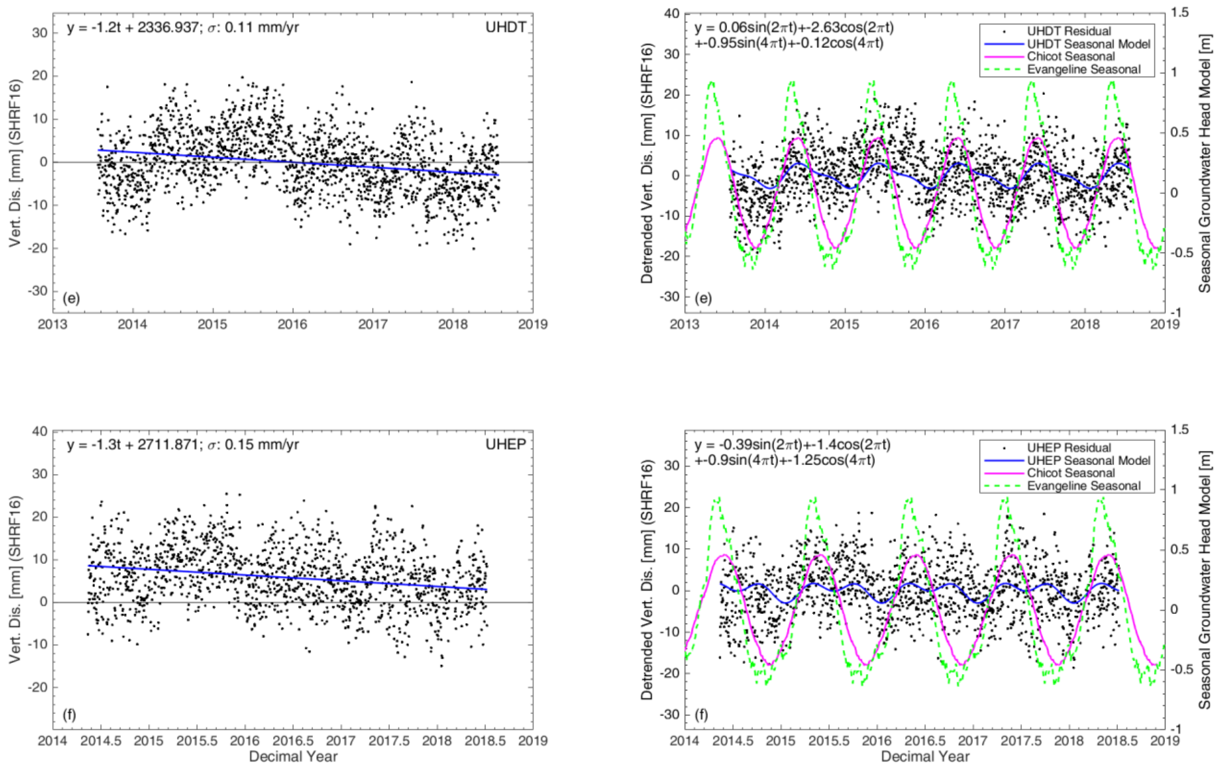

Figure 7-3 (e-f): Plots displaying GPS vertical displacement time-series (left column) and comparison of GPS and groundwater seasonal signals (right column) for stations UHDT and UHEP. Locations of GPS stations are shown in **Figure 7-1**.

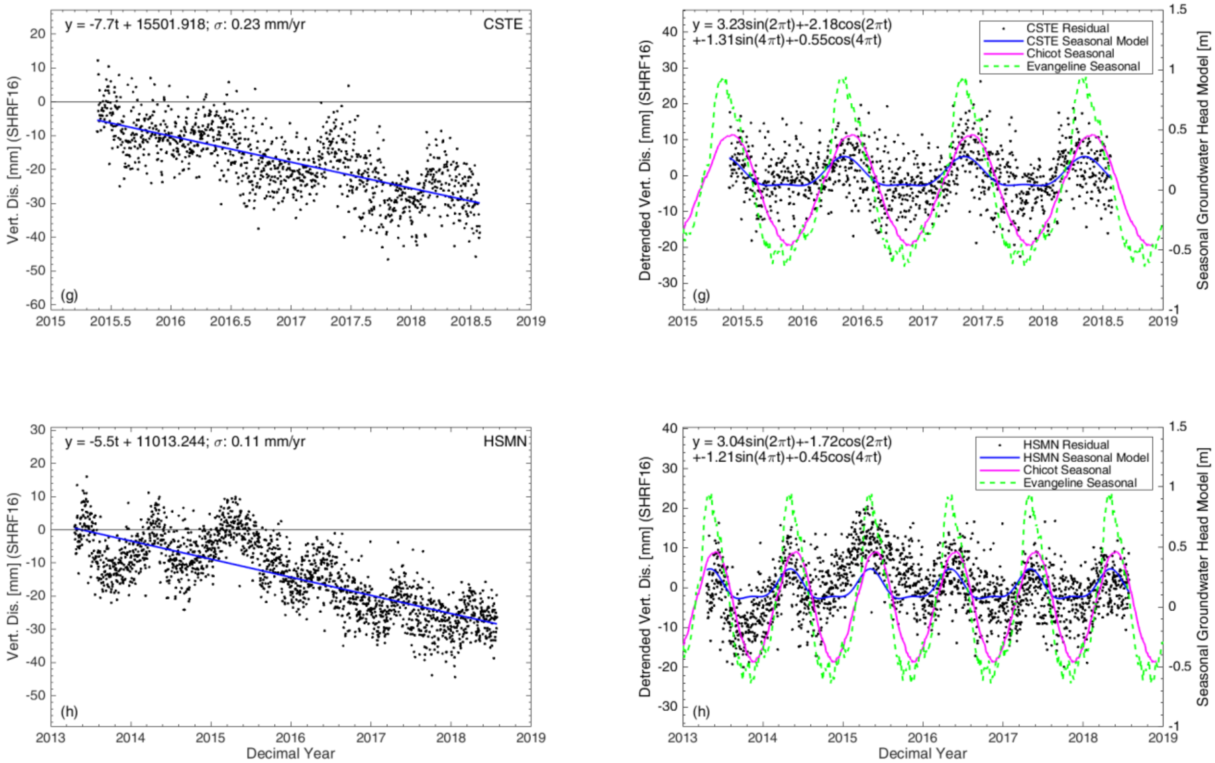

Figure 7-3 (g-h): Plots displaying GPS vertical displacement time-series (left column) and comparison of GPS and groundwater seasonal signals (right column) for stations CSTE and HSMN. Locations of GPS stations are shown in **Figure 7-1**.

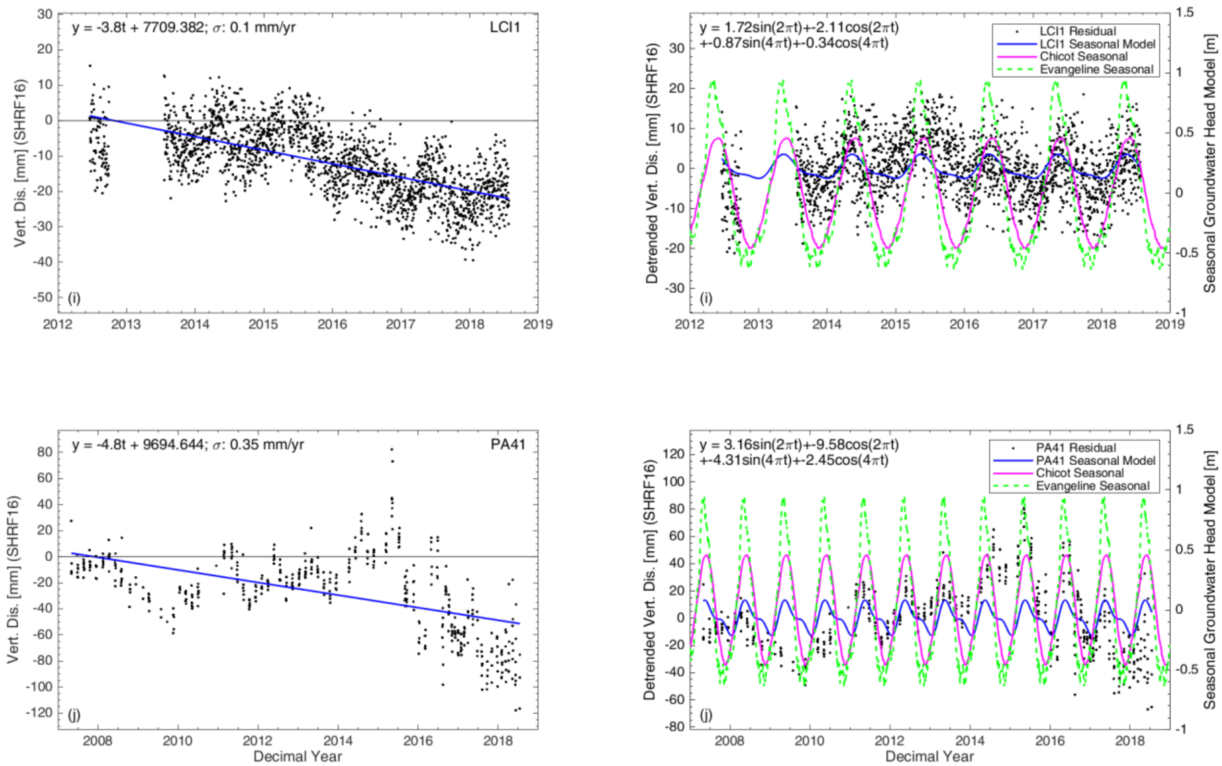

Figure 7-3 (i-j): Plots displaying GPS vertical displacement time-series (left column) and comparison of GPS and groundwater seasonal signals (right column) for stations LCI1 and PA41. Locations of GPS stations are shown in **Figure 7-1**.

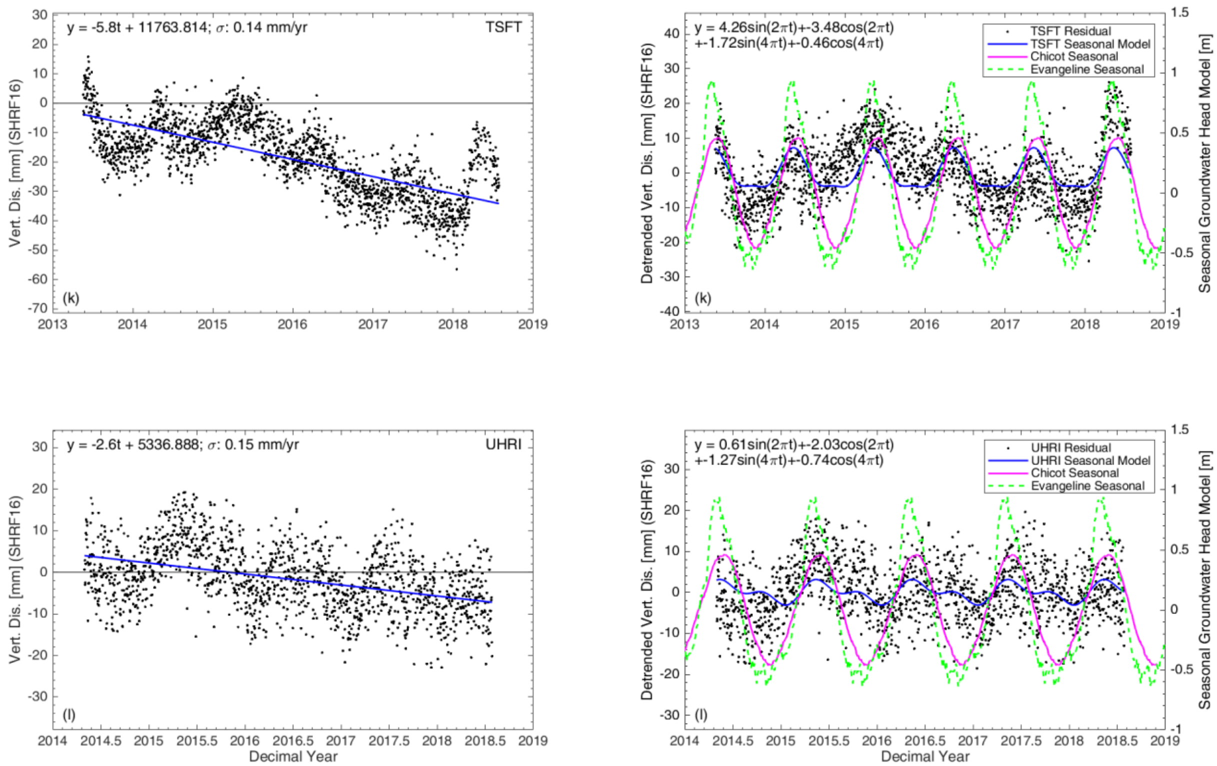

Figure 7-3 (k-l): Plots displaying GPS vertical displacement time-series (left column) and comparison of GPS and groundwater seasonal signals (right column) for stations TSFT and UHRI. Locations of GPS stations are shown in **Figure 7-1**.

8 PRECONSOLIDATION HEAD ESTIMATES IN THE HOUSTON SHIP CHANNEL AND DOWNTOWN HOUSTON

8.1 PREVIOUS ESTIMATES: HOLZER (1981)

Preconsolidation head levels have been thoroughly addressed in the literature, especially in studies regarding groundwater flow simulations (Larson et al., 2001; Li and Zhang 2018). A thorough investigation of preconsolidation heads in several regions throughout the United States, including Greater Houston, was conducted by Holzer (1981). Holzer (1981) evaluated the ratio of land subsidence per unit level decline in hydraulic head during the beginning of anthropogenic groundwater production within Greater Houston. Each examined site in the region displayed a bilinear relationship in this ratio, which was interpreted to result from the change of elastic to inelastic compaction once hydraulic heads fell below preconsolidation head levels. Aquifer conditions prior till anthropogenic production were widely considered to be naturally over-consolidated, and, as such, the initial ratio of land subsidence per unit level decline in hydraulic head was interpreted to coincide with elastic compaction. A sharp increase in the ratio was interpreted to indicate the beginning of inelastic compaction resulting from hydraulic heads falling below the preconsolidation head level.

In total, five leveling benchmark sites accompanied by nearby groundwater observation well data were analyzed by Holzer (1981) to determine preconsolidation head levels. The five sites analyzed are located within the currently observed region of land rebound. A majority of ground water levels investigated were from the Chicot aquifer as it was suggested that compaction in the area was primarily occurring within its extent (Jorgensen, 1974). Estimates obtained by Holzer (1981) represent predevelopment preconsolidation heads and range from -31 to -63 m. These estimates are plotted at their approximate localities in **Figure 8-1** and **Figure 8-2** and will be compared with preconsolidation head estimates derived in this work.

8.2 ESTIMATING PRECONSOLIDATION HEADS

Historically, preconsolidation heads are estimated from a combination of groundwater and sediment compaction data or empirically through groundwater flow simulations. This study aims to utilize available groundwater data in additions to vertical displacement and sediment compaction data from GPS and borehole extensometers sites to estimate preconsolidation heads within the region of observed land rebound. Hydraulic head levels at the onset of land rebound will be utilized as a first-order approximation for preconsolidation head levels. From **Chapter 5**, it was determined from several GPS site localities that land rebound began in the early-2000s (2000-2004). Moreover, several borehole extensometers sites (Baytown **Figure 5-5a**; Pasadena **Figure 5-5b**; Northeast **Figure 5-5c**; Clear Lake **Figure 5-5e**; Seabrook **Figure 5-5h**) experienced appreciable reversal of sediment compaction beginning in 2001 to 2004. Therefore, the year 2002 will serve as the approximate timing for the onset of land rebound within the Downtown Houston and Houston Ship Channel area.

A first-order approximation of preconsolidation heads is made by deriving the potentiometric surfaces of the Chicot and Evangeline aquifers as of 2002 (**Figure 8-1** and **Figure 8-2**). Within the region of observed land rebound, hydraulic heads in the Chicot aquifer predominantly fall between -25 to -65 m. Evangeline heads are slightly deeper and fall predominantly fall between -30 to -70 m in the area of observed land rebound. Geographically, preconsolidation head estimates are shallowest in the southeast and become progressively moving inland to the northwest. Included in **Figure 8-1** and **Figure 8-2** are the estimates of preconsolidation heads derived by Holzer (1981). Estimated preconsolidation heads for the Chicot aquifer differ from estimates made by Holzer (1981) by ~2-15 m and ~4-20 m for the Evangeline aquifer. The 2002 potentiometric surfaces and Holzer (1981) predevelopment preconsolidation head estimates coincide remarkably close when considering that the region has historically undergone substantial aquifer level decline and sediment compaction. Moreover, the gradient in preconsolidation head estimates made in this study coincide with those determined by Holzer (1981). These observed similarities lend confidence in the validity of using the 2002 potentiometric surface heads of the Chicot and Evangeline aquifers as a first-order approximation for preconsolidation head levels.

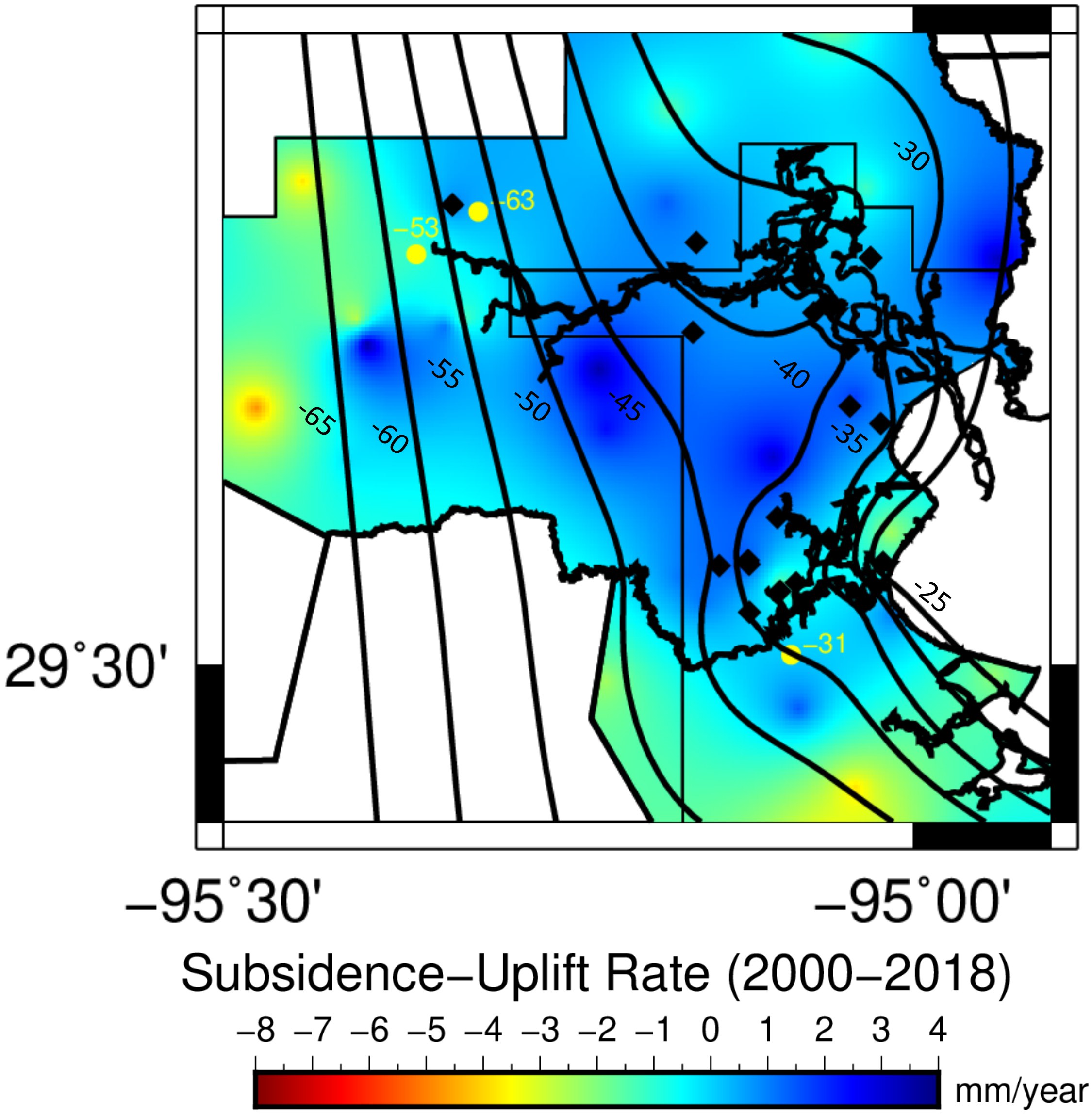

Figure 8-1: Contour map of Chicot aquifer preconsolidation head estimates (*black* contours) in the region of observed land rebound. Preconsolidation head estimates coincide with the potentiometric surface of Chicot aquifer in 2002 when the onset of land rebound occurred. *Yellow* circles indicate preconsolidation head estimates made by Holzer (1981) within the Chicot aquifer. Contours and preconsolidation head estimates are in units of *meters*. *Black* diamonds indicate groundwater observational wells completed in the Chicot aquifer utilized to derive the potentiometric surface.

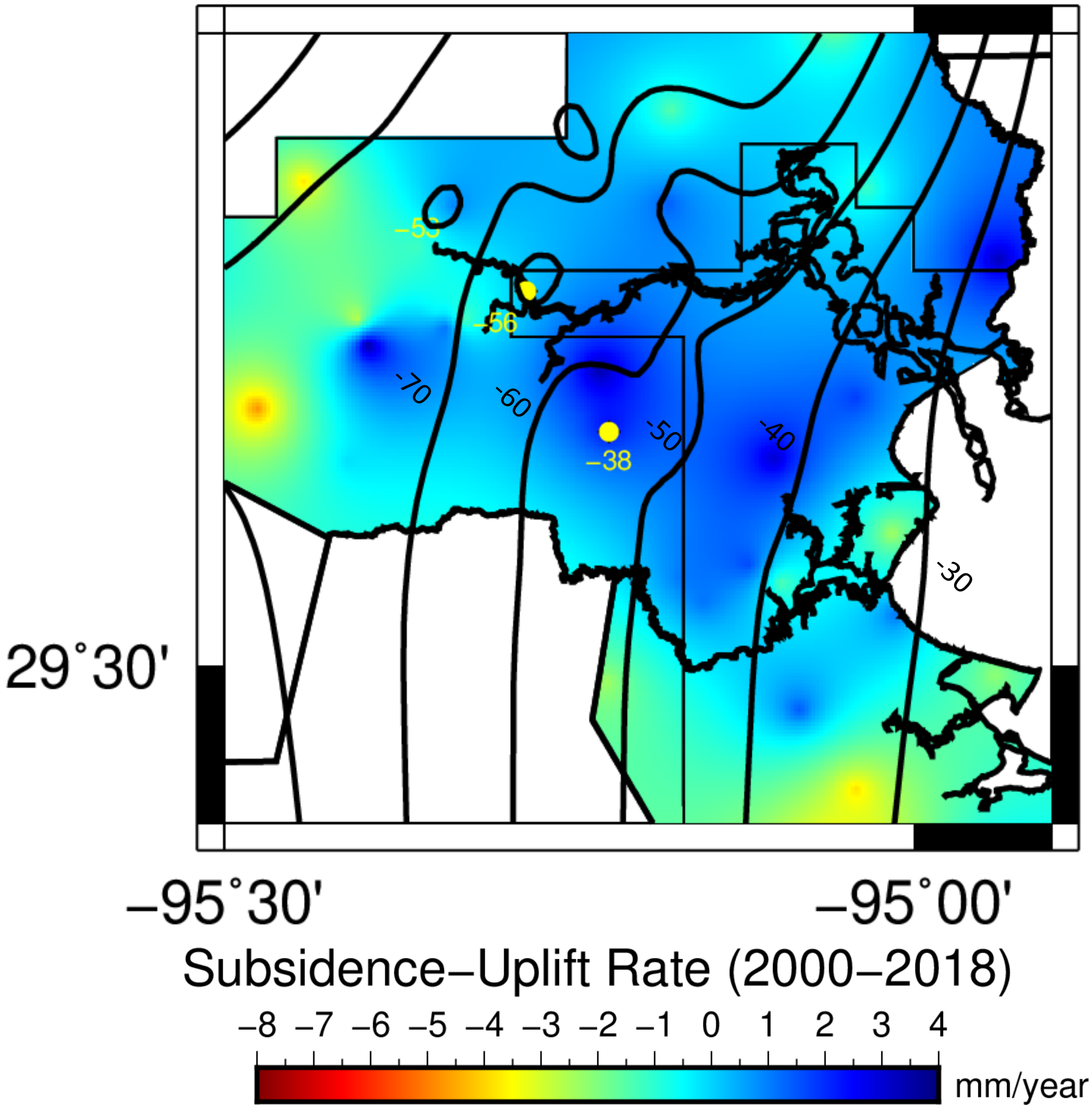

Figure 8-2: Contour map of Evangeline aquifer preconsolidation head estimates (*black* contours) in the region of observed land rebound. Preconsolidation head estimates coincide with the potentiometric surface of Evangeline aquifer in 2002 when the onset of land rebound occurred. *Yellow* circles indicate preconsolidation head estimates made by Holzer (1981) within the Evangeline aquifer. Contours and preconsolidation head estimates are in units of *meters*. *Black* diamonds indicate groundwater observational wells completed in the Chicot aquifer utilized to derive the potentiometric surface.

9 DISCUSSION

Several considerations must be addressed before a definitive conclusion can made on the estimated preconsolidation head levels. While groundwater levels in both the Chicot and Evangeline aquifers were analyzed in the assessment of preconsolidation heads, it is not necessarily definitive that significant compaction had historically occurred in both aquifers during times of land subsidence. Previous work undertaken by Jorgensen (1975) asserted that the majority of sediment compaction in Greater Houston occurs within the confines of the Chicot aquifer. In addition, Jorgensen (1975) also suggested that compaction further north occurs predominantly in the Evangeline aquifer as the thickness in clay within the Chicot aquifer decreases. Observations of sediment compaction at the Clear Lake and Baytown borehole extensometers indicate that compaction is mostly occurring within the extent of the shallower extensometers, which coincides with entire Chicot aquifer and uppermost Evangeline. Furthermore, the performed seasonal analysis indicates that to the southeast, elastic seasonal deformation is dominated by oscillations in the Chicot aquifer, which would then suggest that the majority of sediment compaction is occurring within its extent.

Other considerations include that groundwater observational wells may not necessarily reflect the state of pressure in the entire aquifer system as sediment compaction varies with depth (Gabrysch and Bonnet, 1975). Furthermore, the distribution of compaction with depth is partly dependent upon the vertical distribution of aquitard material and the respective drop in pressure at a compacting layer (Holzer, 1981; Jorgensen, 1975). In other words, when a vertical hydraulic gradient exists, measurements made by a well screened at a given depth may not necessarily reflect the state of hydraulic pressure in the vicinity of a compacting layer. This implies that the values identified as the corresponding preconsolidation heads may not actually truly reflect the true preconsolidation stress of the compacting aquitard material.

Based on the available data, observations, and above considerations, preconsolidation heads in the region of observed land rebound most closely coincides with hydraulic heads of the Chicot and Evangeline aquifers in 2002. Utilizing the 2002 potentiometric surface of the Chicot and Evangeline aquifer as a first-order approximation means that preconsolidation heads range from -25 to -65 m (Chicot) and -30 to -70 m (Evangeline). As previously aforementioned, these estimated value lie in close proximity or are slightly below the values of the predevelopment preconsolidation head estimated by Holzer (1981). Current preconsolidation stress may not necessarily coincide with predevelopment preconsolidation stress, especially in systems which have experienced periods of lowered hydraulic heads and sediment compaction (Galloway et al., 1999). This behavior further supported from experimental consolidation tests (**Figure 9-1**) and has been documented in Salt Lake City, Utah and Antelope Valley, California (Bartlett and Alcorn, 2004; Galloway et al., 1999; Holzer, 1985; Sneed and Galloway, 2000).

Cross-validation of GPS results can be done utilizing Interferometric Synthetic Aperture Radar (InSAR). InSAR provides higher-spatial resolution subsidence measurements than those provided through benchmark releveling, borehole extensometers, and GPS (Buckley et al., 2011). Land subsidence and uplift trends obtained in this study through GPS are concordant with InSAR deformation results obtained from Qu et al. (2015).

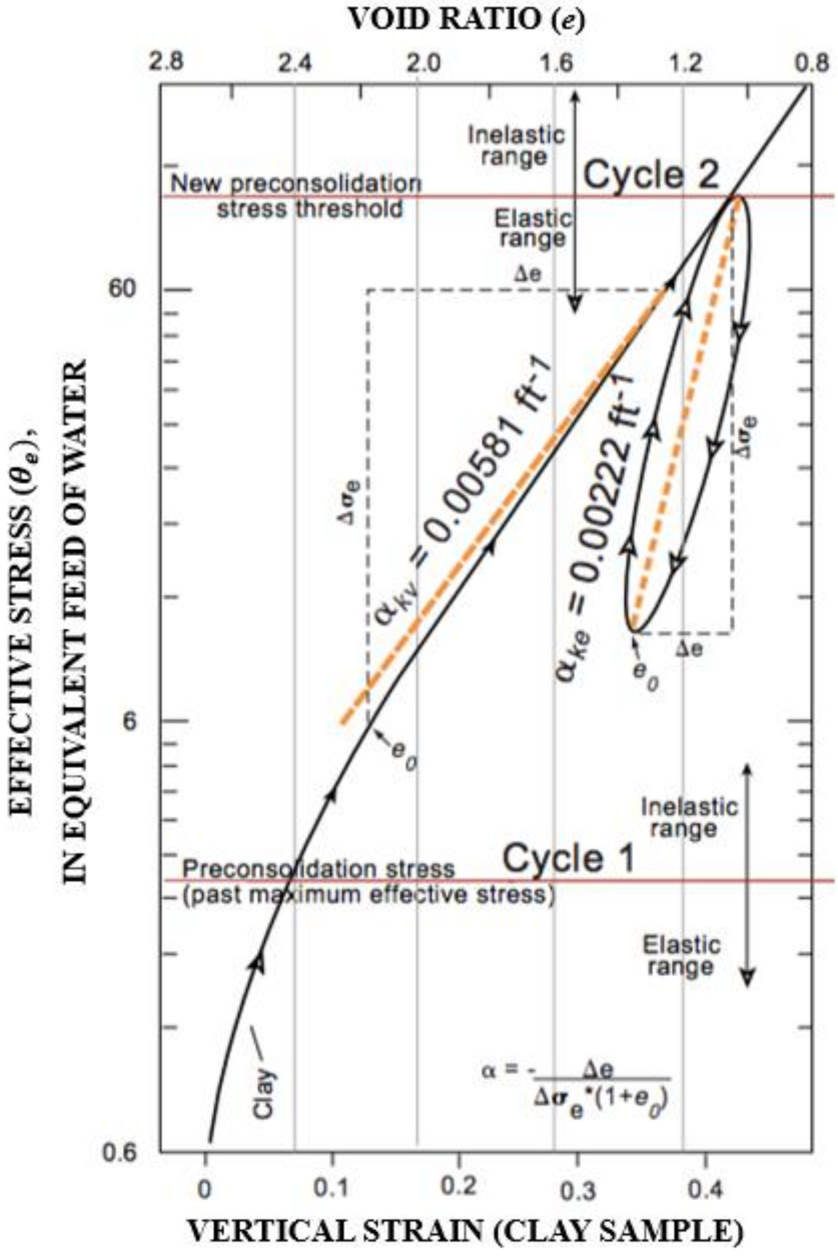

Figure 9-1: Laboratory consolidation test displaying the change in preconsolidation stress after inelastic compaction has occurred. From Sneed and Galloway (2000).

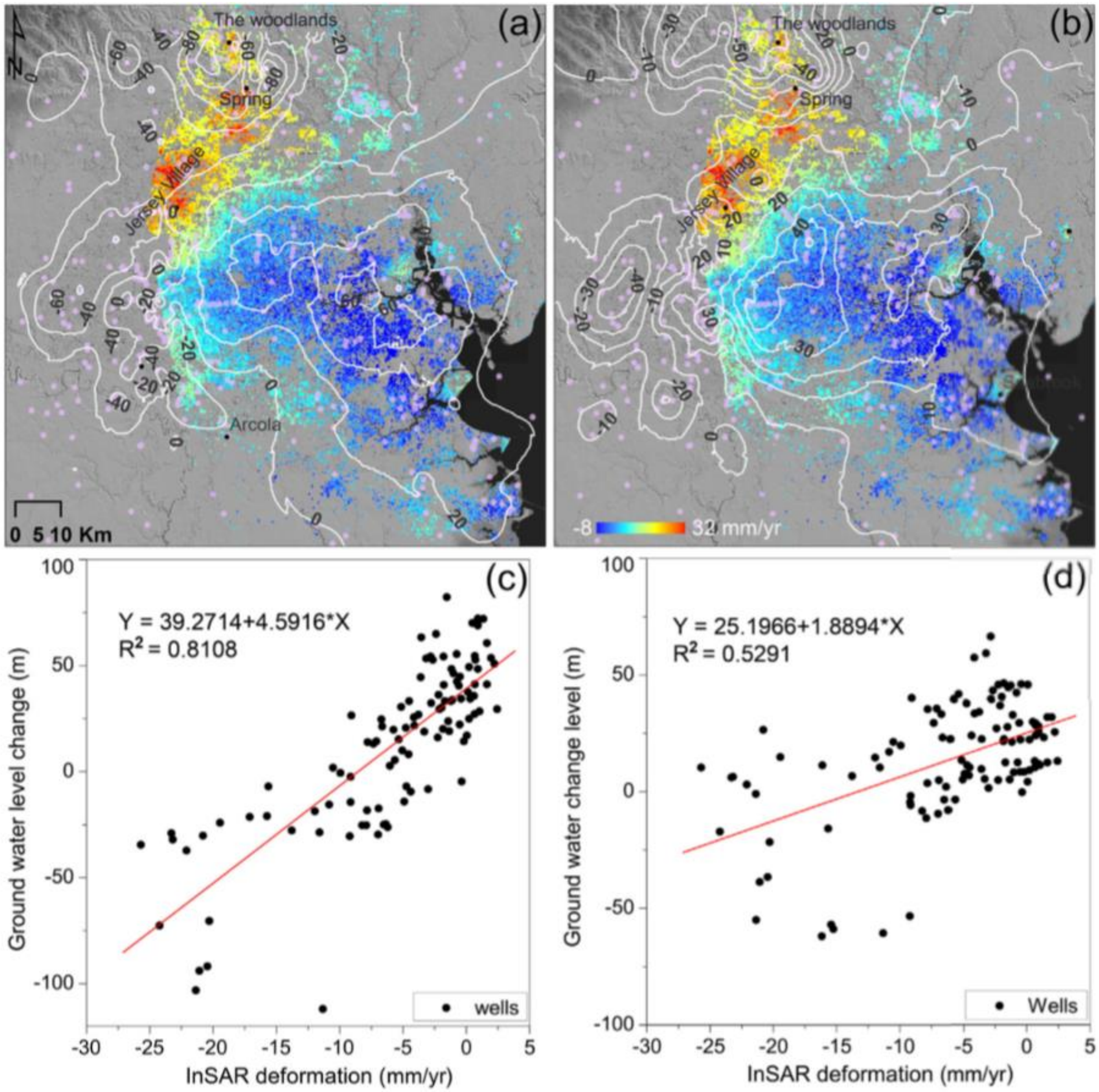

Figure 9-2: Annual InSAR-derived deformation rate during 1993-2011 plotted with groundwater level changes in both the Chicot and Evangeline aquifers (*white* contours in units of *meters*) for the periods (a) 1972-2011 and (b) 1990-2012. *Purple* dots display the locations of groundwater wells utilized to derive the contours. *Warm* colors indicate land subsidence while *cool* colors represent land rebound. (c) Correlation between groundwater level changes from 1977 to 2012 and the InSAR annual deformation rate during 1993–2011. (d) Correlation between groundwater level changes from 1990 to 2012 and the InSAR annual deformation rate from 1993-2011. From Qu et al. (2015).

10 CONCLUSIONS

The arrestment of land subsidence and subsequent land rebound in Downtown Houston and the Houston Ship Channel is the result of replenished groundwater levels past preconsolidation head levels, which ultimately decreases the total vertical effective stress experienced by the aquifer skeletal material. Estimation of preconsolidation head levels are of potential value for government agencies and policymakers in implementing groundwater regulations to avoid irreversible land subsidence. This study closes with the following set of conclusions:

(a) As evident by borehole extensometer observations and seasonal modeling, historical compaction within the region of land rebound primarily occurred within of the Chicot aquifer. Moreover, the compaction in the northwestern part of Houston is predominantly confined within the Evangeline aquifer.

(b) Uplift rates in Downtown Houston and the Houston Ship Channel range from ~0.6-4 mm/year. Localized land subsidence still occurs within HGSD Area I and II at varying rates (~2-8 mm/year)

(c) Preconsolidation heads within the area of observed land rebound lie 25-65 m (Chicot) and 30-70 m (Evangeline) below the land surface

(d) The estimated current preconsolidation heads are relatively similar or slightly lower than previous estimates of predevelopment proncsolidation heads. This would suggest that even though substantial historic sediment compaction occurred, preconsolidation head levels did not change significantly.

(e) Land subsidence is not expected to occur in Downtown Houston and the Houston Ship Channel unless hydraulic heads fall below the estimated preconsolidation head levels. By the same token, if hydraulic heads drop but stay above the estimated preconsolidation head, sediment compaction is expected to be elastic and relatively small in magnitude.

(f) Regionally, groundwater levels in the Chicot and Evangeline aquifers have risen substantially since 2000 indicating that imposed groundwater regulations are quite effective. However, localized decreases in groundwater level are still observed in rapid urban development areas such as The Woodlands and Katy.

REFERENCES

American Association of Petroleum Geologists. (2011). Salt tectonism of the U.S. gulf coast basin (CD-ROM), *GIS-UDRIL* (*Geographic Information System-Upstream Digital Reference Information Library*).

Argus, D. F., Fu, Y., & Landerer, F. W. (2014). Seasonal variation in total water storage in California inferred from GPS observations of vertical land motion. *Geophysical Research Letters*, *41*(6), 1971-1980.

Ashworth, J. B., & Hopkins, J. (1995). Aquifers of Texas: Texas Water Development Board Report 345. *Austin, TX: Texas Water Development Board.*

Baker Jr, E. T. (1979). Stratigraphic and hydrogeologic framework of part of the coastal plain of Texas. *Texas Department of Water Resources*.

Bartlett, S. F., & Alcorn, P. (2004). Estimation of preconsolidation stress and compression ratio from field and laboratory measurements from the I-15 Reconstruction Project, Salt Lake City, Utah. *Utah Department of Transportation*. (No. UT-03.20).

Bawden, G. W., Johnson, M. R., Kasmarek, M. C., Brandt, J., & Middleton, C. S. (2012). Investigation of land subsidence in the Houston-Galveston region of Texas by using the global positioning system and interferometric synthetic aperture radar, 1993-2000 (No. 2012-5211). *US Geological Survey*.

Bird, D. E., Burke, K., Hall, S. A., & Casey, J. F. (2005). Gulf of Mexico tectonic history: Hotspot tracks, crustal boundaries, and early salt distribution. *American Association of Petroleum Geologists (AAPG) Bulletin*, *89*(3), 311-328.

Bull, W. B. (1975). Land Subsidence Due to Ground-water Withdrawal in the Los Banos Kettleman City Area, California: Part 2. Subsidence and Compaction of Deposits. *US Government Printing Office*.

Buckley, S. M., Rosen, P. A., Hensley, S., & Tapley, B. D. (2003). Land subsidence in Houston, Texas, measured by radar interferometry and constrained by extensometers. *Journal of Geophysical Research: Solid Earth*, *108*(B11).

Chen, C. T., Hu, J. C., Lu, C. Y., Lee, J. C., & Chan, Y. C. (2007). Thirty-year land elevation change from subsidence to uplift following the termination of groundwater pumping and its geological implications in the Metropolitan Taipei Basin, Northern Taiwan. *Engineering Geology*, *95*(1-2), 30-47.

Chowdhury, A. H., & Mace, R. E. (2003). A groundwater availability model of the Gulf Coast aquifer in the Lower Rio Grande Valley, Texas: Numerical simulations through 2050. *Texas Water Development Board Report, October 2003, 171 p*.

Chowdhury, A. H., & Turco, M. J. (2006). Geology of the Gulf Coast Aquifer, Texas. *Texas Water Development Board Report*, *365*.

Cleveland, R. B., Cleveland, W. S., McRae, J. E., & Terpenning, I. (1990). STL: A seasonal trend decomposition. *Journal of Official Statistics, 6*(1), 3-73.

Coplin, L. S., & Galloway, D. (1999). Houston-Galveston, Texas. *Land subsidence in the United States: US Geological Survey Circular*, *1182*, 35-48.

Dixon, T. H., Amelung, F., Ferretti, A., Novali, F., Rocca, F., Dokka, R., Sella, G., Kim, S., Wdowinski, S., & Whitman, D. (2006). Space geodesy: Subsidence and flooding in New Orleans. *Nature, 441*(7093), 587.

Frazier, D. E. (1969). Depositional episodes: their relationship to Quaternary sea-level fluctuations in the Gulf Coast region. *Journal of Sedimentary Research*, *86*(9), 1008-1033.

Gabrysch, R. K., & Bonnet, C. W. (1975). Land-surface subsidence in the Houston Galveston region, Texas. *The Bulletin of the Houston Geological Society*, 15(4), 1.

Galloway, D. L., Jones, D. R., & Ingebritsen, S. E. (1999). Land subsidence in the United States. *US Geological Survey*, 1182, 1-177.

Galloway, W. E. (2008). Depositional evolution of the Gulf of Mexico sedimentary basin. *Sedimentary Basins of the World*, *5*, 505-549.

Galloway, D. L., & Burbey, T. J. (2011). Regional land subsidence accompanying groundwater extraction. *Hydrogeology Journal*, *19*(8), 1459-1486.

Guier, W. H., & Weiffenbach, G. C. (1997). Genesis of satellite navigation. *Johns Hopkins APL Technical Digest*, *18*(2), 178-181.

HGSD (Harris-Galveston Subsidence District). (2013). The subsidence district 2013 annual groundwater report. Retrieved from: http://hgsubsidence.org/wp-content/uploads/2013/07/HG-GW-Report-2013-Final.pdf.

Hoffmann, J., Zebker, H. A., Galloway, D. L., & Amelung, F. (2001). Seasonal subsidence and rebound in Las Vegas Valley, Nevada, observed by synthetic aperture radar interferometry. *Water Resources Research*, *37*(6), 1551-1566.

Holzer, T. L. (1981). Preconsolidation stress of aquifer systems in areas of induced land subsidence. *Water Resources Research*, *17*(3), 693-703.

Holzer, T. L. (1984). Ground failure induced by ground-water withdrawal from unconsolidated sediment. *Reviews in Engineering Geology*, *6*, 67-105.

Holzer, T. L. (1995). History of the aquitard-drainage model in land subsidence case studies and current research. In *Land subsidence case studies and current research. Proceedings of the Dr. Joseph F. Poland Symposium on Land Subsidence* (pp. 7-12).

Holzer, T. L., & Galloway, D. L. (2005). Impacts of land subsidence caused by withdrawal of underground fluids in the United States. *Humans as Geologic Agents*, *16*, 87-99.

Hosman, R. L. (1991). Regional stratigraphy and subsurface geology of Cenozoic deposits, Gulf Coastal Plain, south-central United States (No. 91-66). *US Geological Survey*.

Jackson, M. P. A., & Seni, S. J. (1983). Geometry and evolution of salt structures in a marginal rift basin of the Gulf of Mexico, east Texas. *Geology*, *11*(3), 131-135.

Jackson, M. P., & Talbot, C. J. (1986). External shapes, strain rates, and dynamics of salt structures. *Geological Society of America Bulletin*, *97*(3), 305-323.

Jorgensen, D. G. (1974). Analog-model studies of ground-water hydrology in the Houston District, Texas (No. 74-113). *US Geological Survey*.

Kasmarek, M. C., Gabrysch, R. K., & Johnson, M. R. (2009). Estimated Land-Surface Subsidence in Harris County, Texas, 1915-17 to 2001. *US Department of the Interior, US Geological Survey*.

Kasmarek, M. C., Johnson, M. R., & Ramage, J. K. (2012). Water-level Altitudes 2012, and Water-level Changes in the Chicot, Evangeline, and Jasper Aquifers and Compaction 1973-2011 in the Chicot and Evangeline Aquifers, Houston Galveston Region, Texas. *US Department of the Interior, US Geological Survey*.

Kasmarek, M. C., & Robinson, J. L. (2004). Hydrogeology and simulation of ground water flow and land-surface subsidence in the northern part of the Gulf Coast aquifer system, Texas (No. 2004). *US Geological Survey*.

Kasmarek, M. C., & Strom, E. W. (2002). Hydrogeology and simulation of groundwater flow and land-surface subsidence in the Chicot and Evangeline aquifers, Houston Area, Texas. Austin, Texas: US Geological Survey. *Water Resources Investigations Report*, 02-4022.

Kearns, T. J., Wang, G., Bao, Y., Jiang, J., & Lee, D. (2015). Current land subsidence and groundwater level changes in the Houston Metropolitan Area (2005 2012). *Journal of Surveying Engineering*, *141*(4), 1-16.

Kearns, T. J., Wang, G., Turco, M., Welch, J., Tsibanos, V., & Liu, H. (2018). Houston16: A stable geodetic reference frame for subsidence and faulting study in the Houston metropolitan area, Texas, US. *Geodesy and Geodynamics*, https://doi.org/10.1016/j.geog.2018.05.005.

Khan, S. D., Huang, Z., & Karacay, A. (2014). Study of ground subsidence in northwest Harris county using GPS, LiDAR, and InSAR techniques. *Natural Hazards*, *73*(3), 1143-1173.

Konikow, L. F., & Kendy, E. (2005). Groundwater depletion: A global problem. *Hydrogeology Journal*, *13*(1), 317-320.

Krijnen, H., & de Heus, H. (1995, October). Application of GPS with sub-centimeter accuracy for subsidence monitoring. In *Proceedings of the 5th International Symposium on Land Subsidence, The Haque, Netherlands* (pp. 16-20).

Larson, K. J., Başağaoğlu, H., & Marino, M. A. (2001). Prediction of optimal safe ground water yield and land subsidence in the Los Banos-Kettleman City area, California, using a calibrated numerical simulation model. *Journal of Hydrology*, *242*(1-2), 79-102.

Leake, S. A. (1990). Interbed storage changes and compaction in models of regional groundwater flow. *Water Resources Research*, *26*(9), 1939-1950.

Levenberg, K. (1944). A method for the solution of certain non-linear problems in least squares. *Quarterly of Applied Mathematics*, *2*(2), 164-168.

Li, L., & Zhang, M. (2018). Inverse modeling of interbed parameters and transmissivity using land subsidence and drawdown data. *Stochastic Environmental Research and Risk Assessment*, *32*(4), 921-930.

Little, R. J., & Rubin, D. B. (2019). Statistical analysis with missing data (Vol. 793). *Wiley*.

Lofgren, B. E., & Klausing, R. L. (1969). Land subsidence due to ground-water withdrawal, Tulare-Wasco area, California (Vol. 437). *US Government Printing Office*.

Marquardt, D. W. (1963). An algorithm for least-squares estimation of nonlinear parameters. *Journal of the Society for Industrial and Applied Mathematics*, *11*(2), 431-441.

Mousavi, S. M., Naggr, M. H., & Shamsai, S. (2000). Application of GPS to evaluate land subsidence in Iran. In *Proc., of the Sixth Int. Symp. on Land Subsidence, 2*, 107-112.

Osmanoğlu, B., Dixon, T. H., Wdowinski, S., Cabral-Cano, E., & Jiang, Y. (2011). Mexico City subsidence observed with persistent scatterer InSAR. *International Journal of Applied Earth Observation and Geoinformation*, *13*(1), 1-12.

Pittman, D. W. (1994). *Growth history and structural analysis of Sugarland dome, Fort Bend county, Texas* (Doctoral dissertation, University of Houston).

Píriz, R., Calle, D., Mozo, A., Navarro, P., Rodríguez, D., & Tobías, G. (2009). Orbits and clocks for GLONASS precise-point-positioning. In *Proc. ION GNSS* (pp. 2415-2424).

Qu, F., Lu, Z., Zhang, Q., Bawden, G. W., Kim, J. W., Zhao, C., & Qu, W. (2015). Mapping ground deformation over Houston–Galveston, Texas using multi-temporal InSAR. *Remote Sensing of Environment*, *169*, 290-306.

Rebischung, P., Griffiths, J., Ray, J., Schmid, R., Collilieux, X., & Garayt, B. (2012). IGS08: the IGS realization of ITRF2008. *GPS Solutions*, *16*(4), 483-494.

Rice, J. R., & Cleary, M. P. (1976). Some basic stress diffusion solutions for fluid saturated elastic porous media with compressible constituents. *Reviews of Geophysics*, *14*(2), 227-241.

Riley, F. S. (1998). Mechanics of aquifer systems —The scientific legacy of Joseph F. Poland. In *Land subsidence case studies and current research: Proceedings of the Dr. Joseph F. Poland Symposium on Land Subsidence: Belmont, Calif., Star Publishing Co., Association of Engineering Geologists Special Publication, 8*, 13 27.

Ryder, P. D. (1996). Ground water atlas of the United States: Oklahoma, Texas. *Hydrologic Investigations Atlas*.

Salvador, A. (1991). Origin and development of the Gulf of Mexico basin. *The Gulf of Mexico Basin*, 389-44.

Schiffman, R. L. (1958). Consolidation of soil under time-dependant loading and varying permeability. In *Highway Research Board Proceedings*, *37*, 584-617.

Schmidt, D. A., & Bürgmann, R. (2003). Time-dependent land uplift and subsidence in the Santa Clara valley, California, from a large interferometric synthetic aperture radar data set. *Journal of Geophysical Research: Solid Earth*, *108*(B9), 2416-2429.

Schumann, H. H., & Poland, J. F. (1969). Land subsidence, earth fissures, and groundwater withdrawal in south-central Arizona, USA. In *International Symposium on Subsidence, Tokyo* (Vol. 295302), 295-302.

Shah, S. D., & Lanning-Rush, J. (2005). Principal faults in the Houston, Texas, metropolitan area. *US Department of the Interior, US Geological Survey*.

Smith, S. (1982). Ground water hydrology for water well contractors. *National Water Well Association*.

Sneed, M., & Galloway, D. L. (2000). Aquifer-system compaction and land subsidence: measurements, analyses, and simulations-the Holly Site, Edwards Air Force Base, Antelope Valley, California (No. 2000-4015). *US Geological Survey*.

Terzaghi, K. A. R. L. (1925). Principles of soil mechanics. *Engineering News-Record*, *95* (19-27), 19-32.

Tolman, C. F., & Poland, J. F. (1940). Ground-water, salt-water infiltration, and ground surface recession in Santa Clara Valley, Santa Clara County, California. *Eos, Transactions American Geophysical Union*, *21*(1), 23-35.

USGS (United States Geological Survey (2002). Houston-Galveston Bay area, Texas, from Space—a new tool for mapping land subsidence. *US Geological Survey Fact Sheet 110*, *2*.

Wang, G., Bao, Y., Gan, W., Geng, J., Xiao, G., & Shen, J. S. (2018). NChina16: A stable geodetic reference frame for geological hazard studies in North China. *Journal of Geodynamics*, *115*, 10-22.

Wang, G., Turco, M., Soler, T., Kearns, T. J., & Welch, J. (2017). Comparisons of OPUS and PPP solutions for subsidence monitoring in the greater Houston area. *Journal of Surveying Engineering*, *143*(4), 1-14.

Wang, G., Welch, J., Kearns, T. J., Yang, L., & Serna Jr, J. (2015). Introduction to GPS geodetic infrastructure for land subsidence monitoring in Houston, Texas, USA. *Proceedings of the International Association of Hydrological Sciences*, *372*, 297-303.

Wang, G., Yu, J., Kearns, T. J., & Ortega, J. (2014). Assessing the accuracy of long-term subsidence derived from borehole extensometer data using GPS observations: Case study in Houston, Texas. *Journal of Surveying Engineering*, *140*(3), 1-7.

Wessel, P., Smith, W. H., Scharroo, R., Luis, J., & Wobbe, F. (2013). Generic mapping tools: improved version released. *Eos, Transactions American Geophysical Union*, *94*(45), 409-410.

Wilson, A. M., & Gorelick, S. (1996). The effects of pulsed pumping on land subsidence in the Santa Clara Valley, California. *Journal of Hydrology, 174*(3-4), 375-396.

Yu, J., Wang, G., Kearns, T. J., & Yang, L. (2014). Is there deep-seated subsidence in the Houston-Galveston area?. *International Journal of Geophysics*, *2014*, 1-11.

Zilkoski, D. B., Hall, L. W., Mitchell, G. J., Kammula, V., Singh, A., Chrismer, W. M., & Neighbors, R. J. (2003). The Harris-Galveston coastal subsidence district/national geodetic survey automated global positioning system subsidence monitoring project. In *Proceedings of the US Geological Survey Subsidence Interest Group Conference* (pp. 13-28). US Geological Survey.

Zumberge, J. F., Heflin, M. B., Jefferson, D. C., Watkins, M. M., & Webb, F. H. (1997). Precise point positioning for the efficient and robust analysis of GPS data from large networks. *Journal of Geophysical Research: Solid Earth, 102*(B3), 5005 5017.

APPENDIX I: VERTICAL DISPLACEMENT GPS TIME-SERIES

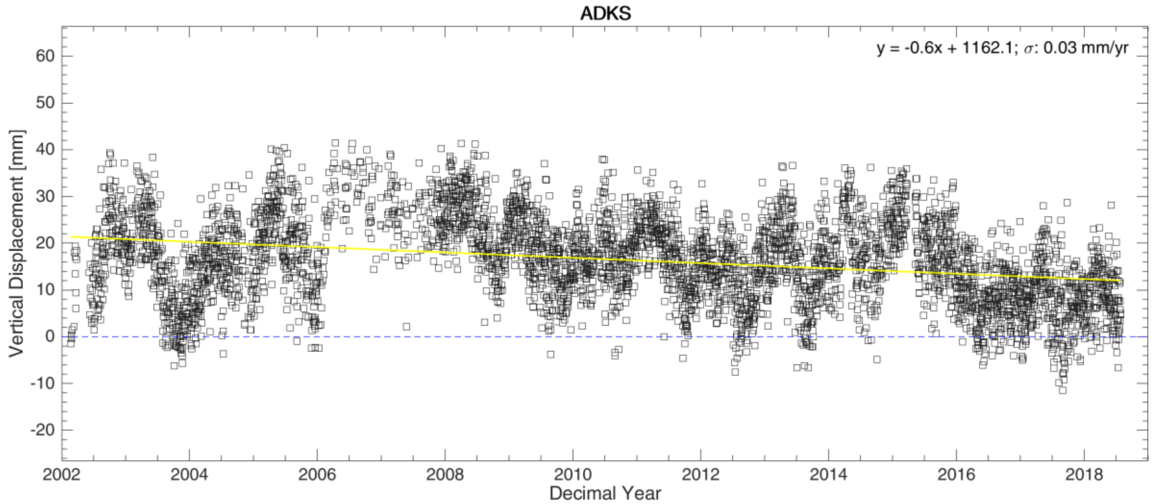

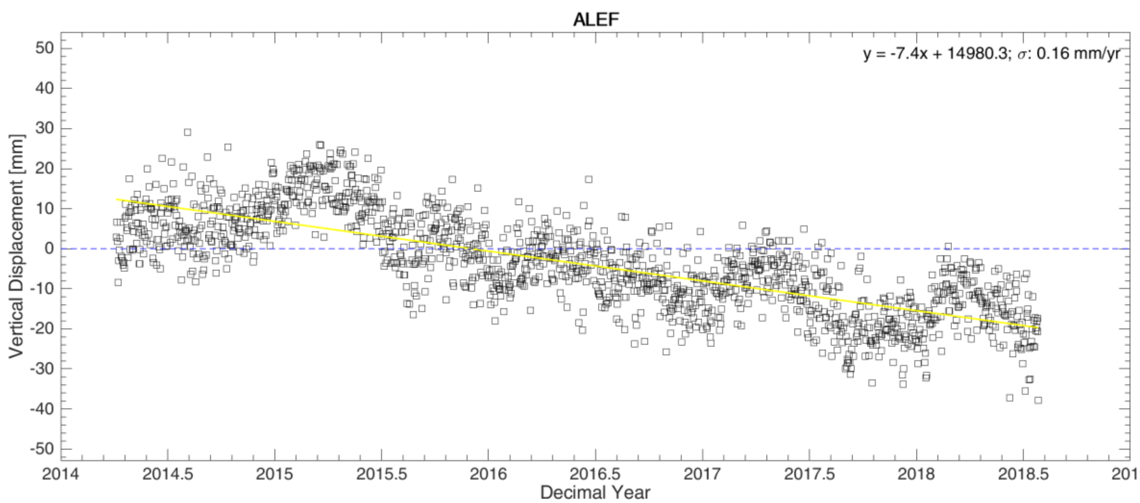

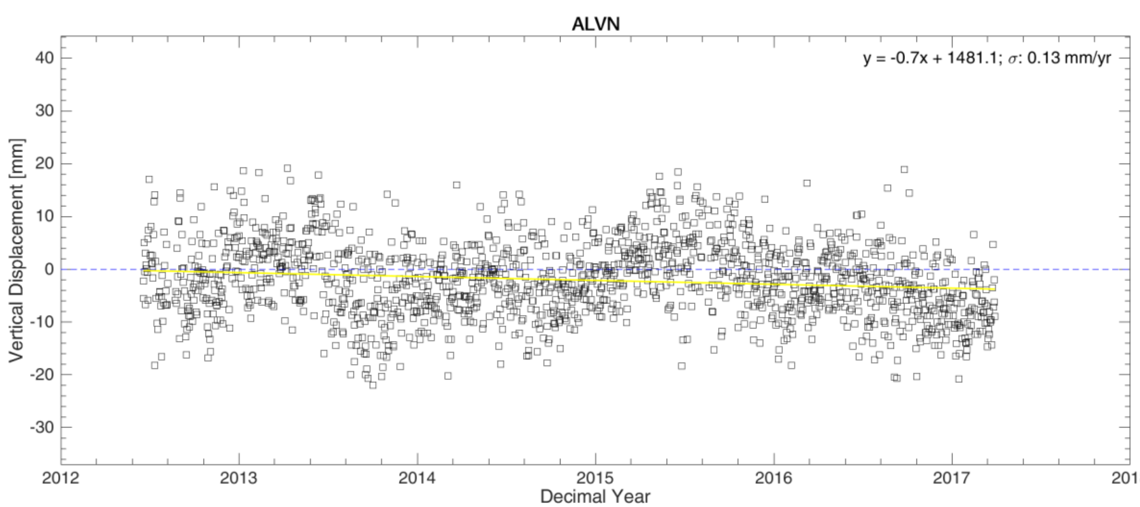

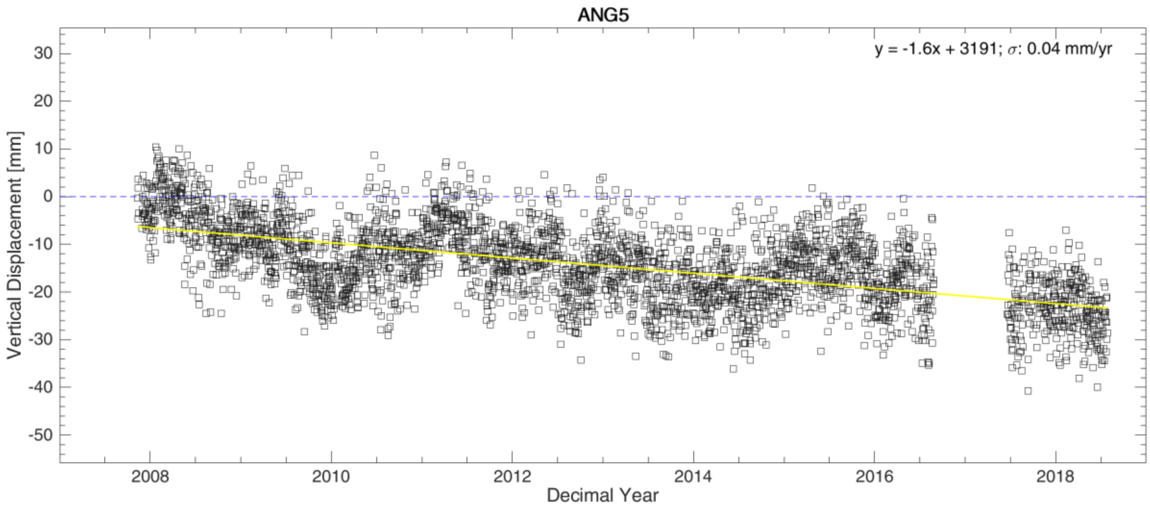
ANG5
y = -1.6x + 3191; σ: 0.04 mm/yr
Vertical Displacement [mm]
Decimal Year

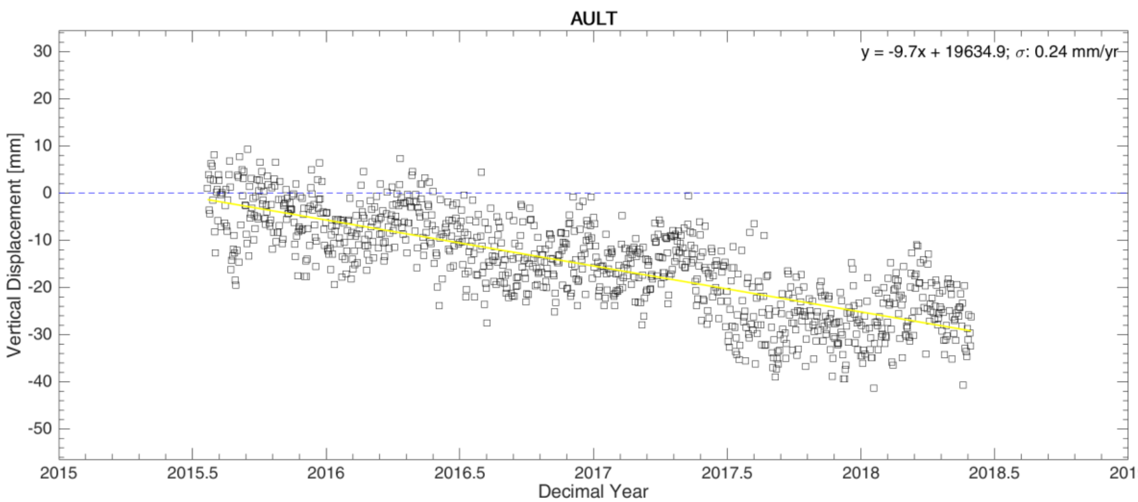
AULT
y = -9.7x + 19634.9; σ: 0.24 mm/yr
Vertical Displacement [mm]
Decimal Year

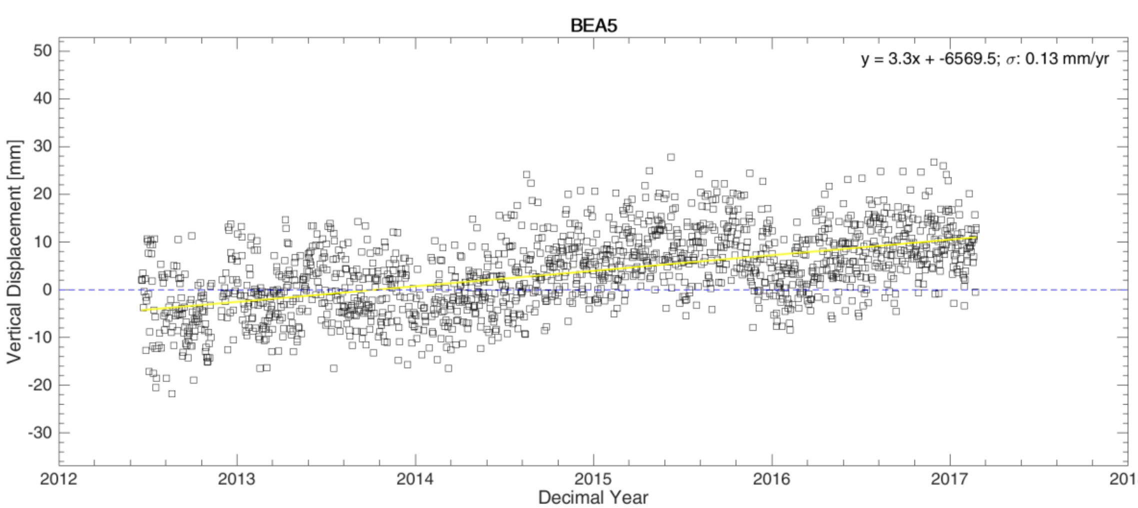
BEA5
y = 3.3x + -6569.5; σ: 0.13 mm/yr
Vertical Displacement [mm]
Decimal Year

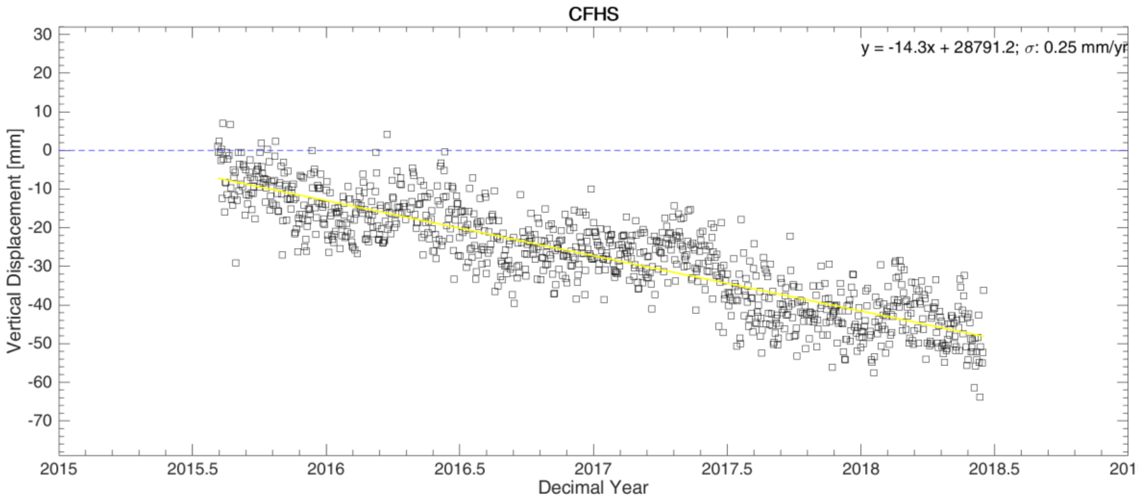
CFHS
y = -14.3x + 28791.2; σ: 0.25 mm/yr
Vertical Displacement [mm]
Decimal Year

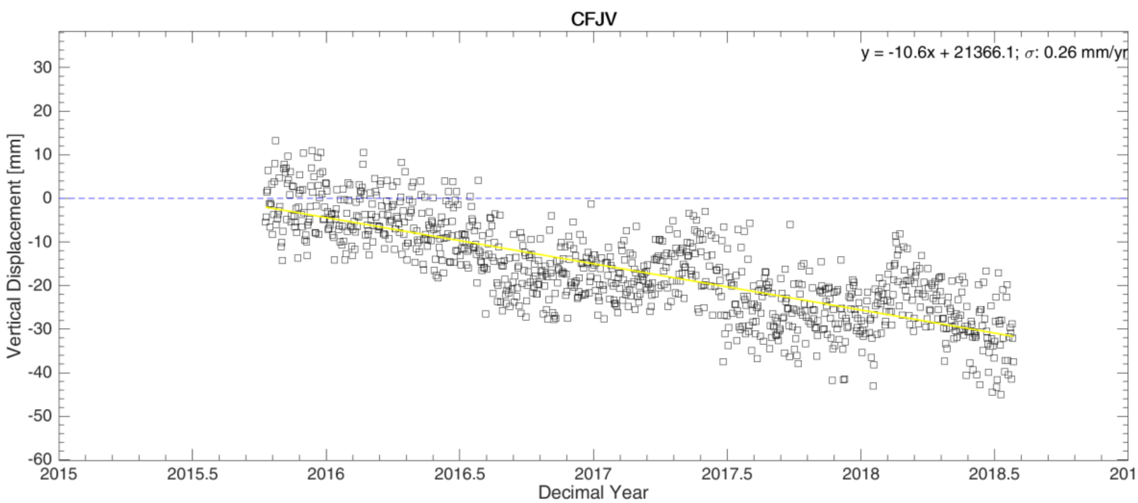
CFJV
y = -10.6x + 21366.1; σ: 0.26 mm/yr
Vertical Displacement [mm]
Decimal Year

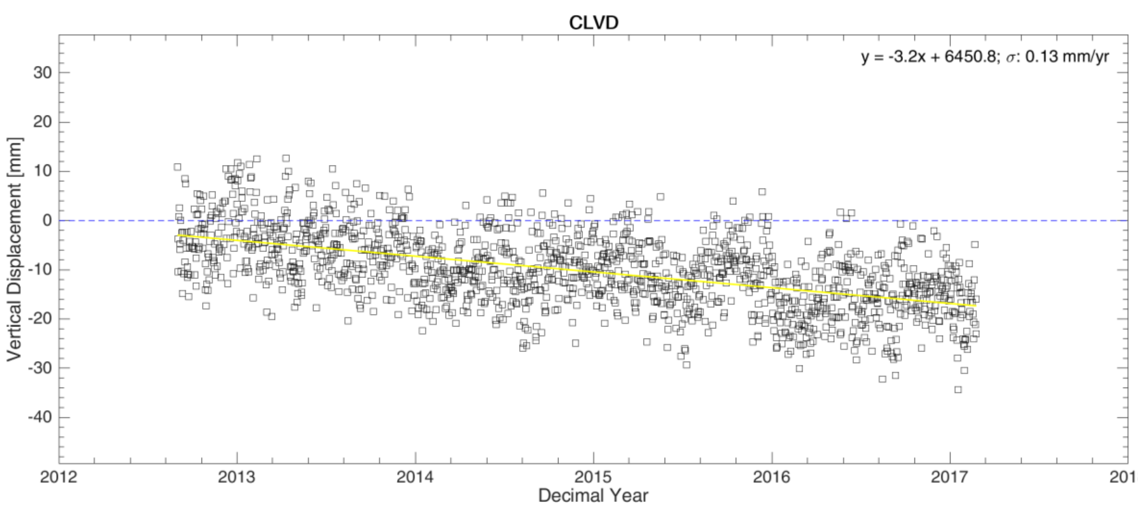
CLVD
y = -3.2x + 6450.8; σ: 0.13 mm/yr
Vertical Displacement [mm]
Decimal Year

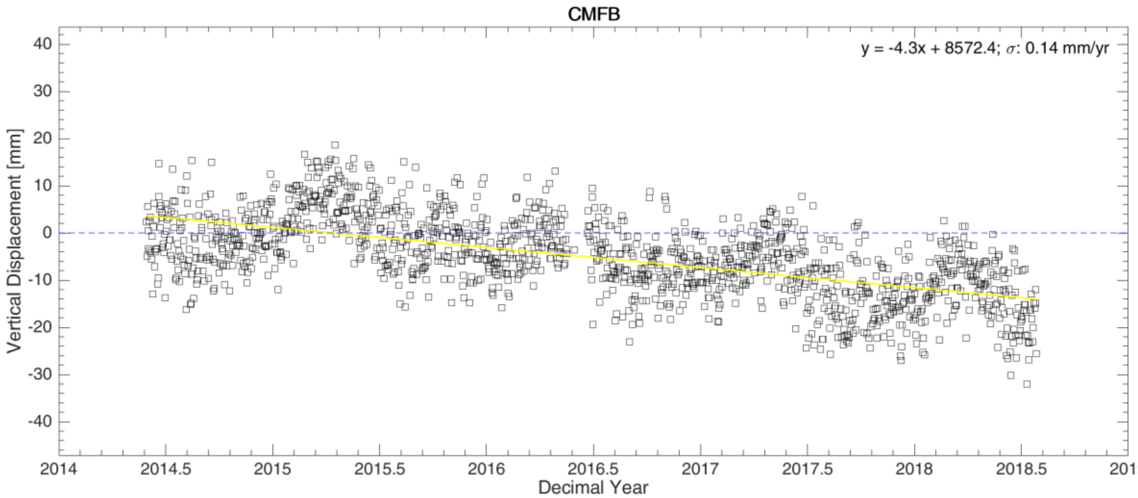
CMFB
y = -4.3x + 8572.4; σ: 0.14 mm/yr
Vertical Displacement [mm]
Decimal Year

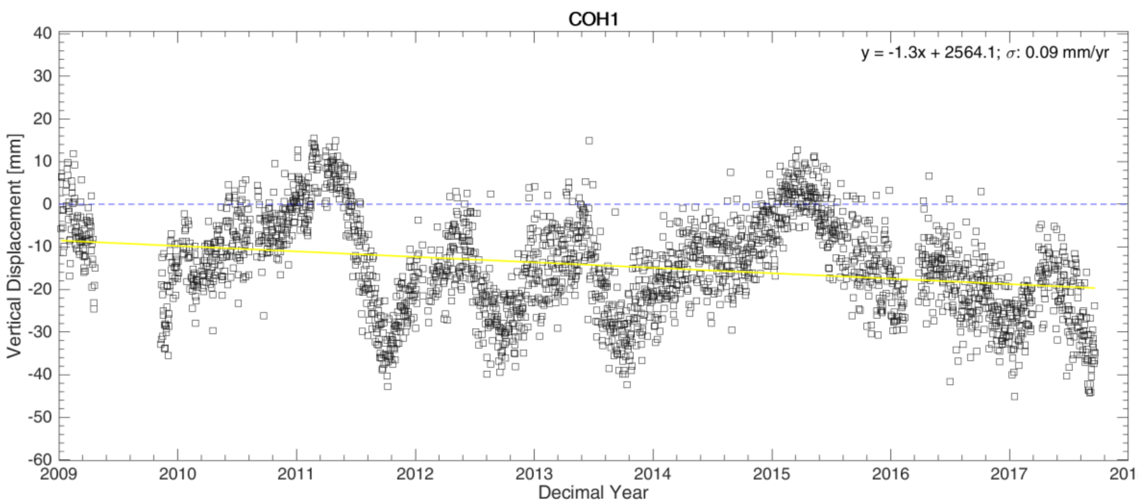
COH1
y = -1.3x + 2564.1; σ: 0.09 mm/yr
Vertical Displacement [mm]
Decimal Year

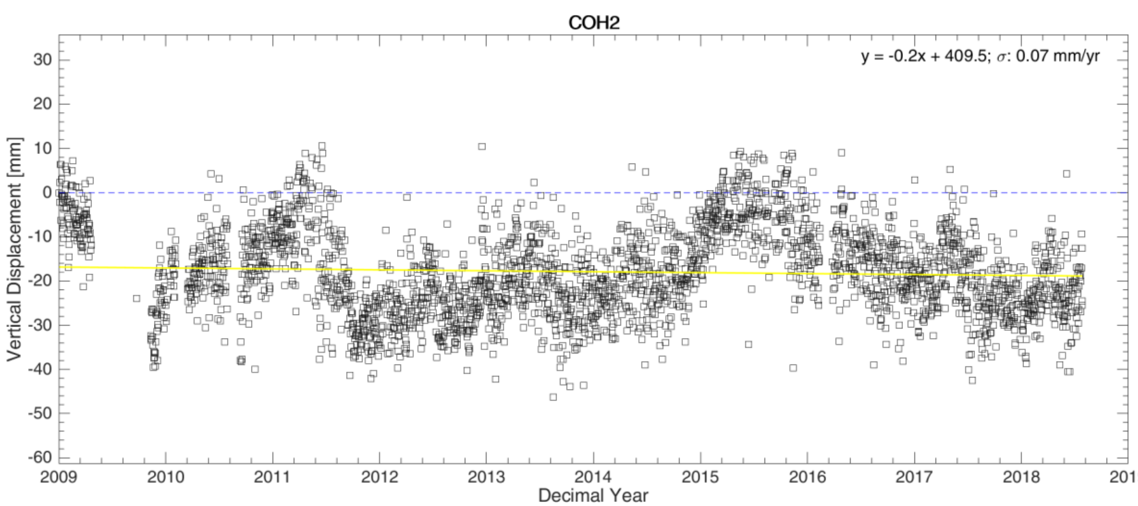
COH2
y = -0.2x + 409.5; σ: 0.07 mm/yr
Vertical Displacement [mm]
Decimal Year

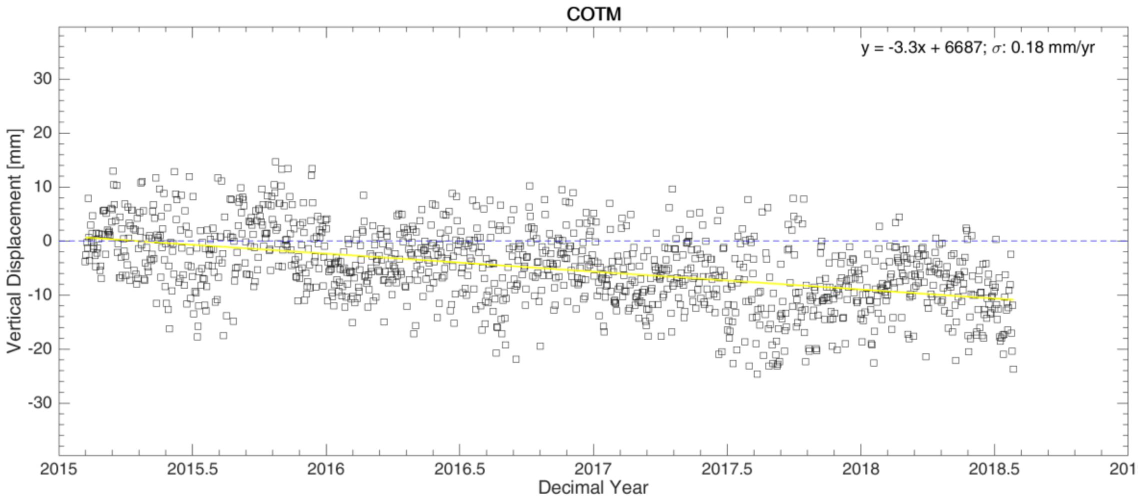
COTM
y = -3.3x + 6687; σ: 0.18 mm/yr
Vertical Displacement [mm]
30
20
10
0
-10
-20
-30
2015
2015.5
2016
2016.5
2017
2017.5
2018
2018.5
2019
Decimal Year

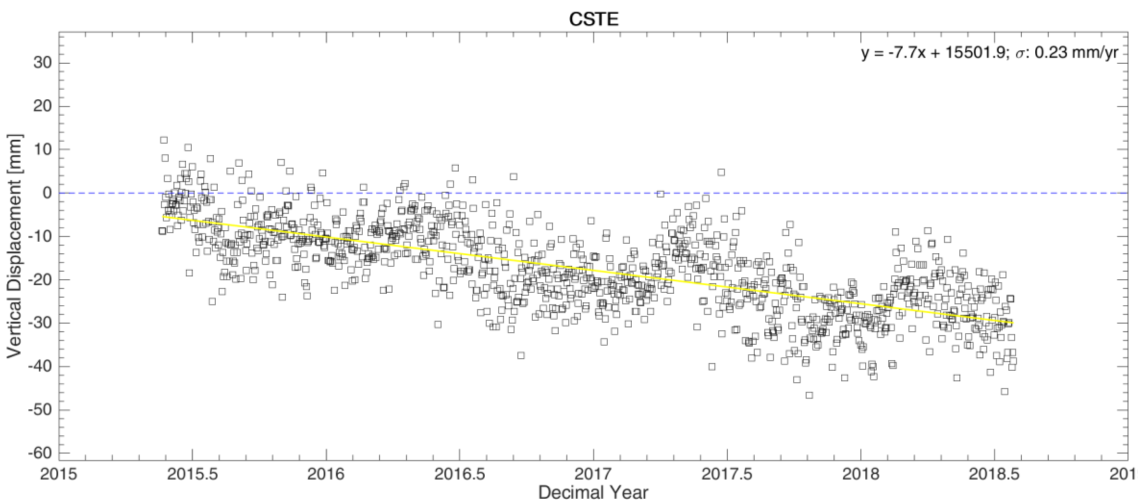
CSTE
y = -7.7x + 15501.9; σ: 0.23 mm/yr
Vertical Displacement [mm]
30
20
10
0
-10
-20
-30
-40
-50
-60
2015
2015.5
2016
2016.5
2017
2017.5
2018
2018.5
2019
Decimal Year

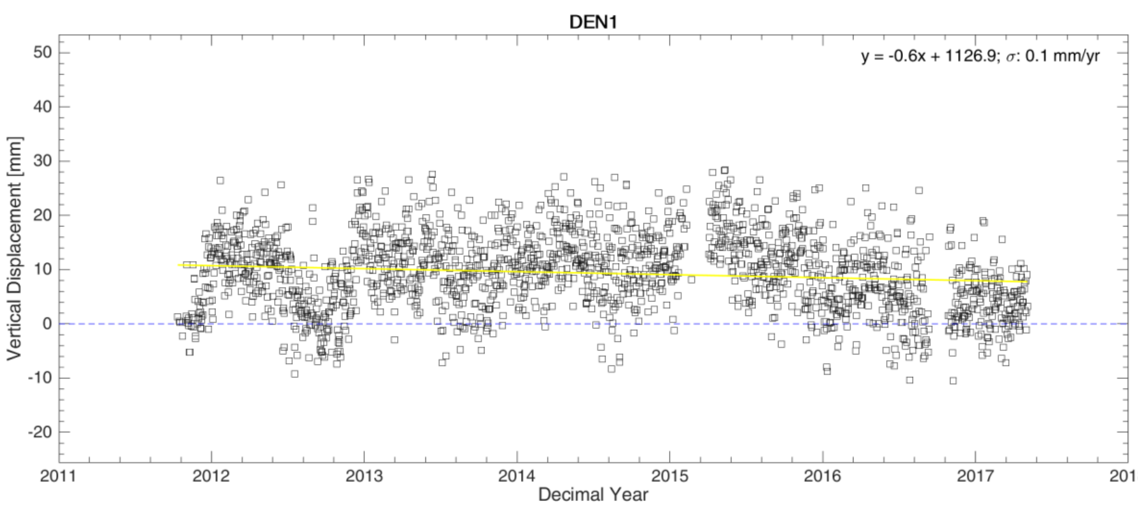
DEN1
y = -0.6x + 1126.9; σ: 0.1 mm/yr
Vertical Displacement [mm]
50
40
30
20
10
0
-10
-20
2011
2012
2013
2014
2015
2016
2017
2018
Decimal Year

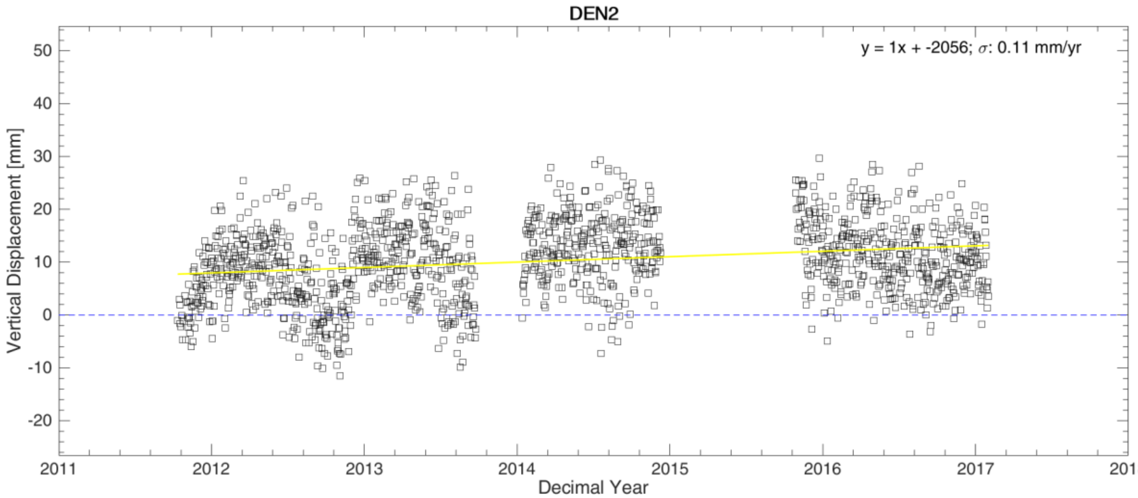
DEN2
y = 1x + -2056; σ: 0.11 mm/yr
Vertical Displacement [mm]
Decimal Year

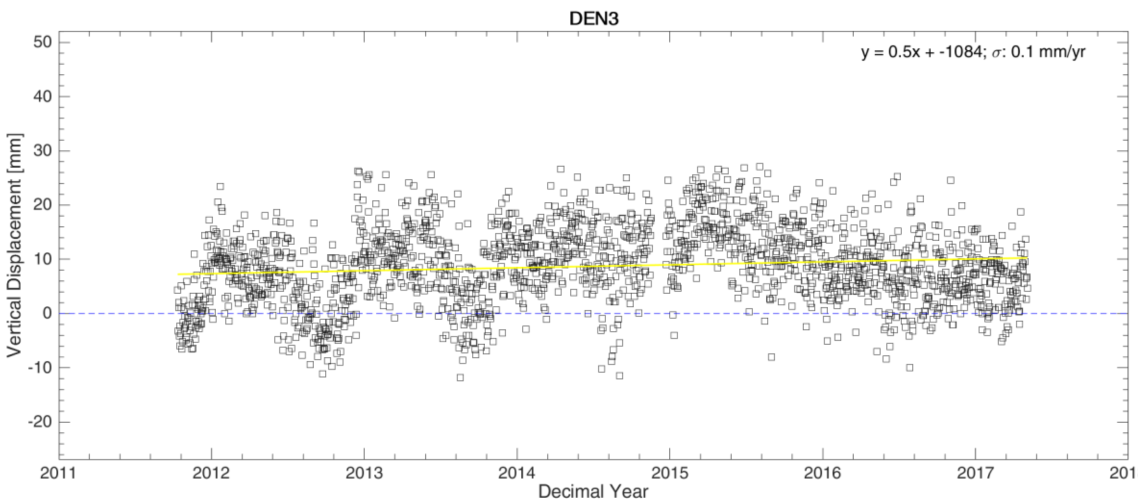
DEN3
y = 0.5x + -1084; σ: 0.1 mm/yr
Vertical Displacement [mm]
Decimal Year

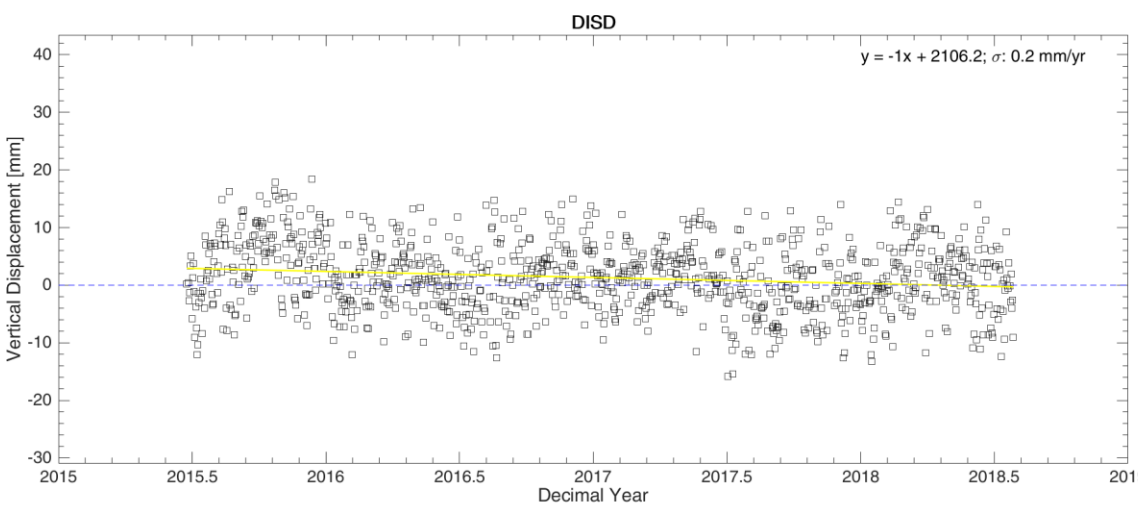
DISD
y = -1x + 2106.2; σ: 0.2 mm/yr
Vertical Displacement [mm]
Decimal Year

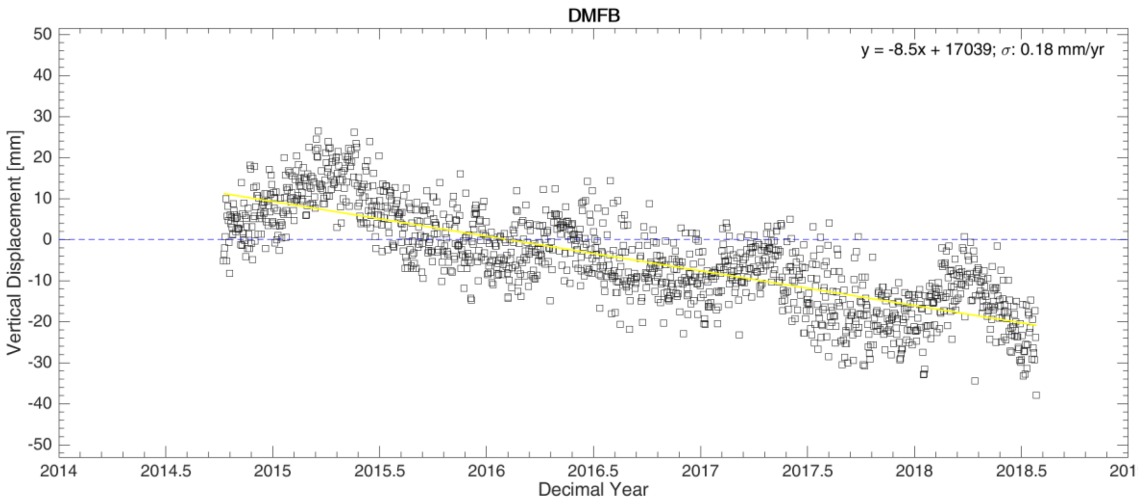
DMFB
y = -8.5x + 17039; σ: 0.18 mm/yr
Vertical Displacement [mm]
Decimal Year

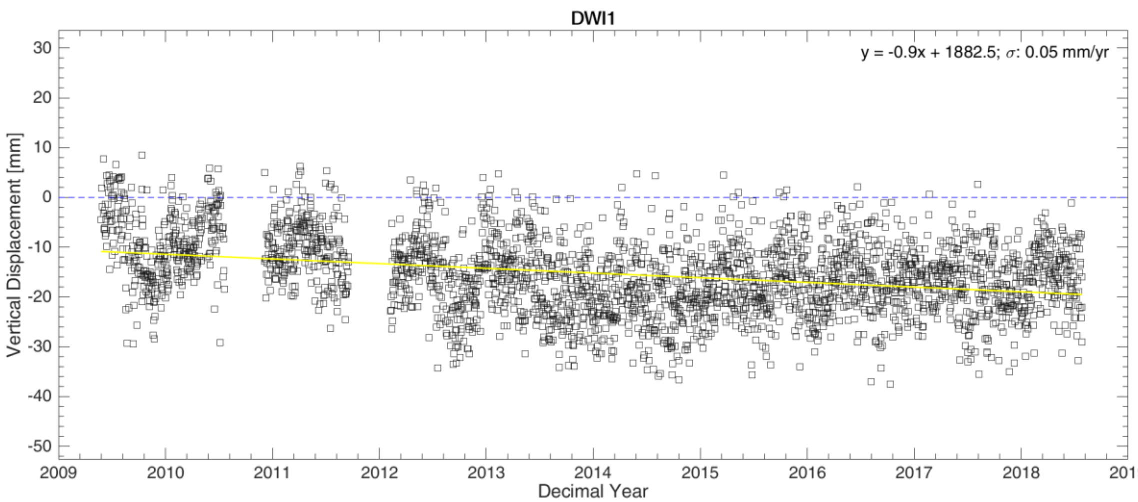
DWI1
y = -0.9x + 1882.5; σ: 0.05 mm/yr
Vertical Displacement [mm]
Decimal Year

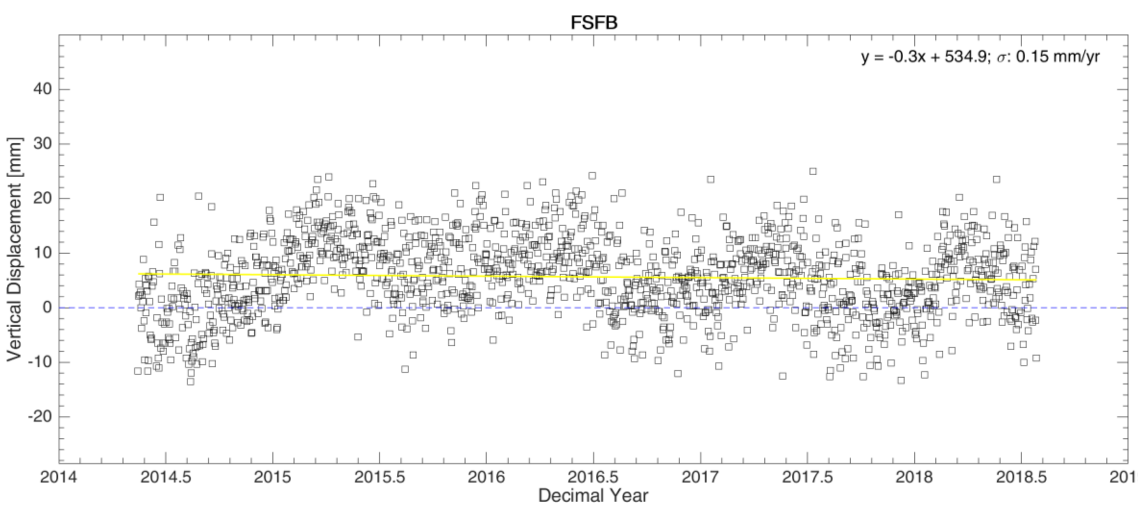
FSFB
y = -0.3x + 534.9; σ: 0.15 mm/yr
Vertical Displacement [mm]
Decimal Year

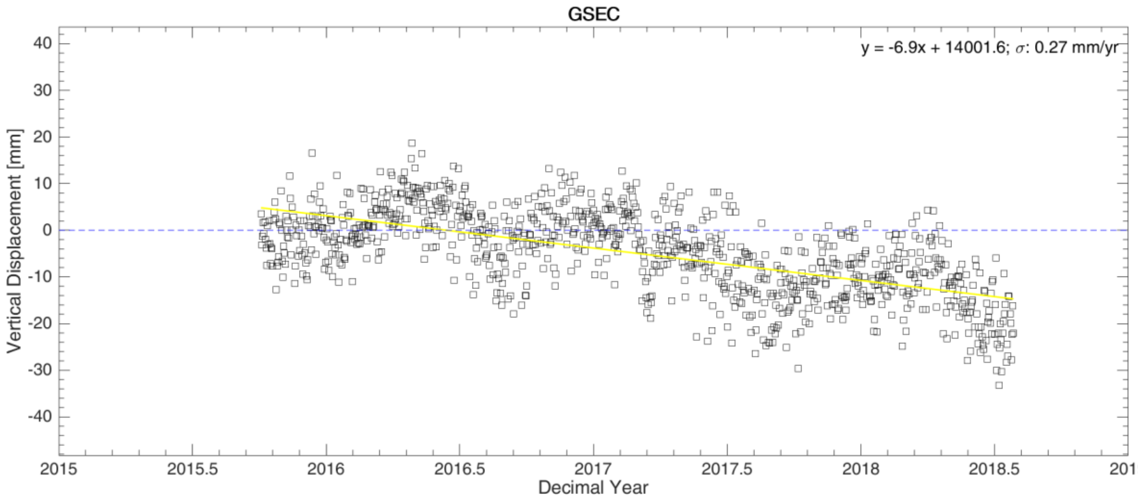
GSEC
y = -6.9x + 14001.6; σ: 0.27 mm/yr
Vertical Displacement [mm]
Decimal Year

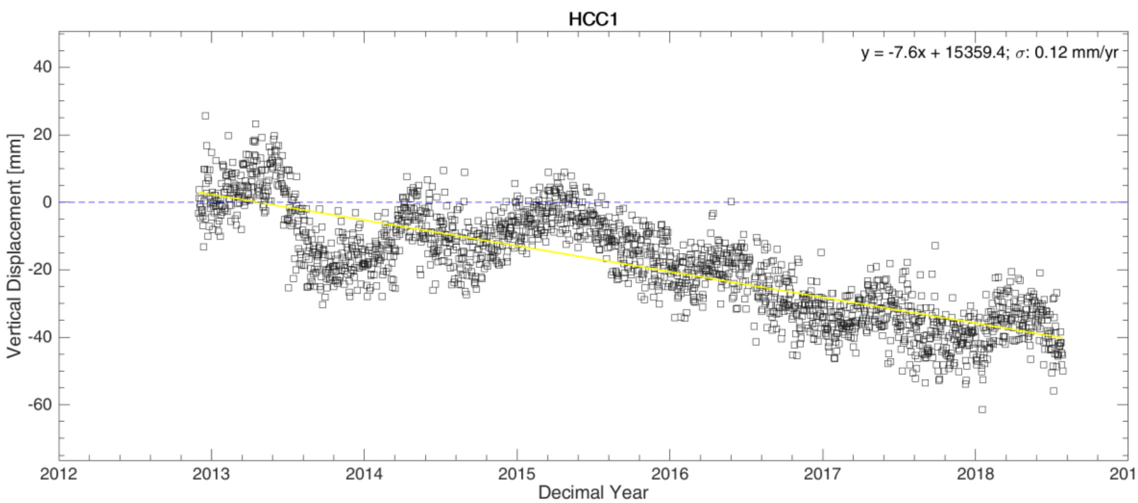
HCC1
y = -7.6x + 15359.4; σ: 0.12 mm/yr
Vertical Displacement [mm]
Decimal Year

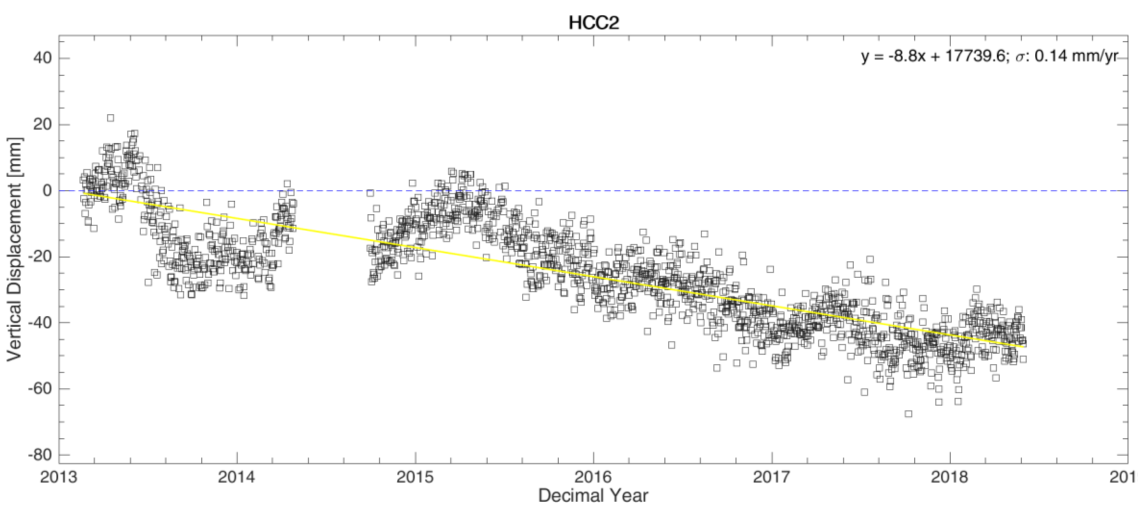
HCC2
y = -8.8x + 17739.6; σ: 0.14 mm/yr
Vertical Displacement [mm]
Decimal Year

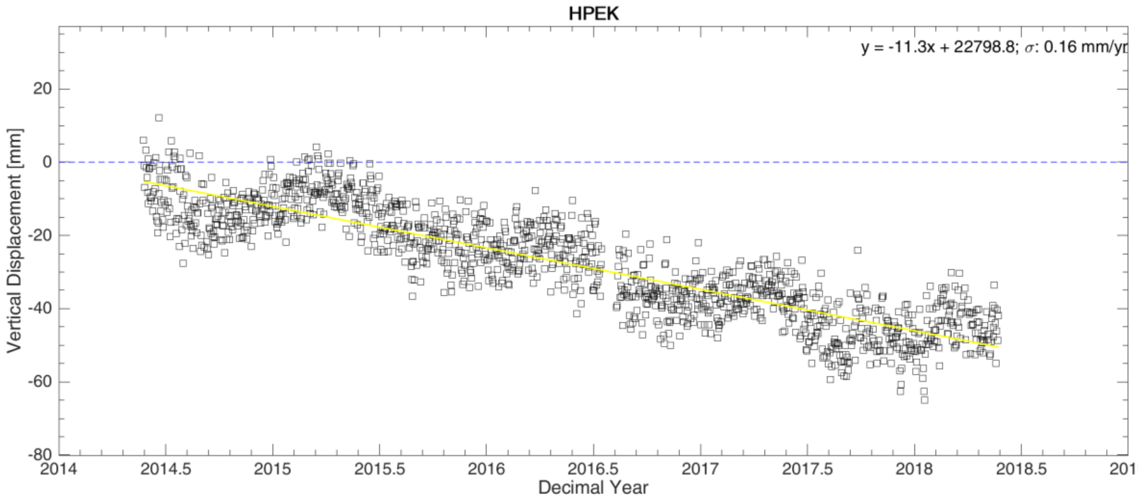
HPEK
y = -11.3x + 22798.8; σ: 0.16 mm/yr
Vertical Displacement [mm]
Decimal Year

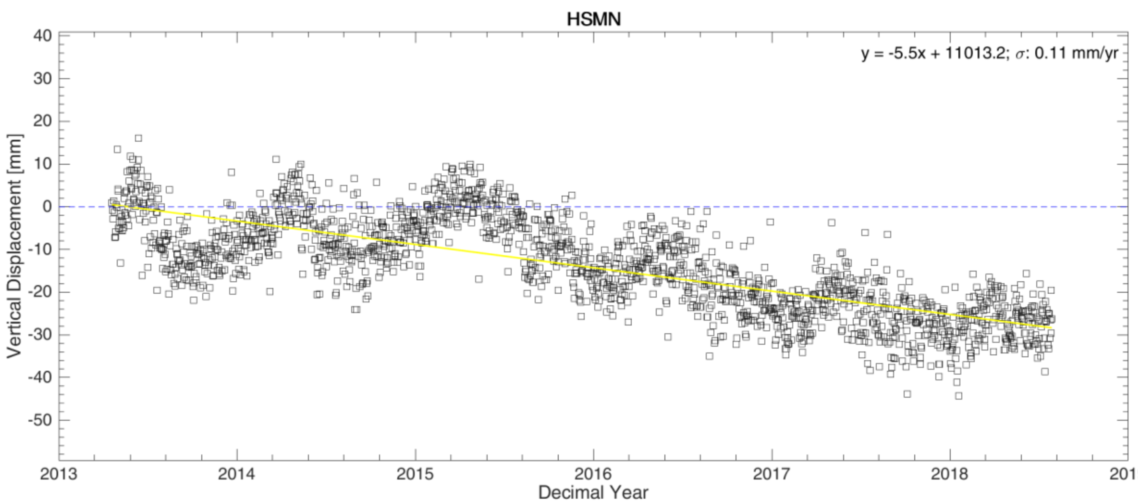
HSMN
y = -5.5x + 11013.2; σ: 0.11 mm/yr
Vertical Displacement [mm]
Decimal Year

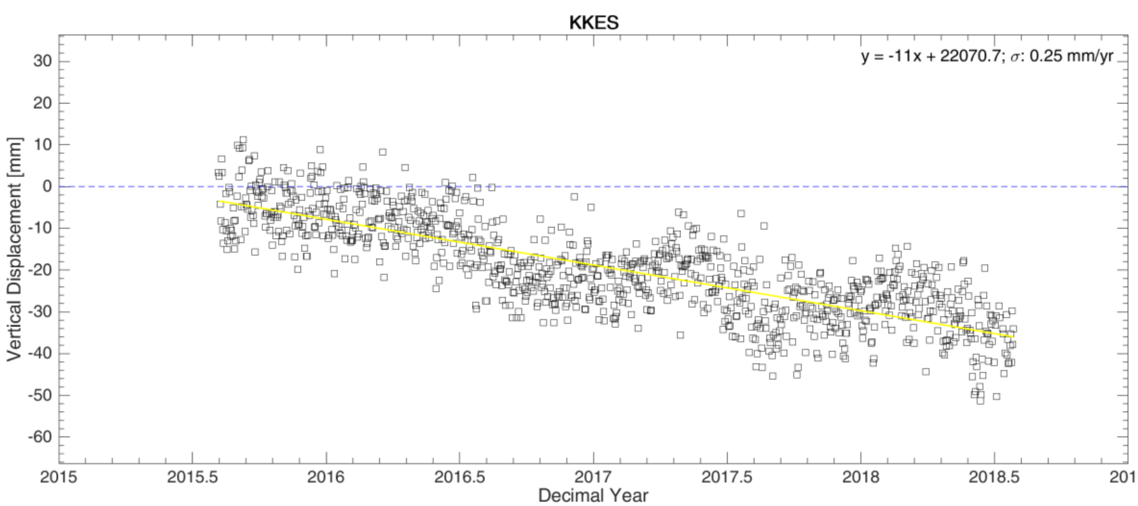
KKES
y = -11x + 22070.7; σ: 0.25 mm/yr
Vertical Displacement [mm]
Decimal Year

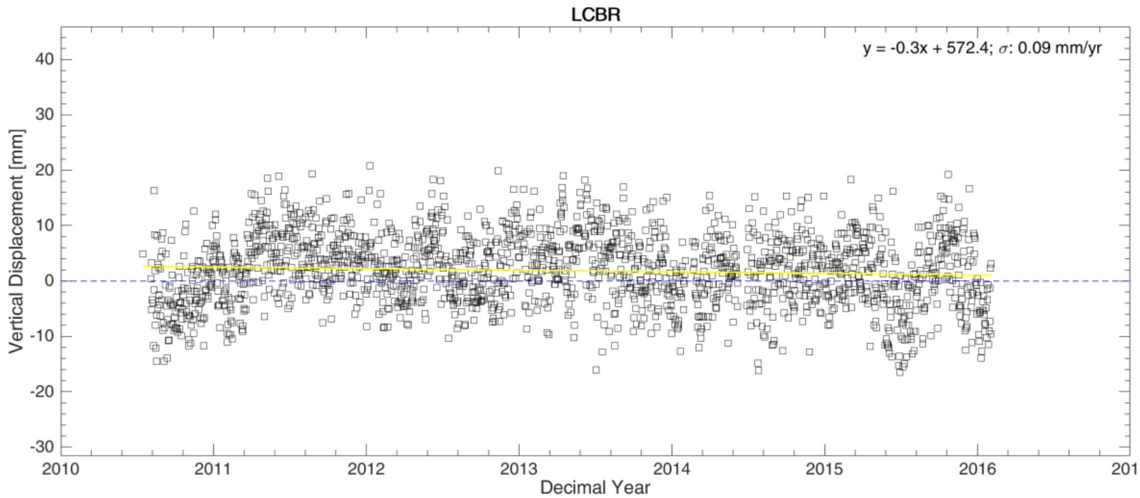
LCBR
y = -0.3x + 572.4; σ: 0.09 mm/yr
Vertical Displacement [mm]
Decimal Year

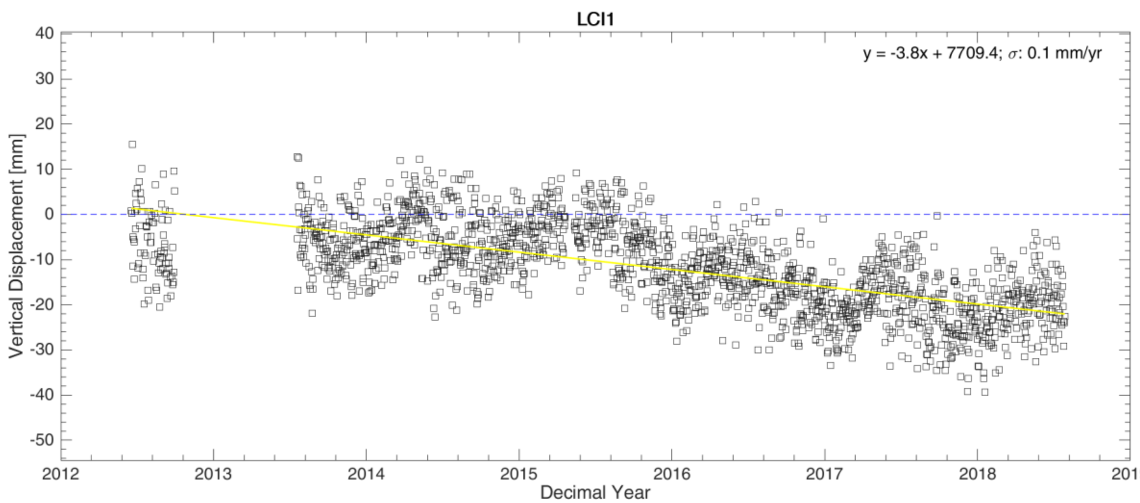
LCI1
y = -3.8x + 7709.4; σ: 0.1 mm/yr
Vertical Displacement [mm]
Decimal Year

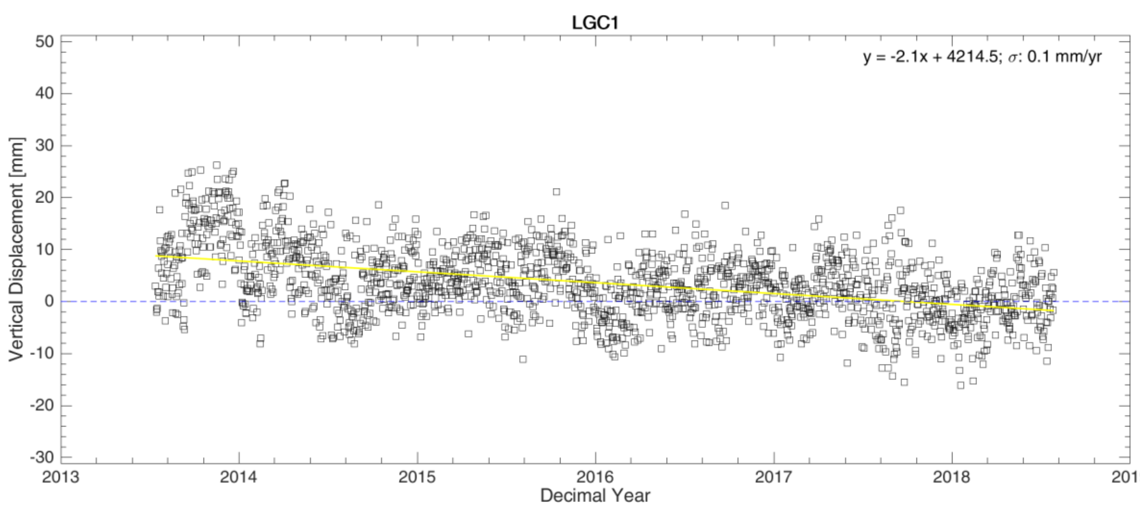
LGC1
y = -2.1x + 4214.5; σ: 0.1 mm/yr
Vertical Displacement [mm]
Decimal Year

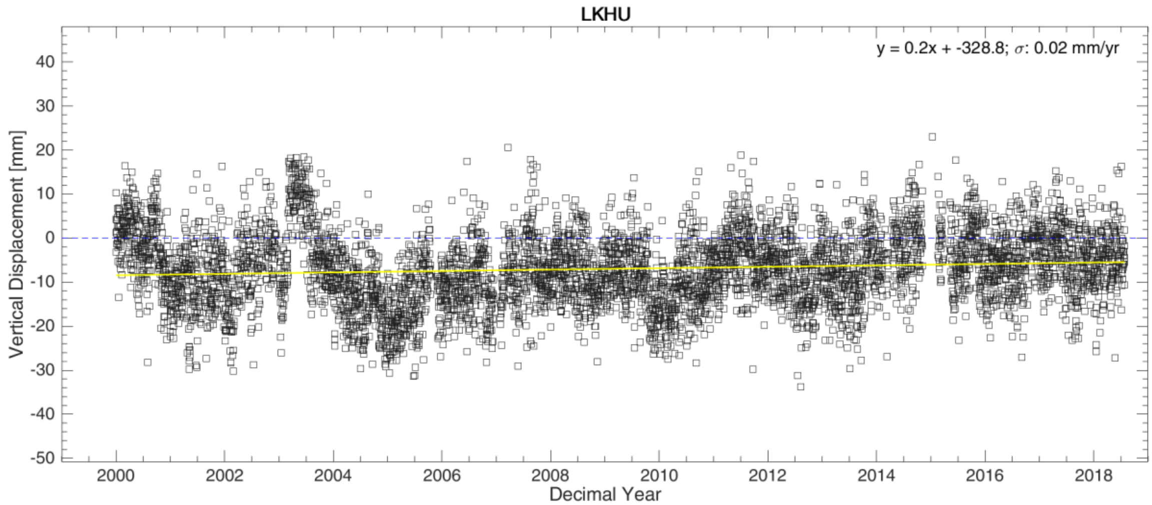
LKHU
y = 0.2x + -328.8; σ: 0.02 mm/yr
Vertical Displacement [mm]
Decimal Year

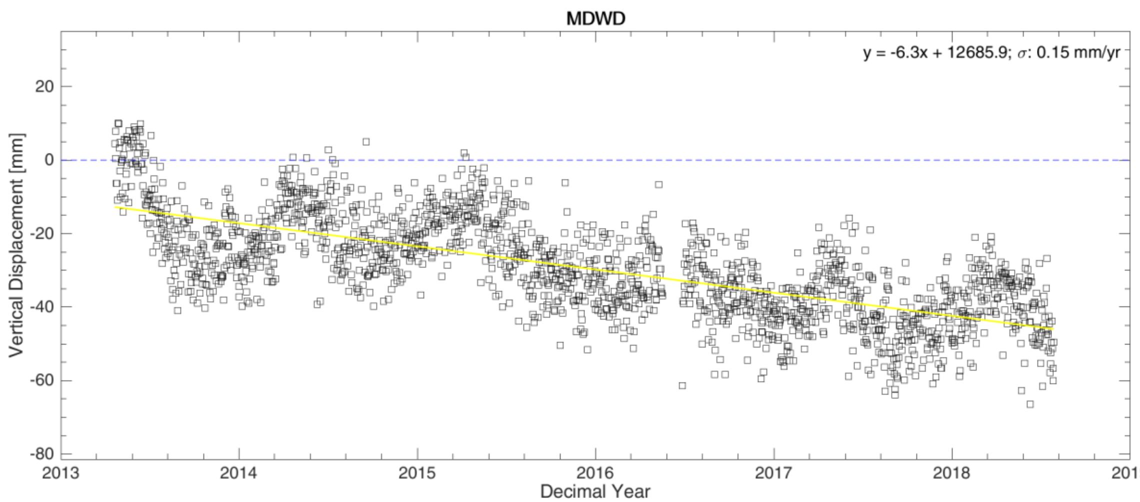
MDWD
y = -6.3x + 12685.9; σ: 0.15 mm/yr
Vertical Displacement [mm]
Decimal Year

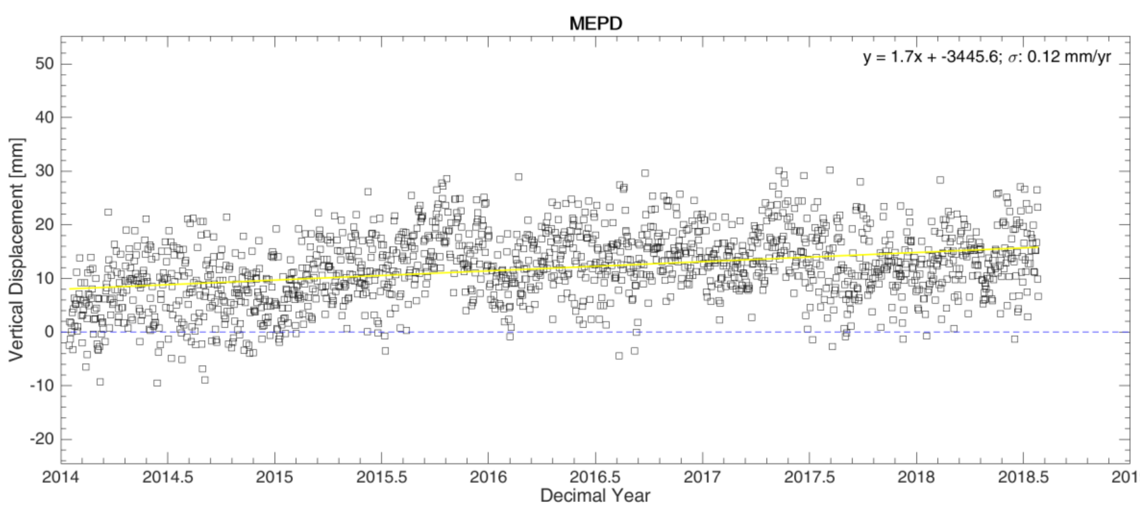
MEPD
y = 1.7x + -3445.6; σ: 0.12 mm/yr
Vertical Displacement [mm]
Decimal Year

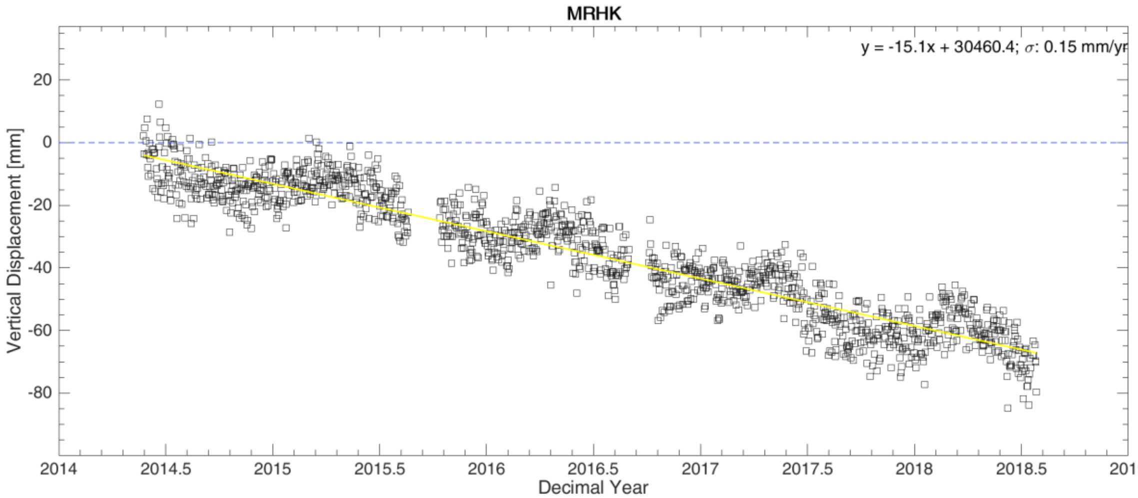
MRHK
y = -15.1x + 30460.4; σ: 0.15 mm/yr
Vertical Displacement [mm]
Decimal Year

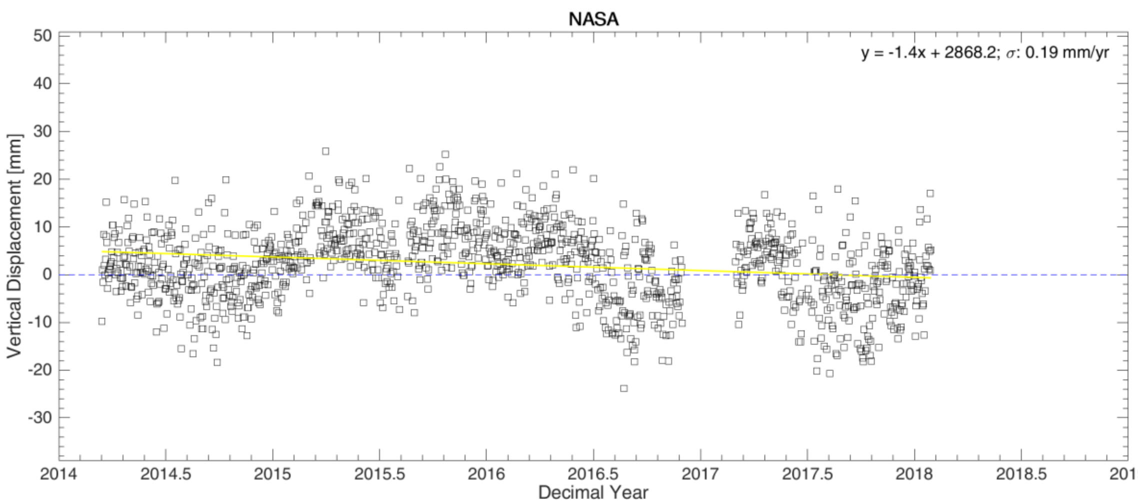
NASA
y = -1.4x + 2868.2; σ: 0.19 mm/yr
Vertical Displacement [mm]
Decimal Year

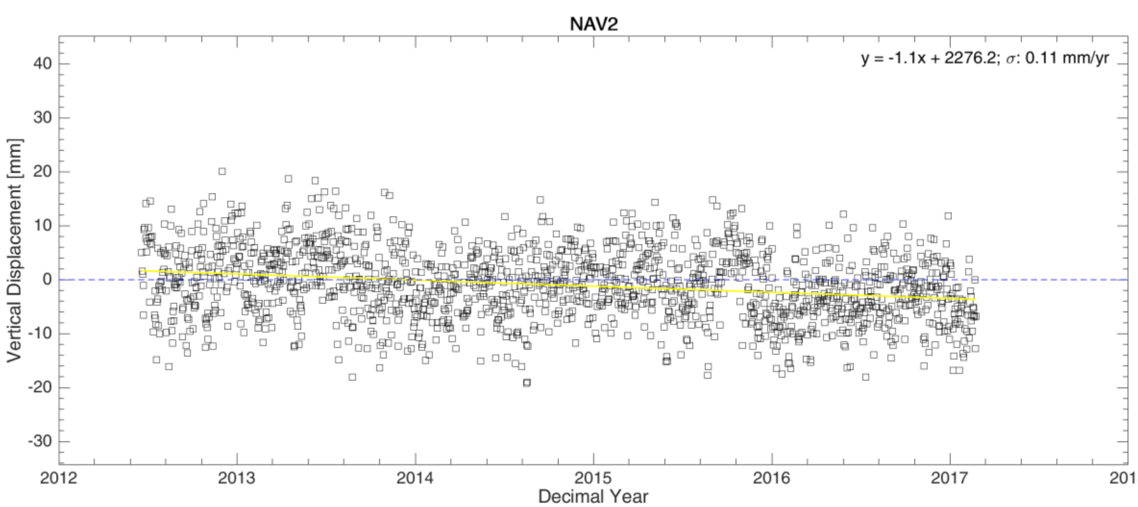
NAV2
y = -1.1x + 2276.2; σ: 0.11 mm/yr
Vertical Displacement [mm]
Decimal Year

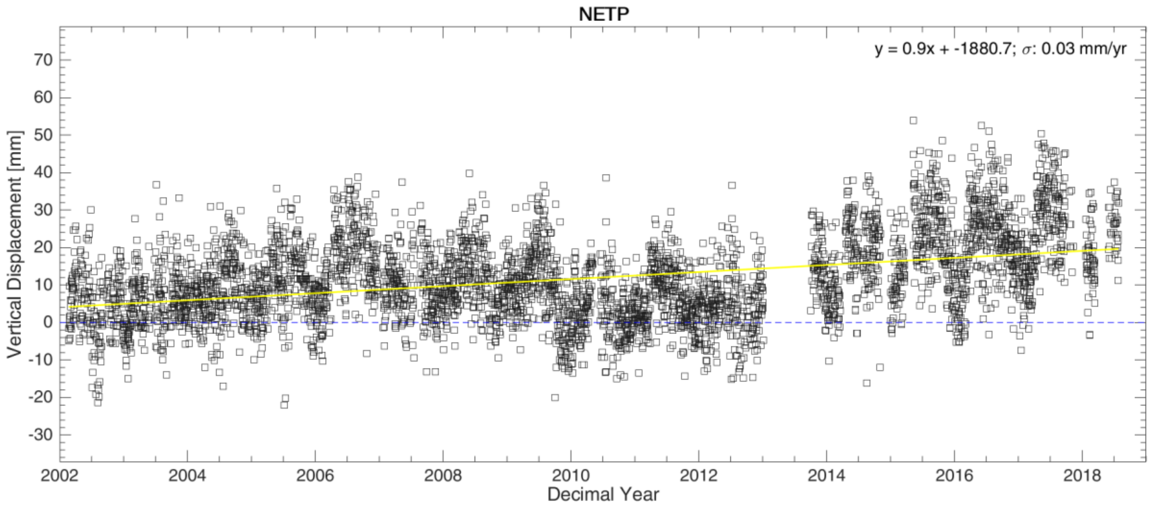
NETP
y = 0.9x + -1880.7; σ: 0.03 mm/yr
Vertical Displacement [mm]
Decimal Year

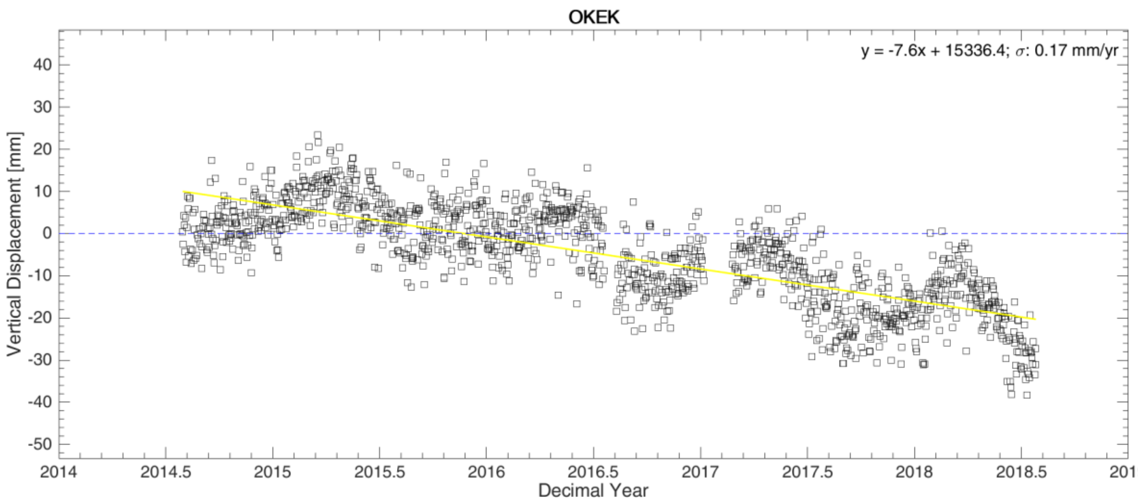
OKEK
y = -7.6x + 15336.4; σ: 0.17 mm/yr
Vertical Displacement [mm]
Decimal Year

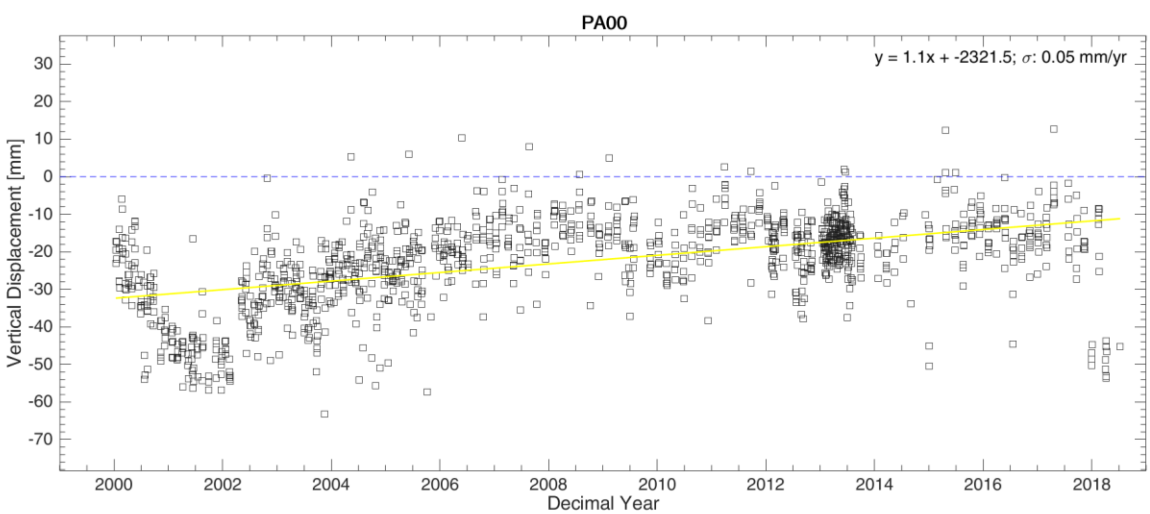
PA00
y = 1.1x + -2321.5; σ: 0.05 mm/yr
Vertical Displacement [mm]
Decimal Year

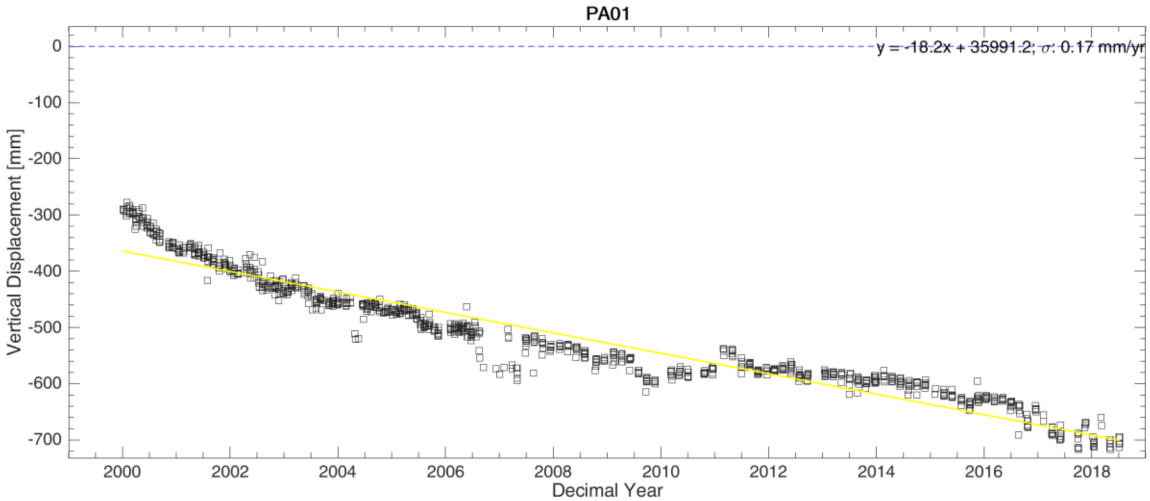
PA01
y = -18.2x + 35991.2; σ: 0.17 mm/yr
Vertical Displacement [mm]
Decimal Year

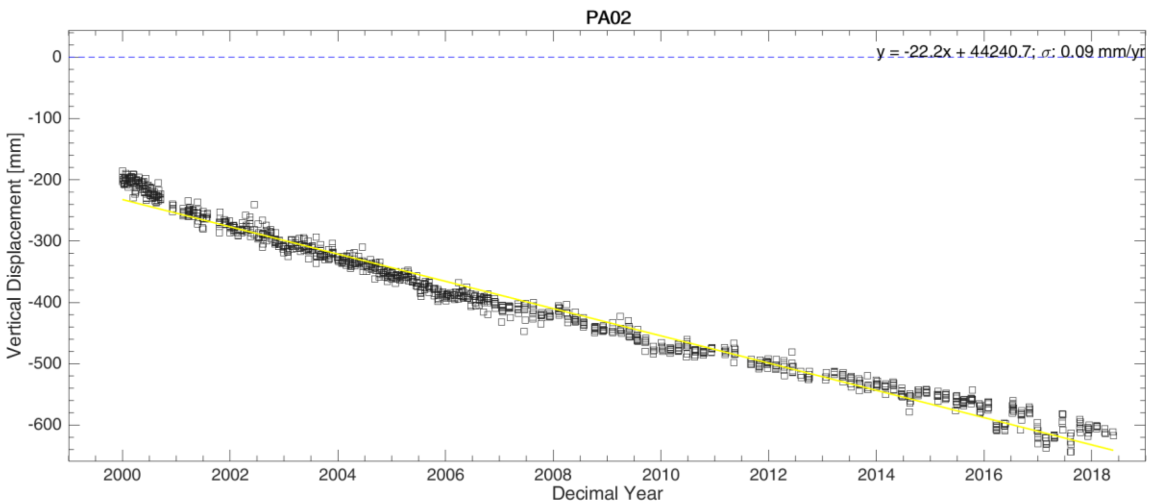
PA02
y = -22.2x + 44240.7; σ: 0.09 mm/yr
Vertical Displacement [mm]
Decimal Year

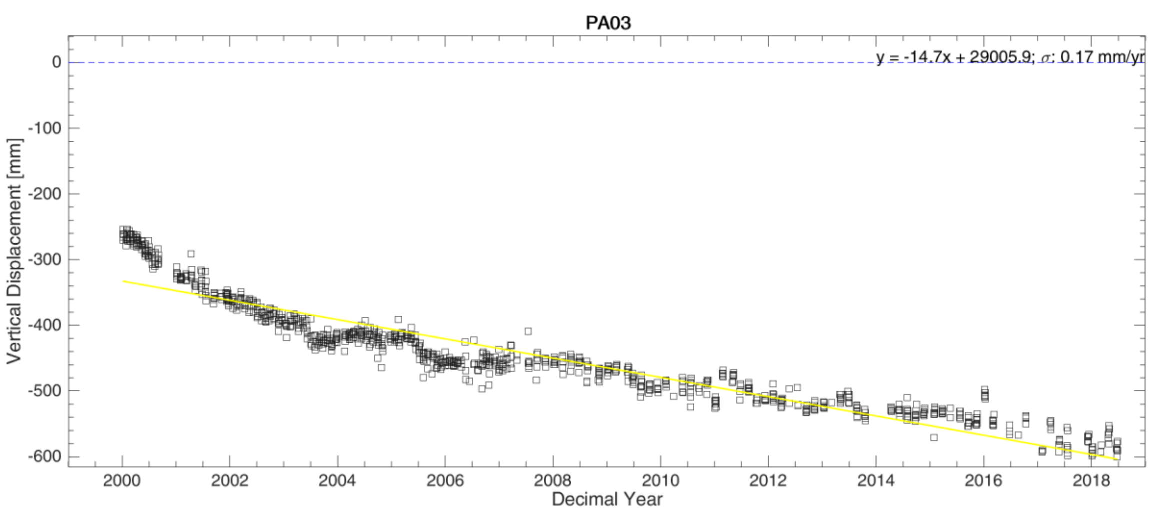
PA03
y = -14.7x + 29005.9; σ: 0.17 mm/yr
Vertical Displacement [mm]
Decimal Year

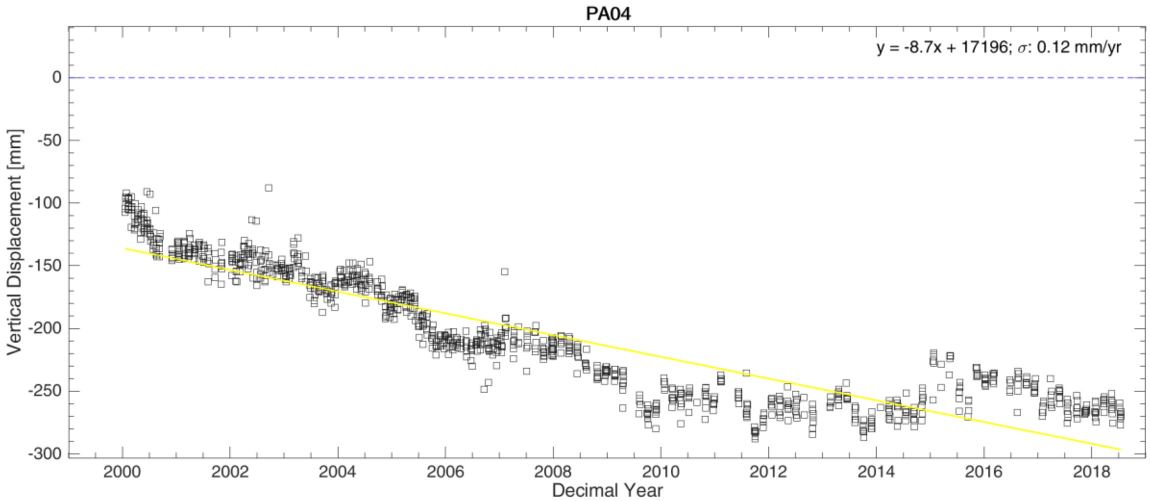

PA04
y = -8.7x + 17196; σ: 0.12 mm/yr
Vertical Displacement [mm]
Decimal Year

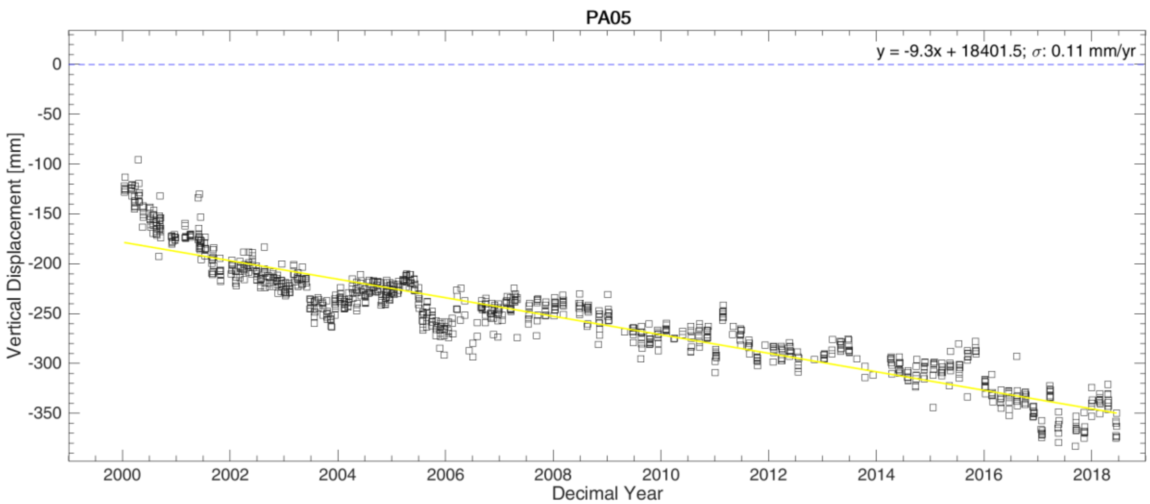

PA05
y = -9.3x + 18401.5; σ: 0.11 mm/yr
Vertical Displacement [mm]
Decimal Year

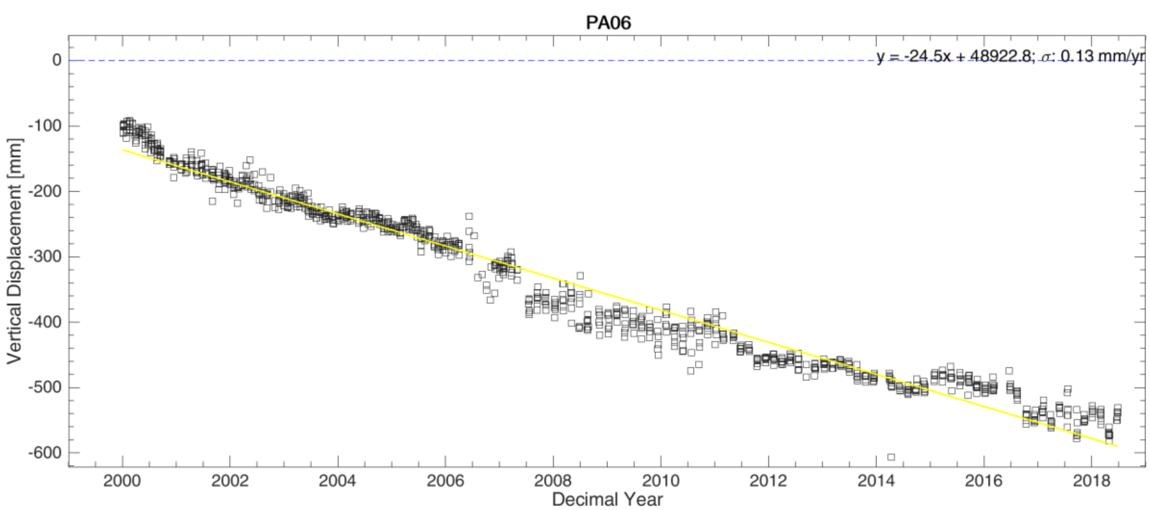

PA06
y = -24.5x + 48922.8; σ: 0.13 mm/yr
Vertical Displacement [mm]
Decimal Year

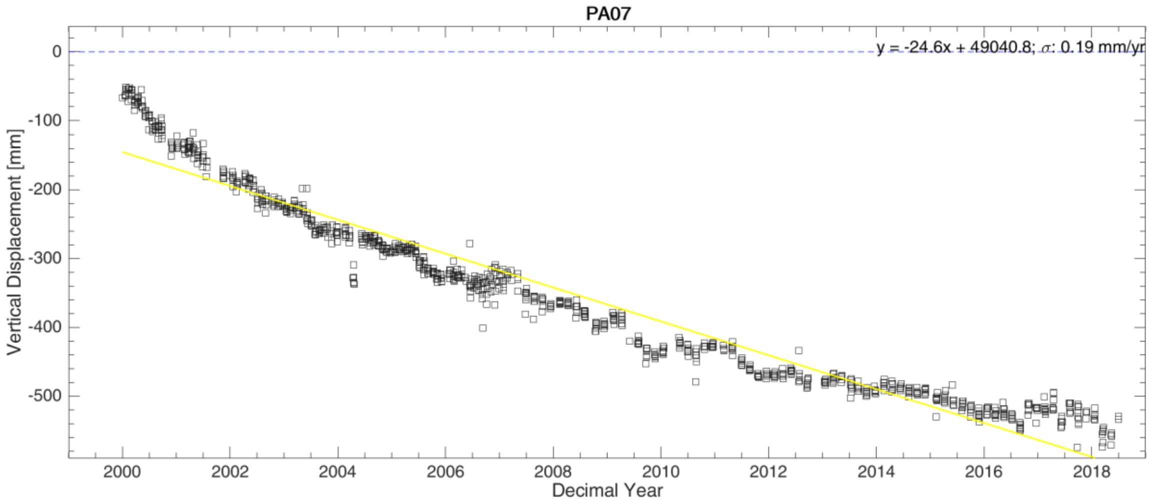
PA07
y = -24.6x + 49040.8; σ: 0.19 mm/yr
Vertical Displacement [mm]
Decimal Year

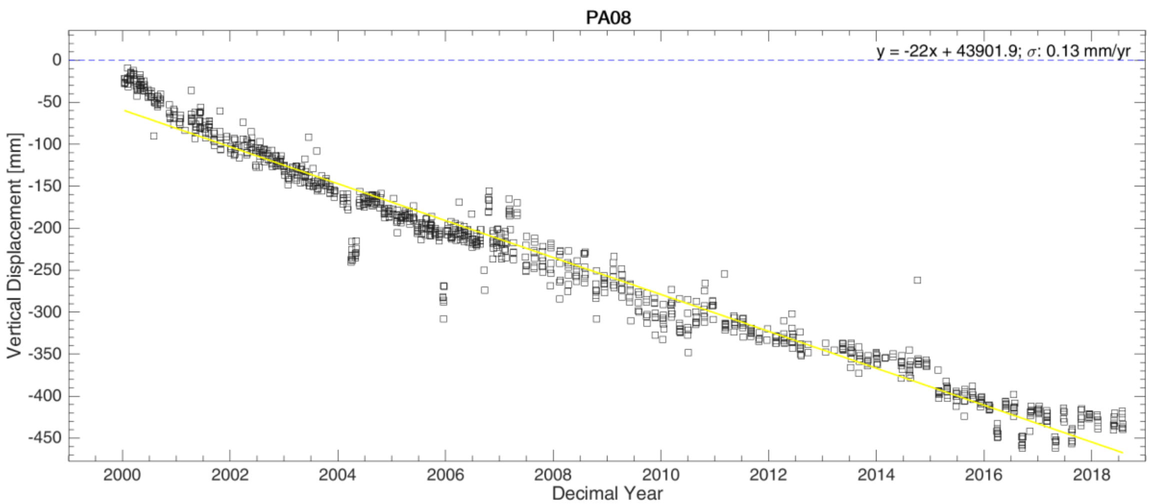
PA08
y = -22x + 43901.9; σ: 0.13 mm/yr
Vertical Displacement [mm]
Decimal Year

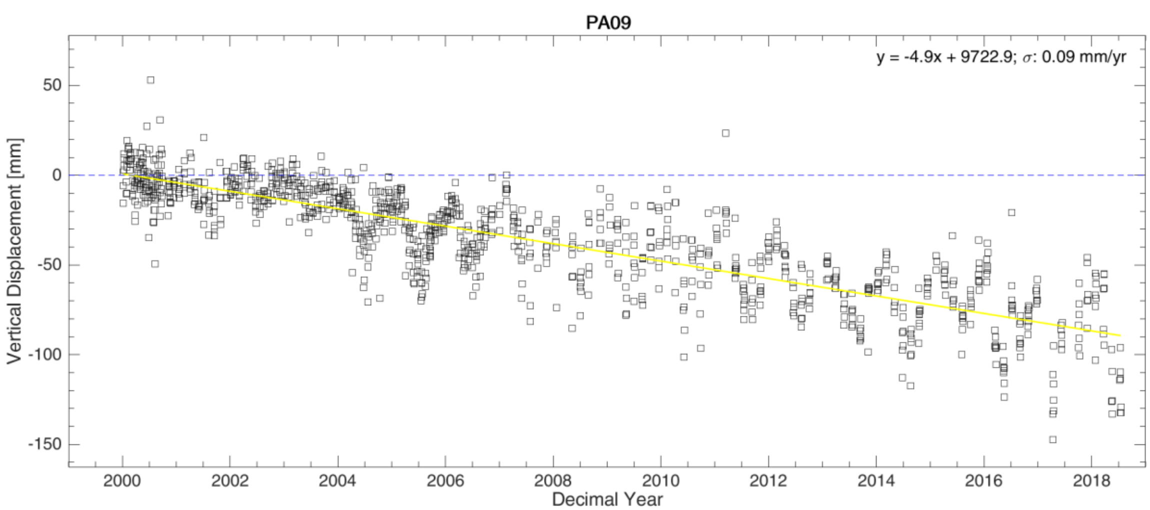
PA09
y = -4.9x + 9722.9; σ: 0.09 mm/yr
Vertical Displacement [mm]
Decimal Year

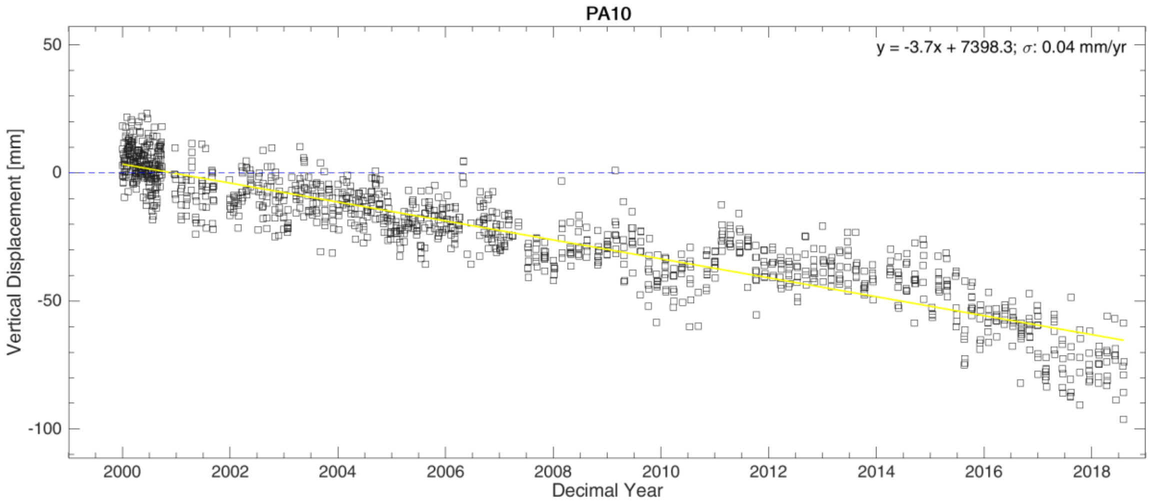
PA10
y = -3.7x + 7398.3; σ: 0.04 mm/yr
Vertical Displacement [mm]
Decimal Year

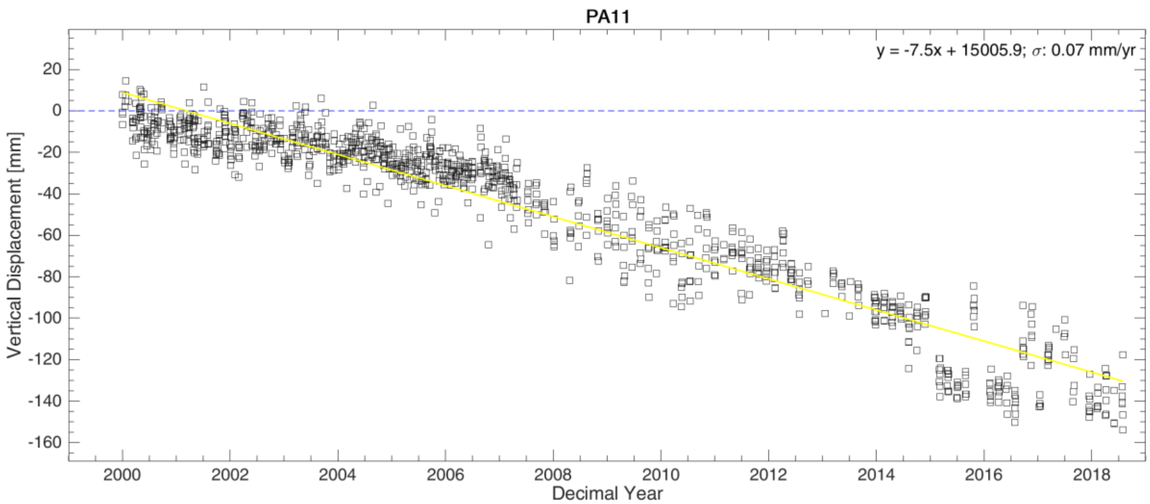
PA11
y = -7.5x + 15005.9; σ: 0.07 mm/yr
Vertical Displacement [mm]
Decimal Year

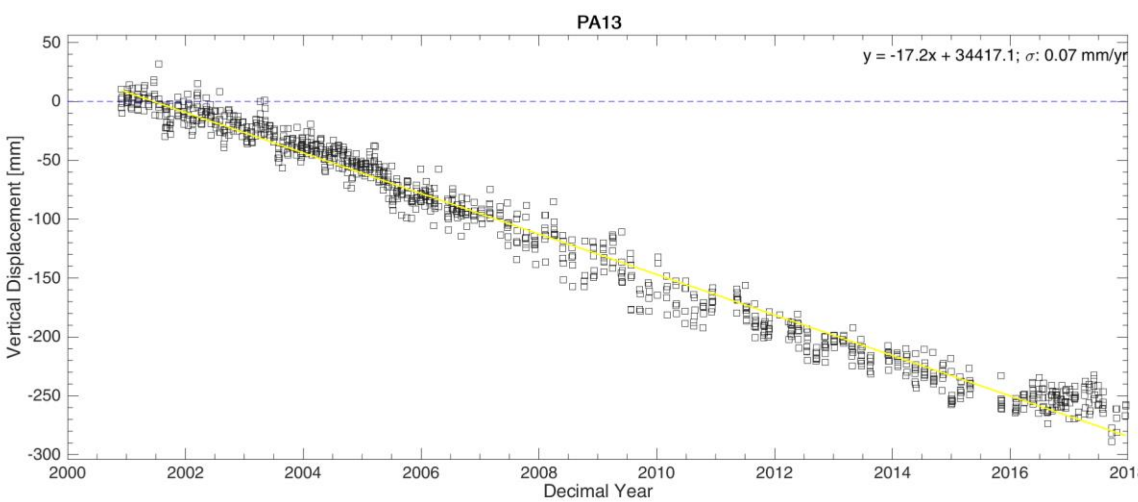
PA13
y = -17.2x + 34417.1; σ: 0.07 mm/yr
Vertical Displacement [mm]
Decimal Year

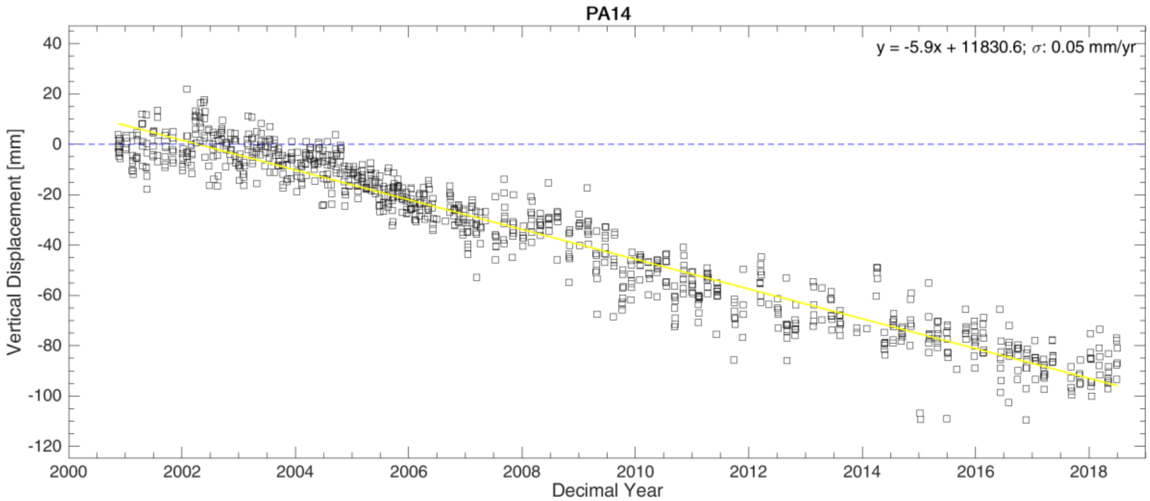
PA14
y = -5.9x + 11830.6; σ: 0.05 mm/yr
Vertical Displacement [mm]
Decimal Year

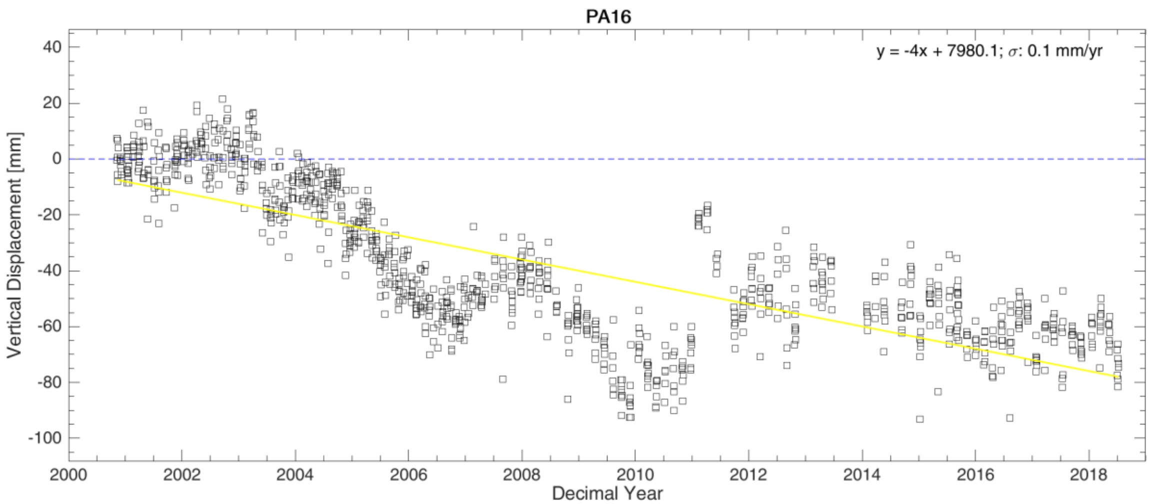
PA16
y = -4x + 7980.1; σ: 0.1 mm/yr
Vertical Displacement [mm]
Decimal Year

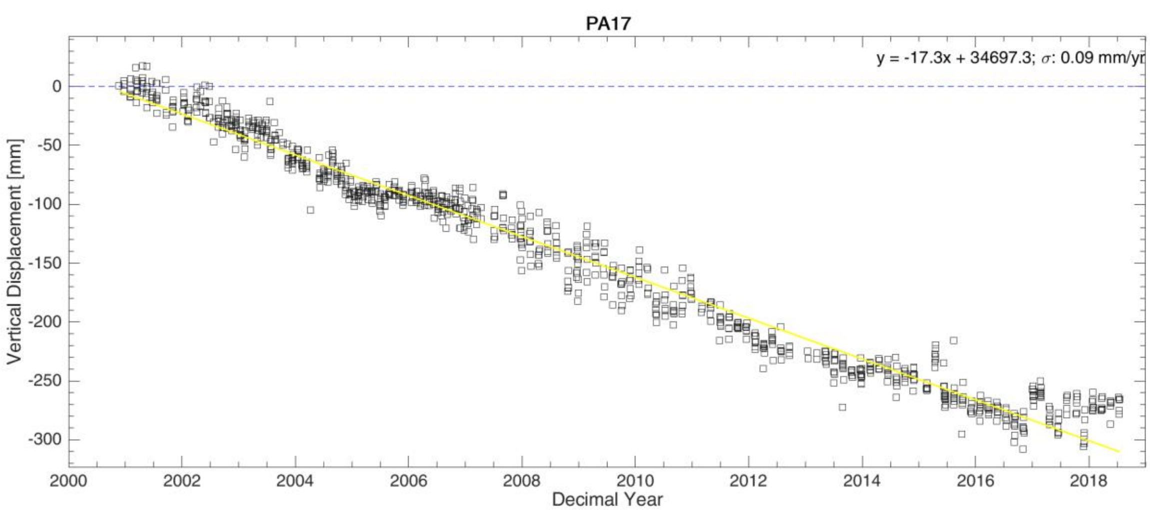
PA17
y = -17.3x + 34697.3; σ: 0.09 mm/yr
Vertical Displacement [mm]
Decimal Year

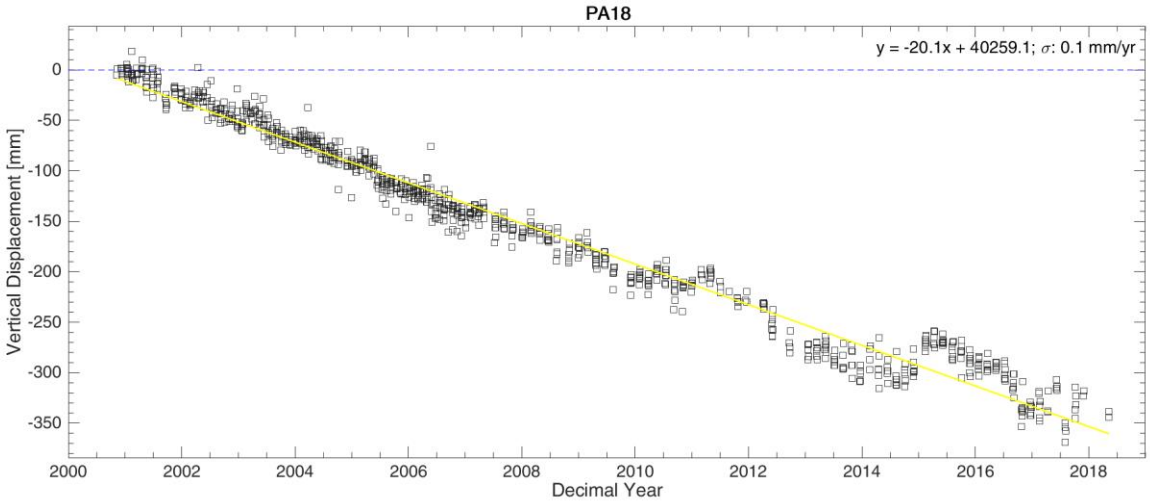
PA18
y = -20.1x + 40259.1; σ: 0.1 mm/yr
Vertical Displacement [mm]
Decimal Year

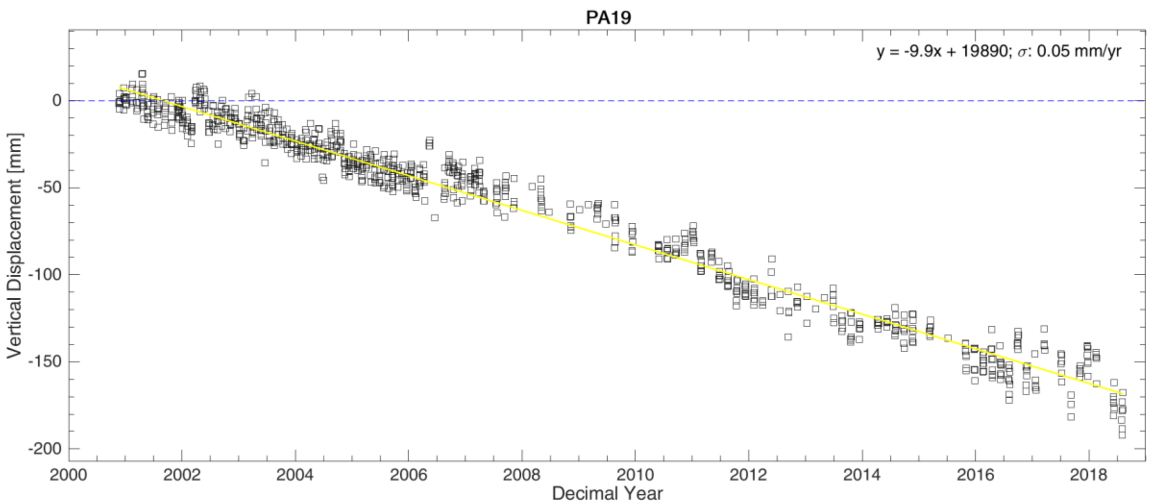
PA19
y = -9.9x + 19890; σ: 0.05 mm/yr
Vertical Displacement [mm]
Decimal Year

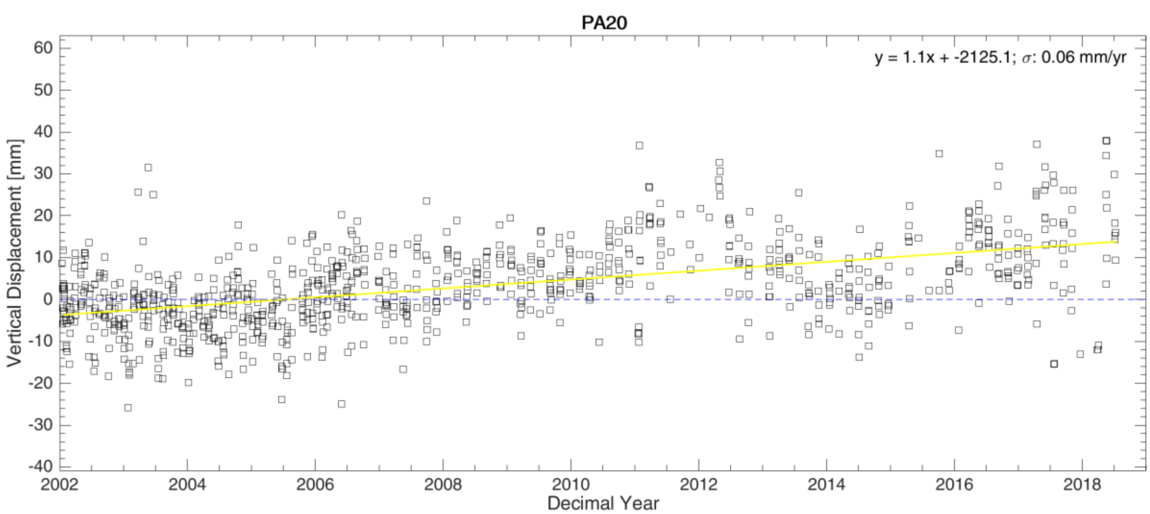
PA20
y = 1.1x + -2125.1; σ: 0.06 mm/yr
Vertical Displacement [mm]
Decimal Year

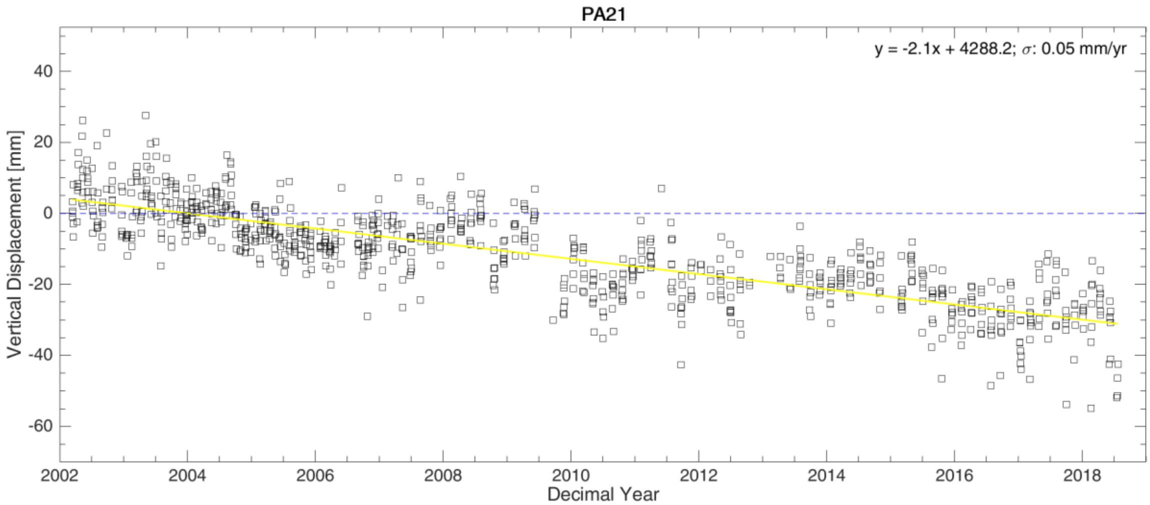
PA21
y = -2.1x + 4288.2; σ: 0.05 mm/yr
Vertical Displacement [mm]
Decimal Year

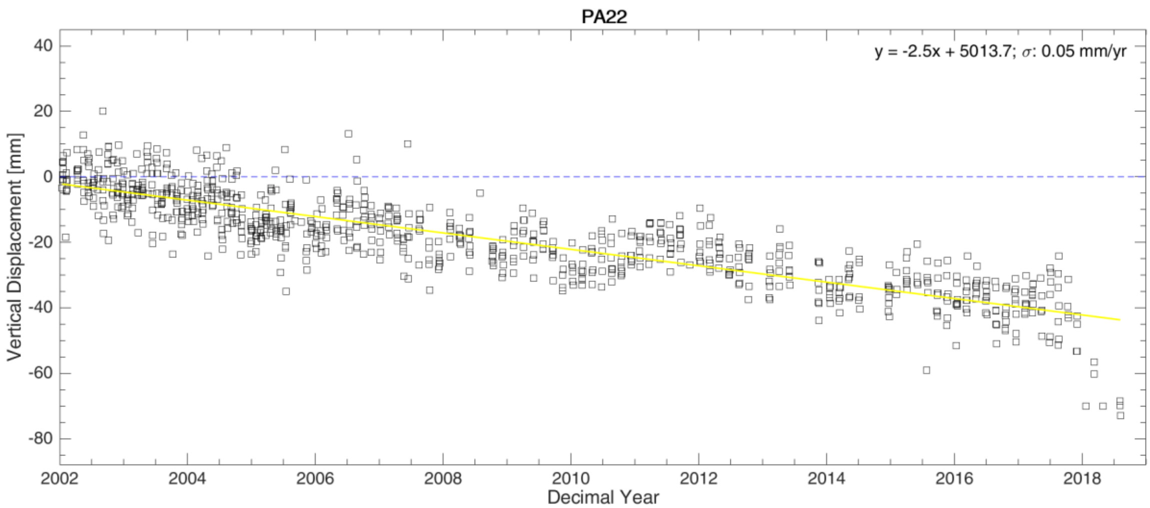
PA22
y = -2.5x + 5013.7; σ: 0.05 mm/yr
Vertical Displacement [mm]
Decimal Year

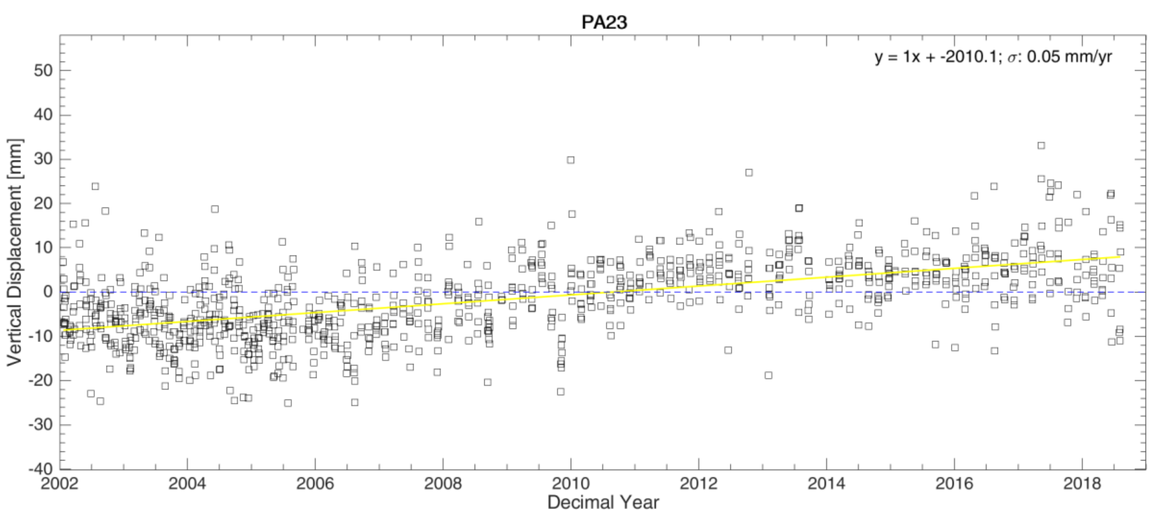
PA23
y = 1x + -2010.1; σ: 0.05 mm/yr
Vertical Displacement [mm]
Decimal Year

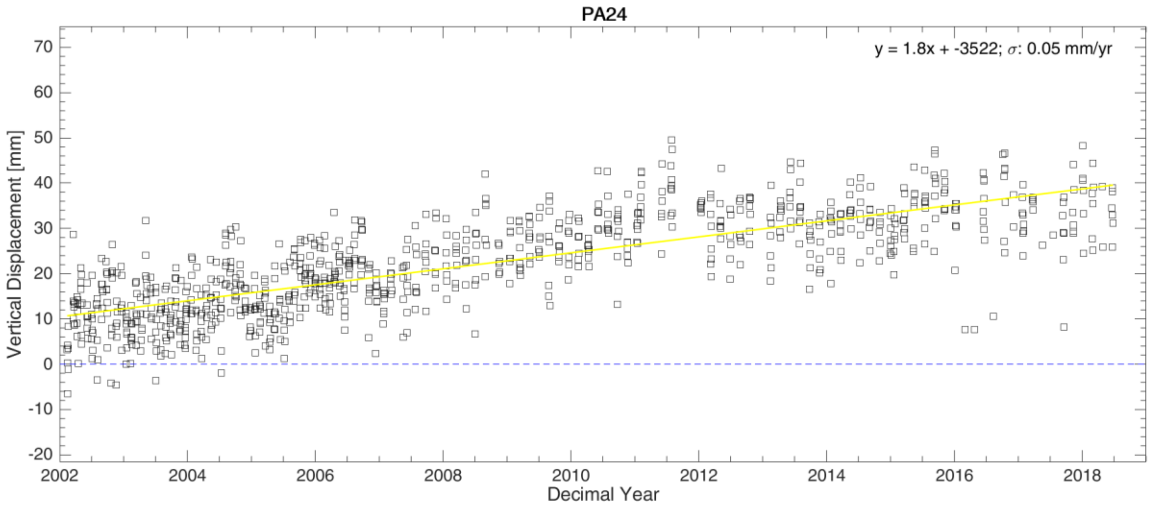
PA24
y = 1.8x + -3522; σ: 0.05 mm/yr
Vertical Displacement [mm]
70
60
50
40
30
20
10
0
-10
-20
2002
2004
2006
2008
2010
2012
2014
2016
2018
Decimal Year

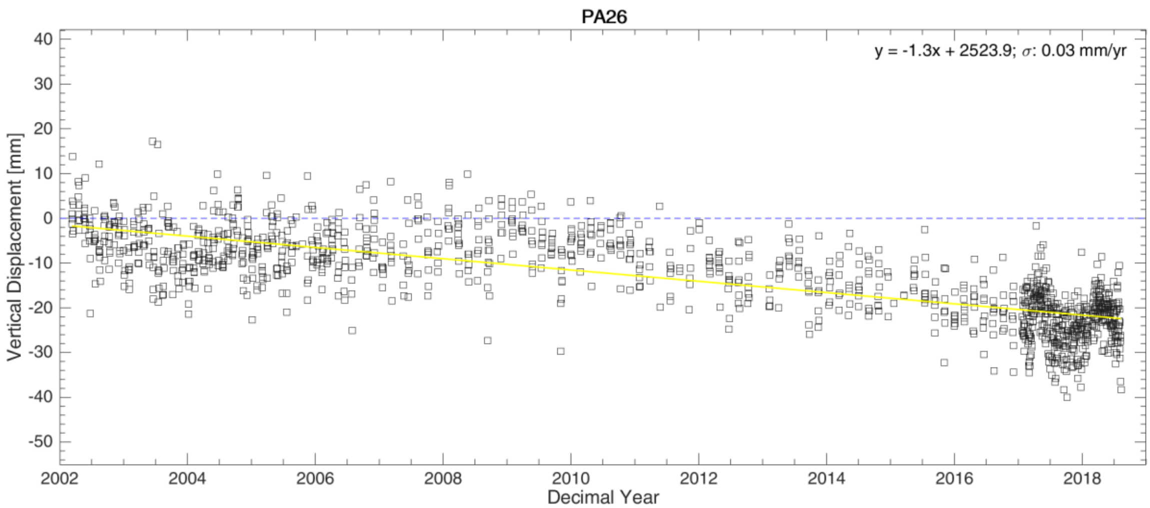
PA26
y = -1.3x + 2523.9; σ: 0.03 mm/yr
Vertical Displacement [mm]
40
30
20
10
0
-10
-20
-30
-40
-50
2002
2004
2006
2008
2010
2012
2014
2016
2018
Decimal Year

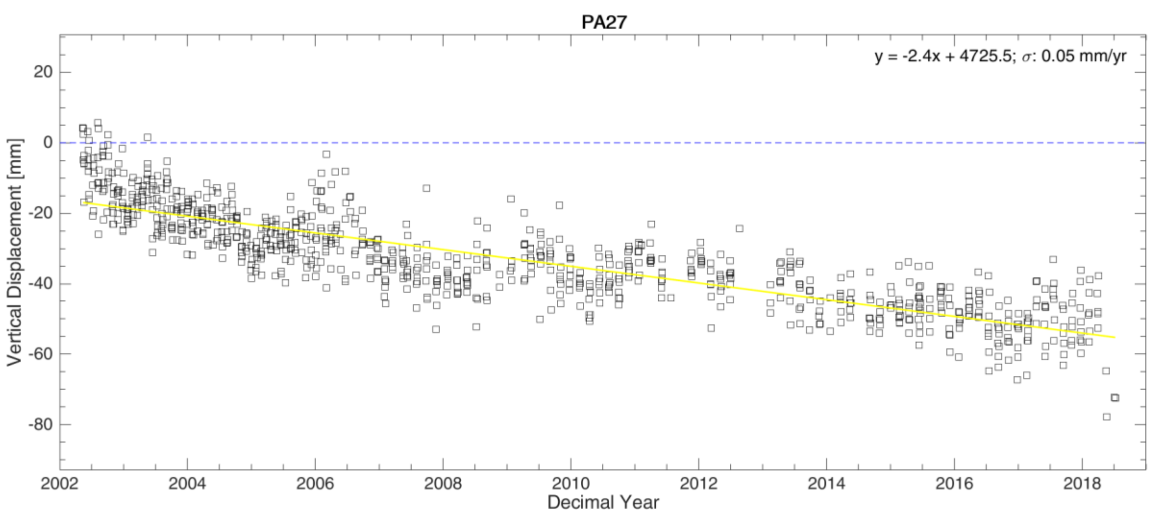
PA27
y = -2.4x + 4725.5; σ: 0.05 mm/yr
Vertical Displacement [mm]
20
0
-20
-40
-60
-80
2002
2004
2006
2008
2010
2012
2014
2016
2018
Decimal Year

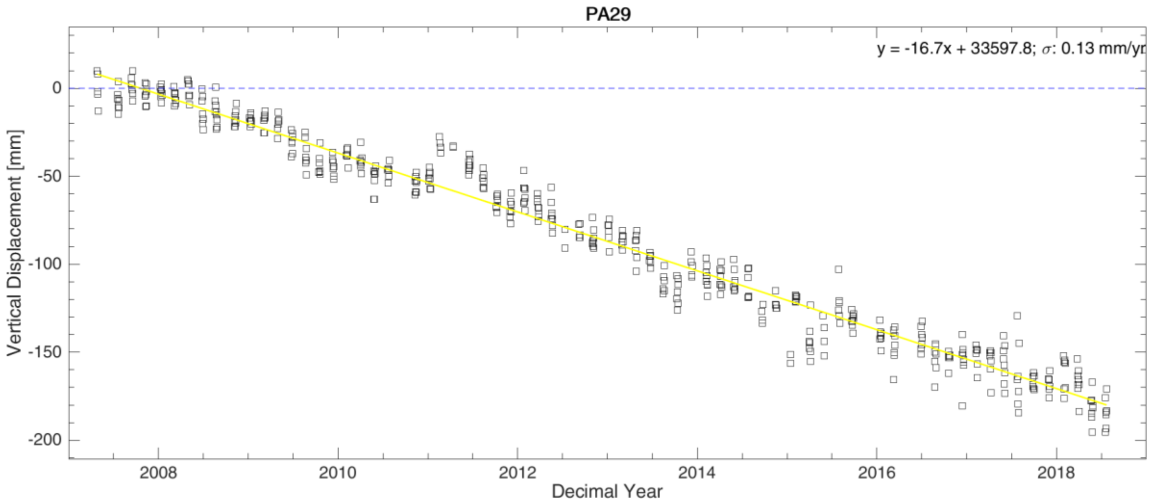
PA29
y = -16.7x + 33597.8; σ: 0.13 mm/yr
Vertical Displacement [mm]
Decimal Year

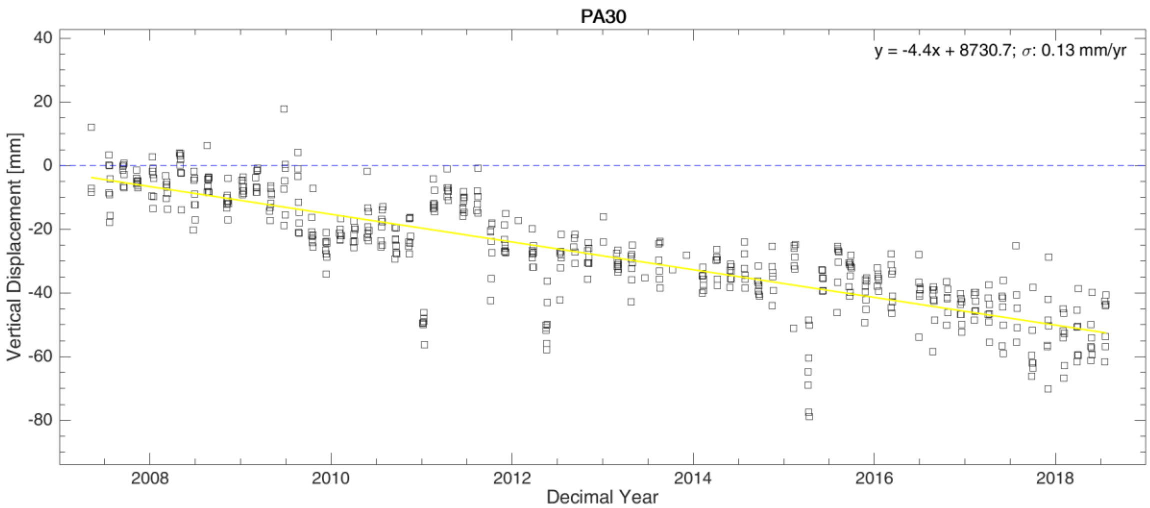
PA30
y = -4.4x + 8730.7; σ: 0.13 mm/yr
Vertical Displacement [mm]
Decimal Year

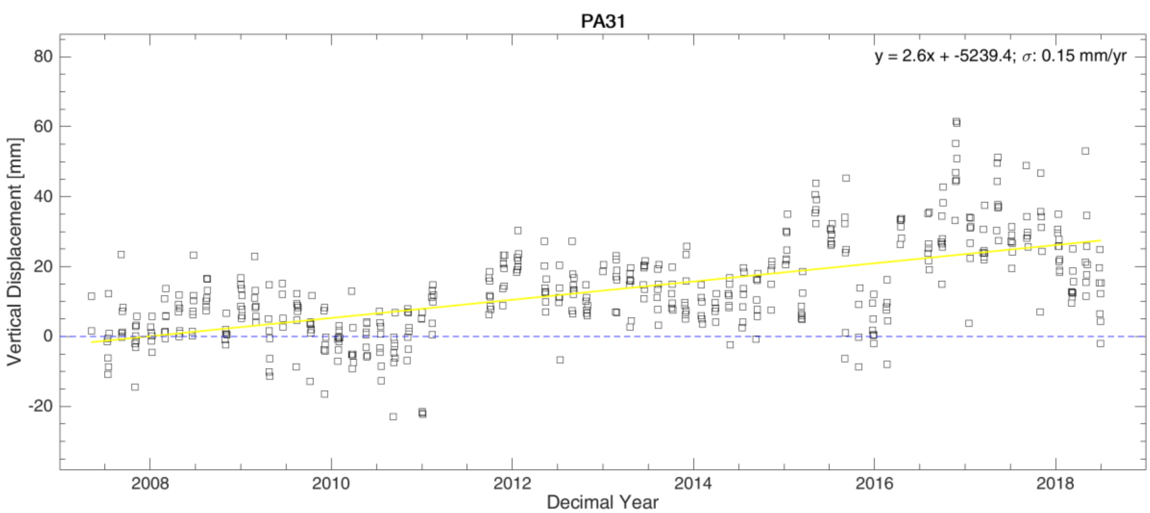
PA31
y = 2.6x + -5239.4; σ: 0.15 mm/yr
Vertical Displacement [mm]
Decimal Year

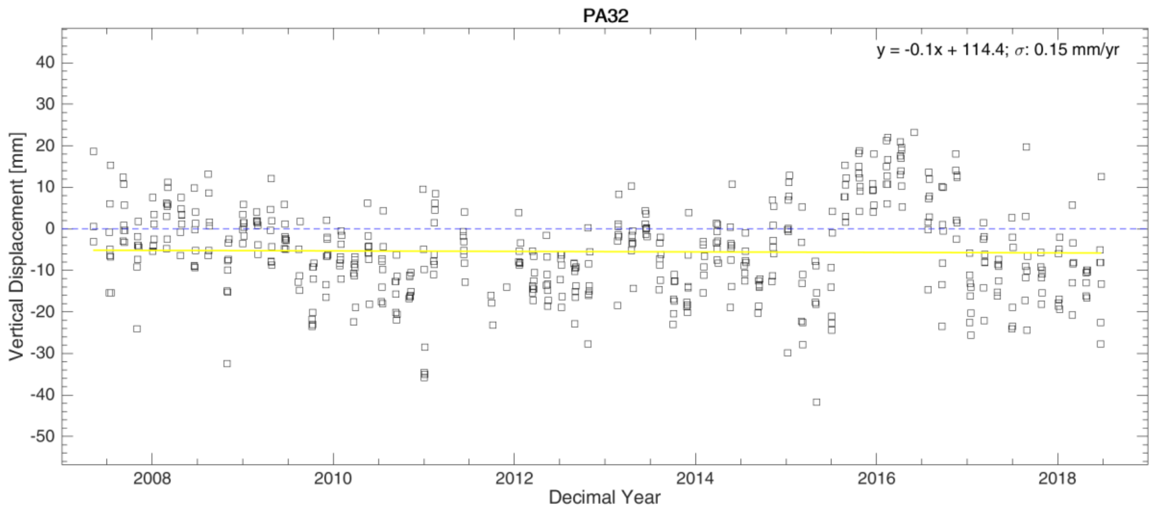
PA32
y = -0.1x + 114.4; σ: 0.15 mm/yr
Vertical Displacement [mm]
Decimal Year

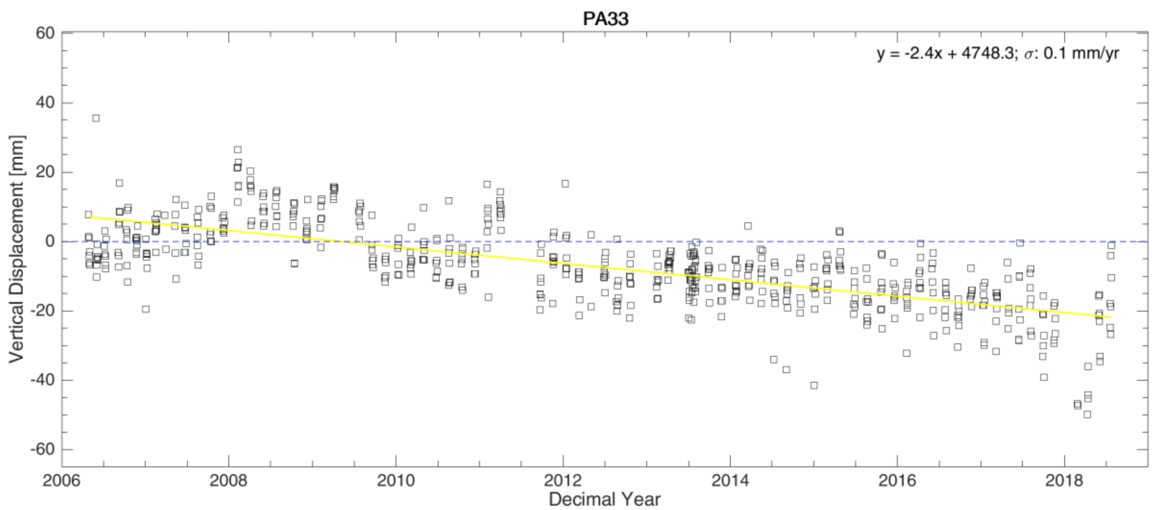
PA33
y = -2.4x + 4748.3; σ: 0.1 mm/yr
Vertical Displacement [mm]
Decimal Year

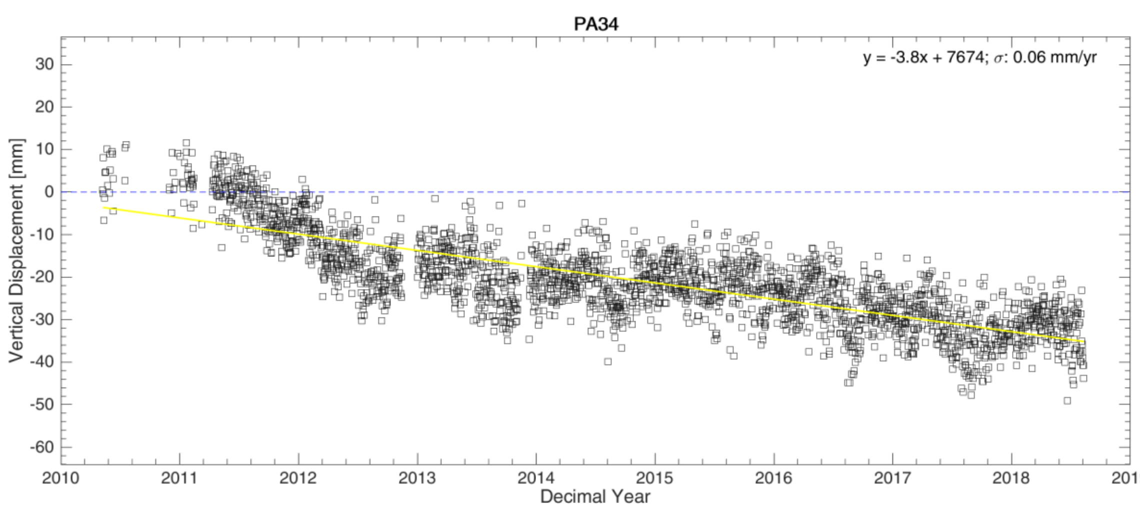
PA34
y = -3.8x + 7674; σ: 0.06 mm/yr
Vertical Displacement [mm]
Decimal Year

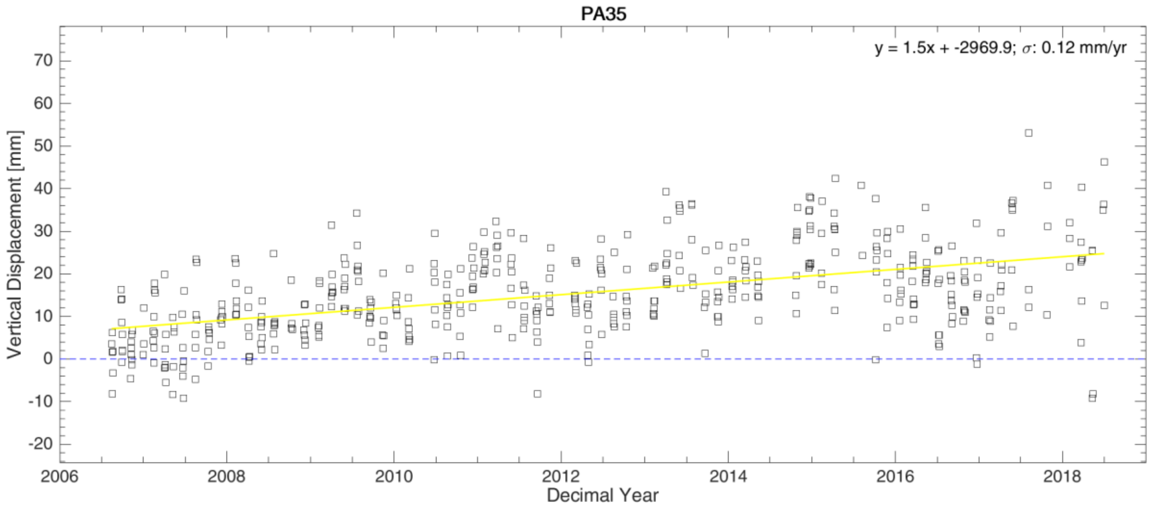
PA35
y = 1.5x + -2969.9; σ: 0.12 mm/yr
Vertical Displacement [mm]
Decimal Year

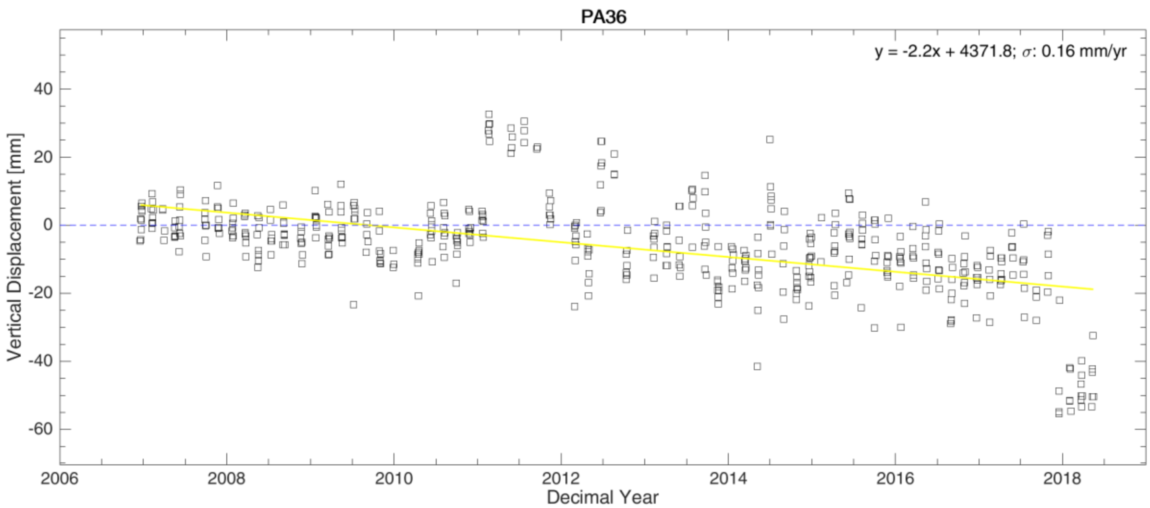
PA36
y = -2.2x + 4371.8; σ: 0.16 mm/yr
Vertical Displacement [mm]
Decimal Year

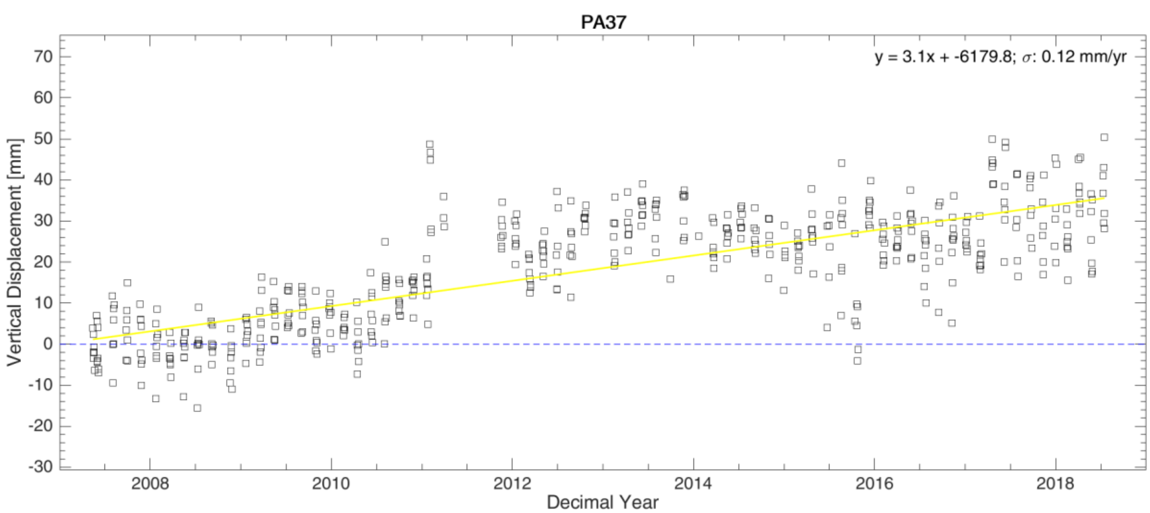
PA37
y = 3.1x + -6179.8; σ: 0.12 mm/yr
Vertical Displacement [mm]
Decimal Year

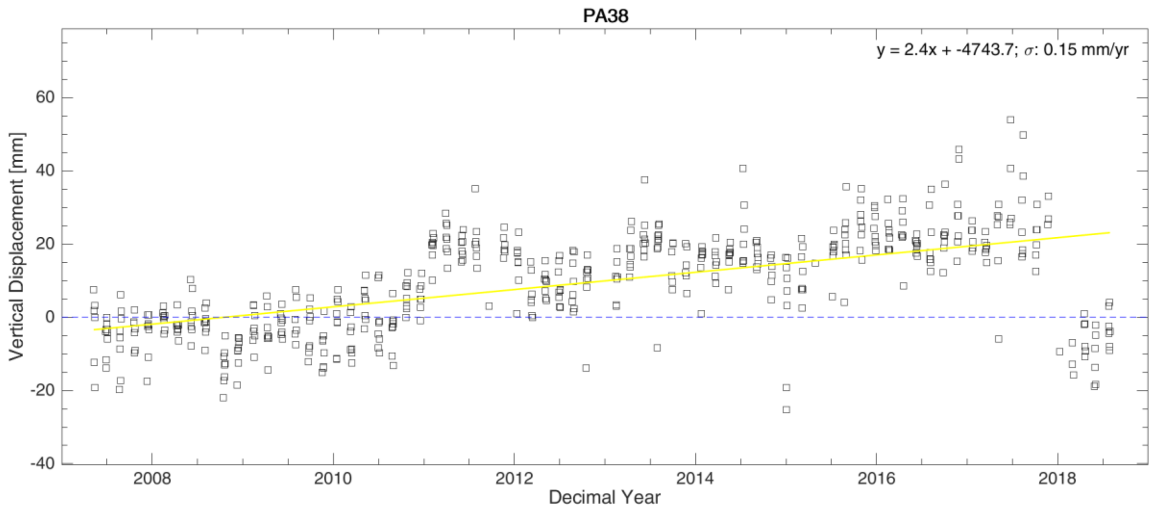
PA38
y = 2.4x + -4743.7; σ: 0.15 mm/yr
Vertical Displacement [mm]
60
40
20
0
-20
-40
2008
2010
2012
2014
2016
2018
Decimal Year

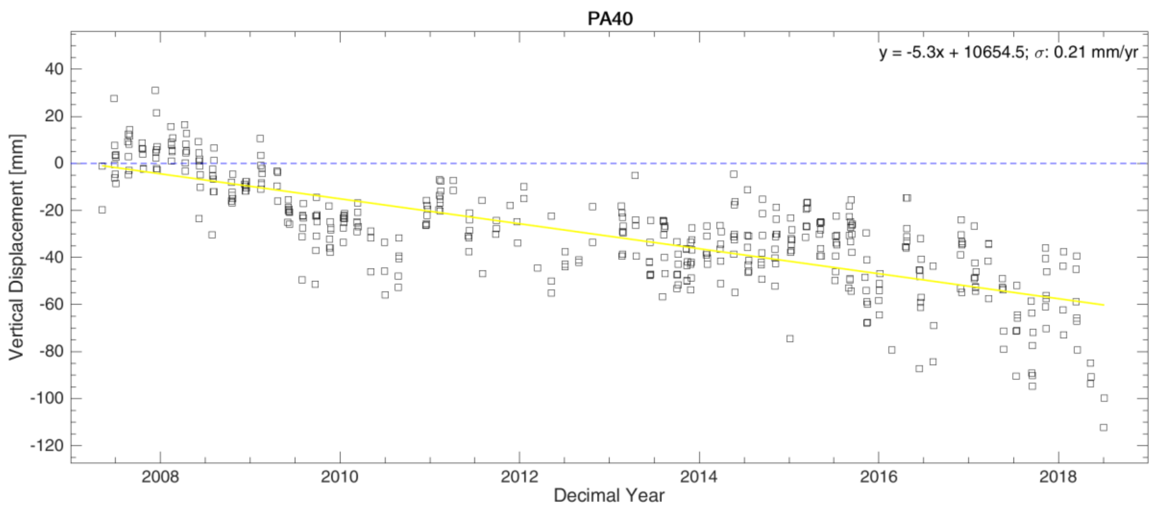
PA40
y = -5.3x + 10654.5; σ: 0.21 mm/yr
Vertical Displacement [mm]
40
20
0
-20
-40
-60
-80
-100
-120
2008
2010
2012
2014
2016
2018
Decimal Year

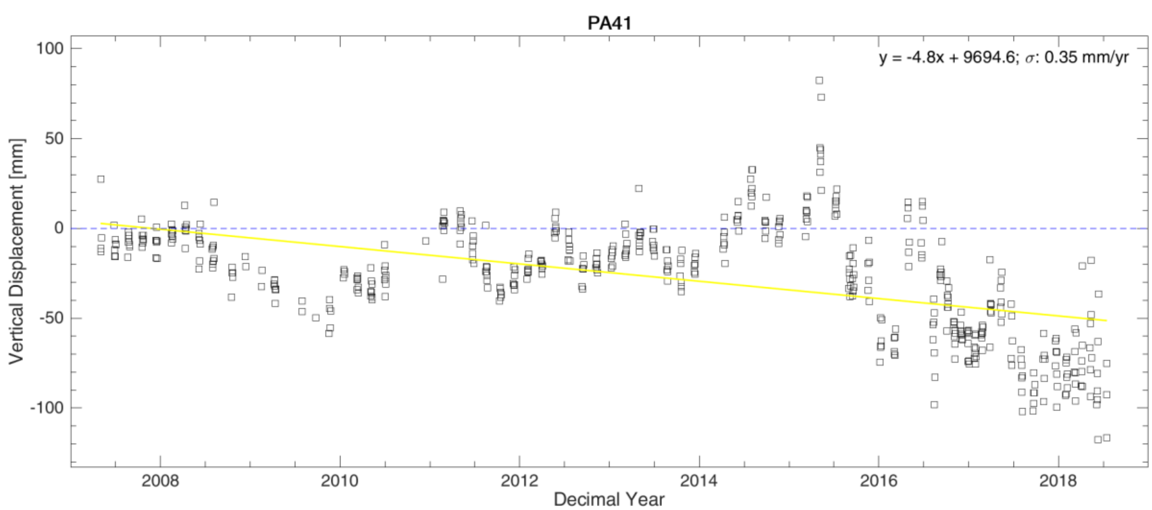
PA41
y = -4.8x + 9694.6; σ: 0.35 mm/yr
Vertical Displacement [mm]
100
50
0
-50
-100
2008
2010
2012
2014
2016
2018
Decimal Year

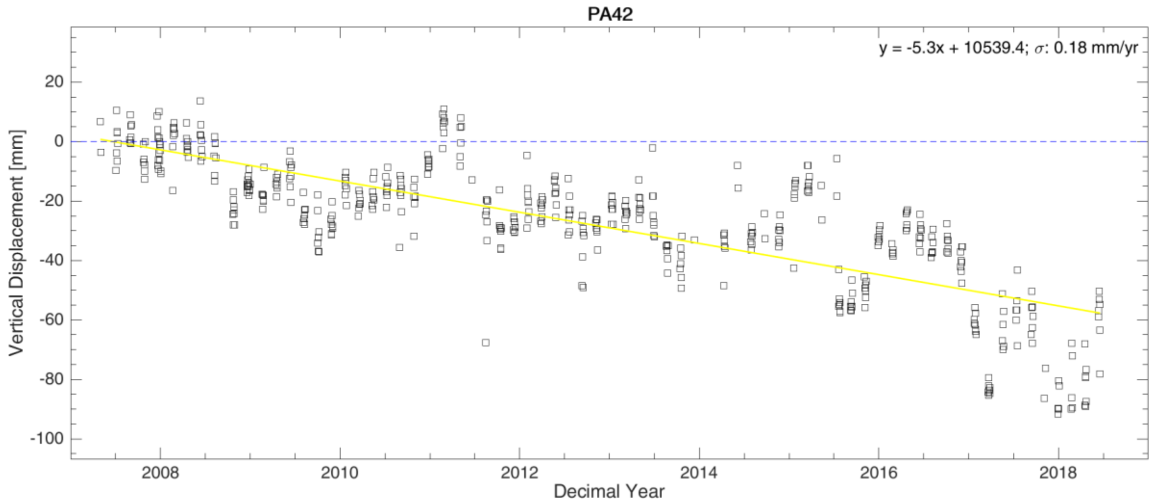
PA42
y = -5.3x + 10539.4; σ: 0.18 mm/yr
Vertical Displacement [mm]
20
0
-20
-40
-60
-80
-100
2008
2010
2012
2014
2016
2018
Decimal Year

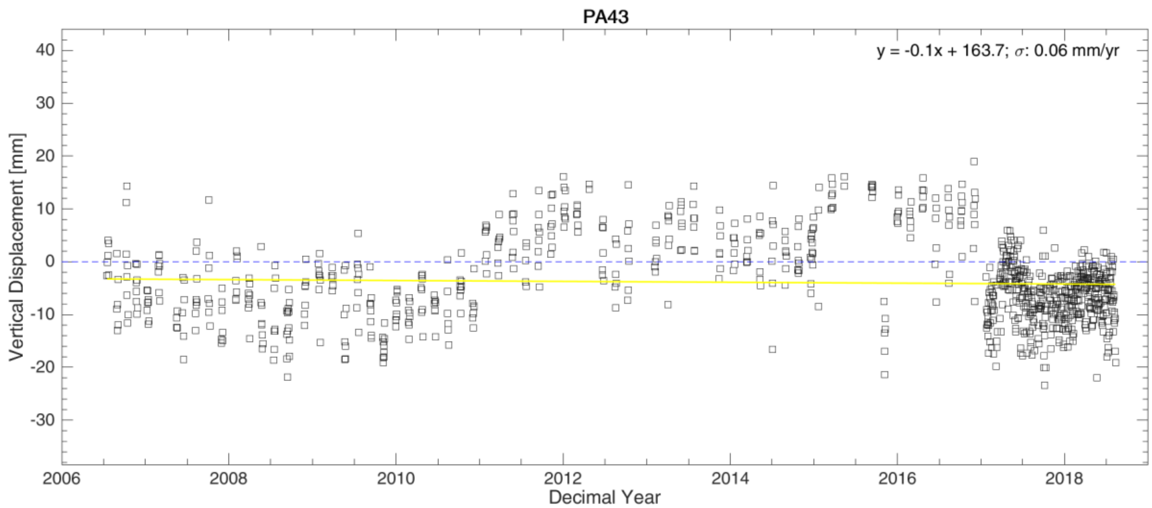
PA43
y = -0.1x + 163.7; σ: 0.06 mm/yr
Vertical Displacement [mm]
40
30
20
10
0
-10
-20
-30
2006
2008
2010
2012
2014
2016
2018
Decimal Year

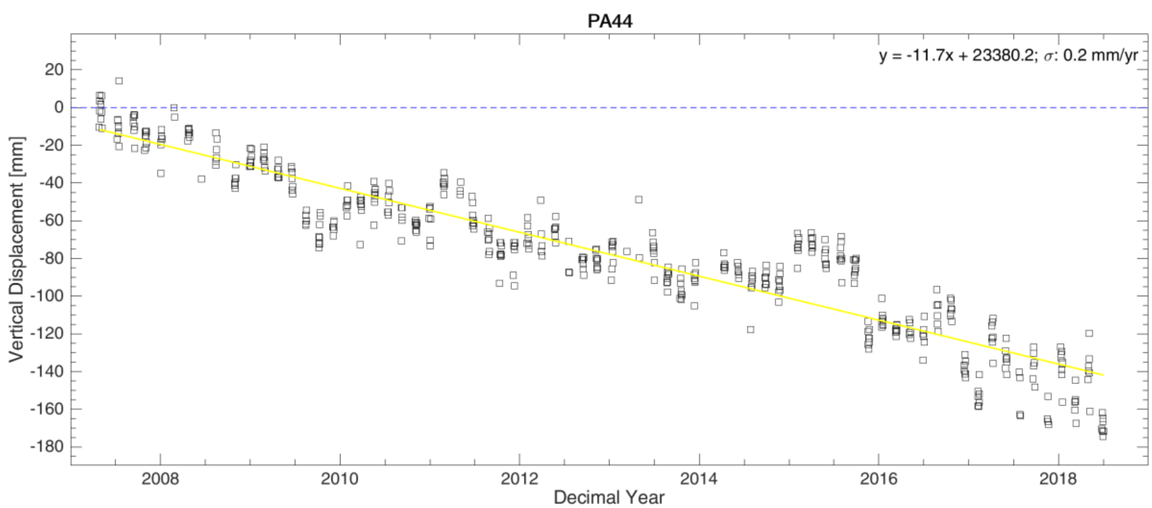
PA44
y = -11.7x + 23380.2; σ: 0.2 mm/yr
Vertical Displacement [mm]
20
0
-20
-40
-60
-80
-100
-120
-140
-160
-180
2008
2010
2012
2014
2016
2018
Decimal Year

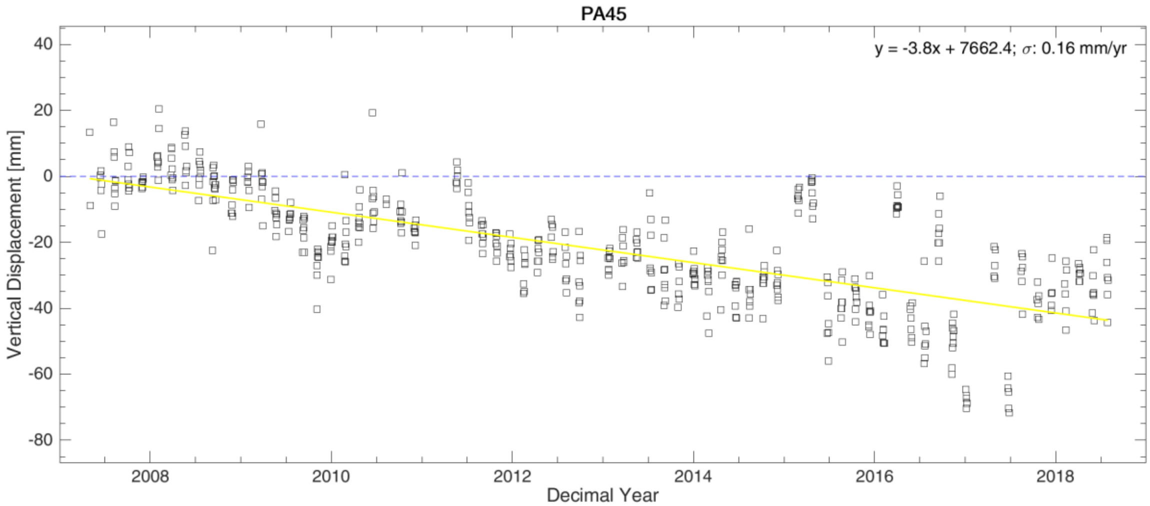
PA45
y = -3.8x + 7662.4; σ: 0.16 mm/yr
Vertical Displacement [mm]
Decimal Year

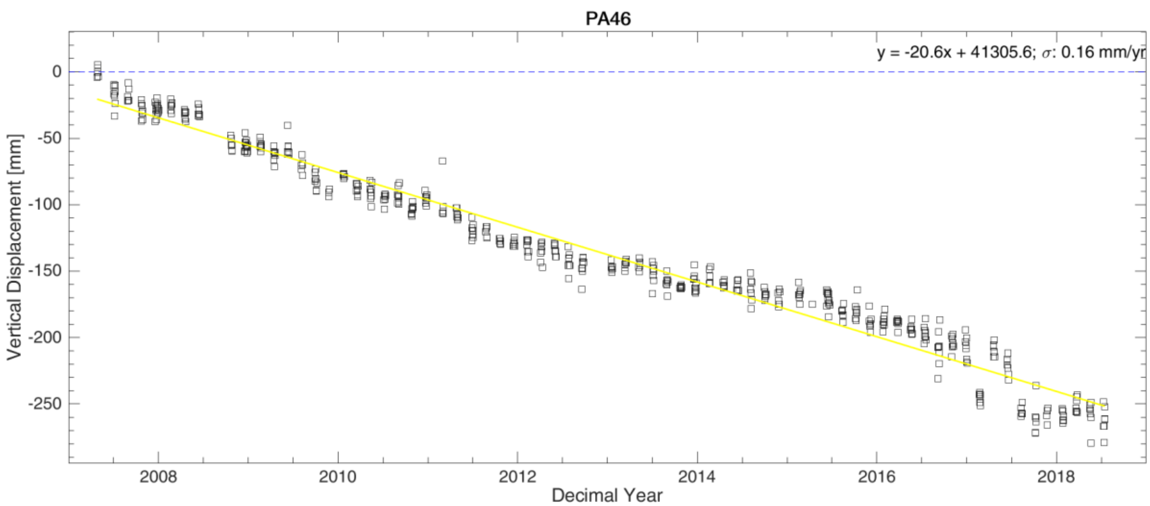
PA46
y = -20.6x + 41305.6; σ: 0.16 mm/yr
Vertical Displacement [mm]
Decimal Year

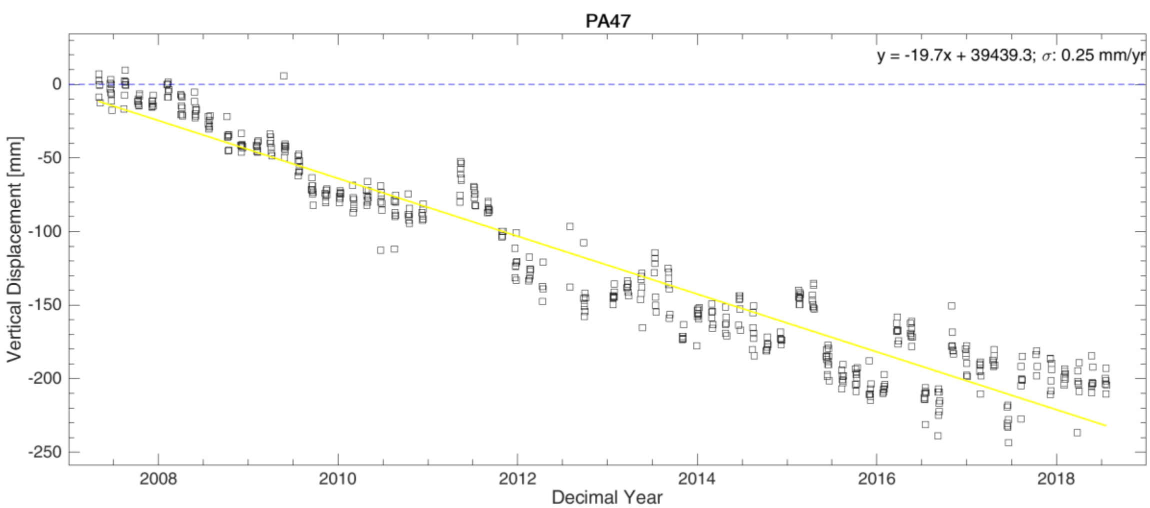
PA47
y = -19.7x + 39439.3; σ: 0.25 mm/yr
Vertical Displacement [mm]
Decimal Year

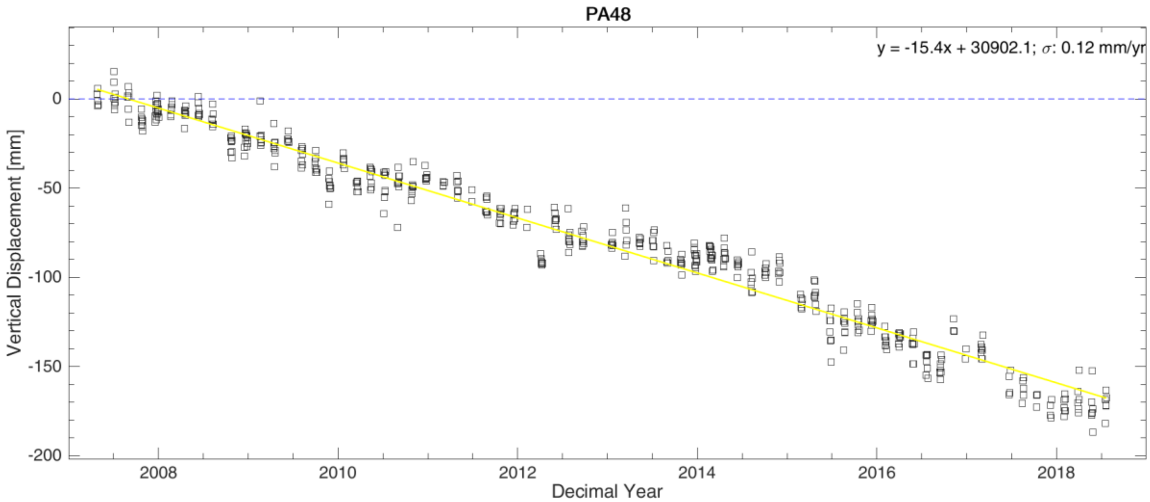
PA48
y = -15.4x + 30902.1; σ: 0.12 mm/yr
Vertical Displacement [mm]
0
-50
-100
-150
-200
2008
2010
2012
2014
2016
2018
Decimal Year

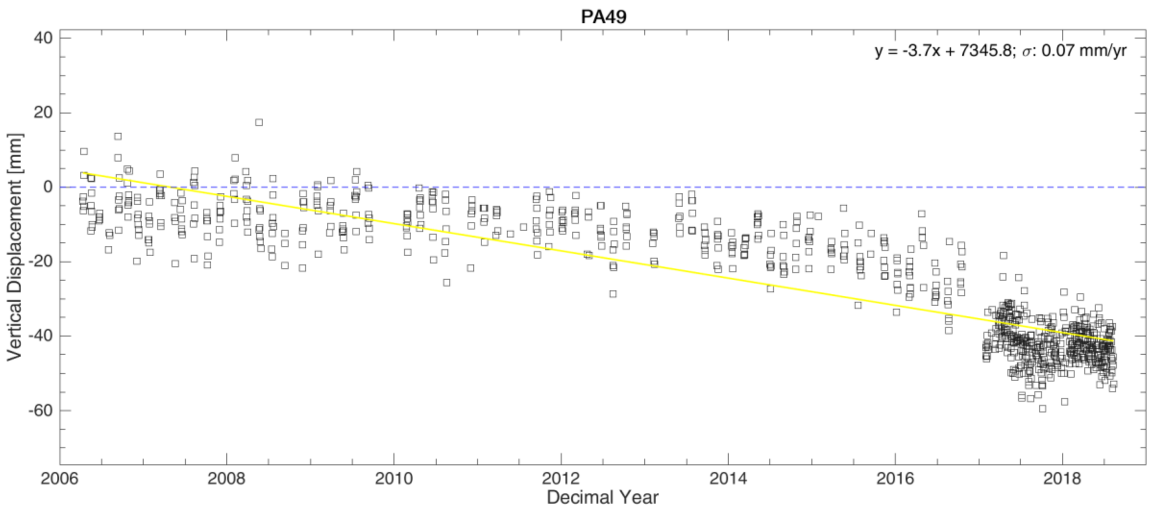
PA49
y = -3.7x + 7345.8; σ: 0.07 mm/yr
Vertical Displacement [mm]
40
20
0
-20
-40
-60
2006
2008
2010
2012
2014
2016
2018
Decimal Year

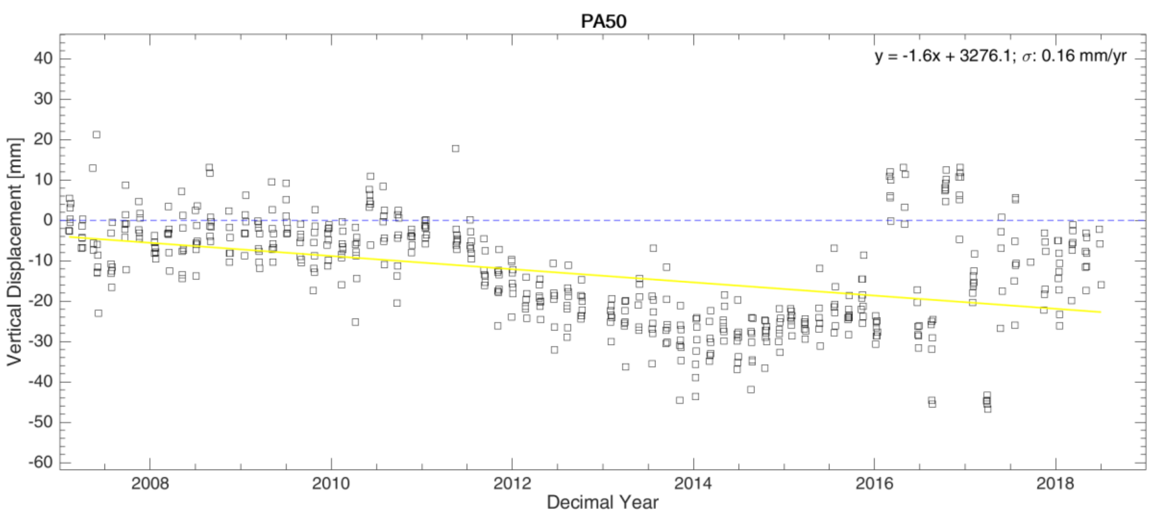
PA50
y = -1.6x + 3276.1; σ: 0.16 mm/yr
Vertical Displacement [mm]
40
30
20
10
0
-10
-20
-30
-40
-50
-60
2008
2010
2012
2014
2016
2018
Decimal Year

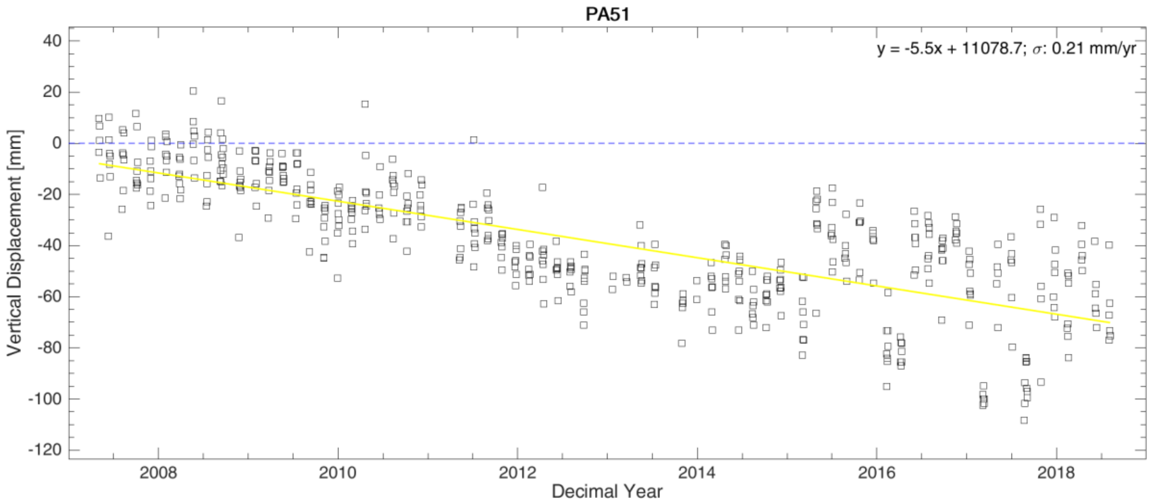
PA51
y = -5.5x + 11078.7; σ: 0.21 mm/yr
Vertical Displacement [mm]
Decimal Year

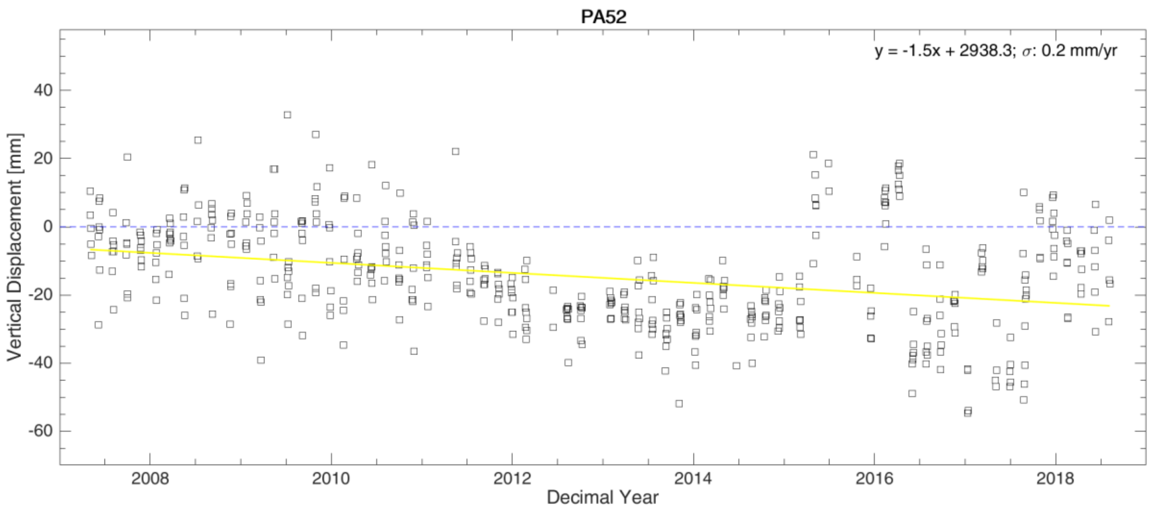
PA52
y = -1.5x + 2938.3; σ: 0.2 mm/yr
Vertical Displacement [mm]
Decimal Year

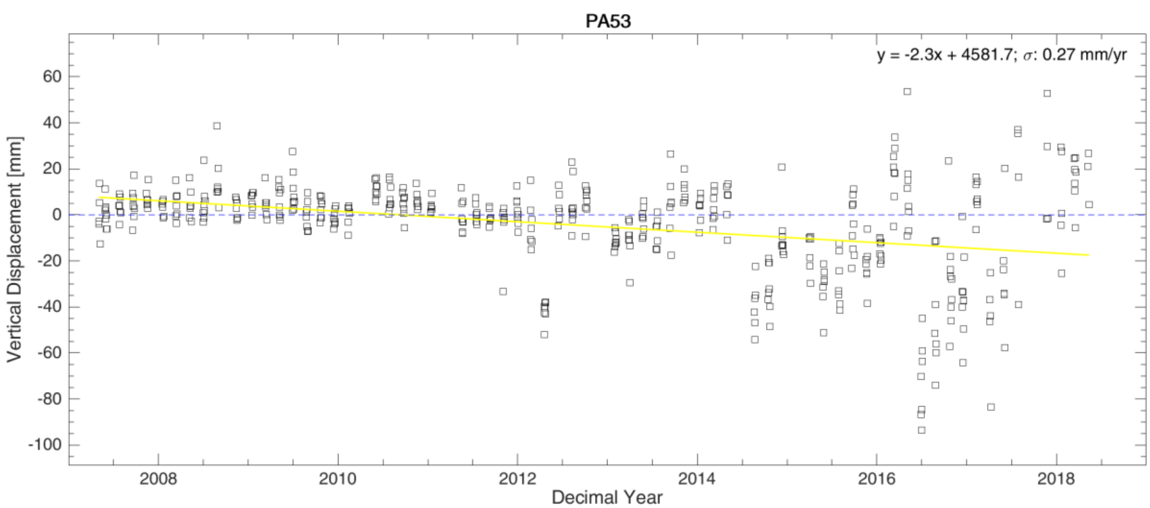
PA53
y = -2.3x + 4581.7; σ: 0.27 mm/yr
Vertical Displacement [mm]
Decimal Year

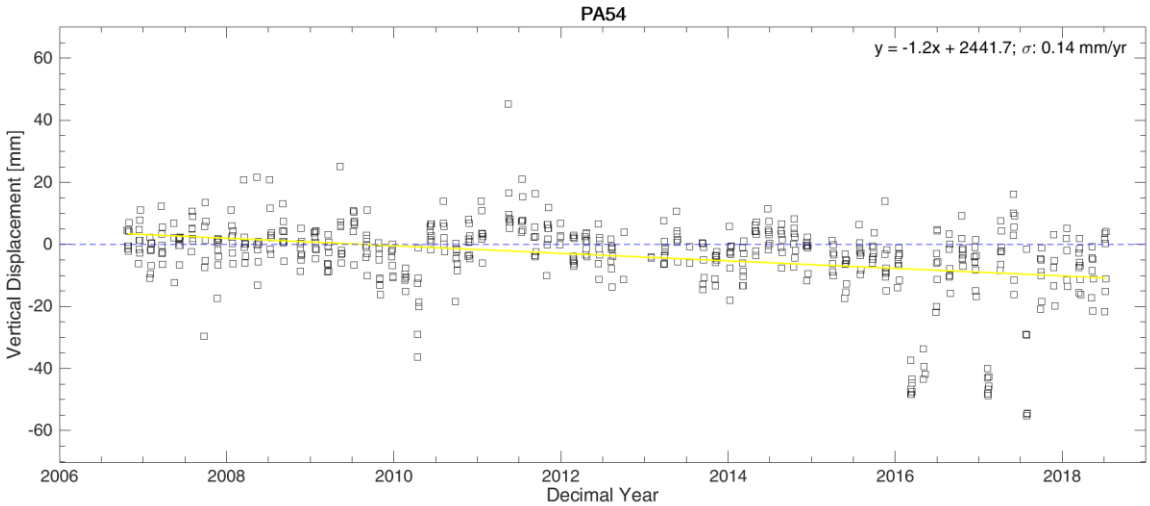
PA54
y = -1.2x + 2441.7; σ: 0.14 mm/yr
Vertical Displacement [mm]
60
40
20
0
-20
-40
-60
2006
2008
2010
2012
2014
2016
2018
Decimal Year

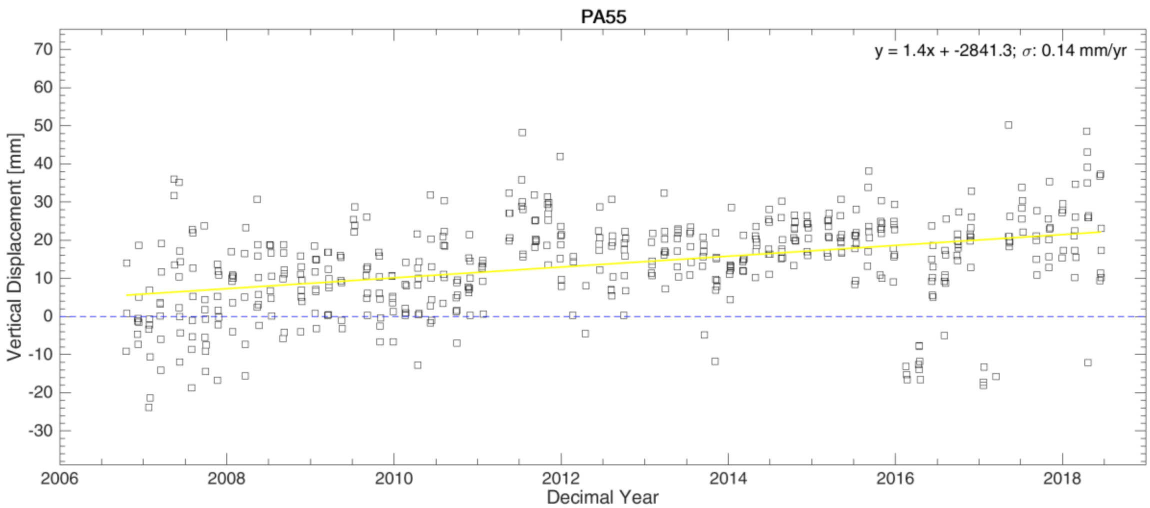
PA55
y = 1.4x + -2841.3; σ: 0.14 mm/yr
Vertical Displacement [mm]
70
60
50
40
30
20
10
0
-10
-20
-30
2006
2008
2010
2012
2014
2016
2018
Decimal Year

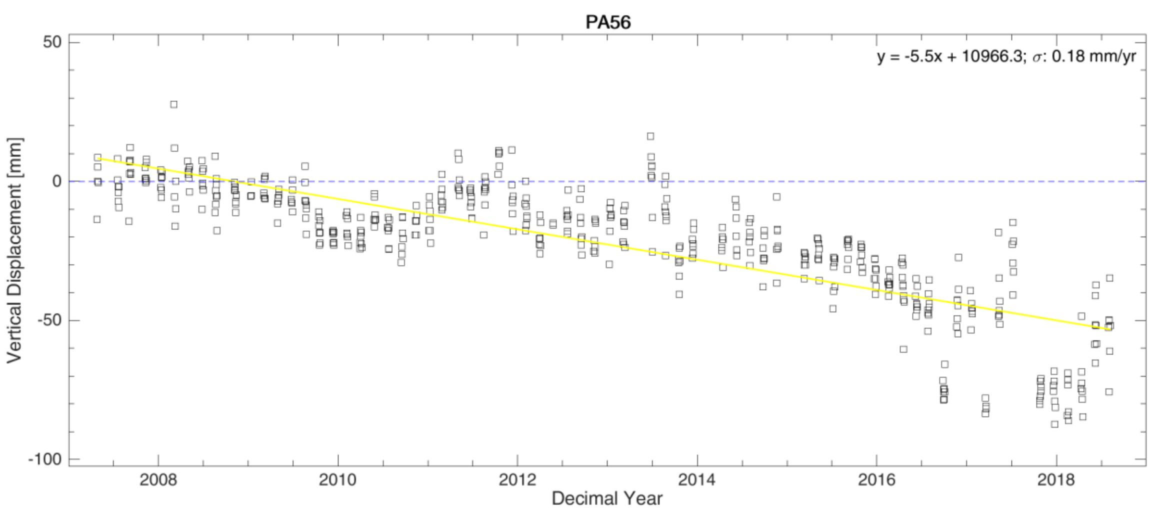
PA56
y = -5.5x + 10966.3; σ: 0.18 mm/yr
Vertical Displacement [mm]
50
0
-50
-100
2008
2010
2012
2014
2016
2018
Decimal Year

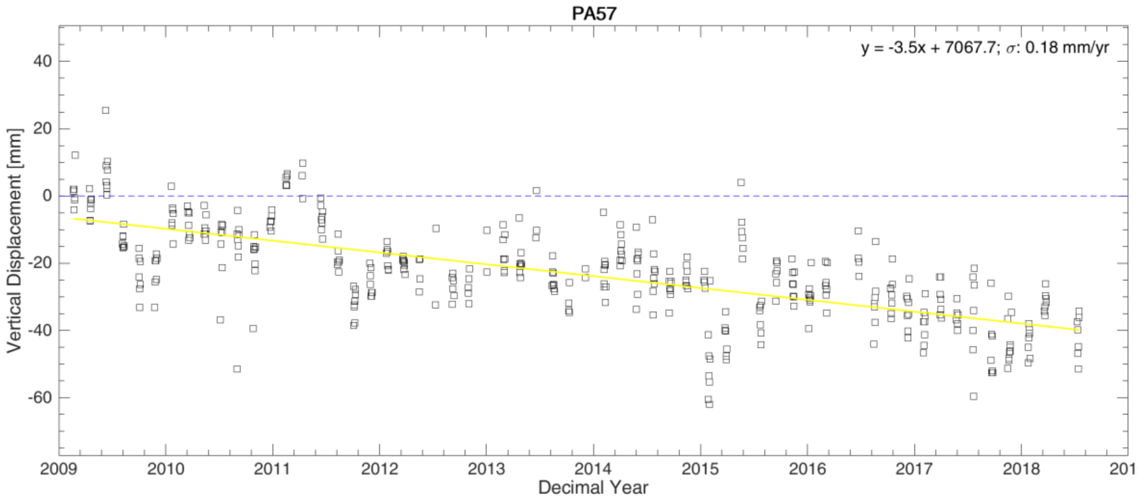
PA57
y = -3.5x + 7067.7; σ: 0.18 mm/yr
Vertical Displacement [mm]
Decimal Year

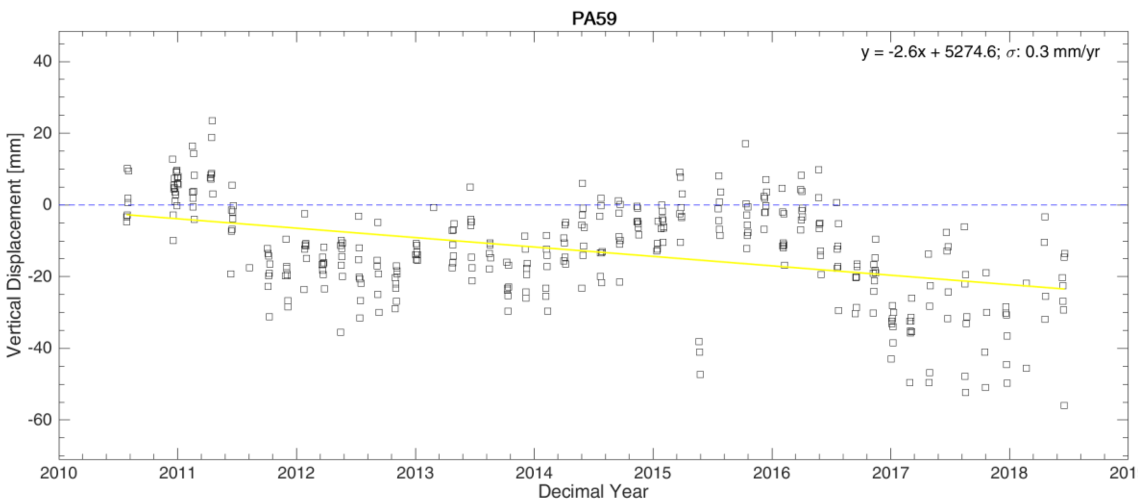
PA59
y = -2.6x + 5274.6; σ: 0.3 mm/yr
Vertical Displacement [mm]
Decimal Year

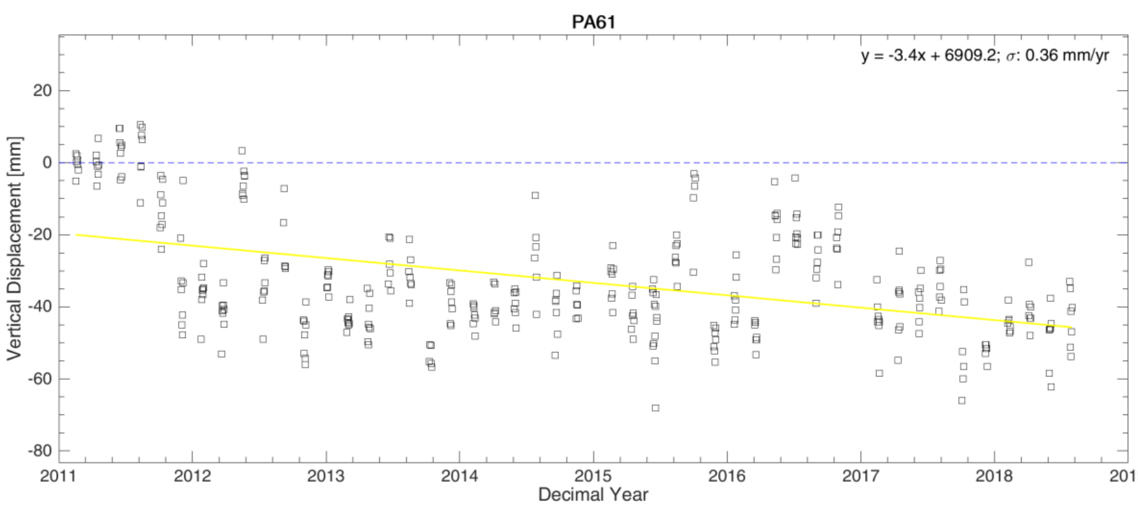
PA61
y = -3.4x + 6909.2; σ: 0.36 mm/yr
Vertical Displacement [mm]
Decimal Year

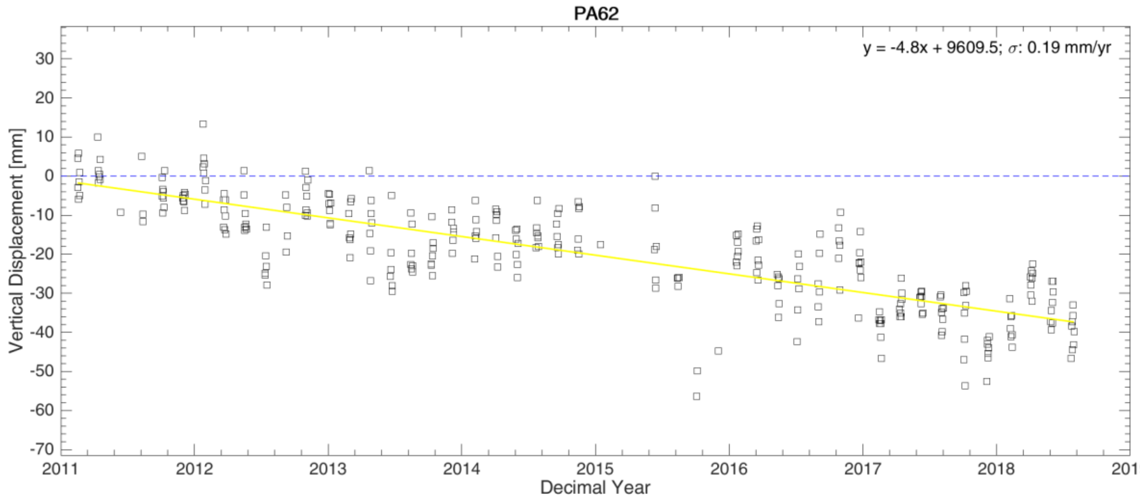
PA62
y = -4.8x + 9609.5; σ: 0.19 mm/yr
Vertical Displacement [mm]
Decimal Year

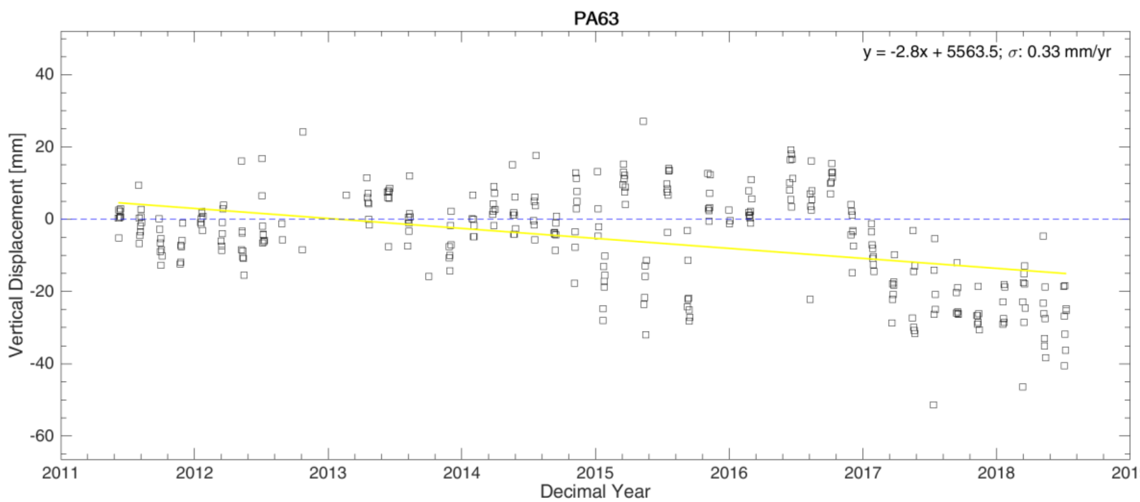
PA63
y = -2.8x + 5563.5; σ: 0.33 mm/yr
Vertical Displacement [mm]
Decimal Year

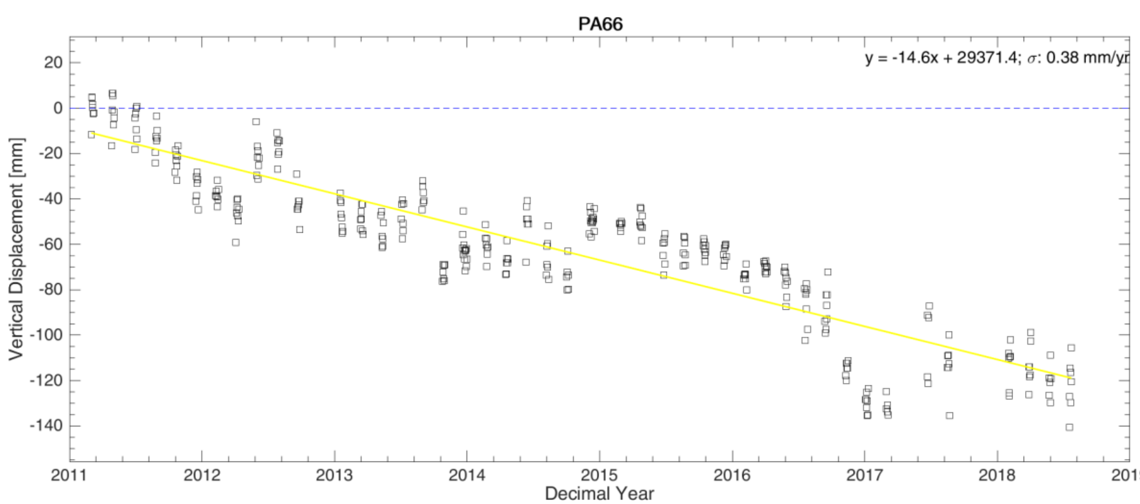
PA66
y = -14.6x + 29371.4; σ: 0.38 mm/yr
Vertical Displacement [mm]
Decimal Year

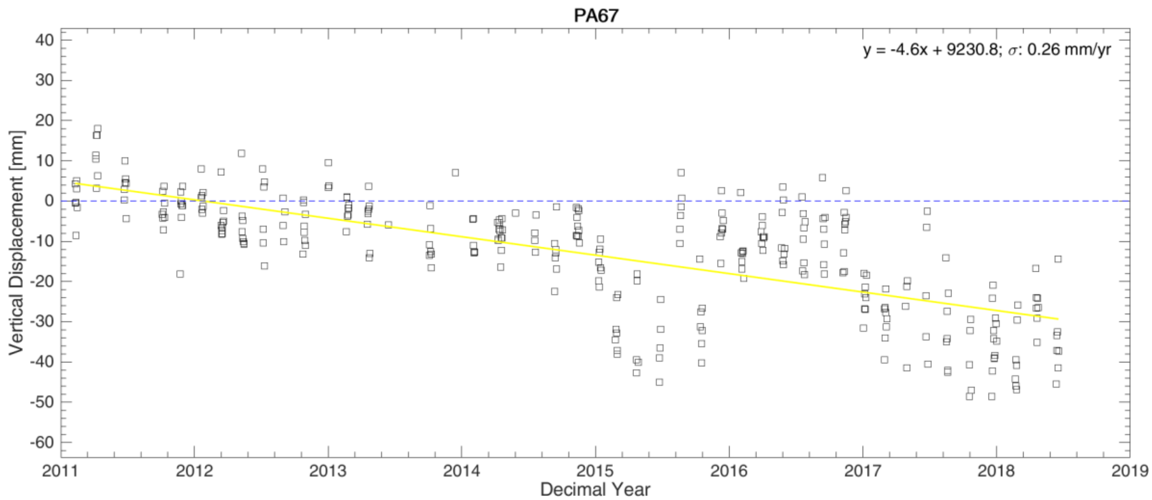
PA67
y = -4.6x + 9230.8; σ: 0.26 mm/yr
Vertical Displacement [mm]
Decimal Year

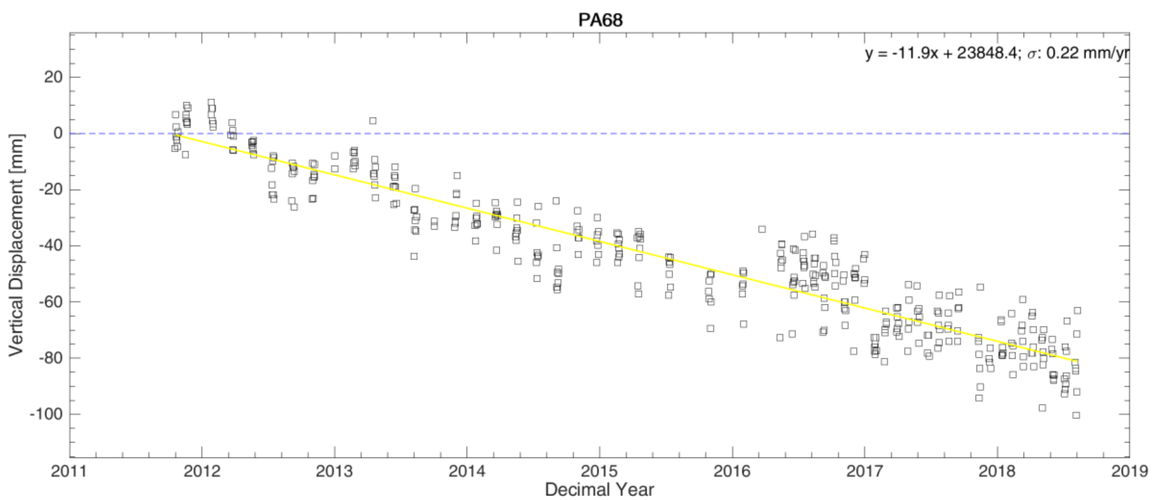
PA68
y = -11.9x + 23848.4; σ: 0.22 mm/yr
Vertical Displacement [mm]
Decimal Year

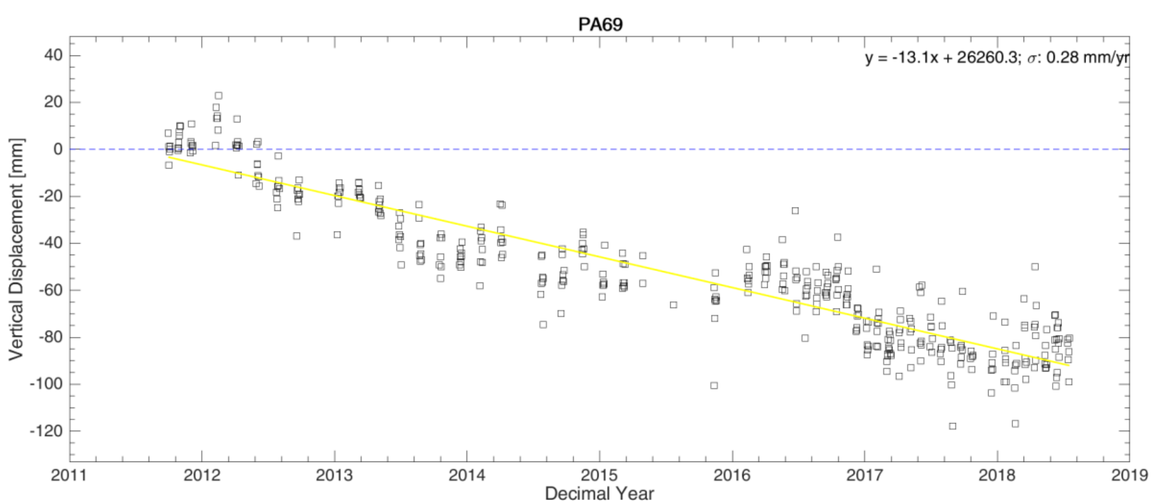
PA69
y = -13.1x + 26260.3; σ: 0.28 mm/yr
Vertical Displacement [mm]
Decimal Year

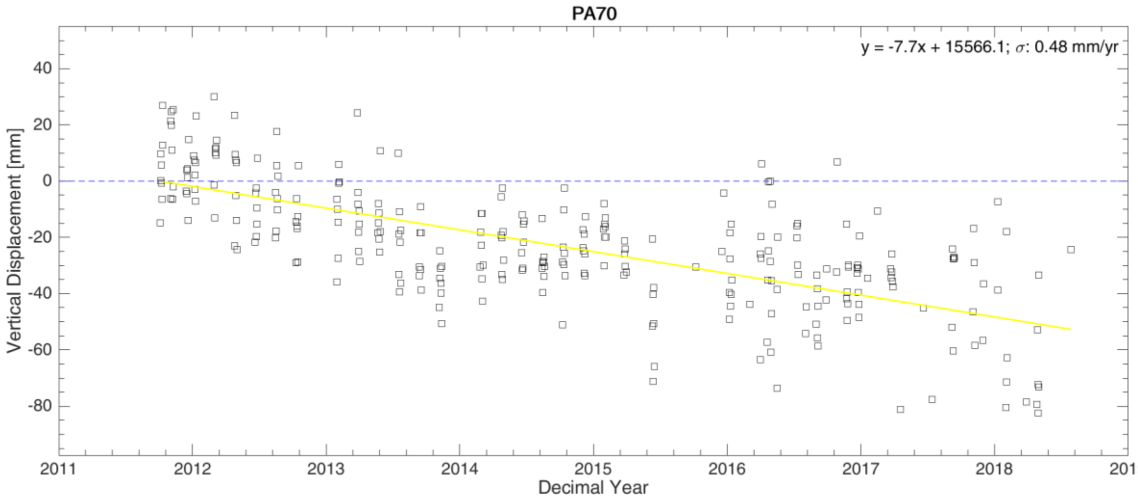
PA70
y = -7.7x + 15566.1; σ: 0.48 mm/yr
Vertical Displacement [mm]
Decimal Year

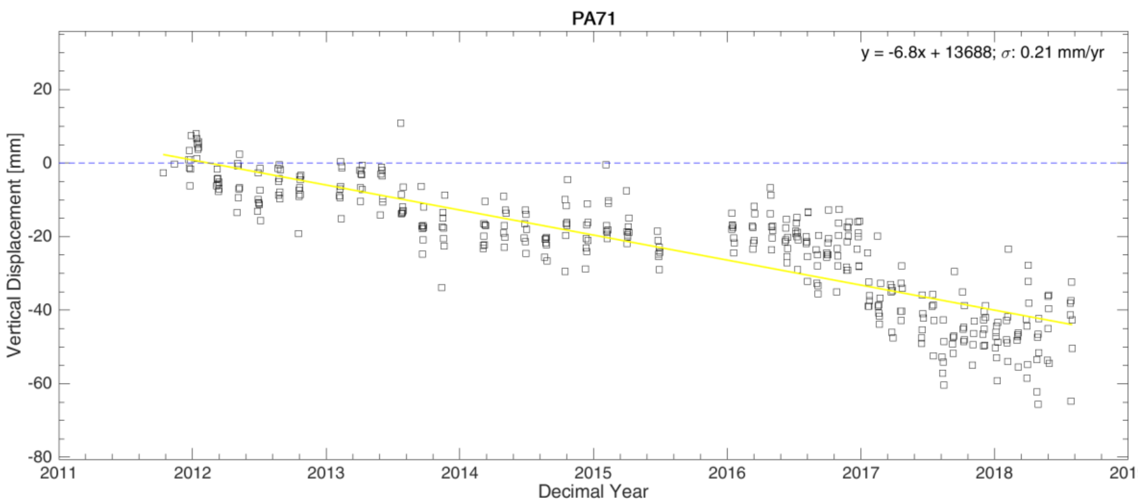
PA71
y = -6.8x + 13688; σ: 0.21 mm/yr
Vertical Displacement [mm]
Decimal Year

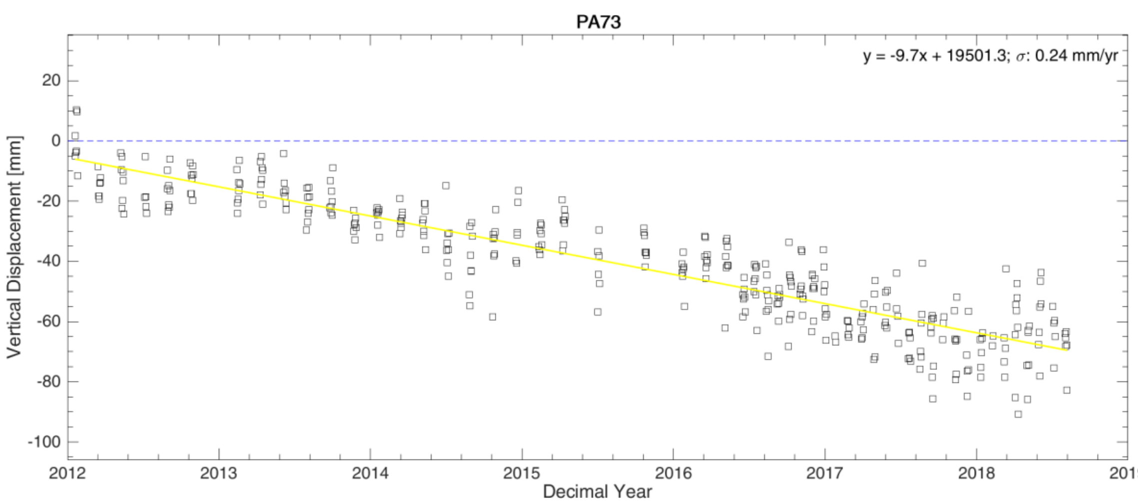
PA73
y = -9.7x + 19501.3; σ: 0.24 mm/yr
Vertical Displacement [mm]
Decimal Year

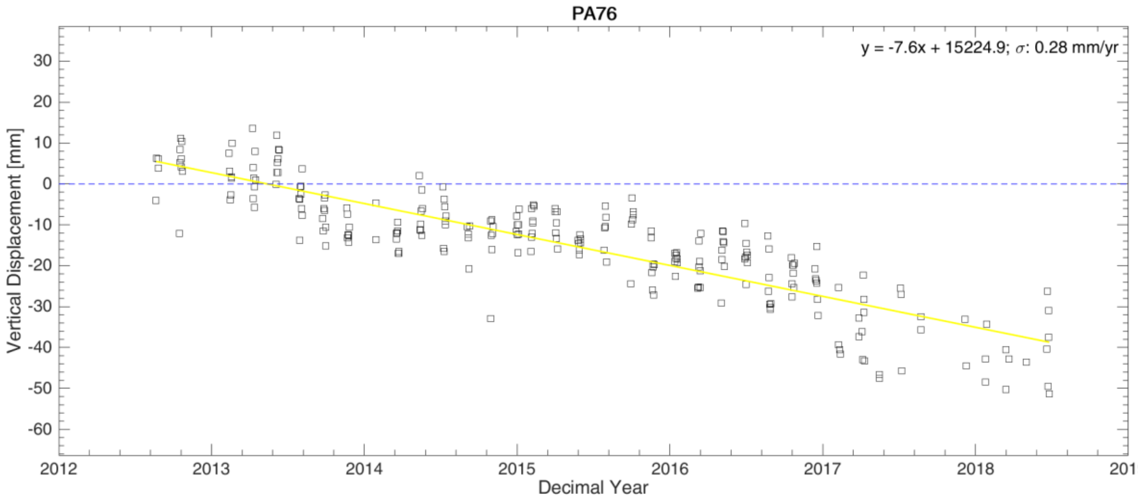
PA76
y = -7.6x + 15224.9; σ: 0.28 mm/yr
Vertical Displacement [mm]
Decimal Year

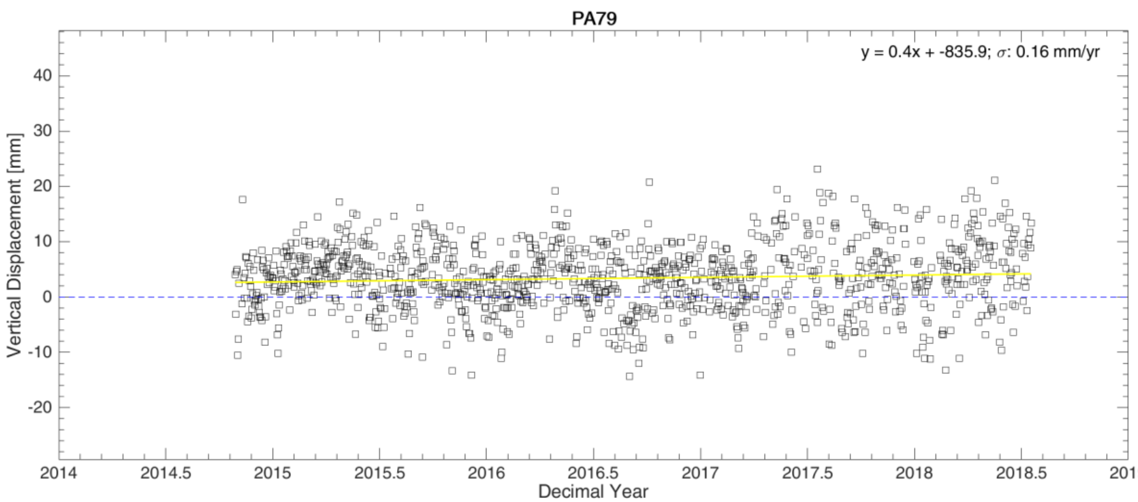
PA79
y = 0.4x + -835.9; σ: 0.16 mm/yr
Vertical Displacement [mm]
Decimal Year

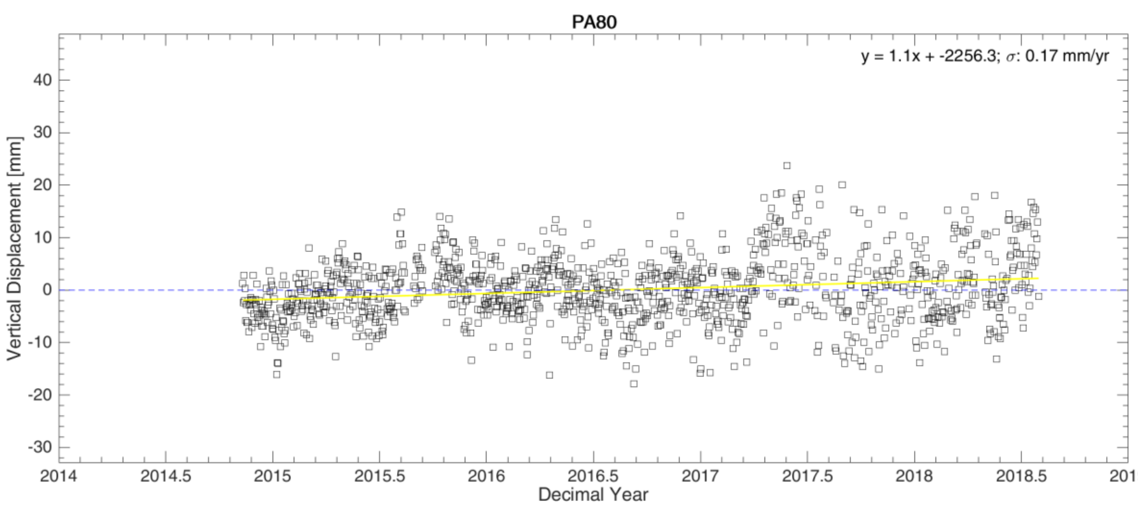
PA80
y = 1.1x + -2256.3; σ: 0.17 mm/yr
Vertical Displacement [mm]
Decimal Year

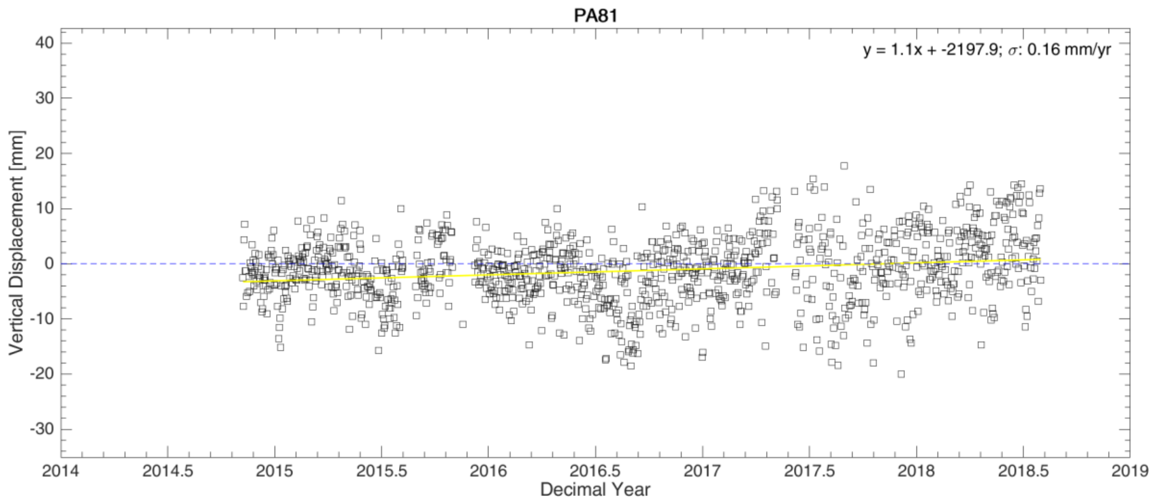
PA81
y = 1.1x + -2197.9; σ: 0.16 mm/yr
Vertical Displacement [mm]
Decimal Year

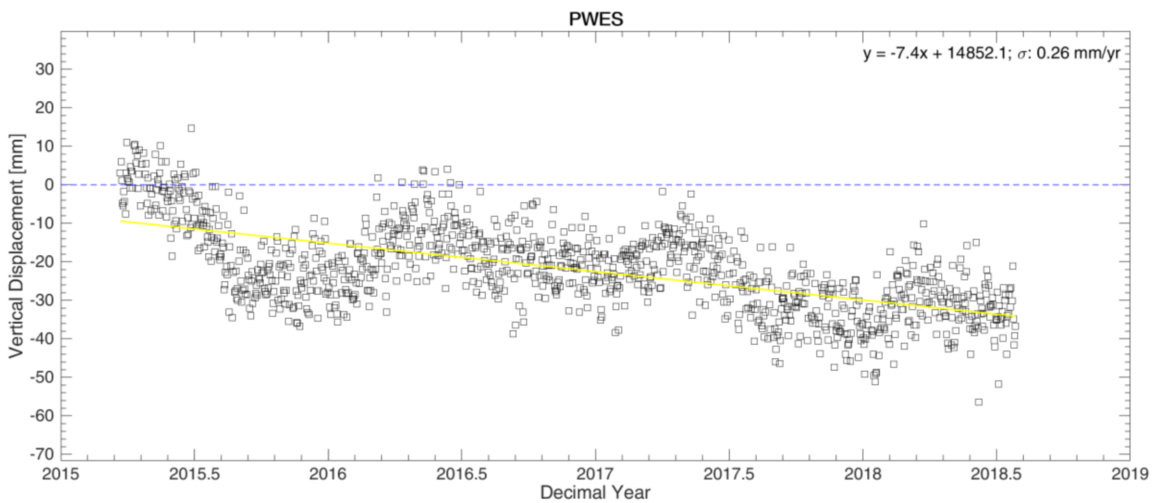
PWES
y = -7.4x + 14852.1; σ: 0.26 mm/yr
Vertical Displacement [mm]
Decimal Year

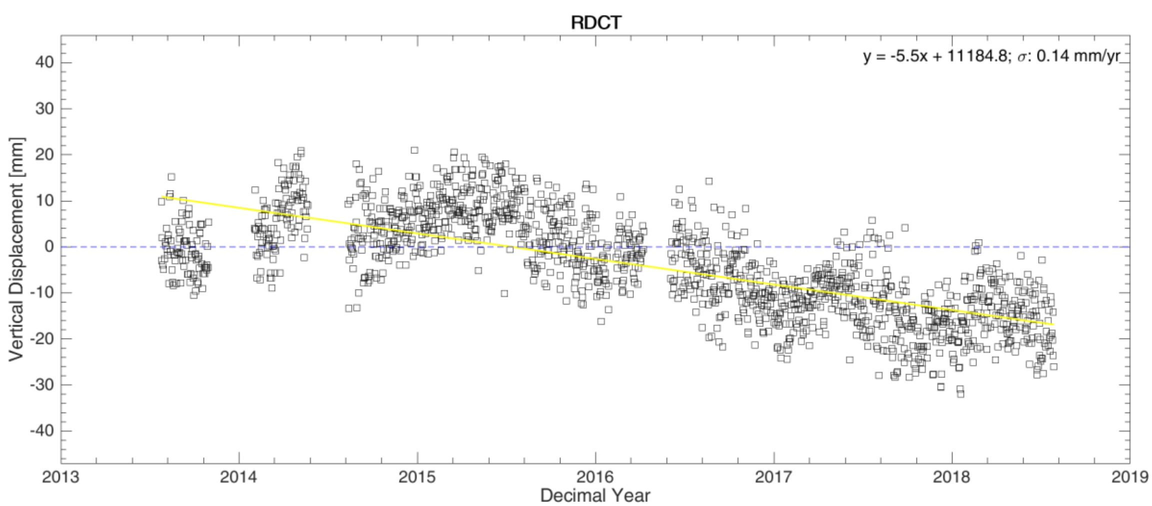
RDCT
y = -5.5x + 11184.8; σ: 0.14 mm/yr
Vertical Displacement [mm]
Decimal Year

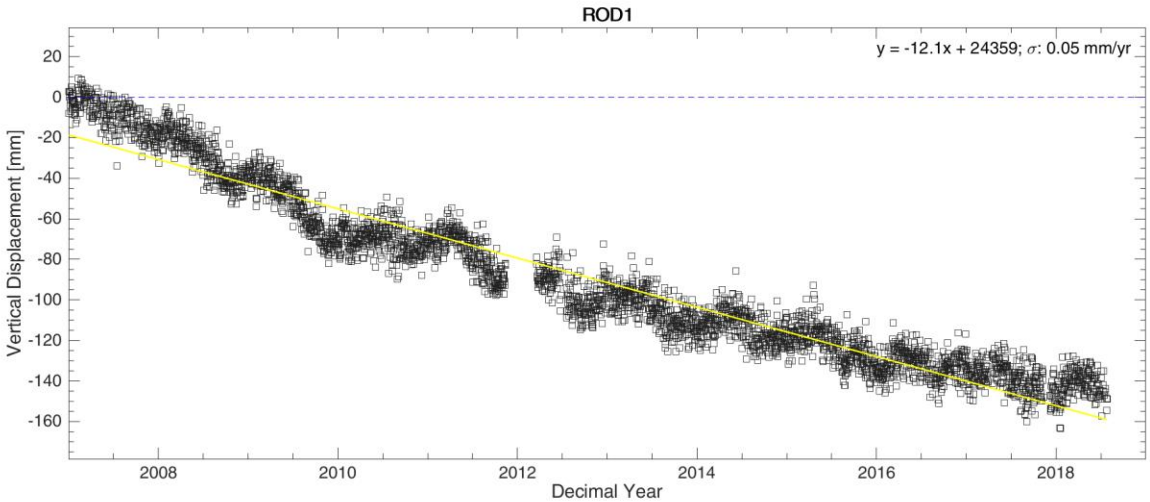
ROD1
y = -12.1x + 24359; σ: 0.05 mm/yr
Vertical Displacement [mm]
Decimal Year

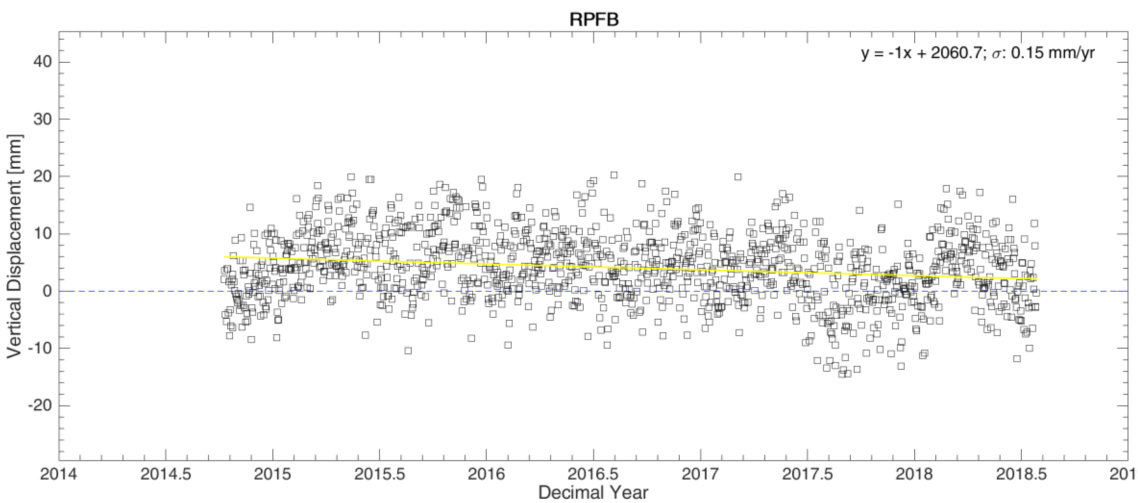
RPFB
y = -1x + 2060.7; σ: 0.15 mm/yr
Vertical Displacement [mm]
Decimal Year

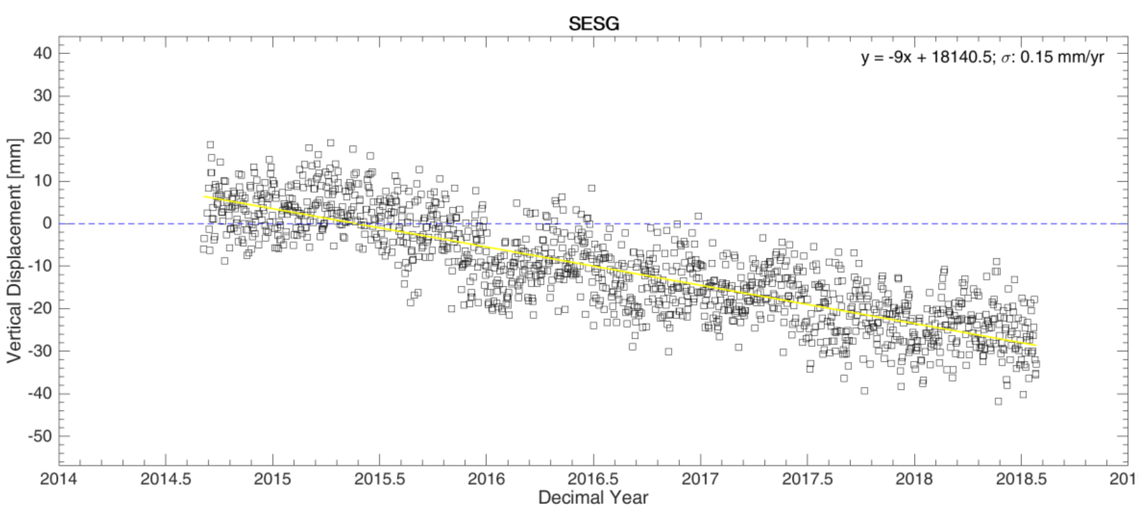
SESG
y = -9x + 18140.5; σ: 0.15 mm/yr
Vertical Displacement [mm]
Decimal Year

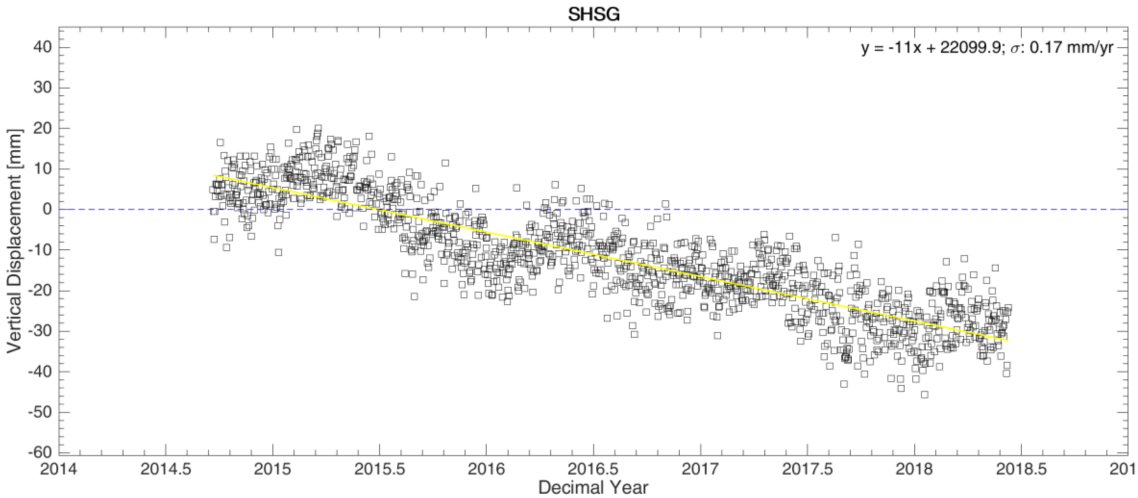
SHSG
y = -11x + 22099.9; σ: 0.17 mm/yr
Vertical Displacement [mm]
Decimal Year

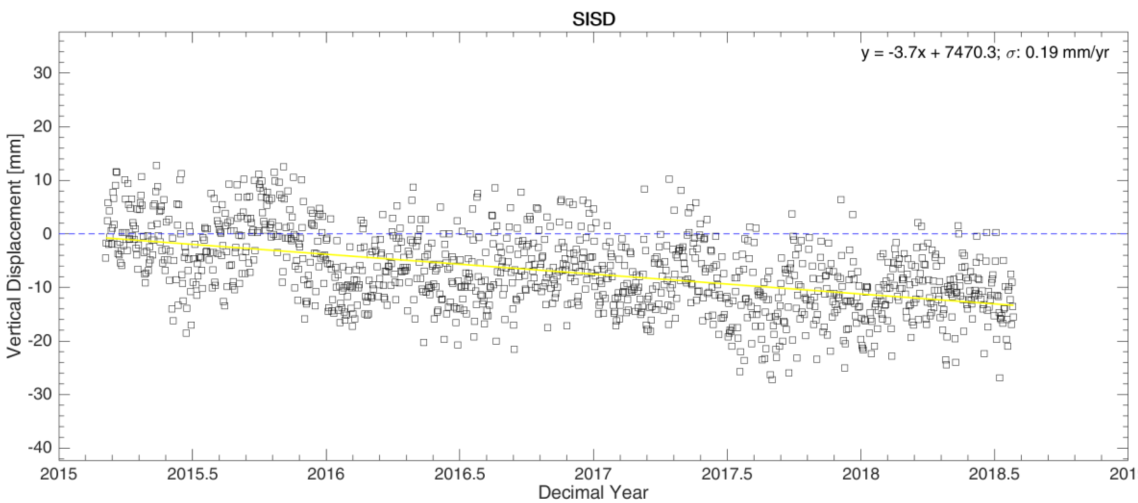
SISD
y = -3.7x + 7470.3; σ: 0.19 mm/yr
Vertical Displacement [mm]
Decimal Year

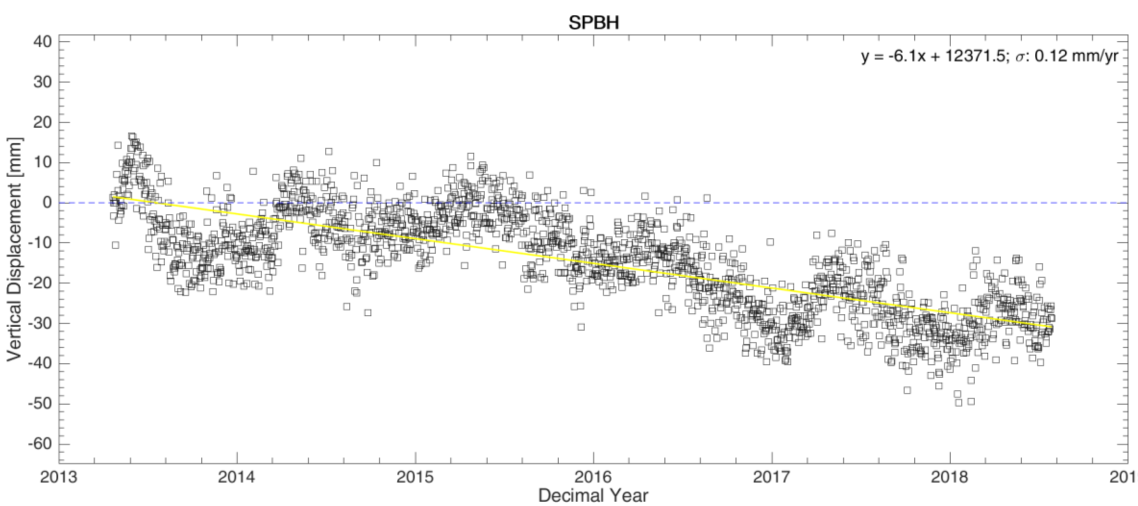
SPBH
y = -6.1x + 12371.5; σ: 0.12 mm/yr
Vertical Displacement [mm]
Decimal Year

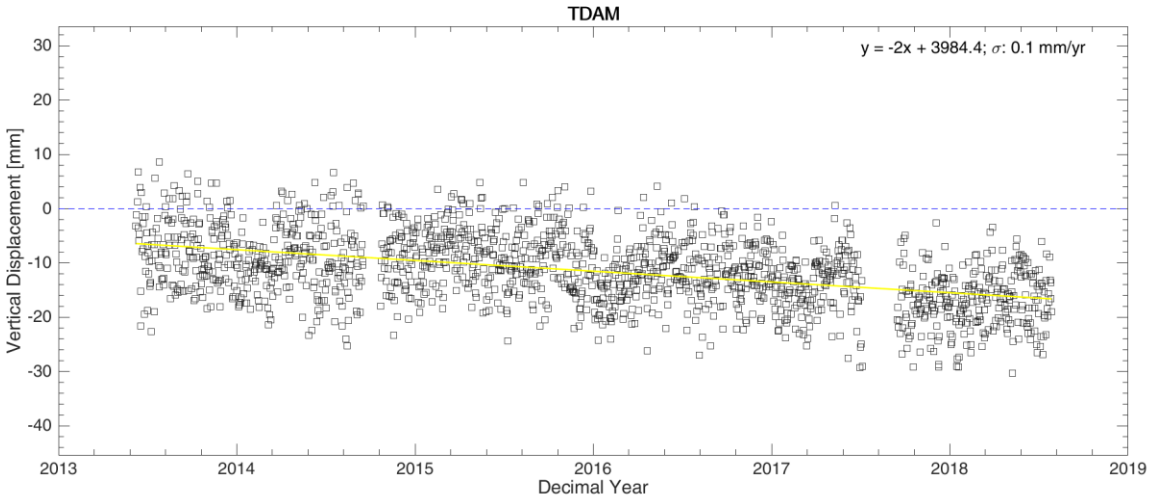
TDAM
y = -2x + 3984.4; σ: 0.1 mm/yr
Vertical Displacement [mm]
Decimal Year
30
20
10
0
-10
-20
-30
-40
2013
2014
2015
2016
2017
2018
2019

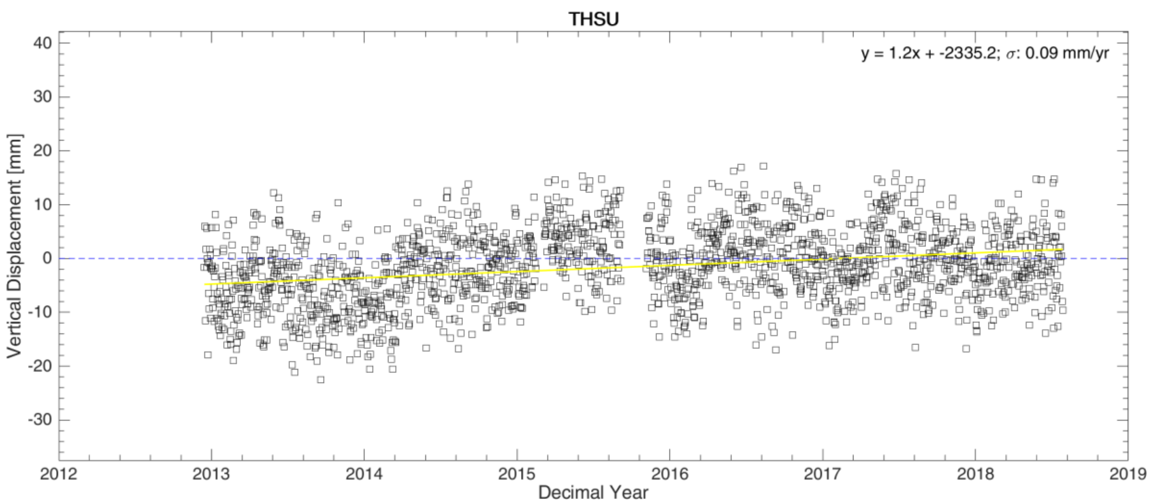
THSU
y = 1.2x + -2335.2; σ: 0.09 mm/yr
Vertical Displacement [mm]
Decimal Year
40
30
20
10
0
-10
-20
-30
2012
2013
2014
2015
2016
2017
2018
2019

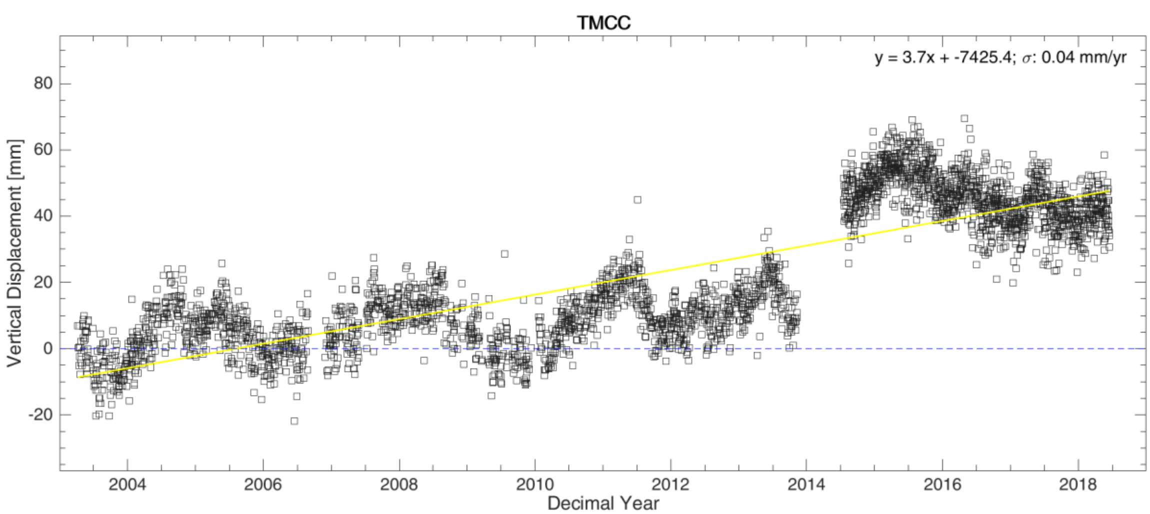
TMCC
y = 3.7x + -7425.4; σ: 0.04 mm/yr
Vertical Displacement [mm]
Decimal Year
80
60
40
20
0
-20
2004
2006
2008
2010
2012
2014
2016
2018

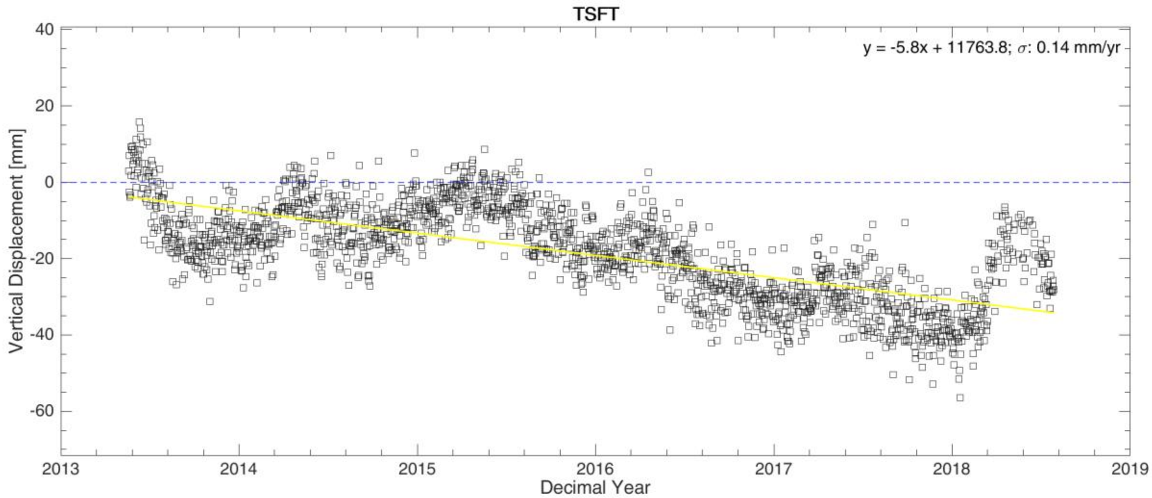
TSFT
y = -5.8x + 11763.8; σ: 0.14 mm/yr
Vertical Displacement [mm]
40
20
0
-20
-40
-60
2013
2014
2015
2016
2017
2018
2019
Decimal Year

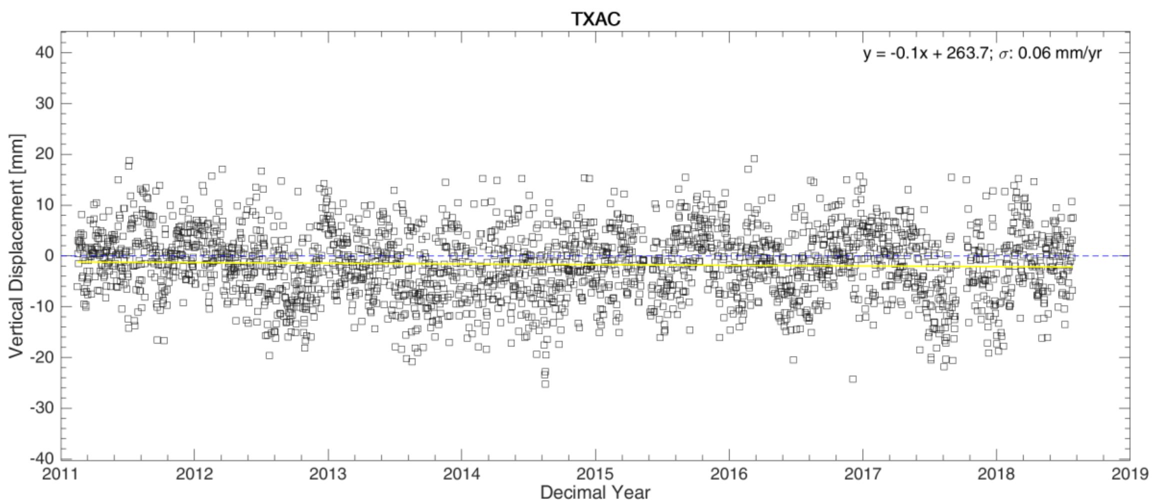
TXAC
y = -0.1x + 263.7; σ: 0.06 mm/yr
Vertical Displacement [mm]
40
30
20
10
0
-10
-20
-30
-40
2011
2012
2013
2014
2015
2016
2017
2018
2019
Decimal Year

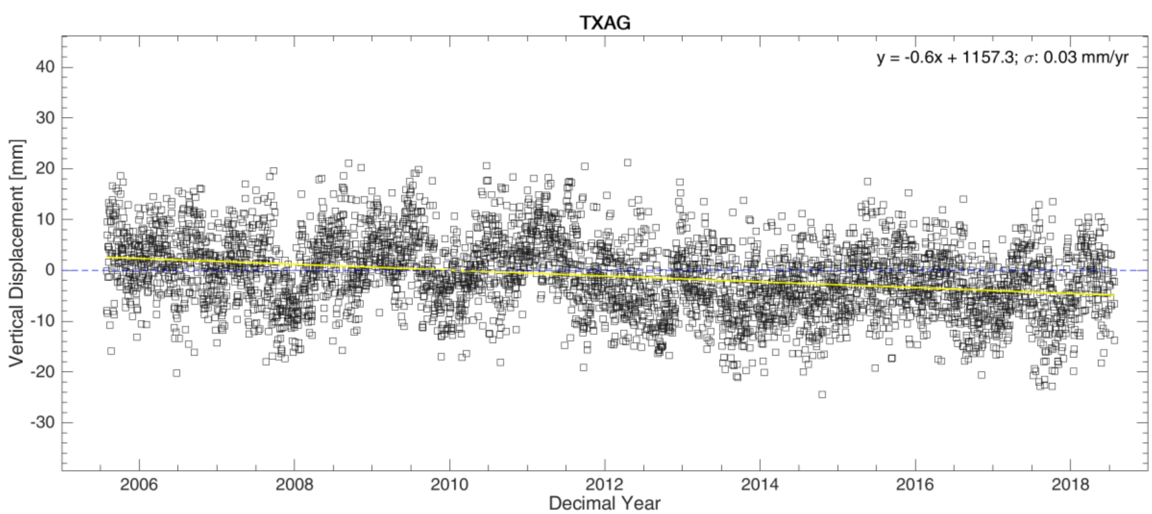
TXAG
y = -0.6x + 1157.3; σ: 0.03 mm/yr
Vertical Displacement [mm]
40
30
20
10
0
-10
-20
-30
2006
2008
2010
2012
2014
2016
2018
Decimal Year

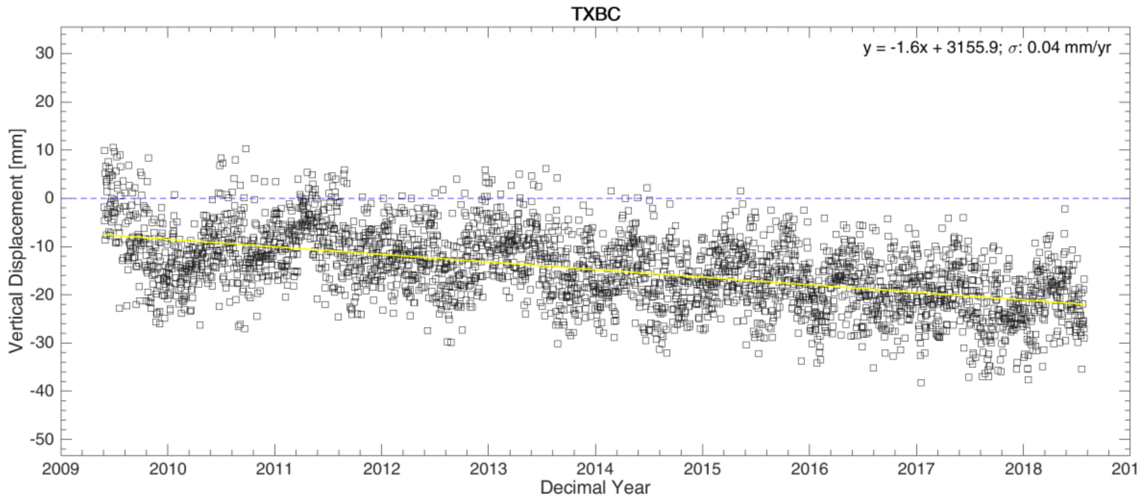
TXBC
y = -1.6x + 3155.9; σ: 0.04 mm/yr
Vertical Displacement [mm]
Decimal Year

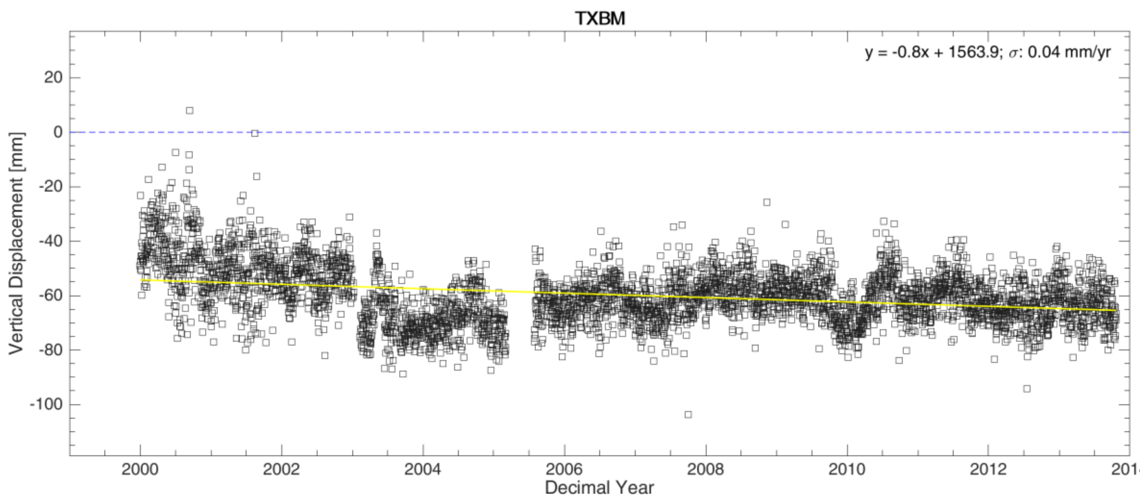
TXBM
y = -0.8x + 1563.9; σ: 0.04 mm/yr
Vertical Displacement [mm]
Decimal Year

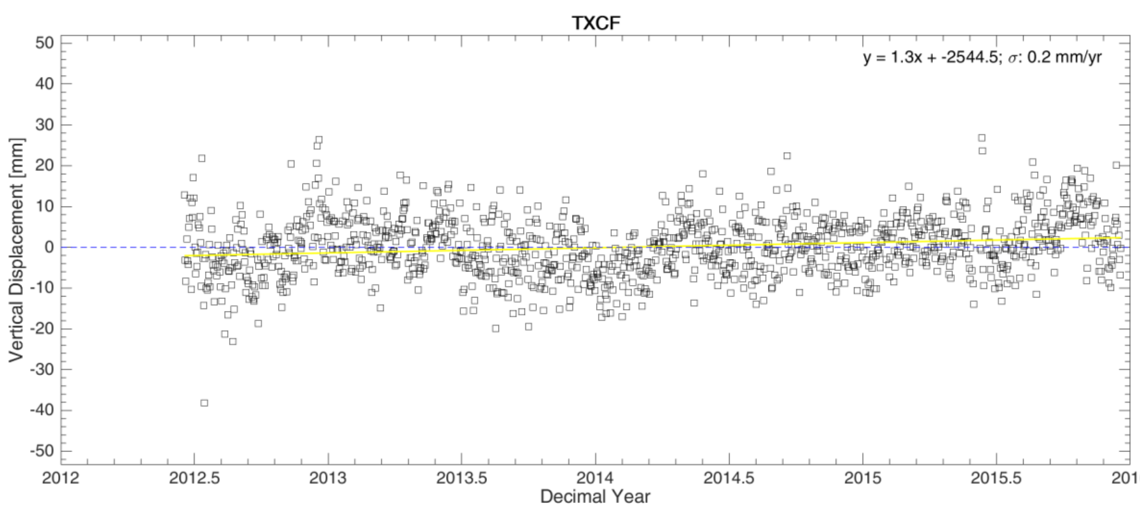
TXCF
y = 1.3x + -2544.5; σ: 0.2 mm/yr
Vertical Displacement [mm]
Decimal Year

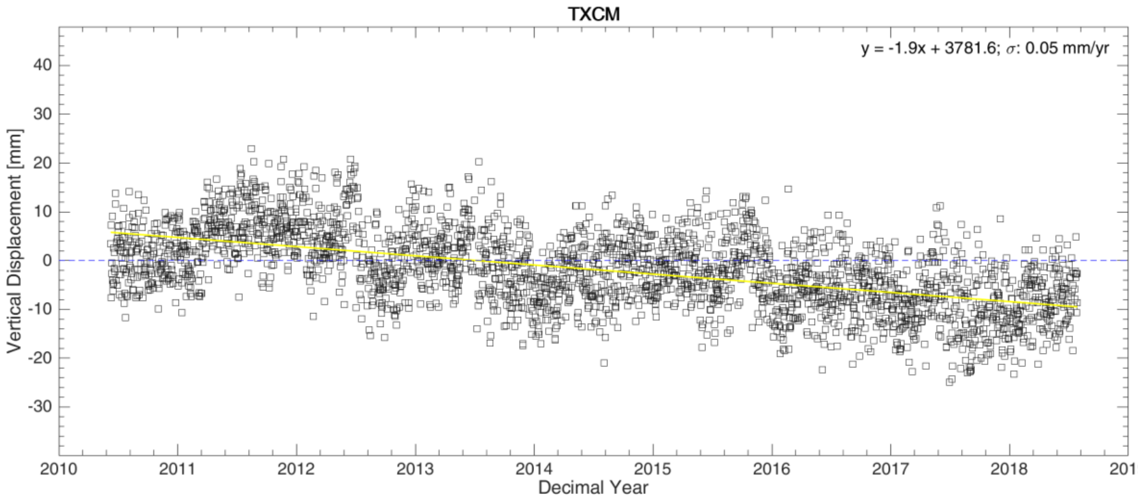
TXCM
y = -1.9x + 3781.6; σ: 0.05 mm/yr
Vertical Displacement [mm]
Decimal Year

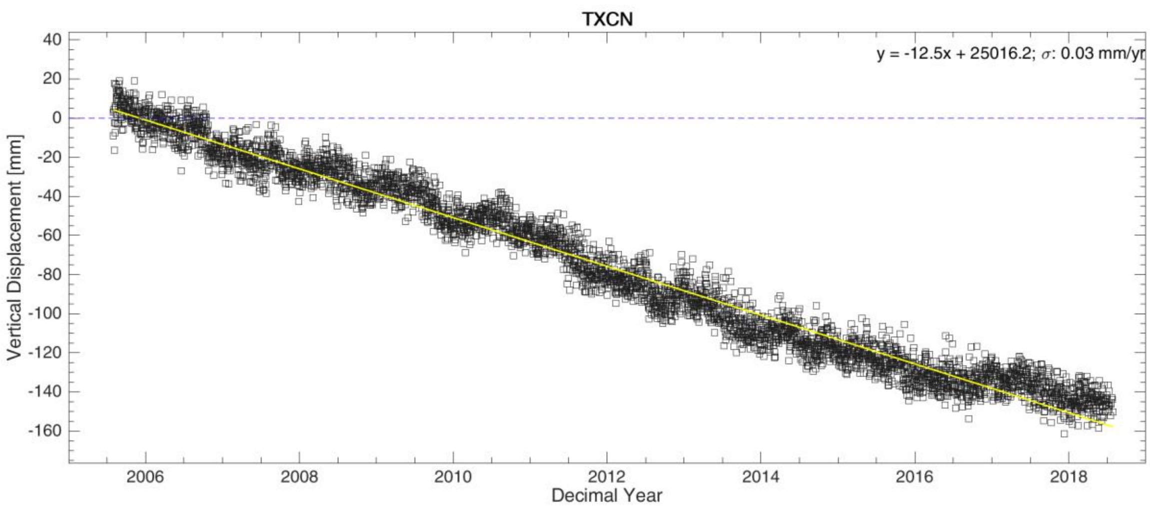
TXCN
y = -12.5x + 25016.2; σ: 0.03 mm/yr
Vertical Displacement [mm]
Decimal Year

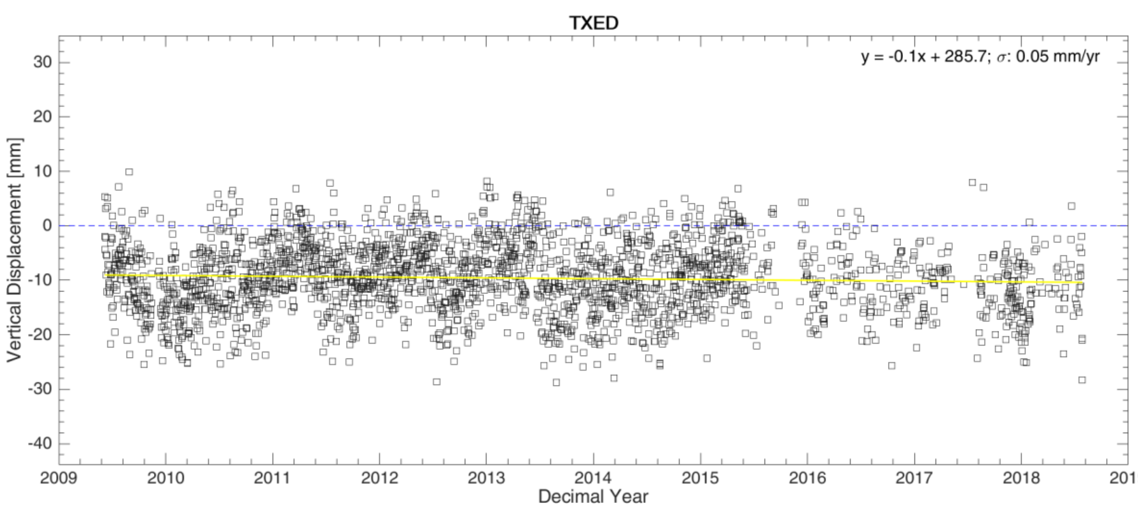
TXED
y = -0.1x + 285.7; σ: 0.05 mm/yr
Vertical Displacement [mm]
Decimal Year

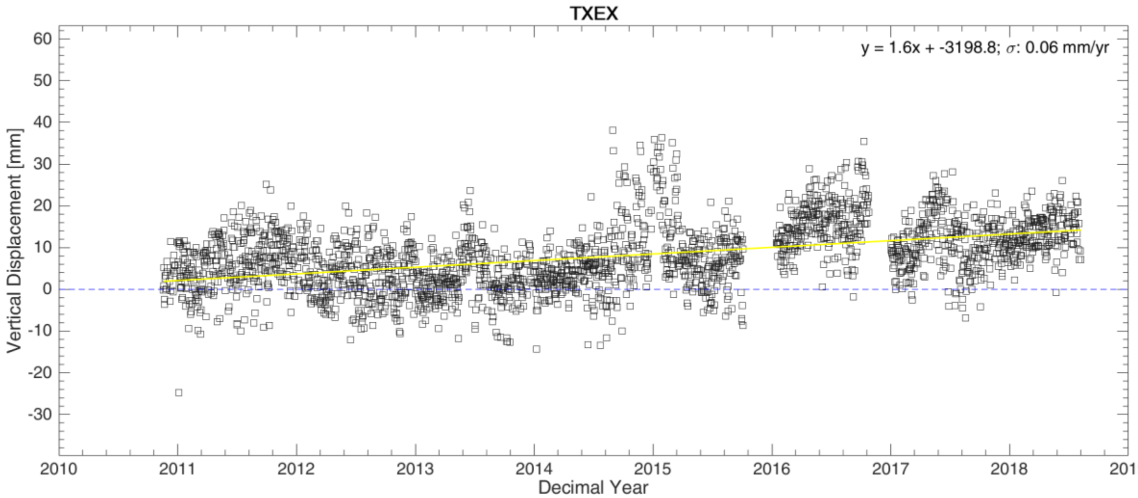
TXEX
y = 1.6x + -3198.8; σ: 0.06 mm/yr
Vertical Displacement [mm]
Decimal Year

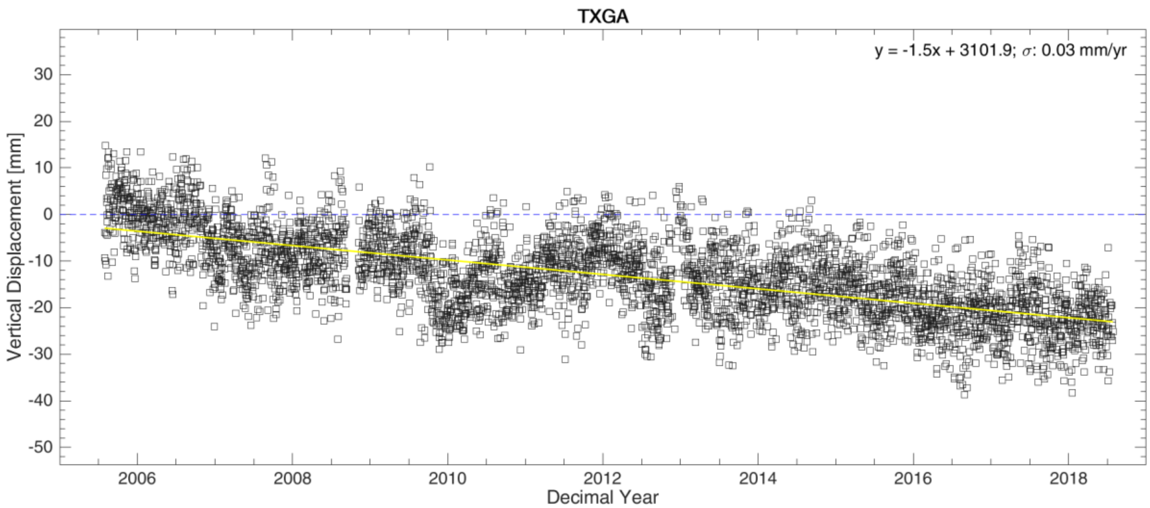
TXGA
y = -1.5x + 3101.9; σ: 0.03 mm/yr
Vertical Displacement [mm]
Decimal Year

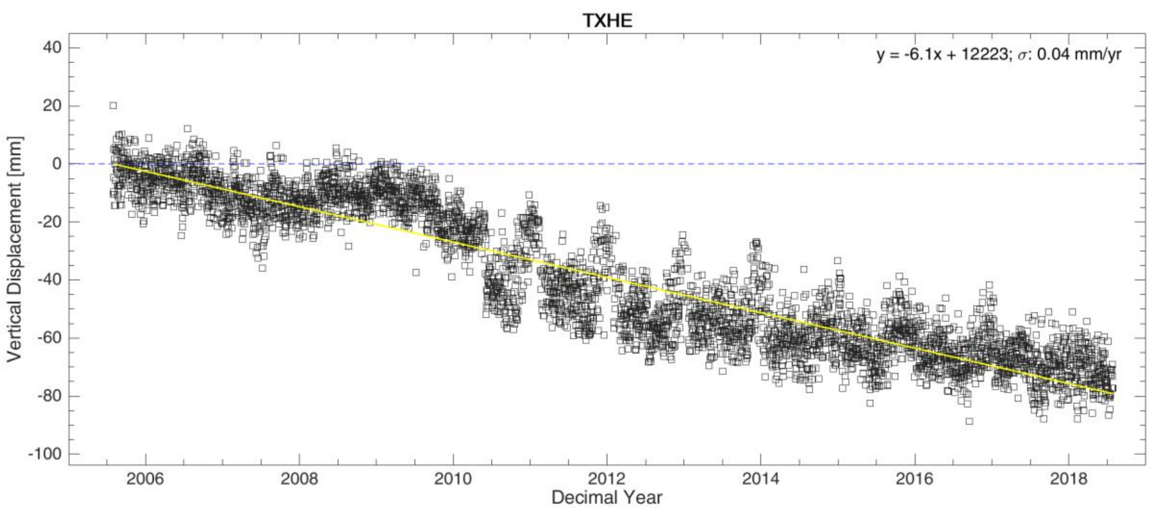
TXHE
y = -6.1x + 12223; σ: 0.04 mm/yr
Vertical Displacement [mm]
Decimal Year

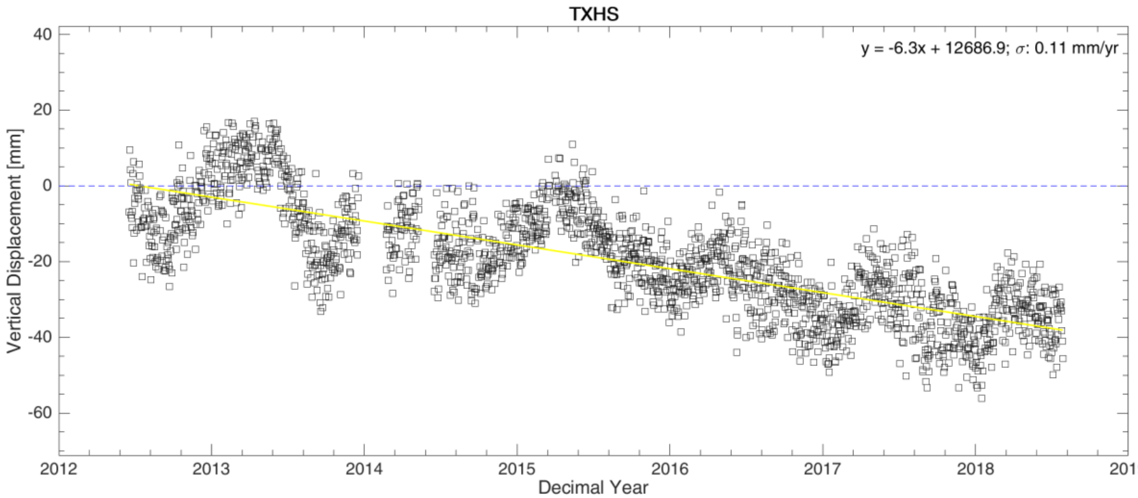
TXHS
y = -6.3x + 12686.9; σ: 0.11 mm/yr
Vertical Displacement [mm]
Decimal Year

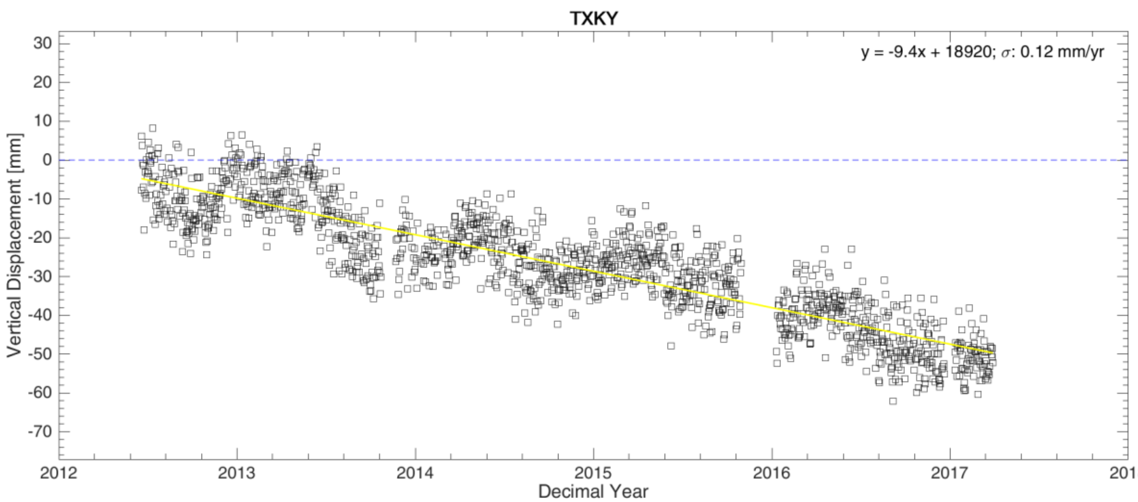
TXKY
y = -9.4x + 18920; σ: 0.12 mm/yr
Vertical Displacement [mm]
Decimal Year

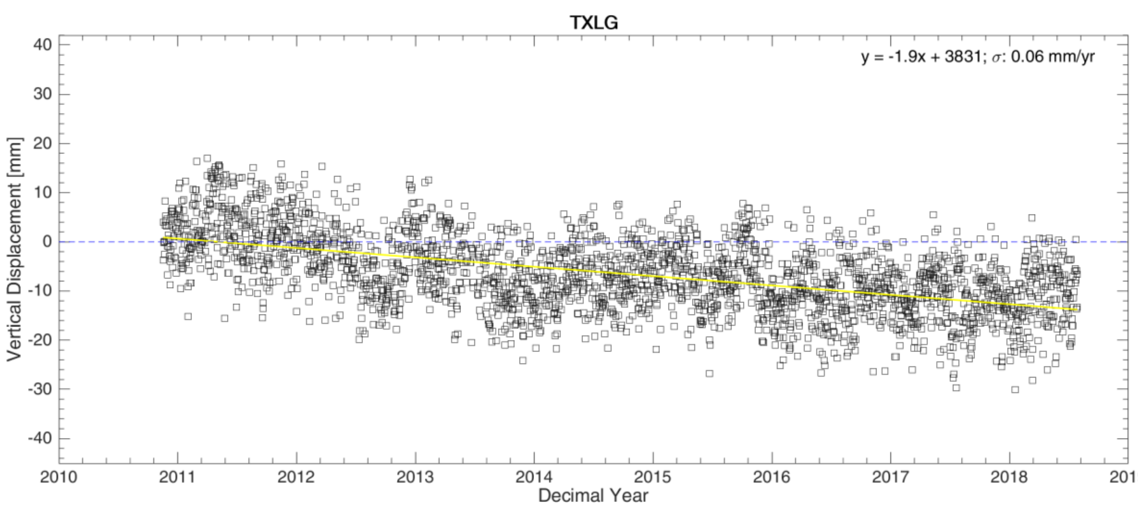
TXLG
y = -1.9x + 3831; σ: 0.06 mm/yr
Vertical Displacement [mm]
Decimal Year

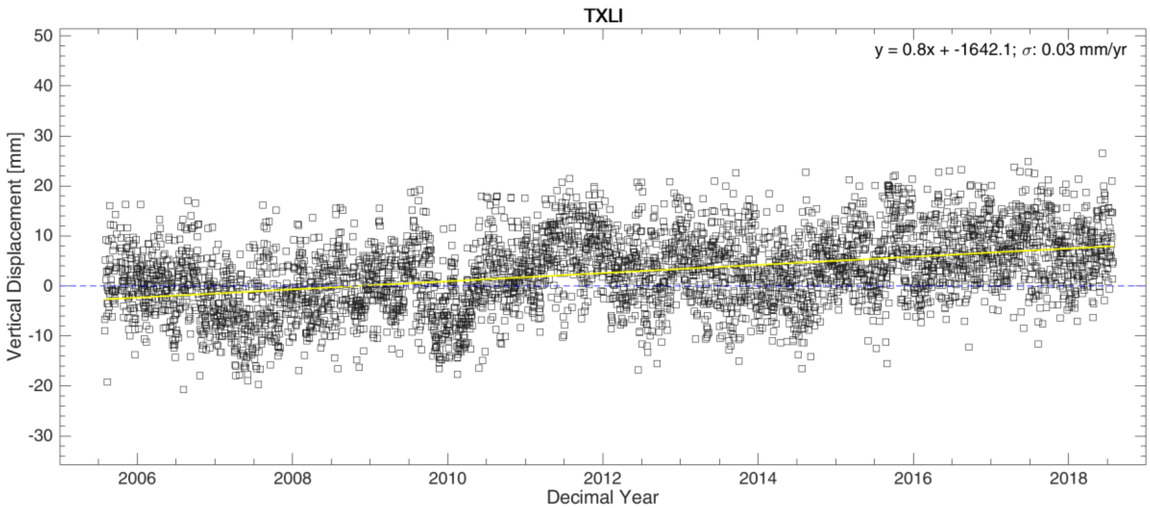
TXLI
y = 0.8x + -1642.1; σ: 0.03 mm/yr
Vertical Displacement [mm]
Decimal Year

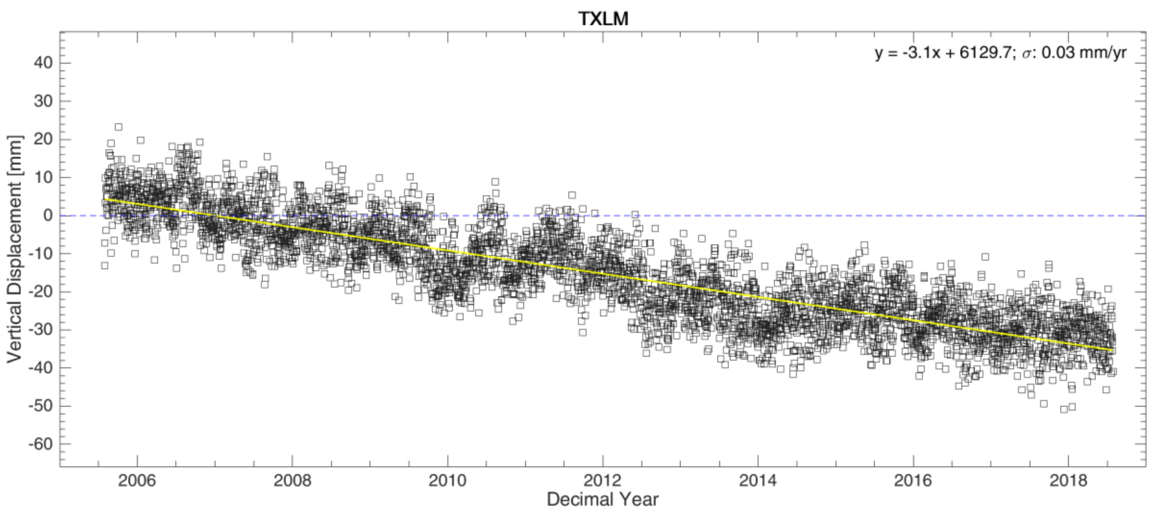
TXLM
y = -3.1x + 6129.7; σ: 0.03 mm/yr
Vertical Displacement [mm]
Decimal Year

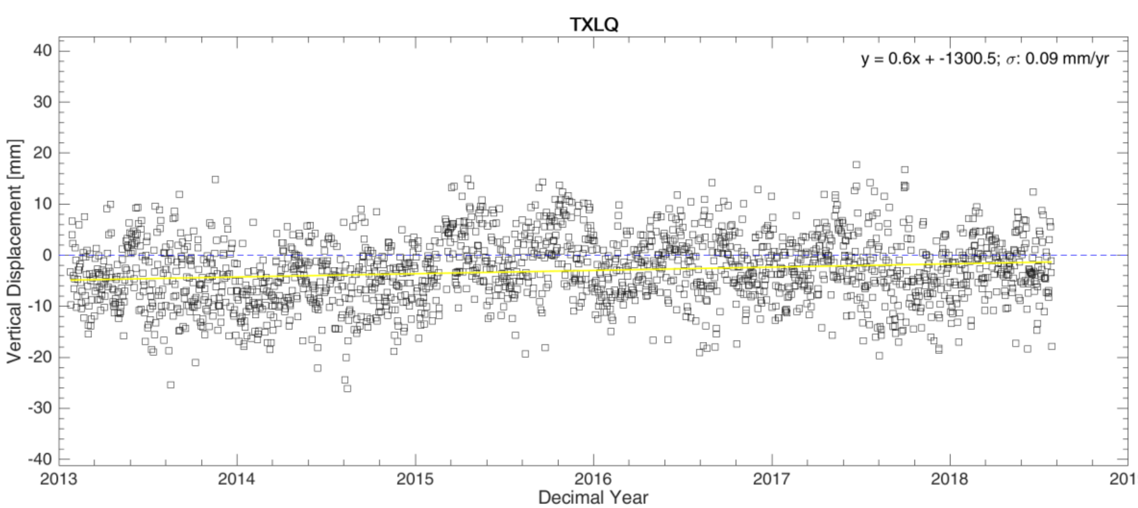
TXLQ
y = 0.6x + -1300.5; σ: 0.09 mm/yr
Vertical Displacement [mm]
Decimal Year

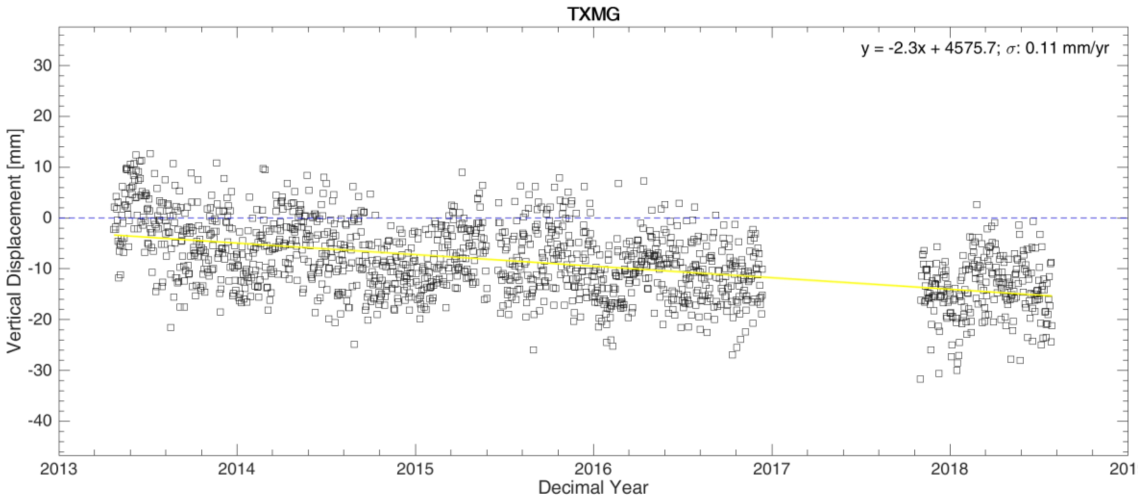
TXMG
y = -2.3x + 4575.7; σ: 0.11 mm/yr
Vertical Displacement [mm]
Decimal Year

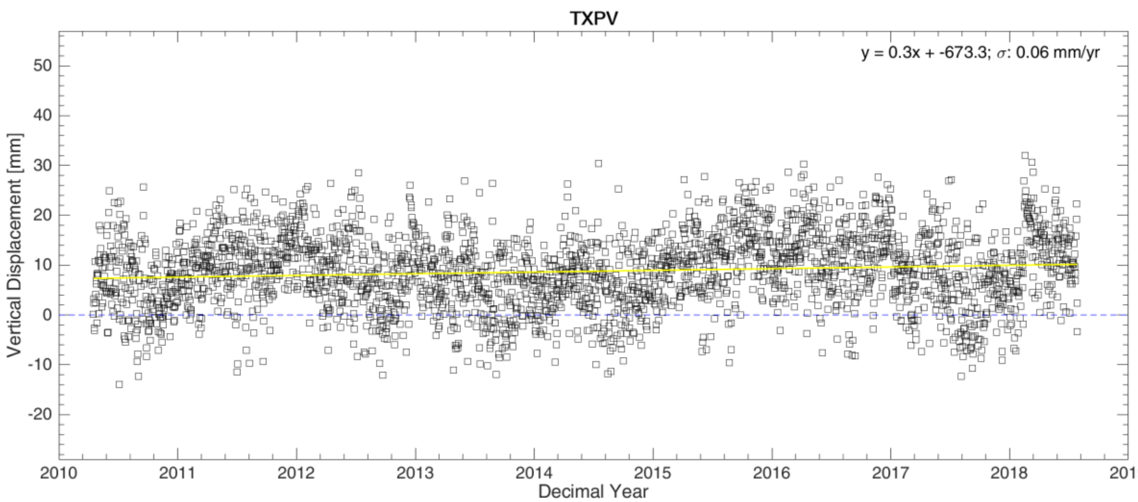
TXPV
y = 0.3x + -673.3; σ: 0.06 mm/yr
Vertical Displacement [mm]
Decimal Year

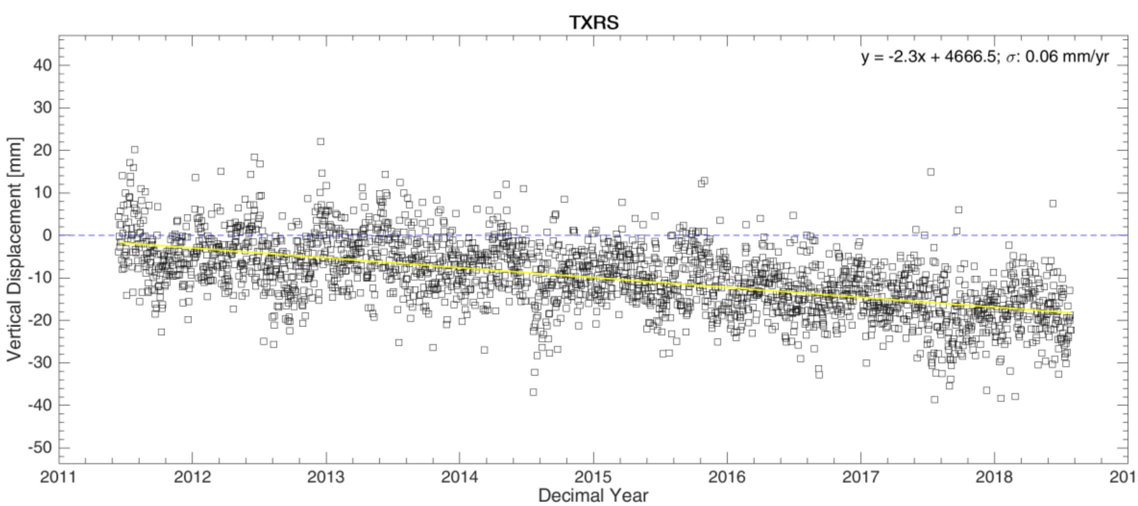
TXRS
y = -2.3x + 4666.5; σ: 0.06 mm/yr
Vertical Displacement [mm]
Decimal Year

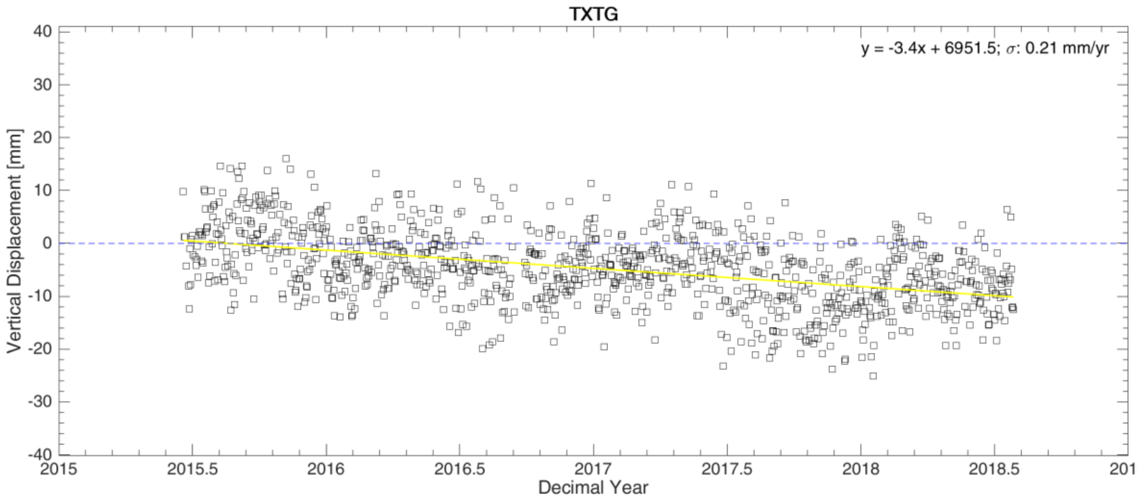
TXTG
y = -3.4x + 6951.5; σ: 0.21 mm/yr
Vertical Displacement [mm]
Decimal Year
40
30
20
10
0
-10
-20
-30
-40
2015
2015.5
2016
2016.5
2017
2017.5
2018
2018.5
2019

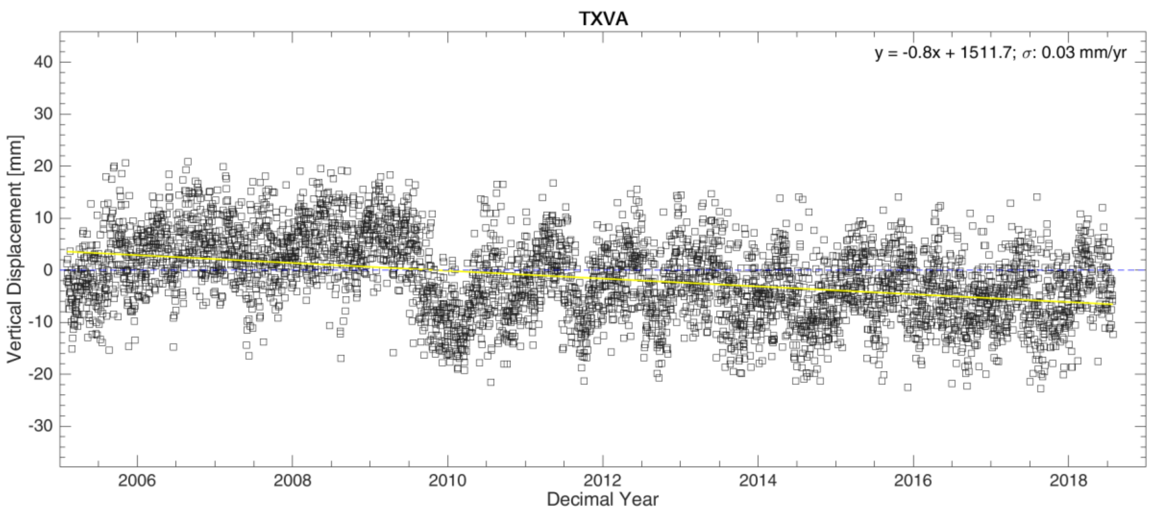
TXVA
y = -0.8x + 1511.7; σ: 0.03 mm/yr
Vertical Displacement [mm]
Decimal Year
40
30
20
10
0
-10
-20
-30
2006
2008
2010
2012
2014
2016
2018

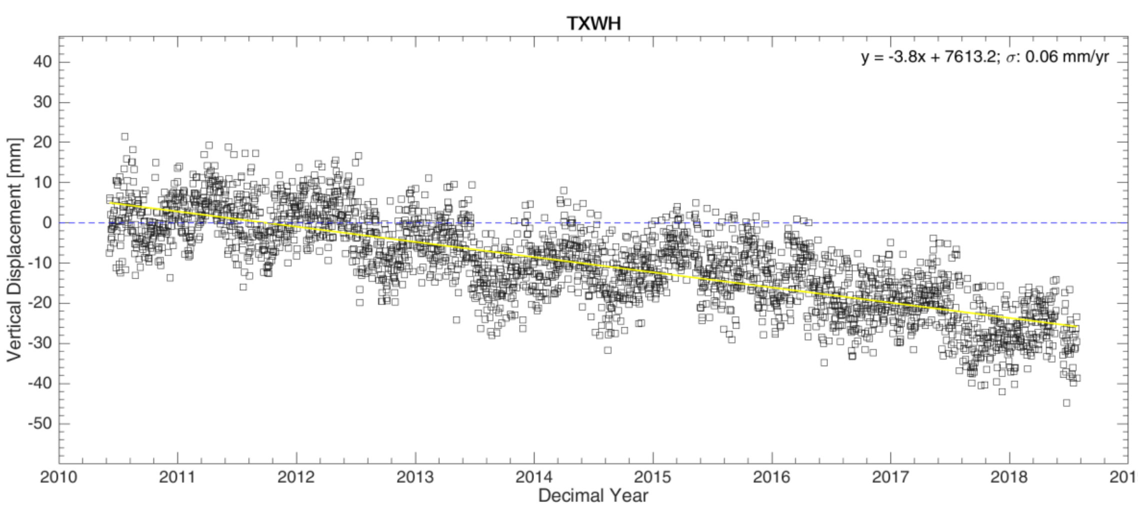
TXWH
y = -3.8x + 7613.2; σ: 0.06 mm/yr
Vertical Displacement [mm]
Decimal Year
40
30
20
10
0
-10
-20
-30
-40
-50
2010
2011
2012
2013
2014
2015
2016
2017
2018
2019

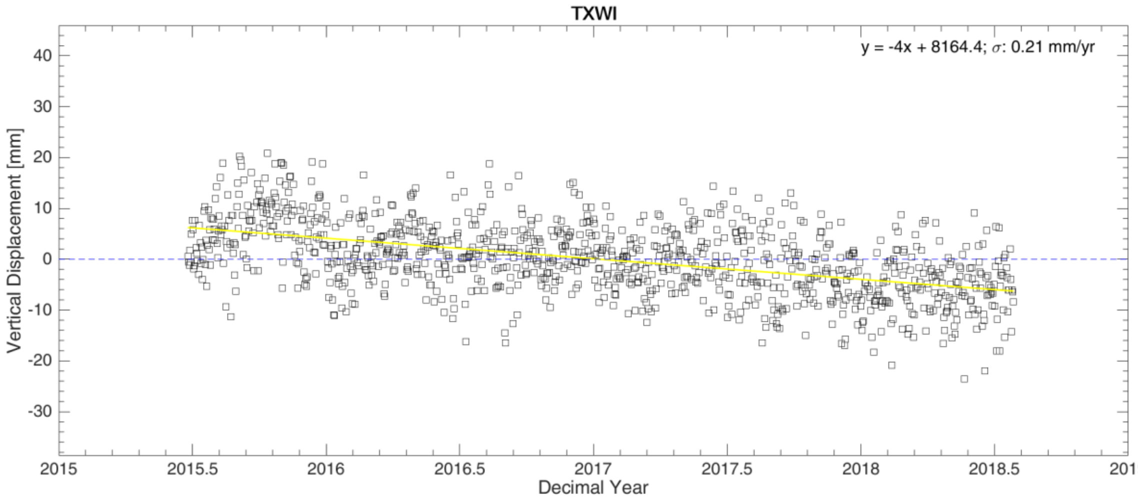
TXWI
y = -4x + 8164.4; σ: 0.21 mm/yr
Vertical Displacement [mm]
Decimal Year

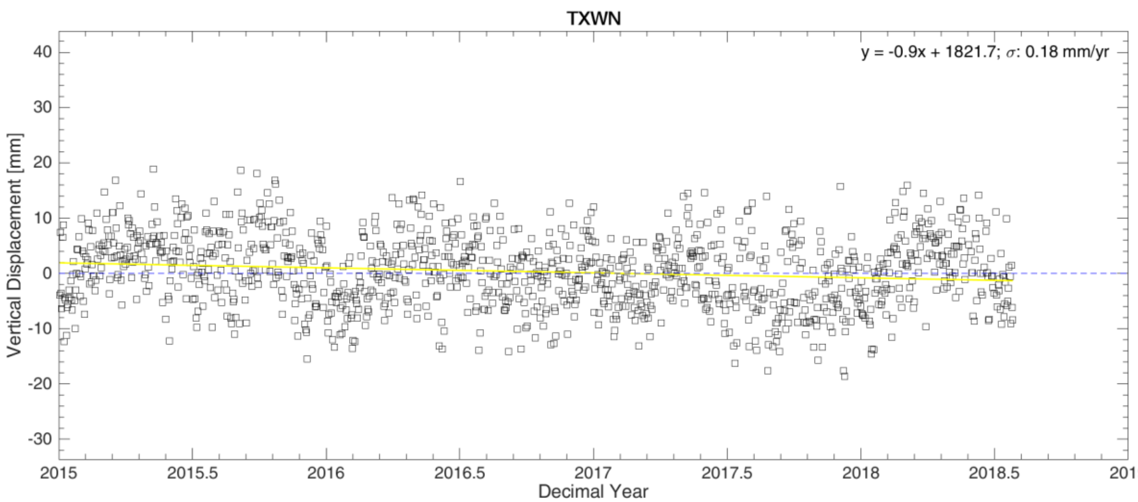
TXWN
y = -0.9x + 1821.7; σ: 0.18 mm/yr
Vertical Displacement [mm]
Decimal Year

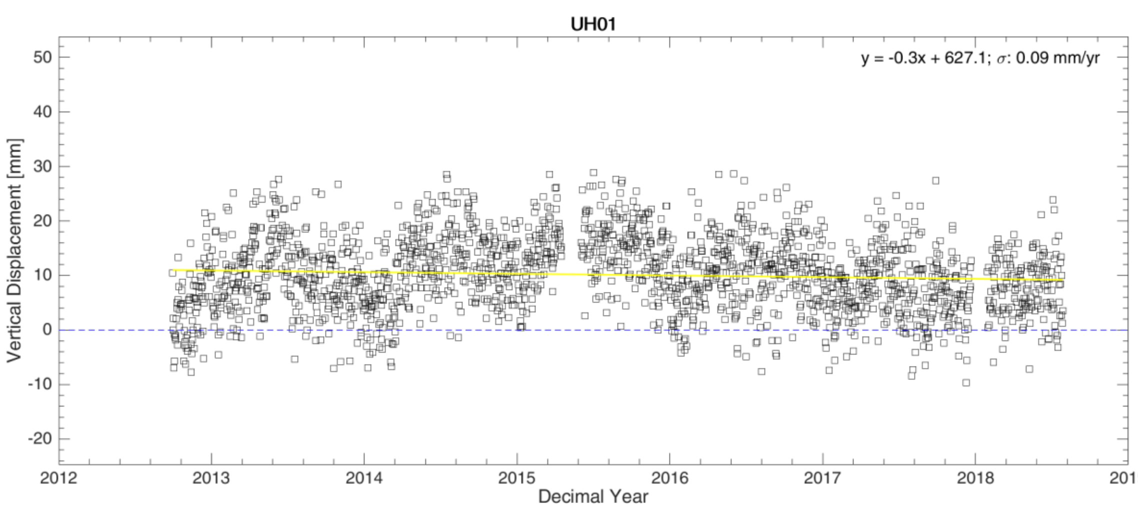
UH01
y = -0.3x + 627.1; σ: 0.09 mm/yr
Vertical Displacement [mm]
Decimal Year

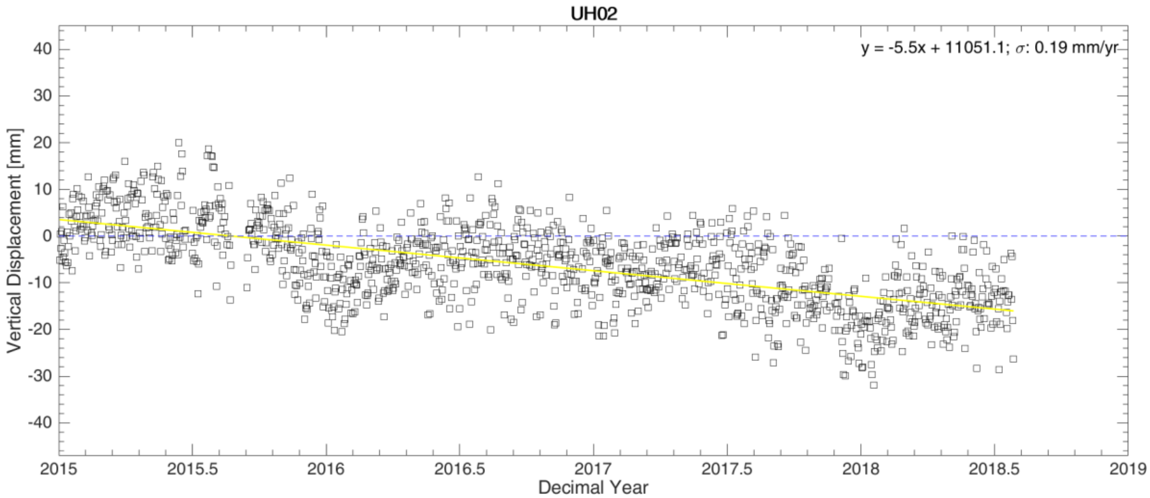
UH02
y = -5.5x + 11051.1; σ: 0.19 mm/yr
Vertical Displacement [mm]
Decimal Year

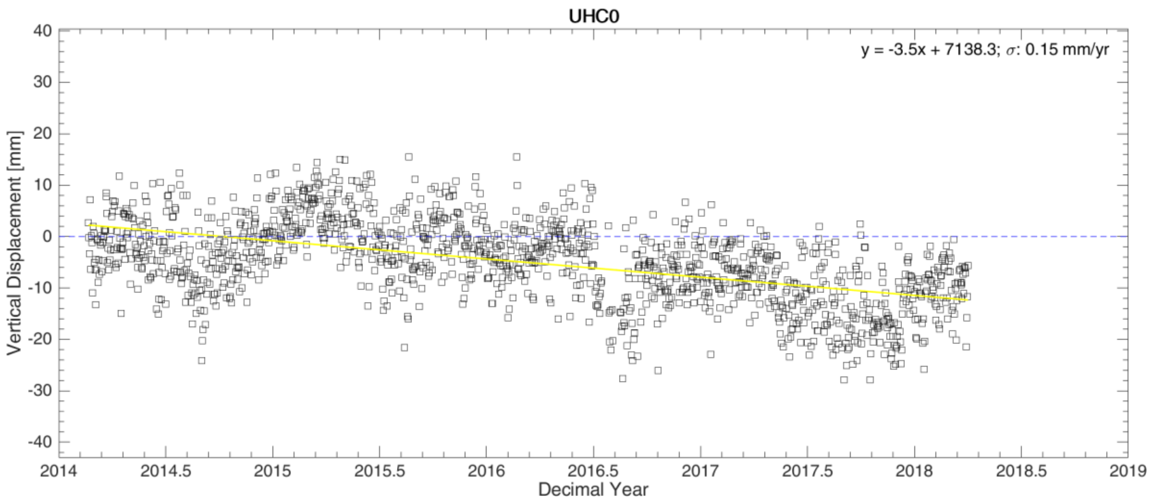
UHC0
y = -3.5x + 7138.3; σ: 0.15 mm/yr
Vertical Displacement [mm]
Decimal Year

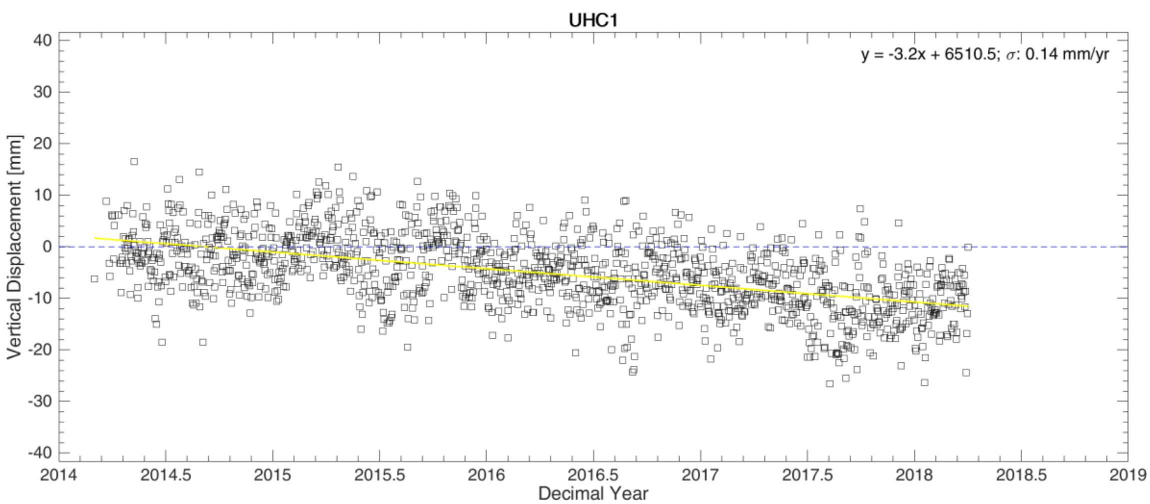
UHC1
y = -3.2x + 6510.5; σ: 0.14 mm/yr
Vertical Displacement [mm]
Decimal Year

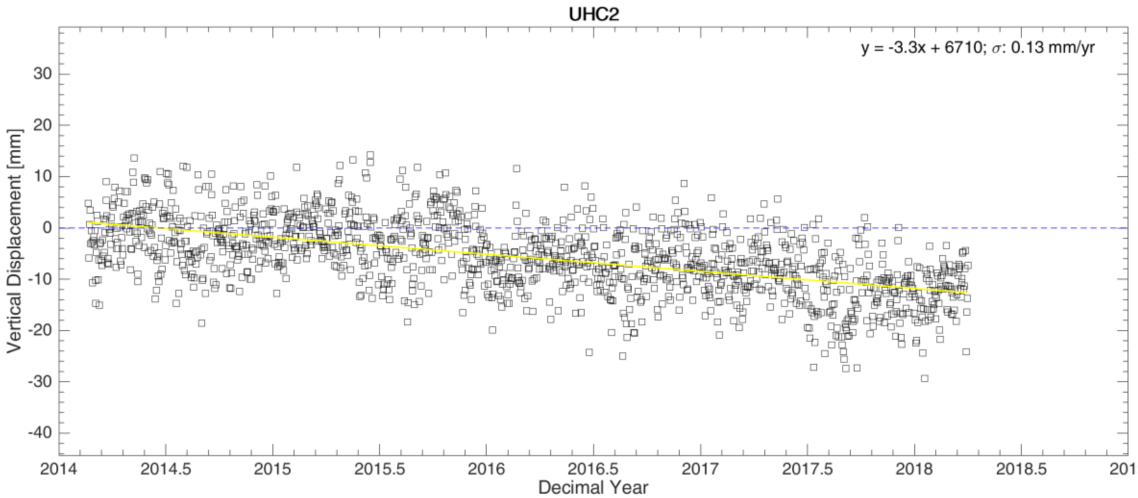
UHC2
y = -3.3x + 6710; σ: 0.13 mm/yr
Vertical Displacement [mm]
Decimal Year

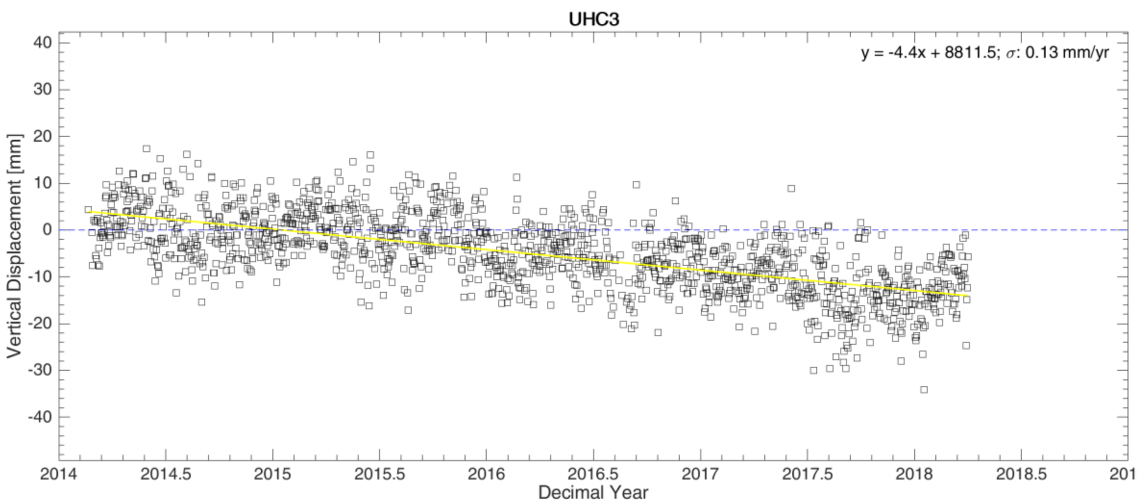
UHC3
y = -4.4x + 8811.5; σ: 0.13 mm/yr
Vertical Displacement [mm]
Decimal Year

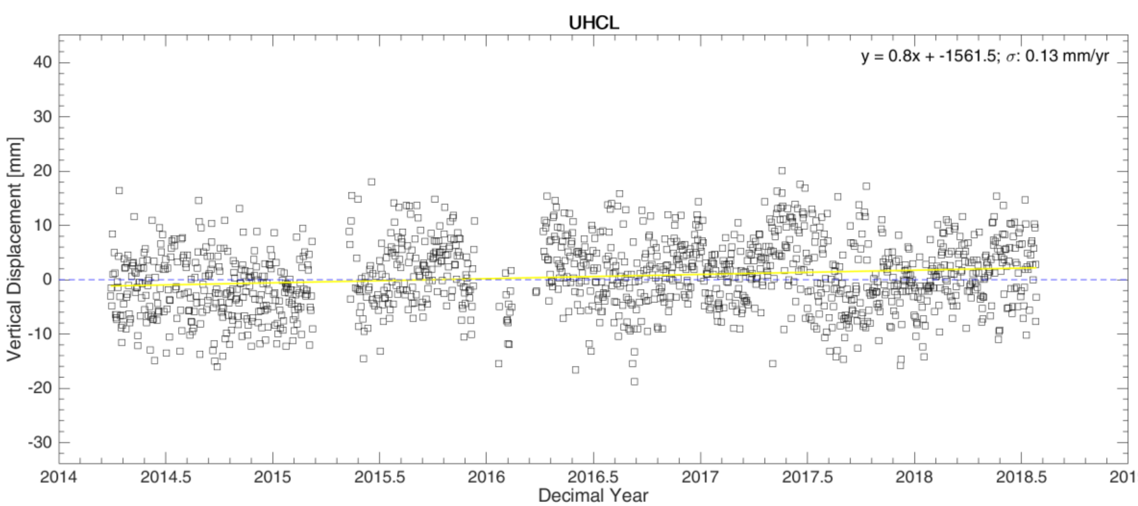
UHCL
y = 0.8x + -1561.5; σ: 0.13 mm/yr
Vertical Displacement [mm]
Decimal Year

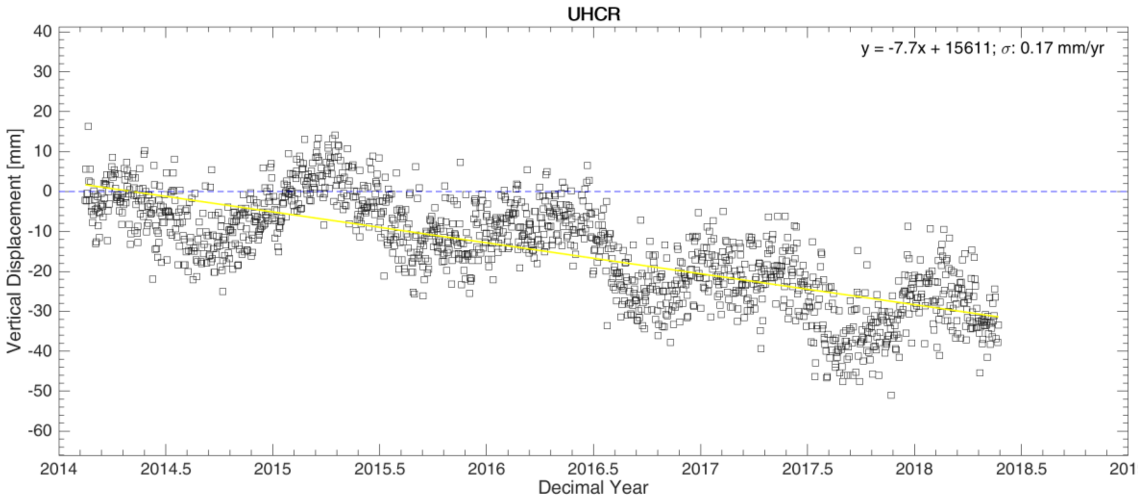
UHCR
y = -7.7x + 15611; σ: 0.17 mm/yr
Vertical Displacement [mm]
Decimal Year

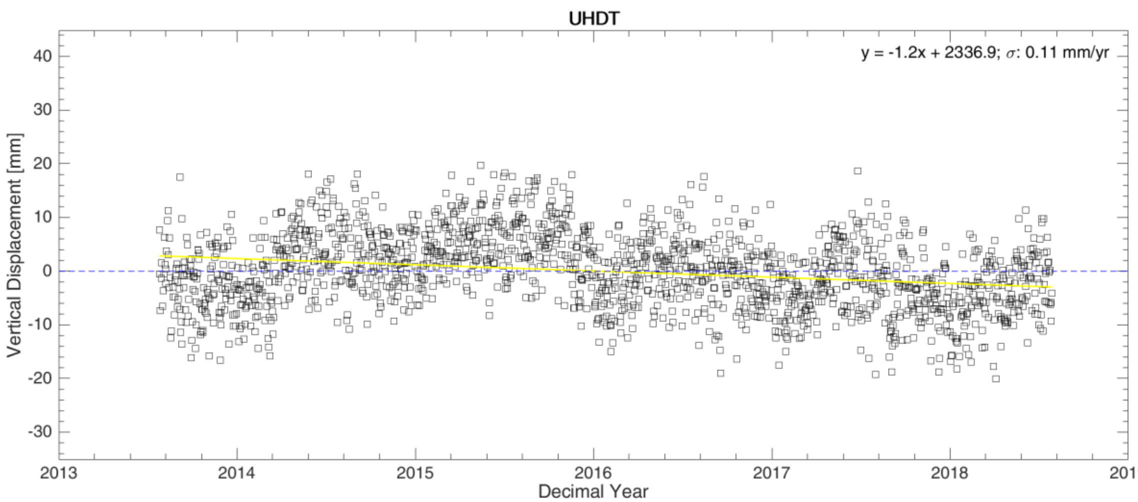
UHDT
y = -1.2x + 2336.9; σ: 0.11 mm/yr
Vertical Displacement [mm]
Decimal Year

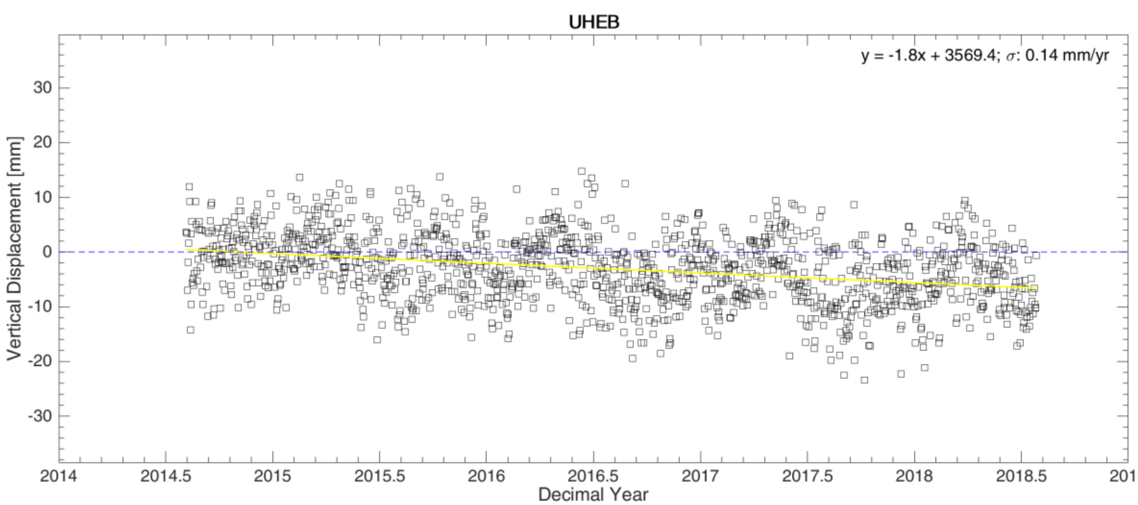
UHEB
y = -1.8x + 3569.4; σ: 0.14 mm/yr
Vertical Displacement [mm]
Decimal Year

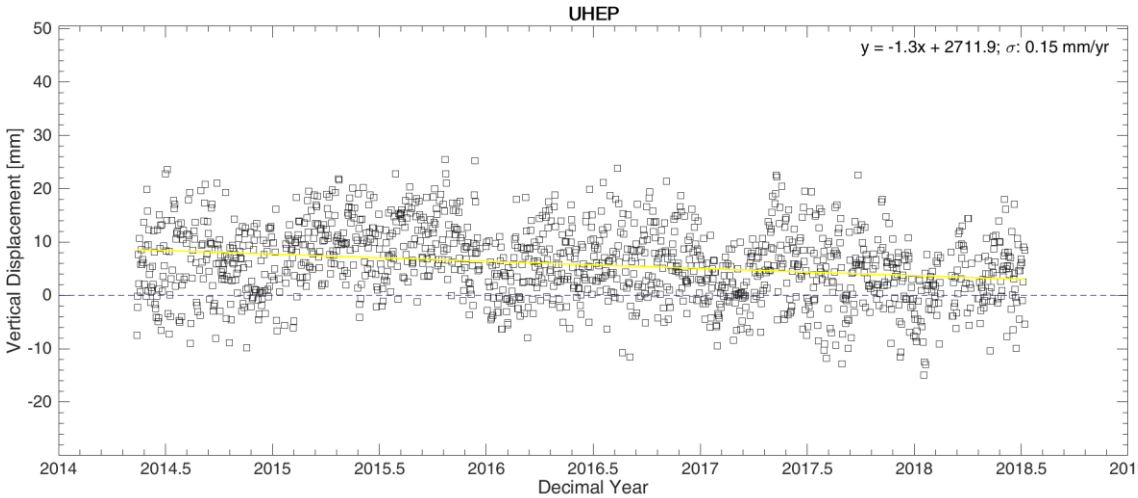
UHEP
y = -1.3x + 2711.9; σ: 0.15 mm/yr
Vertical Displacement [mm]
Decimal Year

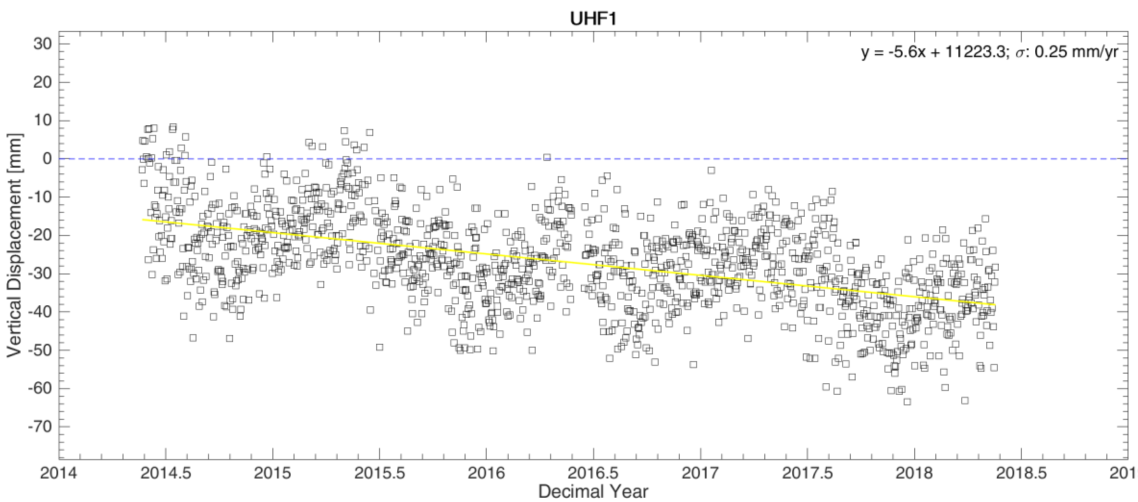
UHF1
y = -5.6x + 11223.3; σ: 0.25 mm/yr
Vertical Displacement [mm]
Decimal Year

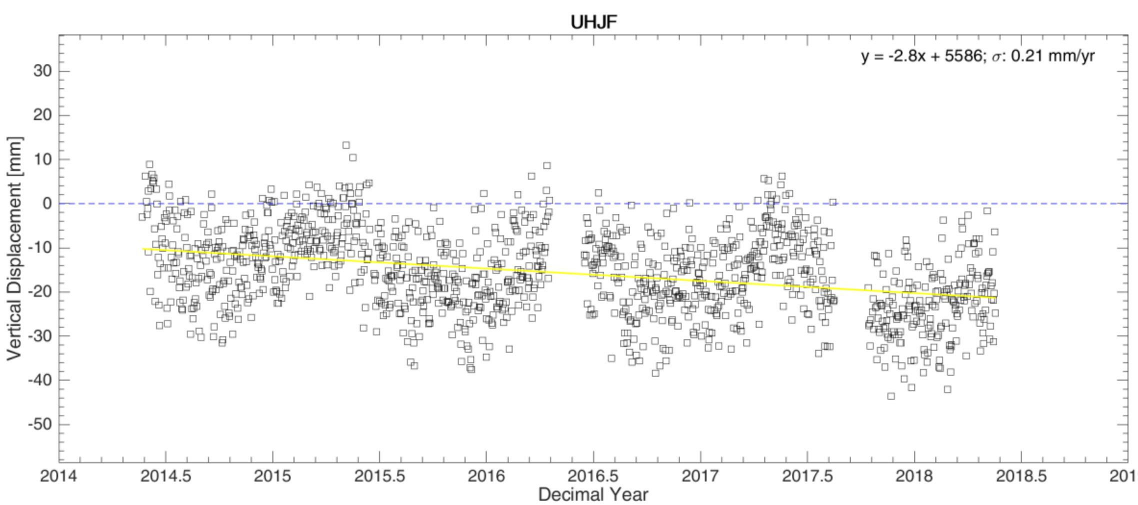
UHJF
y = -2.8x + 5586; σ: 0.21 mm/yr
Vertical Displacement [mm]
Decimal Year

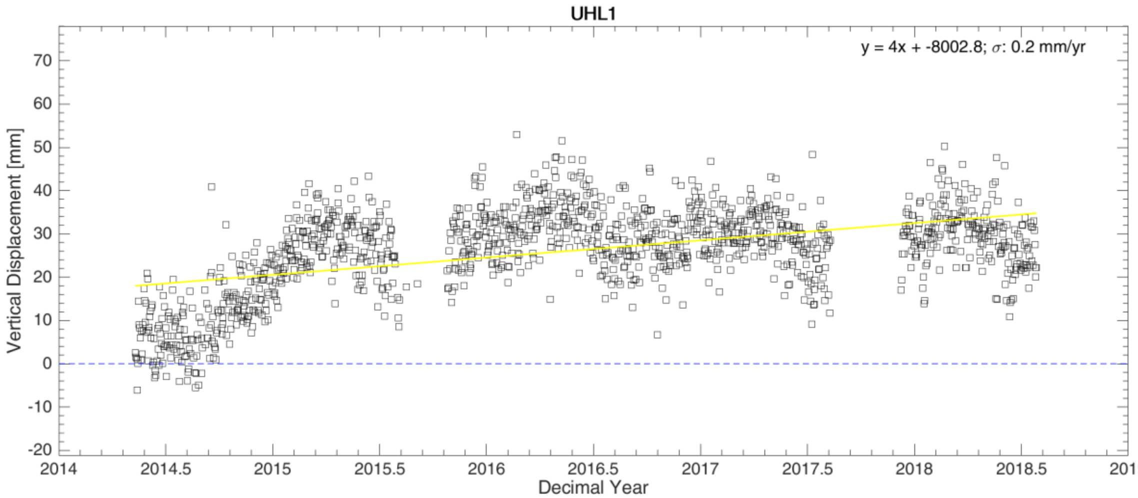
UHL1
y = 4x + -8002.8; σ: 0.2 mm/yr
Vertical Displacement [mm]
Decimal Year

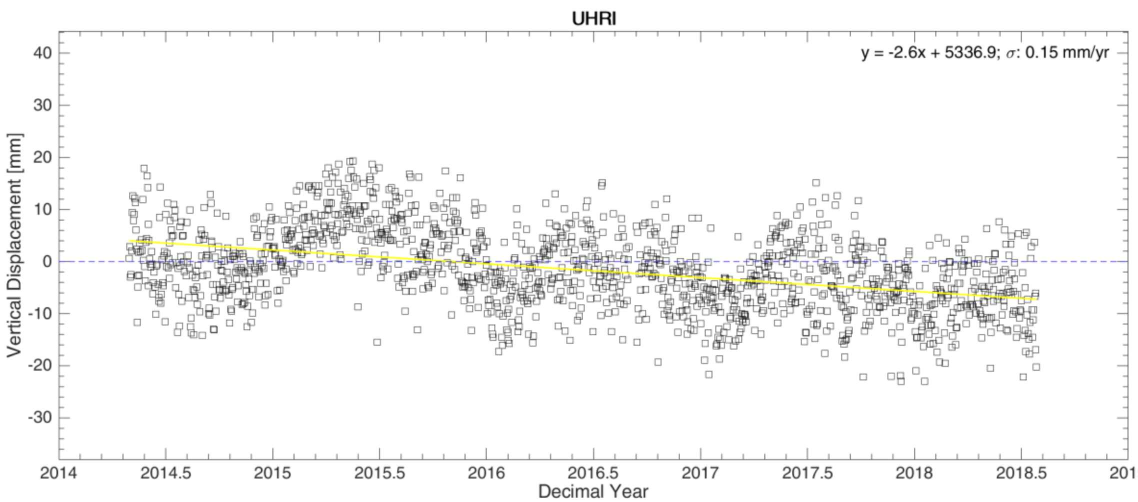
UHRI
y = -2.6x + 5336.9; σ: 0.15 mm/yr
Vertical Displacement [mm]
Decimal Year

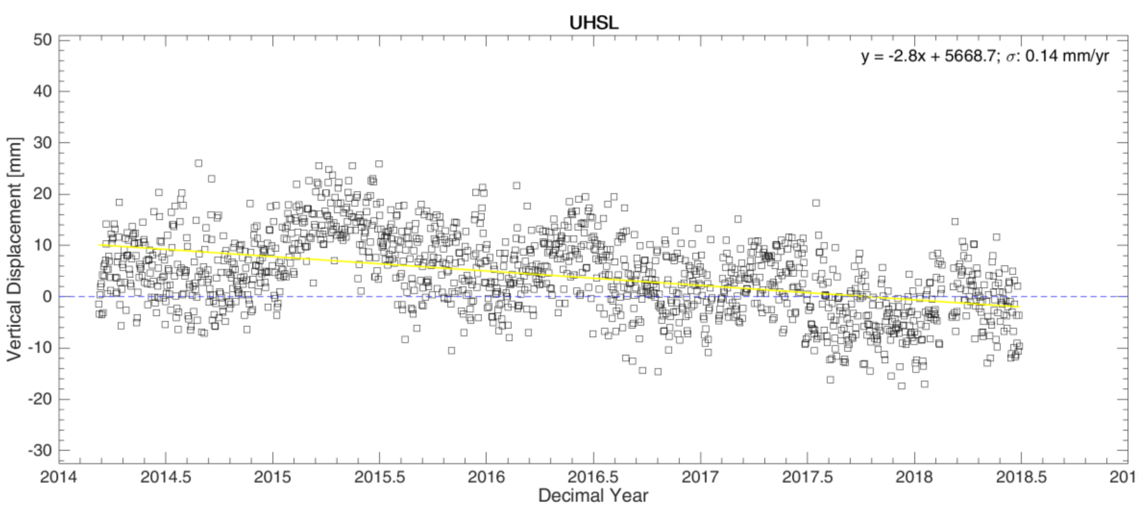
UHSL
y = -2.8x + 5668.7; σ: 0.14 mm/yr
Vertical Displacement [mm]
Decimal Year

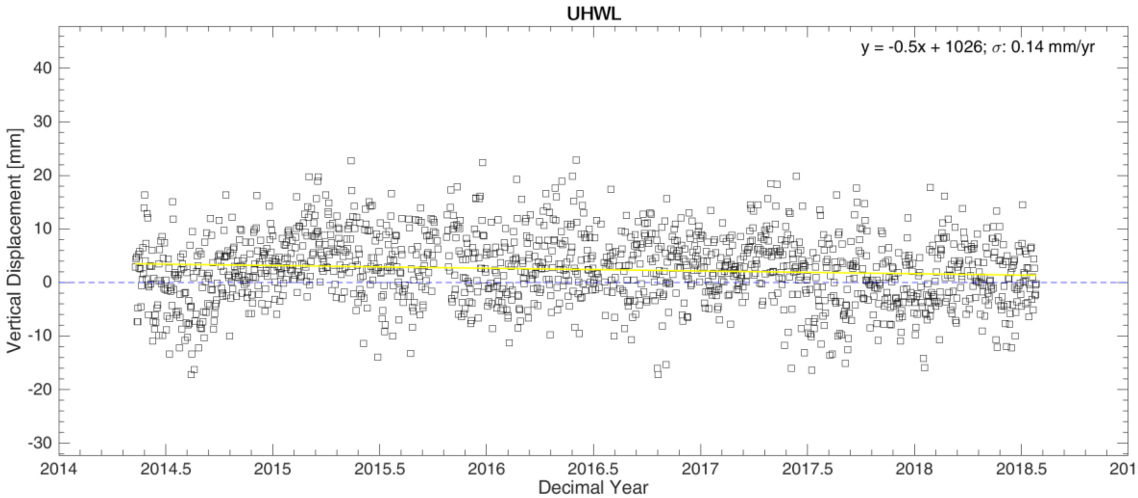
UHWL
y = -0.5x + 1026; σ: 0.14 mm/yr
Vertical Displacement [mm]
Decimal Year

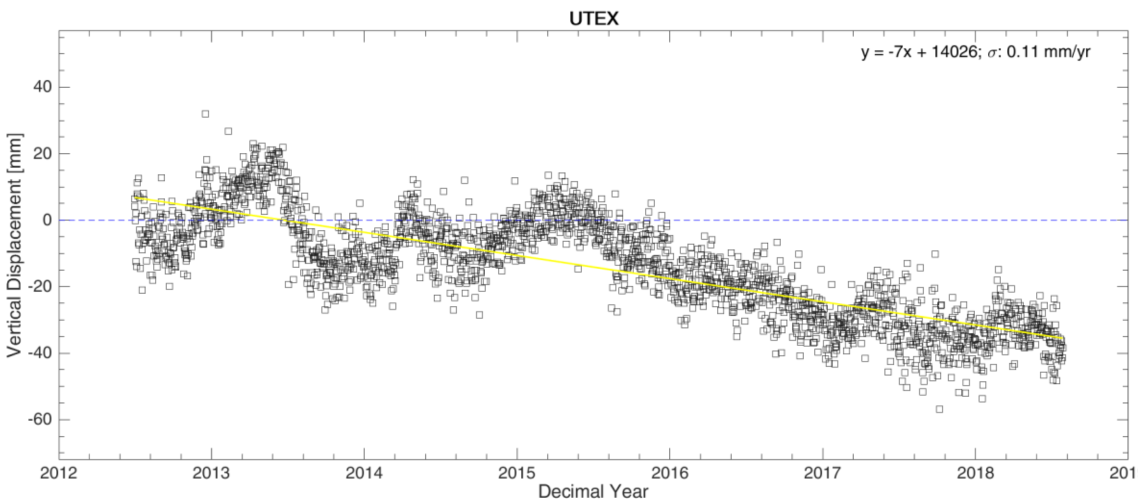
UTEX
y = -7x + 14026; σ: 0.11 mm/yr
Vertical Displacement [mm]
Decimal Year

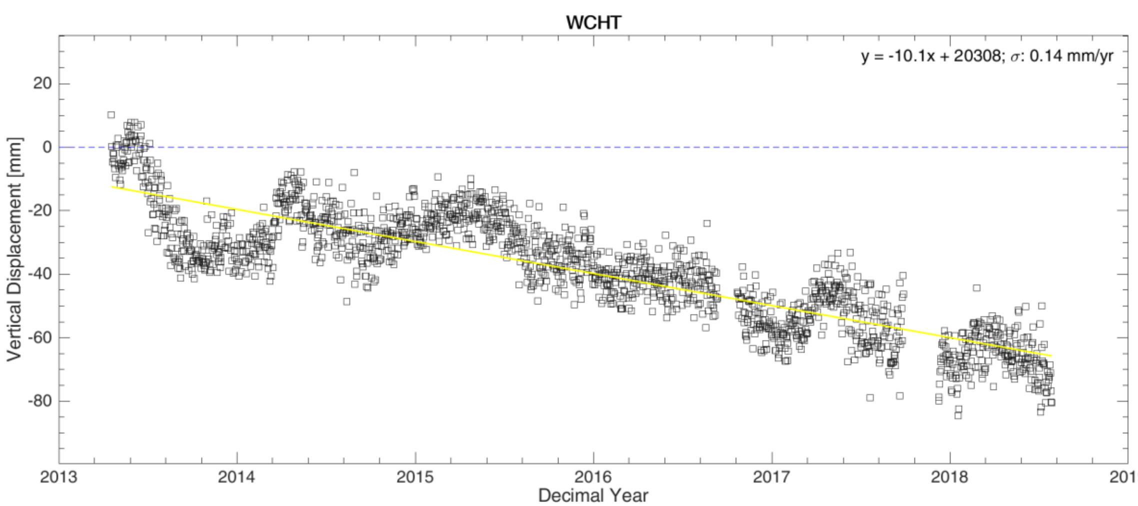
WCHT
y = -10.1x + 20308; σ: 0.14 mm/yr
Vertical Displacement [mm]
Decimal Year

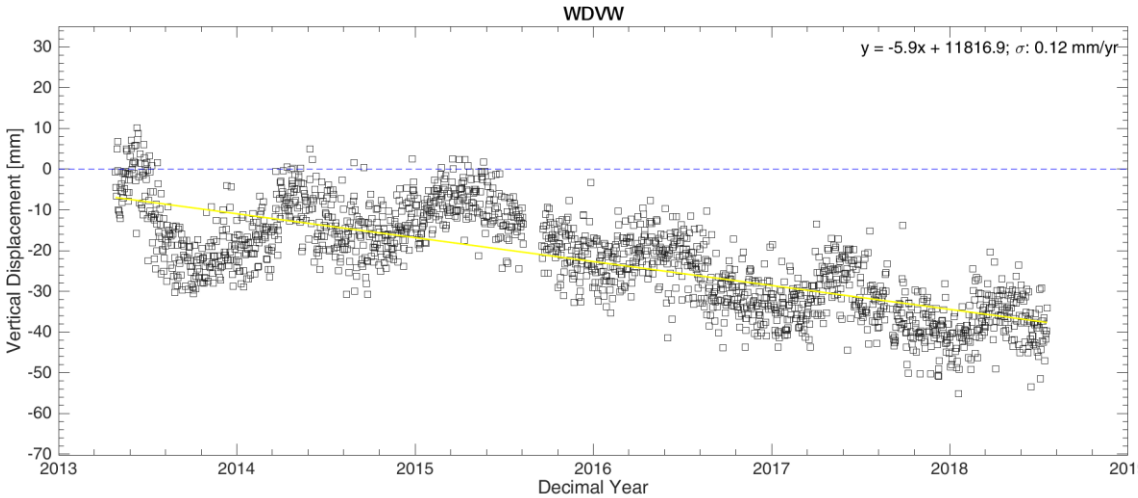
WDVW
y = -5.9x + 11816.9; σ: 0.12 mm/yr
Vertical Displacement [mm]
Decimal Year

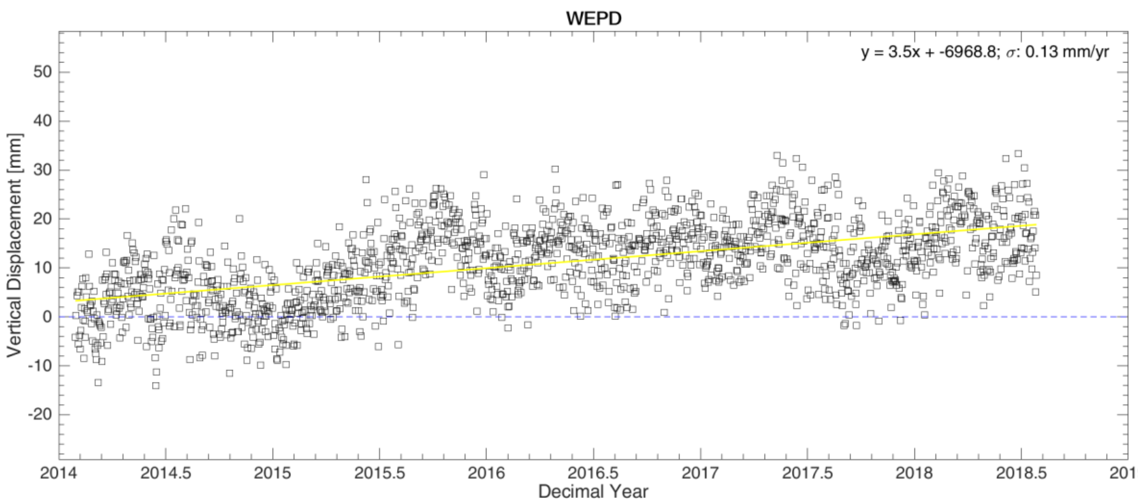
WEPD
y = 3.5x + -6968.8; σ: 0.13 mm/yr
Vertical Displacement [mm]
Decimal Year

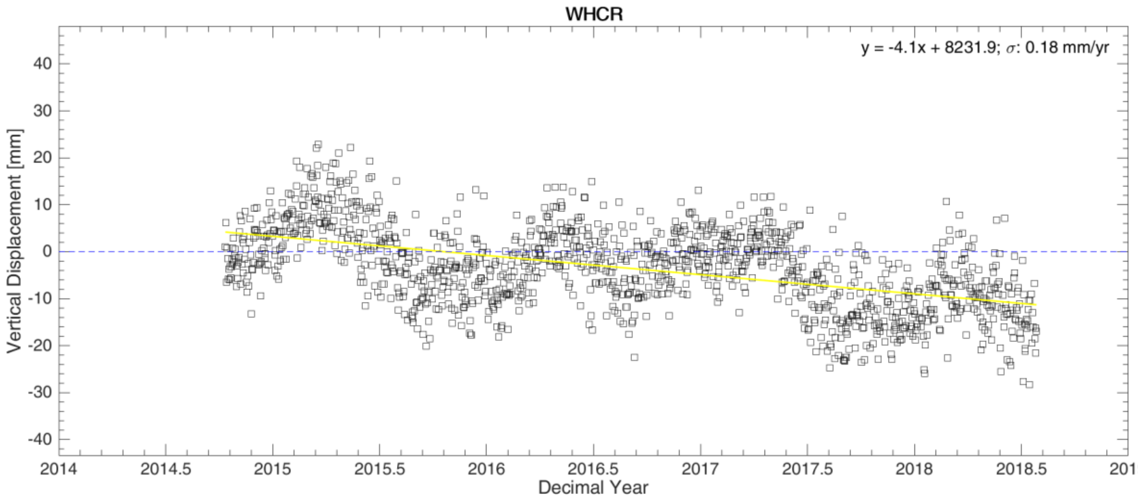
WHCR
y = -4.1x + 8231.9; σ: 0.18 mm/yr
Vertical Displacement [mm]
40
30
20
10
0
-10
-20
-30
-40
2014
2014.5
2015
2015.5
2016
2016.5
2017
2017.5
2018
2018.5
2019
Decimal Year

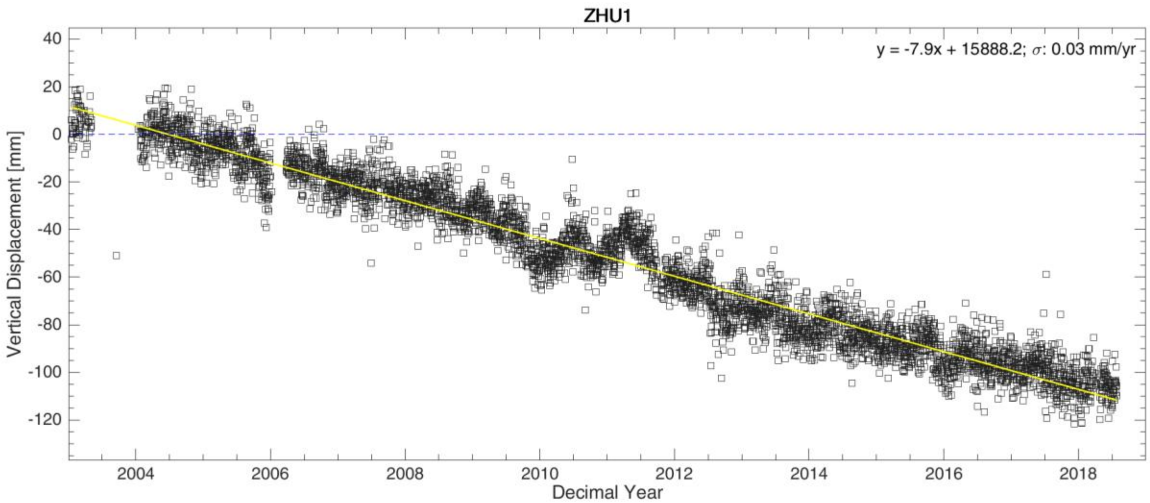
ZHU1
y = -7.9x + 15888.2; σ: 0.03 mm/yr
Vertical Displacement [mm]
40
20
0
-20
-40
-60
-80
-100
-120
2004
2006
2008
2010
2012
2014
2016
2018
Decimal Year

Table AI: Tabulation of GPS site locations, sampling history and respective vertical displacement rate from 2000-2018.

GPS Station	Longitude	Latitude	Site History [years]	Vertical Dis. Rate [mm]	Standard Error (σ) [mm/year]
ADKS	-95.58641	29.79097	16.42	-0.6	0.03
ALEF	-95.63505	29.69183	4.31	-7.4	0.16
ALVN	-95.27762	29.40066	4.78	-0.7	0.13
ANG5	-95.48508	29.30148	10.71	-1.6	0.04
AULT	-95.74466	29.99777	2.86	-9.7	0.24
BEA5	-94.93735	29.75691	4.68	3.3	0.13
CFHS	-95.63193	29.91923	2.86	-14.3	0.25
CFJV	-95.55584	29.88165	2.8	-10.6	0.26
CLVD	-95.09359	30.33505	4.48	-3.2	0.13
CMFB	-95.72879	29.68136	4.16	-4.3	0.14
COH1	-95.54261	29.67034	8.7	-1.3	0.09
COH2	-95.41161	29.62853	9.57	-0.2	0.07
COTM	-94.9982	29.39384	3.47	-3.3	0.18
CSTE	-95.51074	29.79564	3.18	-7.7	0.23
DEN1	-95.25801	29.51041	5.56	-0.6	0.1
DEN2	-95.25396	29.50488	5.31	1	0.11
DEN3	-95.25464	29.49372	5.56	0.5	0.1
DISD	-95.74041	29.28927	3.09	-1	0.2
DMFB	-95.58374	29.62265	3.8	-8.5	0.18
DWI1	-95.40366	29.0136	9.17	-0.9	0.05
FSFB	-95.63045	29.55618	4.2	-0.3	0.15
GSEC	-95.52809	30.1973	2.81	-6.9	0.27
HCC1	-95.56122	29.78787	5.66	-7.6	0.12
HCC2	-95.56202	29.78839	5.27	-8.8	0.14
HPEK	-95.71572	29.75488	4	-11.3	0.16
HSMN	-95.46962	29.80035	5.27	-5.5	0.11
KKES	-95.59493	29.85033	2.97	-11	0.25
LCBR	-96.60192	30.18236	5.55	-0.3	0.09
LCI1	-95.4425	29.80747	6.11	-3.8	0.1
LGC1	-94.07455	30.0446	5.04	-2.1	0.1
LKHU	-95.14576	29.91346	18.57	0.2	0.02
MDWD	-95.59521	29.77138	5.27	-6.3	0.15
MEPD	-95.23959	29.65808	4.53	1.7	0.12
MRHK	-95.74514	29.80414	4.18	-15.1	0.15
NASA	-95.09622	29.55195	3.88	-1.4	0.19
NAV2	-96.06673	30.38162	4.68	-1.1	0.11
NETP	-95.33422	29.79116	16.43	0.9	0.03
OKEK	-95.80331	29.72503	3.99	-7.6	0.17
PA00	-95.15224	29.53862	18.49	1.1	0.05
PA01	-95.61662	29.91188	18.5	-18.2	0.17
PA02	-95.41587	30.00065	18.4	-22.2	0.09
PA03	-95.61338	29.82081	18.47	-14.7	0.17
PA04	-95.59686	29.63039	18.49	-8.7	0.12
PA05	-95.58591	29.79121	18.43	-9.3	0.11
PA06	-95.67779	29.81637	18.47	-24.5	0.13
PA07	-95.57665	29.9363	18.49	-24.6	0.19
PA08	-95.47627	29.97968	18.55	-22	0.13
PA09	-95.07146	30.03813	18.53	-4.9	0.09
PA10	-95.79918	29.56639	18.59	-3.7	0.04
PA11	-95.86522	30.03216	18.58	-7.5	0.07
PA13	-95.48999	30.19481	17.05	-17.2	0.07
PA14	-95.64411	29.47366	17.62	-5.9	0.05
PA16	-95.52724	29.54446	17.67	-4	0.1
PA17	-95.6153	30.09116	17.65	-17.3	0.09
PA18	-95.67823	29.96493	17.5	-20.1	0.1

Table AI *continued*

PA19	-95.80535	29.84112	17.71	-9.9	0.05
PA20	-95.01324	29.53291	16.48	1.1	0.06
PA21	-95.31207	29.54547	16.36	-2.1	0.05
PA22	-95.02071	29.33452	16.56	-2.5	0.05
PA23	-94.91778	29.33508	16.54	1	0.05
PA24	-95.04078	29.6688	16.36	1.8	0.05
PA26	-94.93833	29.21032	16.42	-1.3	0.03
PA27	-95.01555	29.58314	16.15	-2.4	0.05
PA29	-95.82219	29.76902	11.24	-16.7	0.13
PA30	-95.90192	29.68925	11.21	-4.4	0.13
PA31	-95.84838	29.39802	11.15	2.6	0.15
PA32	-95.70731	29.5406	11.13	-0.1	0.15
PA33	-95.22357	29.48991	12.24	-2.4	0.1
PA34	-95.04167	29.42219	8.25	-3.8	0.06
PA35	-95.08244	29.47262	11.88	1.5	0.12
PA36	-94.94162	29.49418	11.4	-2.2	0.16
PA37	-95.10101	29.63071	11.17	3.1	0.12
PA38	-95.22295	29.64927	11.22	2.4	0.15
PA40	-95.4625	29.49329	11.16	-5.3	0.21
PA41	-95.4755	29.66191	11.21	-4.8	0.35
PA42	-95.63535	29.73249	11.13	-5.3	0.18
PA43	-95.1106	29.09325	12.07	-0.1	0.06
PA44	-95.68686	29.88013	11.18	-11.7	0.2
PA45	-95.38545	29.8759	11.25	-3.8	0.16
PA46	-95.60006	30.02997	11.22	-20.6	0.16
PA47	-95.42354	30.08955	11.22	-19.7	0.25
PA48	-95.67171	30.04536	11.24	-15.4	0.12
PA49	-94.70153	29.42245	12.33	-3.7	0.07
PA50	-94.85604	29.84834	11.4	-1.6	0.16
PA51	-95.2842	29.93254	11.26	-5.5	0.21
PA52	-95.17674	29.85202	11.26	-1.5	0.2
PA53	-95.05729	29.90803	11.03	-2.3	0.27
PA54	-95.03439	29.80147	11.71	-1.2	0.14
PA55	-95.1772	29.79419	11.67	1.4	0.14
PA56	-95.81677	29.90262	11.28	-5.5	0.18
PA57	-95.72182	29.68406	9.41	-3.5	0.18
PA59	-95.74042	29.61666	7.89	-2.6	0.3
PA61	-95.97244	29.67539	7.45	-3.4	0.36
PA62	-95.97419	29.59329	7.45	-4.8	0.19
PA63	-95.54741	29.50787	7.09	-2.8	0.33
PA66	-95.76665	30.01717	7.39	-14.6	0.38
PA67	-95.85479	29.53177	7.36	-4.6	0.26
PA68	-95.58681	30.18483	6.81	-11.9	0.22
PA69	-95.45894	30.19897	6.8	-13.1	0.28
PA70	-95.42432	30.29111	6.81	-7.7	0.48
PA71	-95.57886	30.35301	6.8	-6.8	0.21
PA73	-95.73022	30.19343	6.55	-9.7	0.24
PA76	-95.04547	29.36089	5.85	-7.6	0.28
PA79	-95.47127	29.0348	3.72	0.4	0.16
PA80	-95.16513	29.5781	3.72	1.1	0.17
PA81	-95.1698	29.55577	3.73	1.1	0.16
PWES	-95.51057	30.19899	3.35	-7.4	0.26
RDCT	-95.49472	29.81042	5.01	-5.5	0.14
ROD1	-95.5268	30.07235	11.57	-12.1	0.05
RPFB	-95.51365	29.48417	3.8	-1	0.15
SESG	-95.42962	29.98747	3.89	-9	0.15
SHSG	-95.43005	30.05361	3.72	-11	0.17
SISD	-96.17388	29.76219	3.39	-3.7	0.19

Table AI *continued*

SPBH	-95.51504	29.8019	5.27	-6.1	0.12
TDAM	-94.81695	29.31406	5.14	-2	0.1
THSU	-95.33991	29.71401	5.62	1.2	0.09
TMCC	-95.39524	29.70232	15.19	3.7	0.04
TSFT	-95.47996	29.80629	5.19	-5.8	0.14
TXAC	-94.67146	29.7778	7.45	-0.1	0.06
TXAG	-95.41902	29.16416	12.99	-0.6	0.03
TXBC	-95.97237	28.99981	9.17	-1.6	0.04
TXBM	-94.17971	30.16172	13.8	-0.8	0.04
TXCF	-96.57228	29.70366	3.5	1.3	0.2
TXCM	-96.57732	29.70284	8.13	-1.9	0.05
TXCN	-95.44121	30.34895	12.99	-12.5	0.03
TXED	-96.63403	28.96824	9.14	-0.1	0.05
TXEX	-95.11919	29.56366	7.72	1.6	0.06
TXGA	-94.77264	29.32787	12.99	-1.5	0.03
TXHE	-96.06349	30.09903	12.99	-6.1	0.04
TXHS	-95.55551	29.71608	6.11	-6.3	0.11
TXKY	-95.8294	29.82202	4.78	-9.4	0.12
TXLG	-96.8483	29.91675	7.69	-1.9	0.06
TXLI	-94.77103	30.05589	12.99	0.8	0.03
TXLM	-95.02369	29.39222	12.99	-3.1	0.03
TXLQ	-94.95285	29.35796	5.51	0.6	0.09
TXMG	-95.96355	28.9829	5.26	-2.3	0.11
TXPV	-96.61853	28.63818	8.28	0.3	0.06
TXRS	-95.8053	29.5192	7.12	-2.3	0.06
TXTG	-95.29738	29.89752	3.1	-3.4	0.21
TXVA	-96.9096	28.83493	13.48	-0.8	0.03
TXWH	-96.11175	29.32462	8.14	-3.8	0.06
TXWI	-94.37147	29.80577	3.09	-4	0.21
TXWN	-96.09205	29.32876	3.56	-0.9	0.18
UH01	-95.3454	29.72246	5.83	-0.3	0.09
UH02	-95.45715	30.31522	3.57	-5.5	0.19
UHC0	-95.04385	29.39037	4.11	-3.5	0.15
UHC1	-95.04397	29.39037	4.08	-3.2	0.14
UHC2	-95.04393	29.39037	4.11	-3.3	0.13
UHC3	-95.04389	29.39037	4.11	-4.4	0.13
UHCL	-95.10416	29.57774	4.33	0.8	0.13
UHCR	-95.75677	29.72807	4.27	-7.7	0.17
UHDT	-95.35944	29.76596	5.01	-1.2	0.11
UHEB	-96.06604	29.52631	3.98	-1.8	0.14
UHEP	-95.32712	29.71946	4.15	-1.3	0.15
UHF1	-95.4831	30.23625	3.99	-5.6	0.25
UHJF	-95.48307	30.23627	3.99	-2.8	0.21
UHL1	-94.97846	30.05765	4.21	4	0.2
UHRI	-95.40252	29.71923	4.24	-2.6	0.15
UHSL	-95.65154	29.57467	4.3	-2.8	0.14
UHWL	-94.97843	30.05764	4.21	-0.5	0.14
UTEX	-95.56782	29.78589	6.08	-7	0.11
WCHT	-95.58142	29.78283	5.28	-10.1	0.14
WDVW	-95.53307	29.79039	5.23	-5.9	0.12
WEPD	-95.22873	29.68773	4.49	3.5	0.13
WHCR	-95.5054	30.19432	3.79	-4.1	0.18
ZHU1	-95.33143	29.9619	15.53	-7.9	0.03

APPENDIX II: TABLE OF VALUES FOR CHICOT AND EVANGELINE AQUIFER ANALYSIS

Table AII-I: Tabulation of groundwater well information for the Chicot aquifer.

Site ID	Well Depth [m]	Longitude	Latitude	Hydraulic Head (2000) [m]	Hydraulic Head (2018) [m]	Difference [m]
285537095214001	68	-95.3617	28.9269	-13.85	-8.76	5.09
285654095215101	76	-95.3644	28.9489	-13.32	-9.16	4.16
285744095212102	79	-95.3561	28.9625	-10.08	-6.51	3.58
285919095344701	154	-95.5814	28.9889	-14.91	-15.97	-1.06
290000095192602	71	-95.3247	28.9997	-12.20	-11.57	0.62
290216095420102	57	-95.7006	29.0381	-13.69	-12.99	0.70
291138095261501	250	-95.4378	29.1942	-20.85	-22.46	-1.60
291201095200701	293	-95.3356	29.2006	-15.22	-10.97	4.25
291210095484001	144	-95.8114	29.2031	-14.40	-14.64	-0.25
291305095352201	264	-95.5894	29.2197	-21.24	-21.37	-0.13
291338095202401	72	-95.3403	29.2275	-3.77	-3.60	0.17
291344095205101	93	-95.3478	29.2292	-10.29	-9.68	0.61
291545095202401	157	-95.3407	29.2626	-13.87	-14.17	-0.30
291859095152601	107	-95.2575	29.3167	-22.73	-24.11	-1.38
291948095135401	122	-95.2319	29.3303	-22.77	-22.41	0.36
291949095024801	230	-95.0469	29.3306	-20.90	-19.19	1.71
292037095010501	329	-95.0183	29.3439	-18.02	-16.66	1.36
292054095171901	144	-95.2889	29.3486	-23.60	-22.95	0.65
292207094544001	197	-94.9114	29.3689	-15.82	-12.39	3.43
292208095042701	236	-95.0744	29.3692	-22.74	-20.94	1.80
292303094553201	222	-94.9258	29.3844	-17.63	-14.23	3.39
292314094563001	214	-94.9419	29.3875	-14.10	-10.39	3.71
292324094573801	225	-94.9608	29.3903	-17.95	-13.91	4.04
292335095133501	222	-95.2264	29.3931	-42.69	-38.88	3.82
292337094542801	235	-94.9081	29.3939	-17.37	-12.85	4.51
292338095063601	265	-95.1103	29.3942	-31.53	-26.41	5.12
292403095052601	235	-95.0908	29.4011	-31.14	-26.18	4.96
292439094553101	239	-94.9256	29.4111	-16.85	-14.85	2.01
292443095045201	238	-95.0814	29.4122	-31.18	-26.43	4.75
292456095560101	172	-95.9339	29.4158	-15.15	-16.03	-0.88
292458094534201	64	-94.8953	29.4164	-7.82	-6.16	1.66
292458094534202	92	-94.8953	29.4164	-10.44	-8.80	1.65
292458094534203	122	-94.8953	29.4164	-11.67	-9.66	2.01
292458094534204	163	-94.8953	29.4164	-15.92	-13.14	2.78
292458094534206	244	-94.8950	29.4163	-15.86	-13.82	2.04
292458094534207	7	-94.8953	29.4164	-3.79	-3.63	0.16
292459095451901	194	-95.7556	29.4167	-12.95	-13.35	-0.40
292534095044501	247	-95.0794	29.4264	-30.46	-26.22	4.24
292535095151801	210	-95.2553	29.4267	-47.73	-47.59	0.14
292548094565601	211	-94.9494	29.4303	-15.67	-8.70	6.97
292605095571301	180	-95.9539	29.4350	-14.46	-15.68	-1.22
292619095060601	229	-95.1019	29.4389	-32.13	-27.59	4.54
292841094584901	201	-94.9836	29.4808	-25.07	-20.47	4.61
292848094590001	198	-94.9808	29.4783	-25.35	-20.81	4.54
292859095380501	260	-95.6350	29.4833	-42.12	-44.18	-2.06
292900094585501	202	-94.9825	29.4833	-25.49	-21.87	3.61
292903095375501	214	-95.6322	29.4844	-36.88	-37.12	-0.24
292913094584301	203	-94.9786	29.4869	-26.52	-22.15	4.37
292927095195801	146	-95.3331	29.4914	-29.76	-31.10	-1.34
292935094583301	204	-94.9775	29.4925	-31.52	-20.46	11.07

Table AII-I *continued*

292941094563001	204	-94.9419	29.4950	-19.88	-16.25	3.63
292951095335201	114	-95.5647	29.4978	-24.53	-26.01	-1.48
293000095171201	189	-95.2558	29.5503	-50.41	-46.51	3.89
293001095274601	160	-95.4631	29.5006	-34.24	-38.62	-4.39
293005095151801	180	-95.2553	29.5147	-48.91	-34.36	14.54
293007096002001	82	-96.0058	29.5022	-14.97	-15.94	-0.97
293114096001001	93	-96.0031	29.5208	-15.55	-17.05	-1.50
293202095070301	197	-95.1183	29.5331	-40.94	-34.57	6.37
293222095020301	180	-95.0344	29.5397	-34.90	-28.74	6.16
293243095165201	253	-95.2811	29.5461	-55.49	-51.41	4.09
293247095054601	207	-95.0961	29.5464	-39.66	-32.41	7.24
293253095141001	188	-95.2358	29.5483	-48.14	-44.00	4.14
293306095050801	207	-95.0844	29.5519	-36.90	-30.09	6.81
293338095451901	152	-95.7556	29.5608	-22.66	-22.47	0.19
293344095082301	194	-95.1403	29.5628	-45.38	-37.49	7.89
293348095070602	119	-95.1186	29.5636	-34.23	-29.11	5.12
293352095011604	46	-95.0214	29.5647	-5.58	-4.79	0.79
293352095011605	91	-95.0214	29.5647	-22.62	-19.36	3.26
293352095011607	7	-95.0214	29.5647	-1.91	-1.37	0.54
293357095070801	192	-95.1192	29.5661	-41.43	-33.99	7.44
293401095293002	164	-95.4917	29.4008	-32.24	-30.75	1.49
293446095033901	201	-95.0608	29.5797	-38.11	-30.69	7.42
293453095283501	172	-95.4767	29.5817	-69.88	-61.35	8.53
293455095375701	141	-95.6328	29.5822	-43.63	-40.79	2.84
293458095454301	158	-95.7622	29.5831	-31.29	-29.03	2.26
293458095454501	131	-95.7628	29.5831	-29.78	-28.34	1.44
293506095481101	93	-95.8033	29.5853	-20.77	-22.69	-1.92
293528095515701	129	-95.8692	29.5922	-19.74	-20.25	-0.51
293539095054201	186	-95.0981	29.5933	-39.58	-33.50	6.08
293730095443301	96	-95.7428	29.6253	-26.68	-27.38	-0.70
293812095380901	167	-95.6361	29.6369	-62.19	-55.81	6.39
293909095012201	176	-95.0231	29.6528	-37.76	-28.28	9.48
293949095024301	178	-95.0456	29.6639	-37.27	-32.98	4.29
293959095380401	275	-95.6353	29.6667	-73.53	-58.86	14.67
294031095554201	137	-95.9286	29.6756	-16.38	-18.83	-2.45
294158095024701	180	-95.0467	29.6997	-40.64	-31.41	9.23
294206095162602	20	-95.2742	29.7019	-4.43	-4.11	0.31
294219095583601	115	-95.9769	29.7056	-13.44	-14.74	-1.29
294237095093202	119	-95.1592	29.7106	-42.64	-36.26	6.38
294237095093203	30	-95.1592	29.7106	-4.18	-3.89	0.29
294302095411801	195	-95.6883	29.7175	-40.47	-46.33	-5.86
294322095041701	165	-95.0717	29.7231	-40.40	-29.13	11.27
294329095284603	197	-95.4797	29.7250	-86.84	-57.23	29.61
294334095032901	155	-95.0581	29.7269	-31.75	-29.02	2.73
294338095270405	77	-95.4514	29.7275	-52.81	-47.33	5.48
294338095270406	191	-95.4514	29.7275	-71.39	-64.53	6.86
294342095034601	171	-95.0631	29.7286	-40.30	-31.69	8.61
294433095044701	78	-95.0800	29.7428	-33.06	-27.52	5.54
294433095044702	39	-95.0800	29.7428	-4.06	-3.76	0.30
294433095044703	26	-95.0800	29.7428	-4.08	-3.77	0.31
294458095044601	159	-95.0797	29.7497	-38.58	-30.12	8.47
294527095014901	156	-95.0306	29.7578	-35.96	-29.77	6.20
294527095014902	34	-95.0306	29.7578	-6.54	-6.34	0.19
294527095014903	52	-95.0306	29.7578	-25.62	-22.01	3.61
294527095014905	99	-95.0306	29.7578	-33.67	-28.95	4.72
294527095014910	131	-95.0307	29.7578	-35.46	-30.48	4.98
294527095014913	18	-95.0306	29.7578	-3.83	-2.99	0.84
294538095344601	142	-95.5792	29.7608	-54.63	-51.82	2.81

Table AII-I *continued*

294601095041901	141	-95.0736	29.7672	-35.65	-28.51	7.14
294602095092403	64	-95.1569	29.7675	-38.69	-32.46	6.23
294637095022901	152	-95.0417	29.7772	-36.10	-28.80	7.30
294726095351101	15	-95.5867	29.7908	-3.94	-3.74	0.20
294726095351104	72	-95.5867	29.7908	-50.59	-48.97	1.62
294728095200103	148	-95.3339	29.7914	-64.87	-51.04	13.83
294728095200105	91	-95.3339	29.7914	-46.02	-40.59	5.43
294807095484901	73	-95.8192	29.8028	-40.51	-43.03	-2.52
294924095024301	155	-95.0456	29.8236	-34.95	-29.00	5.95
294932094551401	114	-94.9208	29.8258	-30.16	-26.11	4.05
295207095262102	172	-95.4364	29.8686	-83.07	-62.17	20.90
295449095083401	60	-95.1431	29.9139	-27.78	-24.48	3.29
295451095083901	165	-95.1444	29.9144	-49.49	-43.05	6.44
295651095083501	156	-95.1381	29.9456	-51.06	-40.41	10.65
295817095065501	169	-95.1175	29.9722	-38.89	-35.45	3.44
300007095354701	93	-95.5958	30.0019	-43.55	-43.63	-0.08
300447095444101	92	-95.7447	30.0797	-37.63	-40.26	-2.63
300457095245801	69	-95.4164	30.0828	-19.87	-20.89	-1.02
300720095165701	87	-95.2828	30.1225	-43.78	-46.31	-2.52
301358095343301	82	-95.5758	30.2328	-27.17	-28.61	-1.43
301948095290002	80	-95.4836	30.3303	-25.79	-27.33	-1.55
301948095290003	33	-95.4836	30.3300	-16.02	-16.89	-0.87
301948095290004	24	-95.4836	30.3303	-15.97	-16.97	-1.00
285537095214001	68	-95.3617	28.9269	-13.85	-8.76	5.09
285654095215101	76	-95.3644	28.9489	-13.32	-9.16	4.16
285744095212102	79	-95.3561	28.9625	-10.08	-6.51	3.58
285919095344701	154	-95.5814	28.9889	-14.91	-15.97	-1.06
290000095192602	71	-95.3247	28.9997	-12.20	-11.57	0.62
290216095420102	57	-95.7006	29.0381	-13.69	-12.99	0.70
291138095261501	250	-95.4378	29.1942	-20.85	-22.46	-1.60
291201095200701	293	-95.3356	29.2006	-15.22	-10.97	4.25
291210095484001	144	-95.8114	29.2031	-14.40	-14.64	-0.25
291305095352201	264	-95.5894	29.2197	-21.24	-21.37	-0.13
291338095202401	72	-95.3403	29.2275	-3.77	-3.60	0.17
291344095205101	93	-95.3478	29.2292	-10.29	-9.68	0.61
291545095202401	157	-95.3407	29.2626	-13.87	-14.17	-0.30
291859095152601	107	-95.2575	29.3167	-22.73	-24.11	-1.38
291948095135401	122	-95.2319	29.3303	-22.77	-22.41	0.36
291949095024801	230	-95.0469	29.3306	-20.90	-19.19	1.71
292037095010501	329	-95.0183	29.3439	-18.02	-16.66	1.36
292054095171901	144	-95.2889	29.3486	-23.60	-22.95	0.65
292207094544001	197	-94.9114	29.3689	-15.82	-12.39	3.43
292208095042701	236	-95.0744	29.3692	-22.74	-20.94	1.80
292303094553201	222	-94.9258	29.3844	-17.63	-14.23	3.39
292314094563001	214	-94.9419	29.3875	-14.10	-10.39	3.71
292324094573801	225	-94.9608	29.3903	-17.95	-13.91	4.04
292335095133501	222	-95.2264	29.3931	-42.69	-38.88	3.82
292337094542801	235	-94.9081	29.3939	-17.37	-12.85	4.51
292338095063601	265	-95.1103	29.3942	-31.53	-26.41	5.12
292403095052601	235	-95.0908	29.4011	-31.14	-26.18	4.96
292439094553101	239	-94.9256	29.4111	-16.85	-14.85	2.01
292443095045201	238	-95.0814	29.4122	-31.18	-26.43	4.75
292456095560101	172	-95.9339	29.4158	-15.15	-16.03	-0.88
292458094534201	64	-94.8953	29.4164	-7.82	-6.16	1.66
292458094534202	92	-94.8953	29.4164	-10.44	-8.80	1.65
292458094534203	122	-94.8953	29.4164	-11.67	-9.66	2.01
292458094534204	163	-94.8953	29.4164	-15.92	-13.14	2.78
292458094534206	244	-94.8950	29.4163	-15.86	-13.82	2.04

Table AII-I *continued*

292458094534207	7	-94.8953	29.4164	-3.79	-3.63	0.16
292459095451901	194	-95.7556	29.4167	-12.95	-13.35	-0.40
292534095044501	247	-95.0794	29.4264	-30.46	-26.22	4.24
292535095151801	210	-95.2553	29.4267	-47.73	-47.59	0.14
292548094565601	211	-94.9494	29.4303	-15.67	-8.70	6.97
292605095571301	180	-95.9539	29.4350	-14.46	-15.68	-1.22
292619095060601	229	-95.1019	29.4389	-32.13	-27.59	4.54
292841094584901	201	-94.9836	29.4808	-25.07	-20.47	4.61
292848094590001	198	-94.9808	29.4783	-25.35	-20.81	4.54
292859095380501	260	-95.6350	29.4833	-42.12	-44.18	-2.06
292900094585501	202	-94.9825	29.4833	-25.49	-21.87	3.61
292903095375501	214	-95.6322	29.4844	-36.88	-37.12	-0.24
292913094584301	203	-94.9786	29.4869	-26.52	-22.15	4.37
292927095195801	146	-95.3331	29.4914	-29.76	-31.10	-1.34
292935094583301	204	-94.9775	29.4925	-31.52	-20.46	11.07
292941094563001	204	-94.9419	29.4950	-19.88	-16.25	3.63
292951095335201	114	-95.5647	29.4978	-24.53	-26.01	-1.48
293000095171201	189	-95.2558	29.5503	-50.41	-46.51	3.89
293001095274601	160	-95.4631	29.5006	-34.24	-38.62	-4.39
293005095151801	180	-95.2553	29.5147	-48.91	-34.36	14.54
293007096002001	82	-96.0058	29.5022	-14.97	-15.94	-0.97
293114096001001	93	-96.0031	29.5208	-15.55	-17.05	-1.50
293202095070301	197	-95.1183	29.5331	-40.94	-34.57	6.37
293222095020301	180	-95.0344	29.5397	-34.90	-28.74	6.16
293243095165201	253	-95.2811	29.5461	-55.49	-51.41	4.09
293247095054601	207	-95.0961	29.5464	-39.66	-32.41	7.24
293253095141001	188	-95.2358	29.5483	-48.14	-44.00	4.14
293306095050801	207	-95.0844	29.5519	-36.90	-30.09	6.81
293338095451901	152	-95.7556	29.5608	-22.66	-22.47	0.19
293344095082301	194	-95.1403	29.5628	-45.38	-37.49	7.89
293348095070602	119	-95.1186	29.5636	-34.23	-29.11	5.12
293352095011604	46	-95.0214	29.5647	-5.58	-4.79	0.79
293352095011605	91	-95.0214	29.5647	-22.62	-19.36	3.26
293352095011607	7	-95.0214	29.5647	-1.91	-1.37	0.54
293357095070801	192	-95.1192	29.5661	-41.43	-33.99	7.44
293401095293002	164	-95.4917	29.4008	-32.24	-30.75	1.49
293446095033901	201	-95.0608	29.5797	-38.11	-30.69	7.42
293453095283501	172	-95.4767	29.5817	-69.88	-61.35	8.53
293455095375701	141	-95.6328	29.5822	-43.63	-40.79	2.84
293458095454301	158	-95.7622	29.5831	-31.29	-29.03	2.26
293458095454501	131	-95.7628	29.5831	-29.78	-28.34	1.44
293506095481101	93	-95.8033	29.5853	-20.77	-22.69	-1.92
293528095515701	129	-95.8692	29.5922	-19.74	-20.25	-0.51
293539095054201	186	-95.0981	29.5933	-39.58	-33.50	6.08
293730095443301	96	-95.7428	29.6253	-26.68	-27.38	-0.70
293812095380901	167	-95.6361	29.6369	-62.19	-55.81	6.39
293909095012201	176	-95.0231	29.6528	-37.76	-28.28	9.48
293949095024301	178	-95.0456	29.6639	-37.27	-32.98	4.29
293959095380401	275	-95.6353	29.6667	-73.53	-58.86	14.67
294031095554201	137	-95.9286	29.6756	-16.38	-18.83	-2.45
294158095024701	180	-95.0467	29.6997	-40.64	-31.41	9.23
294206095162602	20	-95.2742	29.7019	-4.43	-4.11	0.31
294219095583601	115	-95.9769	29.7056	-13.44	-14.74	-1.29
294237095093202	119	-95.1592	29.7106	-42.64	-36.26	6.38
294237095093203	30	-95.1592	29.7106	-4.18	-3.89	0.29
294302095411801	195	-95.6883	29.7175	-40.47	-46.33	-5.86
294322095041701	165	-95.0717	29.7231	-40.40	-29.13	11.27
294329095284603	197	-95.4797	29.7250	-86.84	-57.23	29.61

Table AII-I *continued*

294334095032901	155	-95.0581	29.7269	-31.75	-29.02	2.73
294338095270405	77	-95.4514	29.7275	-52.81	-47.33	5.48
294338095270406	191	-95.4514	29.7275	-71.39	-64.53	6.86
294342095034601	171	-95.0631	29.7286	-40.30	-31.69	8.61
294433095044701	78	-95.0800	29.7428	-33.06	-27.52	5.54
294433095044702	39	-95.0800	29.7428	-4.06	-3.76	0.30
294433095044703	26	-95.0800	29.7428	-4.08	-3.77	0.31
294458095044601	159	-95.0797	29.7497	-38.58	-30.12	8.47
294527095014901	156	-95.0306	29.7578	-35.96	-29.77	6.20
294527095014902	34	-95.0306	29.7578	-6.54	-6.34	0.19
294527095014903	52	-95.0306	29.7578	-25.62	-22.01	3.61
294527095014905	99	-95.0306	29.7578	-33.67	-28.95	4.72
294527095014910	131	-95.0307	29.7578	-35.46	-30.48	4.98
294527095014913	18	-95.0306	29.7578	-3.83	-2.99	0.84
294538095344601	142	-95.5792	29.7608	-54.63	-51.82	2.81
294601095041901	141	-95.0736	29.7672	-35.65	-28.51	7.14
294602095092403	64	-95.1569	29.7675	-38.69	-32.46	6.23
294637095022901	152	-95.0417	29.7772	-36.10	-28.80	7.30
294726095351101	15	-95.5867	29.7908	-3.94	-3.74	0.20
294726095351104	72	-95.5867	29.7908	-50.59	-48.97	1.62
294728095200103	148	-95.3339	29.7914	-64.87	-51.04	13.83
294728095200105	91	-95.3339	29.7914	-46.02	-40.59	5.43
294807095484901	73	-95.8192	29.8028	-40.51	-43.03	-2.52
294924095024301	155	-95.0456	29.8236	-34.95	-29.00	5.95
294932094551401	114	-94.9208	29.8258	-30.16	-26.11	4.05
295207095262102	172	-95.4364	29.8686	-83.07	-62.17	20.90
295449095083401	60	-95.1431	29.9139	-27.78	-24.48	3.29
295451095083901	165	-95.1444	29.9144	-49.49	-43.05	6.44
295651095083501	156	-95.1381	29.9456	-51.06	-40.41	10.65
295817095065501	169	-95.1175	29.9722	-38.89	-35.45	3.44
300007095354701	93	-95.5958	30.0019	-43.55	-43.63	-0.08
300447095444101	92	-95.7447	30.0797	-37.63	-40.26	-2.63
300457095245801	69	-95.4164	30.0828	-19.87	-20.89	-1.02
300720095165701	87	-95.2828	30.1225	-43.78	-46.31	-2.52
301358095343301	82	-95.5758	30.2328	-27.17	-28.61	-1.43
301948095290002	80	-95.4836	30.3303	-25.79	-27.33	-1.55
301948095290003	33	-95.4836	30.3300	-16.02	-16.89	-0.87
301948095290004	24	-95.4836	30.3303	-15.97	-16.97	-1.00

Table AII-II: Tabulation of groundwater well information for the Chicot aquifer.

Site ID	Well Depth [m]	Longitude	Latitude	Hydraulic Head (2000) [m]	Hydraulic Head (2018) [m]	Difference [m]
292458094534205	323	-94.8953	29.4164	-16.18	-14.20	1.98
292603095150901	214	-95.2533	29.4347	-49.40	-46.34	3.05
292944095550101	297	-95.9172	29.4958	-27.43	-30.94	-3.50
293132095283301	402	-95.4761	29.5258	-64.38	-59.74	4.64
293219095485701	400	-95.8161	29.5389	-45.74	-50.53	-4.79
293226095471601	482	-95.7878	29.5406	-51.00	-56.58	-5.59
293237095504801	359	-95.8469	29.5439	-46.18	-51.85	-5.67
293306095054101	235	-95.0960	29.5519	-38.63	-31.67	6.96
293312095334601	325	-95.5611	29.5533	-65.15	-56.90	8.25
293314095474702	489	-95.7964	29.5531	-52.33	-55.00	-2.67
293321095311401	335	-95.5208	29.5561	-67.23	-57.59	9.64
293332095411301	592	-95.6869	29.5589	-77.79	-70.38	7.42
293340095400501	599	-95.6672	29.5606	-82.40	-71.75	10.65
293348095070601	376	-95.1186	29.5636	-41.94	-35.34	6.60
293348095070603	292	-95.1186	29.5636	-42.08	-35.75	6.32
293348095070604	936	-95.1189	29.5634	-38.01	-40.06	-2.05
293349095070901	530	-95.1193	29.5638	-47.10	-40.26	6.84
293352095011601	421	-95.0215	29.5648	-34.52	-28.54	5.98
293352095011602	421	-95.0214	29.5647	-34.71	-28.40	6.31
293352095011603	399	-95.0214	29.5647	-34.08	-27.75	6.33
293352095011606	280	-95.0214	29.5647	-33.18	-28.50	4.68
293424095330701	366	-95.5519	29.5739	-69.49	-60.72	8.77
293424095330702	402	-95.5522	29.5733	-68.87	-61.08	7.79
293434095311501	399	-95.5208	29.5761	-70.45	-61.00	9.45
293527095271501	320	-95.4544	29.5911	-72.94	-60.19	12.75
293543095274901	372	-95.4639	29.5956	-81.10	-72.48	8.62
293628095312801	383	-95.5239	29.6069	-75.72	-64.58	11.14
293729095440301	430	-95.7344	29.6175	-48.27	-44.25	4.02
293736095365501	507	-95.6167	29.6286	-95.09	-90.67	4.42
293810095370601	457	-95.6186	29.6369	-100.11	-87.56	12.55
293830095373201	541	-95.6261	29.6417	-84.49	-57.66	26.83
293921095441601	418	-95.7378	29.6558	-67.32	-57.29	10.03
293934095342201	314	-95.5731	29.6597	-91.05	-71.54	19.52
293938095351001	336	-95.5864	29.6608	-104.26	-66.15	38.10
293942095124901	283	-95.2128	29.6608	-52.37	-47.56	4.81
293942095283101	529	-95.4744	29.6619	-98.55	-72.38	26.17
293956095120801	421	-95.2025	29.6658	-60.10	-46.39	13.71
294010095350501	308	-95.5839	29.6664	-96.90	-67.44	29.46
294029095354301	364	-95.5956	29.6750	-87.66	-70.64	17.02
294044095280502	455	-95.4683	29.6792	-80.29	-66.65	13.64
294044095301001	539	-95.5031	29.6792	-86.06	-82.03	4.03
294106095171201	267	-95.2869	29.6853	-66.47	-46.51	19.96
294113095361701	508	-95.6050	29.6872	-119.14	-101.77	17.38
294119095335601	450	-95.5642	29.6919	-113.42	-99.69	13.72
294127095342502	442	-95.5739	29.6911	-104.71	-84.44	20.26
294144095410001	268	-95.6839	29.6956	-60.89	-52.47	8.42
294145095371201	425	-95.6203	29.6961	-99.56	-58.94	40.62
294206095162601	303	-95.2741	29.7017	-65.26	-49.49	15.76
294213095322001	460	-95.5392	29.7039	-91.29	-69.52	21.77
294215095301502	472	-95.5044	29.7044	-102.38	-89.73	12.65
294216095301601	296	-95.5047	29.7047	-80.88	-63.72	17.16
294219095470501	332	-95.7869	29.7081	-66.99	-76.87	-9.88
294237095093204	863	-95.1593	29.7102	-37.17	-29.04	8.13
294237095093205	405	-95.1592	29.7106	-57.38	-45.80	11.58
294237095093206	285	-95.1592	29.7106	-57.72	-45.93	11.79

Table AII-II *continued*

294237095093207	554	-95.1592	29.7106	-58.24	-44.74	13.49
294237095093208	223	-95.1592	29.7106	-56.63	-45.50	11.13
294237095342301	329	-95.5733	29.7106	-83.73	-73.19	10.54
294243095371201	418	-95.6203	29.7122	-97.76	-59.11	38.65
294301095341801	491	-95.5719	29.7172	-110.71	-93.65	17.06
294306095371801	398	-95.6219	29.7186	-101.62	-91.31	10.30
294313095365101	342	-95.6144	29.7206	-89.11	-63.62	25.48
294317095313001	491	-95.5239	29.7217	-96.35	-80.30	16.05
294326095293002	426	-95.4919	29.7242	-95.81	-87.74	8.07
294328095290402	463	-95.4847	29.7247	-87.40	-75.87	11.54
294338095270402	719	-95.4508	29.7270	-83.41	-67.20	16.21
294338095270403	592	-95.4514	29.7275	-92.33	-74.48	17.85
294338095270404	437	-95.4514	29.7275	-92.40	-76.57	15.83
294348095270401	599	-95.4514	29.7303	-98.14	-79.57	18.57
294352095385501	433	-95.6489	29.7314	-98.75	-60.10	38.65
294356095391501	244	-95.6544	29.7325	-66.60	-54.58	12.02
294403095141801	366	-95.2386	29.7344	-65.92	-42.12	23.80
294409095105501	600	-95.1822	29.7361	-70.48	-37.11	33.38
294414095364202	403	-95.6119	29.7375	-117.48	-102.33	15.15
294415095165301	274	-95.2817	29.7378	-61.13	-39.49	21.63
294442095450801	360	-95.7525	29.7453	-86.02	-93.94	-7.92
294445095141101	411	-95.2367	29.7461	-62.75	-43.15	19.60
294452095354501	442	-95.5961	29.7481	-115.73	-96.82	18.91
294500095073401	375	-95.1269	29.7506	-58.21	-42.85	15.36
294527095014911	450	-95.0307	29.7578	-39.14	-29.58	9.55
294527095014912	416	-95.0306	29.7578	-47.58	-37.89	9.69
294548095481401	312	-95.8047	29.7625	-67.37	-76.56	-9.18
294607095492201	202	-95.8222	29.7692	-60.32	-71.23	-10.91
294619095142701	307	-95.2419	29.7725	-66.11	-44.47	21.63
294627095375801	346	-95.6367	29.7542	-104.45	-91.07	13.38
294645095104401	372	-95.1792	29.7794	-62.30	-41.10	21.20
294656095382501	357	-95.6406	29.7825	-113.58	-104.35	9.23
294702095394001	393	-95.6639	29.7831	-109.04	-99.57	9.46
294712095401301	425	-95.6706	29.7869	-108.96	-94.54	14.42
294722095165901	273	-95.2833	29.7897	-68.13	-49.11	19.02
294723095370501	522	-95.6183	29.7900	-126.65	-109.14	17.51
294723095382601	377	-95.6408	29.7900	-112.32	-98.23	14.08
294724095351401	480	-95.5872	29.7903	-115.94	-78.36	37.57
294726095351102	549	-95.5861	29.7907	-119.25	-102.60	16.66
294728095200102	486	-95.3339	29.7914	-89.83	-64.36	25.47
294728095200104	315	-95.3339	29.7914	-75.75	-54.98	20.77
294728095200106	661	-95.3340	29.7909	-90.79	-69.89	20.90
294731095414201	407	-95.6944	29.7875	-111.34	-119.51	-8.17
294732095103401	365	-95.1769	29.7944	-59.98	-40.79	19.19
294747095444701	369	-95.7472	29.7969	-87.54	-109.18	-21.64
294753095454001	357	-95.7619	29.7972	-87.61	-102.97	-15.36
294800095344101	355	-95.5783	29.8003	-137.97	-102.80	35.17
294803095105701	354	-95.1828	29.8011	-64.54	-45.16	19.38
294808095485401	216	-95.8197	29.8025	-64.36	-100.01	-35.65
294820095342002	479	-95.5725	29.8058	-134.19	-101.84	32.35
294901095221001	351	-95.3697	29.8172	-76.03	-52.79	23.25
294916095314601	443	-95.5297	29.8214	-138.10	-105.15	32.95
294925095341201	466	-95.5703	29.8247	-138.37	-104.12	34.25
294930095125401	457	-95.2153	29.8253	-67.66	-49.93	17.73
294932095132601	472	-95.2242	29.8258	-79.73	-65.02	14.70
294950095313702	461	-95.5272	29.8308	-180.47	-111.44	69.03
294953095065601	480	-95.1158	29.8317	-19.59	-3.97	15.63
295005095070301	465	-95.1178	29.8350	-74.70	-70.14	4.56

Table AII-II *continued*

295005095071301	479	-95.1206	29.8350	-63.06	-47.45	15.61
295027095312301	450	-95.5233	29.8411	-161.29	-104.98	56.30
295203095261401	498	-95.4378	29.8675	-140.70	-124.50	16.20
295204095261301	328	-95.4375	29.8675	-123.61	-105.51	18.10
295218095572701	256	-95.9578	29.8719	-36.37	-37.79	-1.42
295228095065101	496	-95.1147	29.8747	-50.26	-38.52	11.74
295228095263101	506	-95.4419	29.8744	-139.41	-125.93	13.47
295229095062701	478	-95.1078	29.8750	-57.83	-42.98	14.84
295229095074101	490	-95.1278	29.8756	-58.02	-45.50	12.53
295240095375601	417	-95.6325	29.8769	-149.62	-133.80	15.82
295243095383101	420	-95.6406	29.8789	-139.09	-121.93	17.16
295249095364701	438	-95.6133	29.8800	-160.68	-139.53	21.14
295251095264502	518	-95.4458	29.8811	-118.47	-89.30	29.16
295252095300401	290	-95.5014	29.8814	-115.30	-89.38	25.93
295254095361901	440	-95.6056	29.8825	-159.85	-120.82	39.04
295259095065401	475	-95.1153	29.8831	-51.89	-39.46	12.43
295306095270502	451	-95.4514	29.8850	-116.72	-98.26	18.46
295316095562801	305	-95.9414	29.8881	-37.00	-32.67	4.33
295449095084102	458	-95.1450	29.9139	-57.40	-52.12	5.28
295449095084103	213	-95.1450	29.9139	-53.68	-46.36	7.32
295449095084104	319	-95.1450	29.9139	-54.83	-48.86	5.97
295449095084105	591	-95.1455	29.9132	-49.99	-49.17	0.81
295529095043501	297	-95.0802	29.9251	-43.64	-37.04	6.60
295544095462401	295	-95.7742	29.9289	-33.58	-34.07	-0.49
295553095191201	512	-95.3194	29.9319	-92.62	-79.87	12.75
295605095184701	338	-95.3144	29.9347	-66.14	-58.20	7.94
295644095261001	320	-95.4367	29.9458	-115.38	-99.57	15.81
295850095201301	471	-95.3375	29.9803	-89.29	-86.80	2.50
295855095204301	469	-95.3456	29.9819	-90.78	-79.47	11.30
300018095225701	302	-95.3844	30.0075	-83.45	-74.92	8.54
300037095084802	367	-95.1469	30.0106	-51.13	-53.77	-2.64
300050095275301	355	-95.4644	30.0142	-105.85	-82.63	23.22
300053095292601	360	-95.4925	30.0139	-114.28	-79.47	34.81
300123095264501	314	-95.4461	30.0233	-94.99	-75.29	19.69
300133095065101	308	-95.1150	30.0269	-41.60	-46.86	-5.26
300146095241801	171	-95.4053	30.0297	-74.63	-69.87	4.77
300239095212601	221	-95.3575	30.0444	-67.22	-63.41	3.81
300251095265401	327	-95.4475	30.0486	-112.99	-114.61	-1.62
300258095145301	319	-95.2428	30.0661	-50.28	-51.94	-1.66
300301095361301	162	-95.6042	30.0508	-55.70	-68.80	-13.10
300318095553401	170	-95.9261	30.0550	-47.33	-51.18	-3.86
300334095113401	335	-95.1894	30.0631	-61.96	-59.47	2.49
300408095115201	323	-95.1983	30.0692	-54.51	-53.45	1.06
300507095280201	305	-95.4675	30.0856	-105.67	-103.79	1.88
300602095145501	235	-95.2489	30.1008	-47.38	-46.74	0.64
300637095240801	154	-95.4019	30.1122	-51.68	-47.50	4.19
300731095270701	277	-95.4522	30.1256	-102.49	-115.44	-12.95
300732095292101	265	-95.4913	30.1248	-113.13	-135.54	-22.41
300740095262701	304	-95.4411	30.1281	-113.99	-120.34	-6.35
300801095393701	196	-95.6606	30.1339	-85.66	-107.94	-22.28
300811095291702	360	-95.4924	30.1382	-105.95	-148.71	-42.76
300816095274701	288	-95.4628	30.1400	-120.95	-133.90	-12.95
300920095271402	312	-95.4542	30.1561	-108.37	-133.93	-25.55
300925095132501	189	-95.2236	30.1569	-31.32	-40.78	-9.46
300925095264501	308	-95.4461	30.1572	-104.54	-119.29	-14.74
301007095303001	321	-95.5081	30.1689	-114.51	-134.08	-19.57
301033095300602	314	-95.5019	30.1753	-115.61	-132.40	-16.79
301034095283802	305	-95.4772	30.1764	-110.53	-123.19	-12.66

Table AII-II *continued*

301108095293201	306	-95.4922	30.1847	-104.53	-128.63	-24.10
301136095212101	141	-95.3558	30.1933	-47.62	-54.12	-6.50
301220095305502	324	-95.5153	30.2056	-108.11	-141.99	-33.88
301225095315902	341	-95.5328	30.2067	-90.88	-135.52	-44.64
301234095255801	250	-95.4331	30.2094	-92.20	-113.80	-21.60
301256095270401	305	-95.4514	30.2158	-79.72	-123.19	-43.47
301309095313001	271	-95.5247	30.2189	-92.99	-129.92	-36.93
301516095264301	214	-95.4456	30.2547	-70.68	-105.62	-34.94
301853095180701	105	-95.3022	30.3150	-30.41	-31.83	-1.42
301904095414801	119	-95.6967	30.3181	-60.04	-70.77	-10.73
302511095300001	102	-95.5047	30.4203	-70.92	-71.91	-0.99